THE UNIVERSITY OF CHICAGO

PHOTOEMISSION ELECTRON MICROSCOPY OF HETEROGENEOUS TWO-DIMENSIONAL AND BIOLOGICAL MATERIALS

A DISSERTATION SUBMITTED TO
THE FACULTY OF THE DIVISION OF THE PHYSICAL SCIENCES
IN CANDIDACY FOR THE DEGREE OF
DOCTOR OF PHILOSOPHY

DEPARTMENT OF CHEMISTRY

BY
RUIYU LI

CHICAGO, ILLINOIS
AUGUST 2024

Dedication Text

To my family.

TABLE OF CONTENTS

LIST OF FIGURES

LIST OF TABLES

ACKNOWLEDGMENTS

I didn't anticipate my PhD to be such a unique experience before graduate school, joining a brand new lab as the first student, and working on incredibly interdisciplinary research projects, and I owe the credit to my advisor Prof. Sarah King. I am grateful for the opportunity to participate in the design and building of a new research lab, and I appreciate the discussion and guidance Sarah full-heartedly offered that led me to grow into a more independent experimentalist. Sarah has demonstrated an excellent example of a female scientist who strives for her academic success with unbelievable confidence. Her passion for pursuing scientific unknowns, her courage to embrace challenges, and her creativity for problem-solving, shall always be inspiring. I hope those professional qualities continue to live with me in my next career destinations.

In addition to Sarah's supervision, I want to express my sincere gratitude to my committee members, Prof. Greg Engel and Prof. Steven Sibener. Throughout my PhD years, Greg has offered many valuable scientific comments and insightful professional advice. Moreover, the great relationship with his group members is not only substantially beneficial to my research progress but also exceptionally supportive of my milestones in graduate school including candidacy preparation, graduation, and job search. Steve has always been the friendliest lab neighbor. He and his group generously provided immense help for the initial lab construction as well as incisive discussion for project development. I truly enjoyed listening to the sharp comments from Steve each time which forced me to reflect on my experimental design and refine my critical thinking.

I'd like to take the opportunity to thank my wonderful group members, without whom I cannot make my steps through graduate school. I spent most time in the lab with Prakriti, particularly during the difficult time of the pandemic. She built my fundamental knowledge of ultrafast lasers and UHV techniques, and intellectually encouraged my pursuit of excellent science as well as a balanced life. Nasim and I have been alongside each other since our first summer of PhD, and we were the only international students in the group for the longest time. I am so lucky to share similar enthusiasm and recognition with her through the ups and downs in the past six years. I owe many thanks to Janek, who significantly deepened my physics and engineering understanding and elevated my bars for scientific practices. I respect his strict criticisms of my experiments and data interpretation, but at the same time, I cannot appreciate more for his compliments on things that I could have performed better. Joey is an amazing colleague with exceptional patience. I admire that he always puts his head down but is devoted to the most challenging research obstacles. I will miss Clare, for her assertive yet relaxing way of discussion that constantly refreshes my way of thinking. And most importantly, I will miss all the delightful conversations around our cats. Ashley brought so much laughter into the group, not only for her impressive inputs on molecular chemistry, but also for her efforts to drag people to extended group events. I will not forget to thank Anoushka, for sending me so much warmth and fulfillment as a mentor, and allowing me to witness the non-stopping diligence and initiative from a young researcher.

I am so grateful for having my friends around, although they come and go at different phases of my life. My cohort, particularly Sid and Nikita, I wouldn't know how to survive the first long and depressing Chicago winter and many difficult days to come without you keeping me company. Thanks to Ziwan, Cheng, Tong, and many other friends of the small community, I could pull my body out of the lab and step into the wilderness on fabulous road trips as well as taste the unmatched homemade Chinese cuisine. I am deeply regretful to lose my climbing partners, Emily and Da, who introduced the sport that evolved my physical and mental strength. The climbing routine and the gourmet dinners after kept my working weeks bright and full of hope.

My special thanks will absolutely go to Ruian, who has accompanied me dearly through joys and tears for the last two years of this long journey. Other than being great partners and friends, I appreciate his constant punches for intellectual stimulation when I was stuck in low self-esteem. I thank him, above all, for introducing Squirrel, the most wonderful cat, into my life, and elevating the whole experience of emotional support.

Finally, I can't say enough thanks to my beloved family who are thousands of miles away in China, and I owe many apologies to them for not being able to visit often because of the pandemic. Thank you to my parents, who have always trusted me in every life decision, and offered unconditional love and support, even when it's hard for them to see me struggle from afar. I am thankful to have my cousins, for their constant comfort and sharing of the better side of life. Last but not least, many many thanks to my grandmother. She is a respected independent woman of her generation. Her encouragement and inspiration to face life obstacles have sustained me in the past and will still be in the future.

ABSTRACT

The engineering of nanoscale materials can fundamentally determine the macroscopic device functionalities for modern technologies. Similarly, there is also a hierarchy of length scales in nature that connects full-body biological activities with organ-level behavior, and eventually with molecular structures that are also on the nanometer scale. The design for high-performance and reproducible applications is constantly disturbed by structural heterogeneity such as edges, grain boundaries, and variations in domains and phases. The modified material morphology can lead to unique electronic states that impact the ultrafast dynamics of charge transfer or charge recombination. Structural variations are also ubiquitous in biological systems and they are critical to the functional forms of living systems. The knowledge of the structure-property relationship in both fields is highly demanded to achieve controlled, predictable functionalities of either device engineering or a biological body. In this thesis, we present our approaches to entangling the nanoscale heterogeneous information using a novel technique, photoemission electron microscopy, or PEEM. In particular, we will focus on the study of two-dimensional materials and neurological tissues with several variations of PEEM configurations.

Chapter 1 introduces the motivations for this thesis, explains the necessary theory background on photoemission and electron imaging, exemplifies PEEM applications that are closely related to this thesis, and provides a summary of the system of study, including 2D black phosphorus, a perylene diimide (PDI)/MoS_2 bilayer heterostructure, and ultrathin mouse brain sections. Chapter 2 describes the details of the experimental apparatus constructed to realize the research goal. We will cover an ultrafast laser as well as two distinct PEEM systems, and explain the setups for polarization-dependent and time-resolved PEEM experiments. Chapter 3 discusses current progress and challenges for preparing and characterizing mechanically exfoliated 2D materials. Chapter 4 details the study of edge-specific characteristics of 2D black phosphorus using polarization-dependent PEEM. Chapter

5 discusses a time-resolved PEEM study on the nanoscale ultrafast dynamics of PDI/MoS_2 bilayer heterostructures. Chapter 6 introduces the applications of PEEM to neuroscience and demonstrates the potential for fast 3D imaging as well as the contrast mechanism of osmium-stained biological tissues. Chapter 7 extends the previous discussion and presents a few ongoing experiments that open the opportunities of PEEM to wider applications.

CHAPTER 1

INTRODUCTION

1.1 Overview

Tracing the morphological variations and dynamical changes of heterogeneous systems with simultaneously high spatial and temporal resolution is crucial to material science as well as more diverse fields of research such as biology. In particular, visualizing the electronic structure and its time evolution of two-dimensional (2D) materials with nanometer resolution attracts great interest scientifically and technologically. The potential applications of nanofabrication, such as semiconductor-based electronic and optoelectronic devices, intrinsically rely on the behavior of the system out of its equilibrium state. A deep understanding of how spatially varying fundamental interactions may modify the material properties is required on their signification timescale. Similarly, the understanding of brain function, an important branch of neuroscience, demands analogous knowledge of the structure-function relationship between neuronal networks and biological behaviors. The description of fine cellular structures of a nervous system, however, faces tremendous challenges, as the 3D reconstruction of synaptic-level neuron images for a whole mammalian brain (for instance, a mouse brain) would be enormously expensive, inherently hindered by insufficient data acquisition speed. This dissertation describes a technical solution to both fields by employing a novel photoemission electron microscopy (PEEM), which allows the observation of ultrafast dynamics of 2D materials on the nanoscale and shows great potential for fast image collection of large-volume biological samples.

1.2 Heterogeneity of material systems

1.2.1 Morphology-property relationship in 2D materials

Two-dimensional (2D) materials, as a class of low-dimensional nanomaterial, have attracted tremendous research interest since the discovery of graphene two decades ago.[1] 2D materials consist of atomically thin, covalently bonded crystal lattices that are weakly bound to adjacent layers via van der Waals interactions.[2,3] This structure makes 2D materials relatively easy to isolate, either by a "top-down" method such as mechanical exfoliation from a bulk crystal,[4–7] or a "bottom-down" approach such as crystal growth via chemical vapor deposition (CVD).[8–10] The flexibility to construct mixed heterostructure or mismatch the rotational alignment of the atomic layers opens the avenues to create a wide range of van der Waals heterostructures for exploring new physics and applications.

On the nanometer atomic scale, quantitative changes in physicochemical properties connected to the size effect can be observed. For example, 2D materials can exhibit distinct electronic and phononic structures compared to the bulk crystal when they are thinned to a few-layer regime.[11,12] In particular, due to quantum confinement and reduced dielectric screening in the low dimensionality, the Coulomb interactions between charge carriers are significantly enhanced. In semiconductors, this leads to the formation of excitons with extraordinarily large binding energies that dominate the optical and electronic response of the 2D materials.[13] The exciton behaviors, such as charge separation and transport, are subject to modifications in the dielectric environment such as substrates or capping layers. Thus, this tunability facilitates manipulations of charge carrier properties for the design of unique devices.

The real-world application of 2D materials deviates from the ideal models, as chemical and structural inhomogeneity are prevalent during fabrication processing. Figure 1.1(a) and (b) show examples of a polycrystalline graphene sample[9] and a mechanically exfoliated black phosphorus flake[14], where grain boundaries and step edges can be observed on the micrometer scale in the optical images. Morphological disorder perturbs the local electronic structure of the materials and leads to a spatial modulation of physical properties. Raja *et al* measured the local fluctuations of an h-BN encapsulated WS_2 sample and showed the strong spatial variations of material bandgap on a 30×30 μm^2 area (Figure 1.1(c)).[13] Shi et al. addressed the lower-energy edge state in 2D perovskite, demonstrating higher mobilities in free carrier transport along the edges (Figure 1.1(d)).[15] As those spatial variations approach the device scale, the performance of electronics can widely fluctuate, affecting device reproducibility. These heterogeneous performances have motivated intense research efforts to minimize defective sites via chemical engineering[16] or to exploit material imperfections by intentional control.[13,17] PDI8–CN_2 organic thin film transistors fabricated in two growth orientations and the carrier mobility varies by two orders of magnitude depending on the orientation and molecular packing (Figure 1.1(e)).[18] Local strain relaxation can also be modulated on the nanoscale, as shown in Figure 1.1(f), where the reversibility of the strain response of a monolayer WSe_2 flake can be controlled by the amount of force applied on the sample.[19] In all these scenarios, a fundamental understanding of the underlying relationship between nanoscale morphology and the electronic structure, and ultimately the impact on material functionality, is imperative to unleashing the technological potential of 2D materials.

Black phosphorus

This thesis addresses the morphology-property relation by examining two model systems: 2D black phosphorus and an organic/inorganic mixed system composed of a monolayer molecular film perylene diimide and monolayer MoS_2. Black phosphorus (BP) is an elemental layered material that has attracted increasing attention in the 2D community. The electronic structure of BP varies depending on the layer thickness, and the direct optical bandgap is widely tunable from 0.3 eV in the bulk crystal to 1.5 eV in the monolayer limit[20], with carrier mobility of up to 1000 $cm^2 \cdot V^{-1} \cdot s^{-1}$.[21] BP has a corrugated orthorhombic crystal structure with two distinct perpendicular axes, termed "zigzag" and "armchair". Due to the structural asymmetry, BP features unique in-plane anisotropy in optical absorption,[22,23] electronic structure,[12,20] electrical conductivity,[24,25] and phonon propagation.[26,27] The anisotropic properties allow directional control for charge and energy transport, making BP an ideal candidate for the development of waveguides, broadband

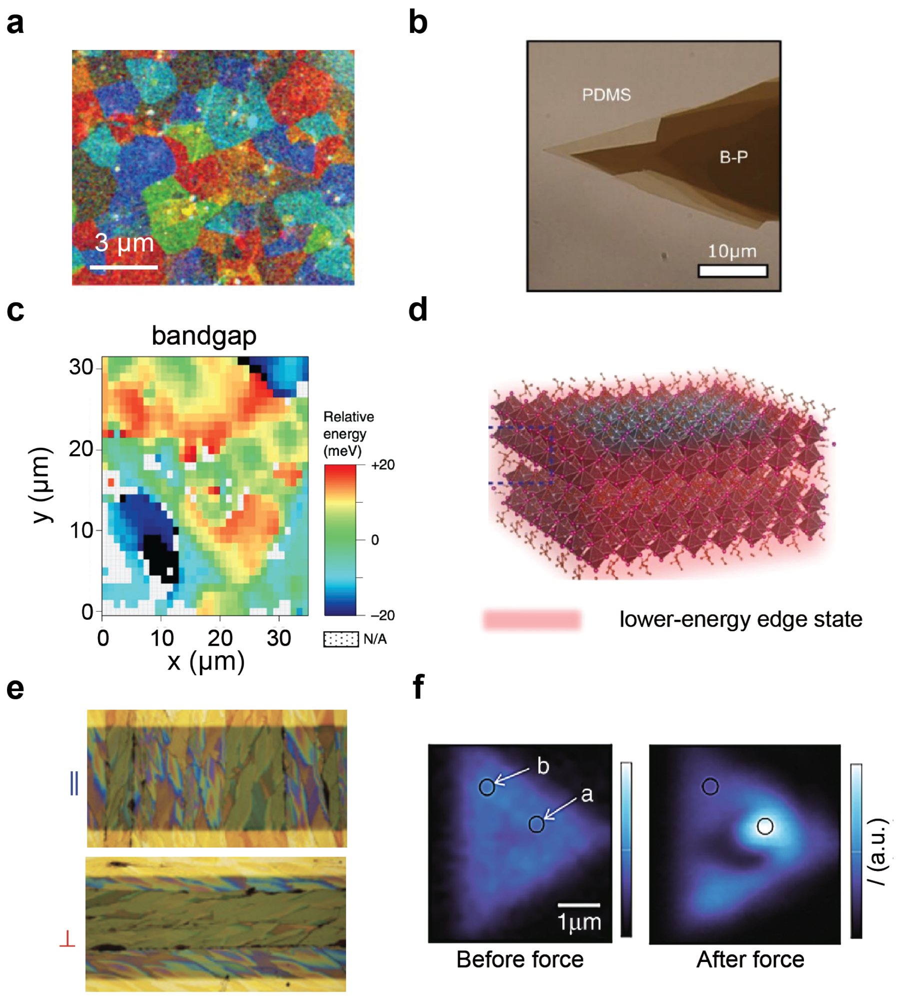

Figure 1.1: Examples of material heterogeneity. (a) False-color image of a polycrystalline graphene sample showing a high density of grain boundaries.[9] (b) Transmission optical image of a black phosphorus flake with regions of different thicknesses.[14] (c) Spatially-varying free-particle bandgap from hyperspatial reflectance spectroscopy of an hBN-encapsulated WS_2 sample.[13] (d) Edge states of 2D halide perovskite.[15] (e) Optical micrographs of parallel (top) and perpendicular (bottom) thin-film-transistor (TFT) devices fabricated from PDI8–CN_2 films.[18] (f) Confocal photoluminescence (PL) images of a strained monolayer WSe_2 before and after applying a force.[19]

photodetectors as well as thermoelectrics.[28–30] Similar to other layered materials, few-layer BP can be isolated by exfoliating from bulk crystals. However, because BP is sensitive to air, and the interlayer interactions of BP are generally stronger than other common materials such as graphene, monolayer BP has been challenging to achieve consistently via mechanical exfoliation. We will discuss experimental explorations in obtaining large-area, high-quality

2D flakes in Chapter 3, and present the work investigating the edge electronic structure of BP in Chapter 4.

TMD heterostructures

Transition metal dichalcogenides (TMD) consist of a large group of layered materials with the chemical form of MX_2, where M is a transition metal and X is a chalcogen. They offer a broad range of variable band structures and tunable bandgaps from insulators to semiconductors and metals. Molybdenum disulfate (MoS_2) is one of the most frequently studied materials in the TMD family. It is a semiconductor and undergoes a transition from an indirect bandgap in the bulk to a direct bandgap in monolayers.[31] MoS_2 has a hexagonal crystal structure, and a monolayer can be obtained either by exfoliation from naturally occurring bulk crystal, or via a bottom-up synthetic approach of chemical vapor deposition.[32] The optical and electronic properties of MoS_2 are heavily dominated by in-plane excitons, and the carrier mobility is on the order of $100\ \mathrm{cm}^2 \cdot \mathrm{V}^{-1} \cdot \mathrm{s}^{-1}$. Other unusual physics has been observed in monolayer MoS_2 such as valley polarization[33] and superconductivity,[34] showing great potential for the development of next-generation electronics in the chip manufacturing market.

The van der Waals integration of 2D materials such as MoS_2 gives rise to intriguing opportunities for superior flexibility and complementary functionalities in device engineering.[2,3] This is realized by vertically stacking the same or distinct 2D material to form 2D heterostructures or moiré superlattices. In those vdW stacks, each layer acts simultaneously, providing synergistic enhancement of overall functionalities. Moreover, surface reconstruction and charge transfer across interfaces in the heterostructure stack present intriguing prospects for fine-tuning the band structure of individual layers. Conventional assemblies of vdW heterostructures have been focused on stacking TMD with TMD, or TMD with another inorganic 2D material such as graphene and hexagonal boron nitride (hBN), and they are typically prepared by transferring one monolayer onto another desired material, usually under an optical microscope with micromanipulators for precise position and alignment control. A more recent direction of constructing 2D heterostructures adopts a bottom-up method to integrate organic semiconductors with TMD materials. The combination of organic and inorganic materials not only boosts the optical absorption efficiency, but also facilitates high chemical tunability of the hybrid structure. Atomically thin TMD can serve as an ultra-flat substrate that enables the growth of thin film molecular crystals via physical vapor deposition (PVD), and the synthesis and growth mechanism have been extensively explored by Mujid.[35] Compared to other integration methods such as spin-coating or drop-casting of molecular films, the controlled growth provides an ordered interface for studying charge transfer or transport in 2D heterostructures, which occurs on a sub-picosecond time scale. As the molecular films have variable orientations and spatially dependent optical properties, the impact of material disorder on the ultrafast dynamics needs to be addressed to fully exploit the industrial use of the hybrid 2D systems. We will describe our understanding of the role of morphologically varying molecular film in the charge carrier dynamics of organic/inorganic heterostructures in Chapter 5.

1.2.2 Electron imaging of nanoscale biological systems

Exploring nanoscale biological systems has long been a pursuit of cell and molecular biology as well as fundamental medical research. Conventional electron microscopy (EM), namely scanning electron microscopy (SEM) and transmission electron microscopy (TEM), uses electron beams to strike the sample surface, and either reflected or transmitted electrons are focused onto the detector to form images with nanometer spatial resolution. EM imaging become a powerful research tool for the direct characterization of structural information,[36] allowing localization of critical biological molecules such as proteins,[37] and even uncovering the dynamical process in living cells.[38]

Fundamentally different from materials, biological samples suffer from their intrinsic properties of high water content, radiation sensitivity, and complex heterogeneity.[39] Biological samples often need to be dehydrated to accommodate electron imaging conditions while preserving the original structure. Besides, most elements in biological samples consist of low atom numbers that typically produce low image contrast in electron imaging. Therefore, optimizations on sample preparation with structural preservation and appropriateness are imperative to attain reliable imaging results. In addition, low electron doses are necessary for SEM and TEM to reduce electron damage to the fragile specimen, but this in turn lowers the signal-to-noise ratio and drastically increases the image acquisition time. Furthermore, the dimension of biological specimens of interest significantly deviates from material systems. The correlation between microscopic structure and material functionalities can be largely learned from 2D projections, whereas for biological samples, a single 2D projection cannot represent the complex structure, which promotes the technological development of 3D imaging in instrumental construction, sample preparation as well as image processing.[40–42]

A riveting application in EM imaging of biological systems is named connectomics. It details the physical basis of neural circuits with large-volume serial electron microscopy (EM) and has emerged as an invaluable tool in the neuroscience armamentarium. Connectomics is an exhaustive mapping of how neurons connect in large volumes of brains enabled by a confluence of advances in 3D EM imaging, sample preparation, and algorithms. However, imaging synaptic resolution connectomes are currently limited to either transmission electron microscopy (TEM) or scanning electron microscopy (SEM). SEM allows for a more reliable section collection of ultra-thin brain slices (UTBS) on solid substrates but is slower due to the inherently sequential nature of scanning microscopy. TEM is wide-field imaging and fast but samples are collected onto grids with thin fragile substrates, increasing the complexity of collecting thousands of UTBS. PEEM combines the strengths of both SEM and TEM, imaging samples on solid substrates with a wide-field imaging technique, and thus has the potential to supersede these techniques. A schematic comparison of the basic imaging concepts of the three types of electron microscopes is shown in Figure 1.2. We detail how we can use photoemission electron microscopy (PEEM) to image UTBS illuminated with UV light and discuss the opportunities for how PEEM can enable the next generation of large-volume connectomes and projectomes in Chapter 6.

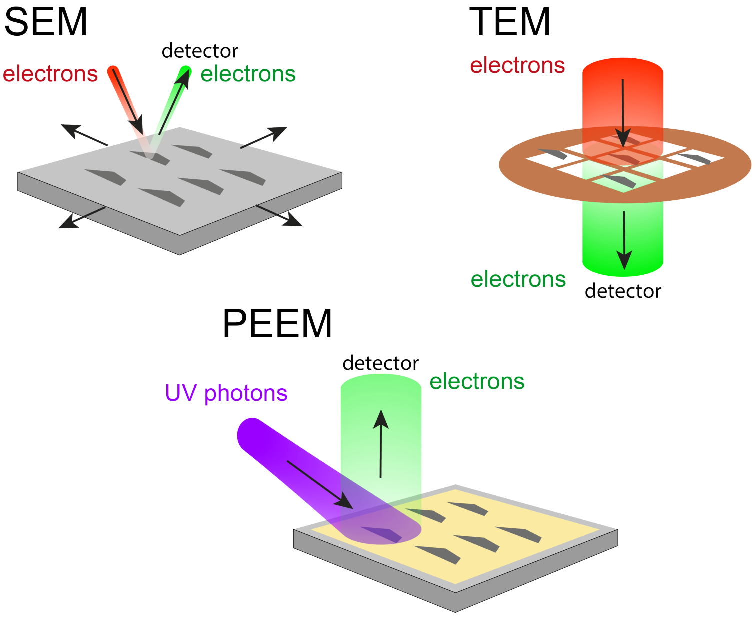

Figure 1.2: Schematic comparison of SEM, TEM and PEEM. Photoemission electron microscopy (PEEM) combines the advantages of SEM and TEM for high-throughput volume electron microscopy (vEM).

1.3 Basic principles of photoemission

PEEM imaging generally consists of two steps: (1) photoelectrons emitting from the sample surface, and (2) focused photoelectrons forming images on the detector. We introduce the basic physical principles of photoemission in this section and will discuss the image formation process in Section 1.4.

1.3.1 General concepts

The fundamental theory behind photoemission is "photon in, electron out". That is, in a photoemission process, the sample is irradiated with light that excites photoelectrons via the photoelectric effect described by Einstein[43] and Lenard.[44] The detachment of electrons from the sample surface occurs when the photon energy of the light exceeds the material work function. In solid-state materials, the work function (Φ) is defined as the energy required to remove an electron from the occupied states of a solid and create a free electron - similar to the ionization energy in molecular systems. The kinetic energy of ejected electrons is related to the electronic structure of the surface by energy conservation

$$E - E_F = E_{kin} + \Phi - h\nu \tag{1.1}$$

where $\mathrm{E} - \mathrm{E_F}$ is the energy of the electrons in the occupied electronic state relative to the Fermi level (E_F), $h\nu$ is the photon energy used for photoexcitation, and $\mathrm{E_{kin}}$ is the kinetic energy of the emitted photoelectrons. The work function of the surface is the energy difference between the Fermi level ($\mathrm{E_F}$) and the vacuum level ($\mathrm{E_{vac}}$). This energy relation is schematically shown in Figure 1.3(a).

In addition, as the parallel momentum ($\mathrm{k}_{||}$) of an electronic state is conserved during photoemission, the angular distribution of emitted electrons contains information about $\mathrm{k}_{||}$ described by

$$k_{||} = \frac{1}{\hbar}\sqrt{2m_e E_{kin}} \sin\theta \tag{1.2}$$

where $\mathrm{m_e}$ is the electron mass and θ is the angle of the emitted photoelectrons (with kinetic energy $\mathrm{E_{kin}}$) with respect to the normal (Figure 1.3(b)). Since photoemission allows the analysis of both kinetic energy and angular distribution, the momentum-dependent electronic structure of the sample under investigation can be directly determined.

The detection depth of a photoemission experiment is defined as the average distance a photoelectron can travel before it scatters inelastically with other particles (thus losing energy). This average travel distance is termed the inelastic mean free path (IMFP). The IMFP depends on the kinetic energy of photoelectrons and the type of materials (organic, inorganic, metal, etc). However, there is a general trend in the kinetic energy and IMFP

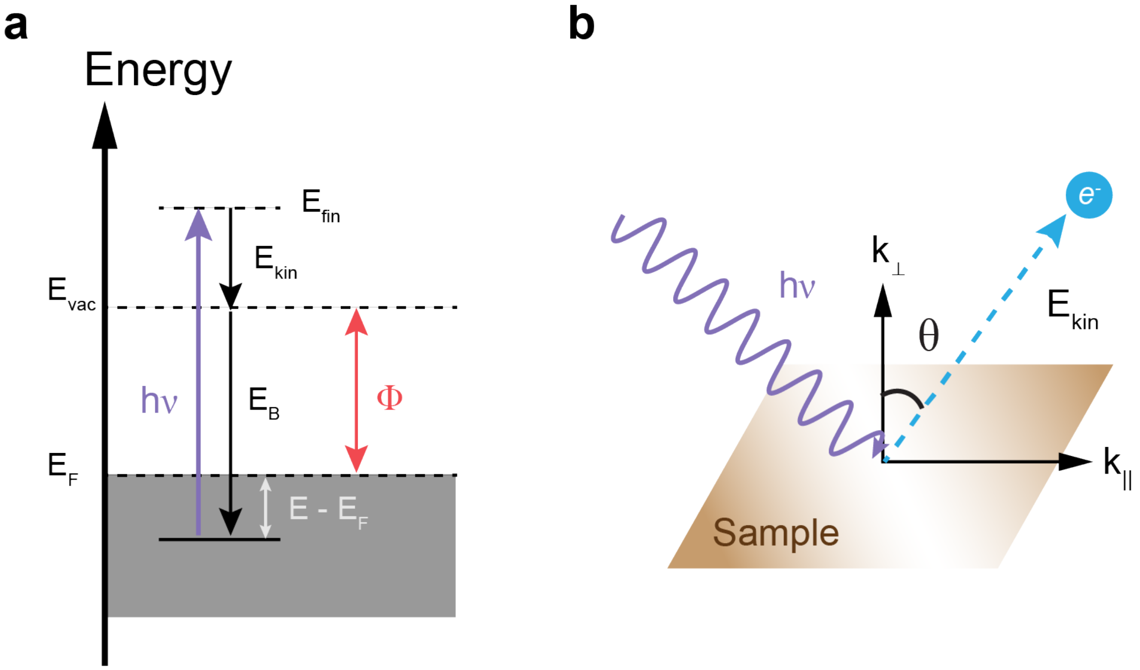

Figure 1.3: Basic scheme of the photoemission process at a metallic surface. (a) Energy diagram showing different energy variables and their relation. (b) Schematic of a photoemission process showing the angular information.

measured from a large group of materials and empirically summarized by researchers in the so-called universal curve, shown in Figure 1.4.[45] This curve is generally a good argument for the surface sensitivity of photoemission experiments, particularly for excitation sources of tens to hundreds of eV (X-ray), as the electrons are primarily emitted from the surface region. For UV experiments, photoelectrons typically have kinetic energies of a few eV, as indicated by the purple shaded box, which puts the probing depth of the experiments presented in this thesis in the range of 4-100 nm. Although this result is only an approximation, it sets the basis for considering the origin of the photoemission signal and assists in data interpretation.

1.3.2 The general interpretation of photoelectron spectra

The proper quantum mechanical treatment of photoemission with the description above is named a one-step model, which forms the basis of the modern theory of photoemission. This model treats all phenomena during the process in a common framework and provides a quantitative interpretation of photoelectron spectra. However, this quantitative analysis

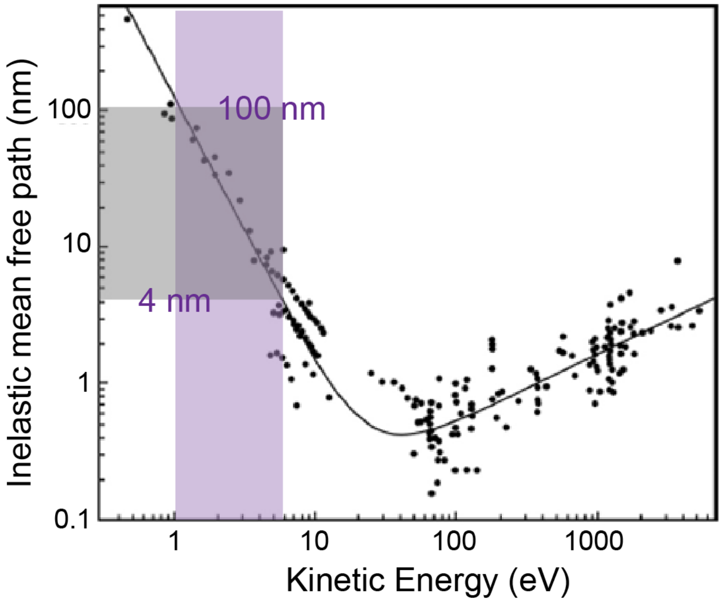

Figure 1.4: The "universal curve" for electron inelastic mean free path in a solid as a function kinetic energy above the Fermi level. The data points are experimentally measured from many materials and the curve is the empirical least square fit. The purple shaded area indicates the typical kinetic energy of photoelectrons in UV photoemission experiments, showing the probing depth is approximately in the range of 4-100 nm. The figure is adapted from the work by Seah and Denc.[45]

means all transition probabilities of electron excitation must be calculated, and the multiple scattering processes of hot electrons at the surface as well as other processes during photoemission must be taken into account.

Alternatively, a three-step mode separates the photoemission of a single electron into three consecutive steps, and is a simpler and more intuitive understanding of the underlying physics of photoemission. The three steps are (1) photoexcitation, (2) hot electron transport to the surface, and (3) transmission of the electron through the surface into the vacuum (or to the detector in a measurement). These steps are interconnected, which makes the three-step model only a qualitative first approximation of photoelectron spectra but useful in many cases. In particular, the lack of accuracy can be a considerable drawback for photoelectron spectroscopy and electron diffraction data analysis, but is less critical for photoemission microscopy where other aspects, such as surface topography and lens aberrations, play more significant roles.[46]

A quantum mechanical description of the photoexcitation process with photon energy **h**ν is governed by *Fermi's Golden Rule*

$$P_{if} = \frac{2\pi}{\hbar} \left| < f|H_{in}|i > + \sum_{n} \frac{< f|H_{in}|n >< n|H_{in}|i >}{\epsilon_i - \epsilon_n} \right|^2 \delta(\epsilon_f - \epsilon_i - h\nu) \qquad (1.3)$$

which gives the transition probability from an initial occupied state $|\Psi_{\mathrm{i}} >$ of the system with energy ϵ_{i} to a normally unoccupied final state $|\Psi_{\mathrm{f}} >$ of the system with energy ϵ_{f} directly or via virtual intermediate state ϵ_{int}, and $\mathrm{H_{int}}$ is the potential coupling the initial state and the final state. The delta function ensures energy conservation.

This formula implies two possible scenarios for a photoemission incidence: (1) the photoelectrons are directly excited by one photon to above the vacuum level, normally referred to as one-photon photoemission, or 1PPE, or (2) a collection of photons, typically with photon energy lower than the work function, promote the electrons out of the surface, referred to as nPPE (n indicates the number of photons involved).

Figure 1.5 represents an exemplary energy scale of a metal during different PE processes. Initially, the occupied electronic states are in the valence band, and electrons form a Fermi-Dirac distribution around the $\mathrm{E_F}$ due to thermal fluctuations. The electronic structure can be directly probed by a photon with energy higher than the work function, and the photoelectrons form a population distribution above $\mathrm{E_{vac}}$ that resembles the initial energy states. The electrons with the highest E_{kin} consist of a Fermi cutoff at the high energy edge of the resulting spectrum, where the energy scale corresponds to the used photon energy hν. Photoelectrons that barely make it to the surface due to energy loss from inelastic scattering form a secondary edge at the low-energy end, and this energy cutoff can be used to determine the work function. In a 2PPE experiment, intermediate states such as valence band maximum (VBM), conduction band minimum (CBM), excitonic states, or trap states, can be accessed via photons with h$\nu < \Phi$. The highest $\mathrm{E_{kin}}$ in this case is the total photon

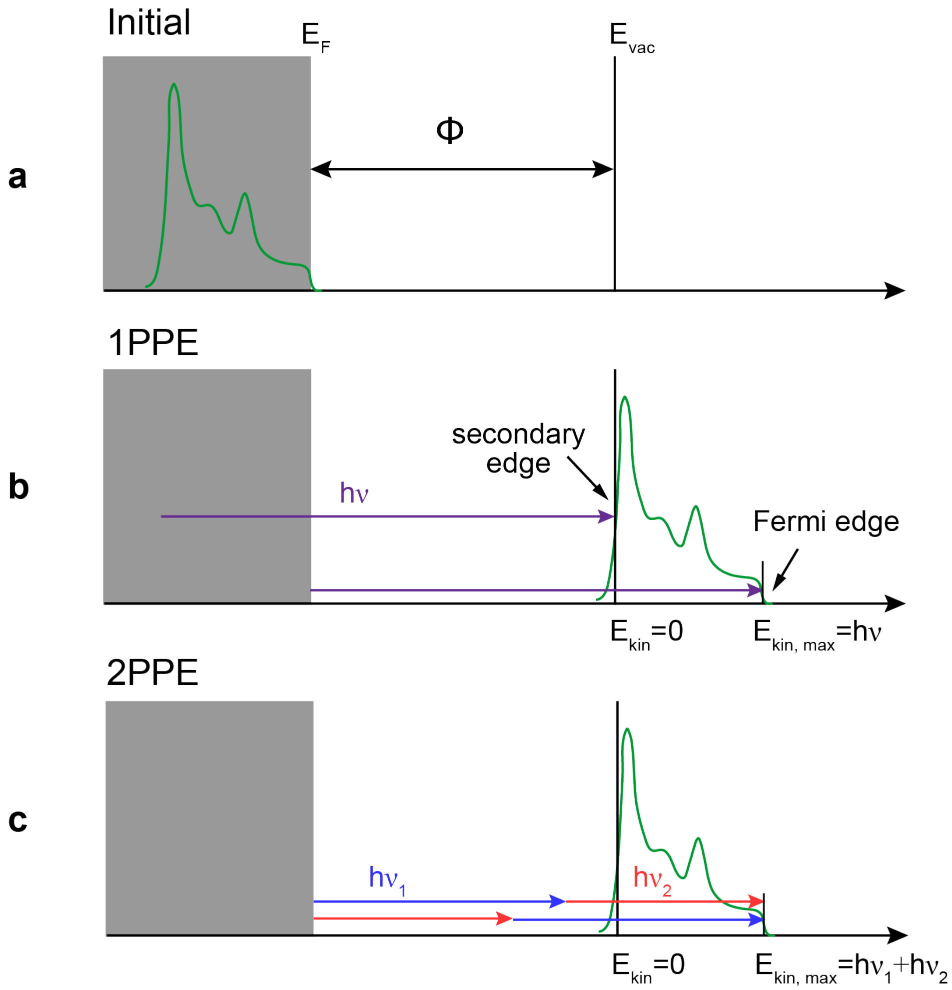

Figure 1.5: Schematic representation of (a) Initial state energy relative to the Fermi level (E_F). (b) One-photon photoemission (1PPE) process. (c) Two-photon photoemission (2PPE) process.

energy $h\nu_1 + h\nu_2$.

1.3.3 Time-resolved photoemission spectroscopy and microscopy

As described above, photoemission processes involving multiple photons permit access to intermediate states. The dynamical processes of the excited electronic states can be directly addressed by applying a pump-probe method to the photoemission measurements, whether spectroscopy or microscopy. The pump-probe method is based on a stroboscopic approach, where "snapshots" of a continuous evolution of the system are captured with a defined time step that's faster than the dynamical event. The basic concept is that, in a solid-state system, the first pulse (pump), as an electromagnetic wave, introduces a perturbation to the system to excite the system to a non-equilibrium state. The intensity variation of certain observables is recorded with an approximately non-perturbing pulse (probe) at a set delay time later until the system recovers to its original equilibrium state. Probing excited state dynamics requires the time resolution of the measurements shorter than the duration of the system evolution. Thanks to the rapid development of pulsed photon sources in the 30-40 years[47], ultrafast processes that occur on a timescale of femtosecond or even attosecond can be readily revealed.

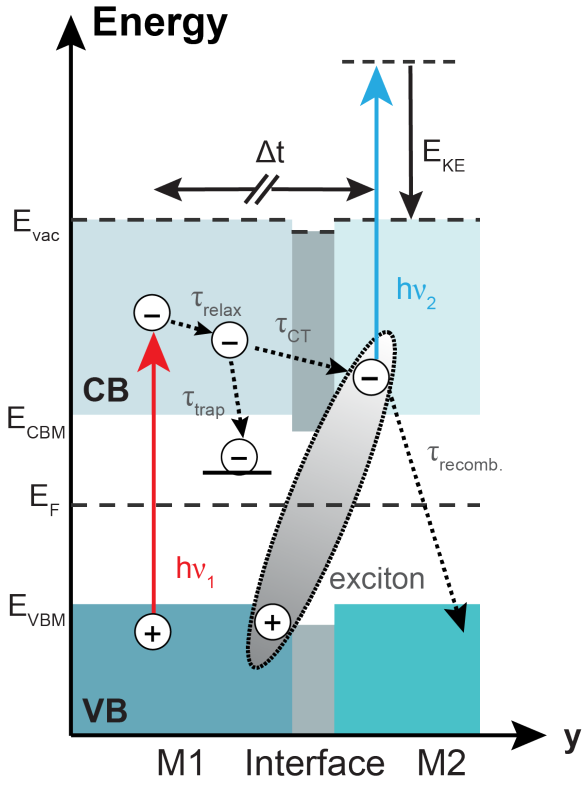

Figure 1.6: Energy diagram for time-resolved photoemission process. M1: Material 1. M2: Material 2. VBM: valence band maximum. CBM: conduction band minimum.

A schematic example in Figure 1.6 demonstrates the time-resolved photoemission process in a heterogeneous solid-state system consisting of two types of materials (M1 and M2) and their interface. The pump pulse ($h\nu_1$) excites the electrons from the valence band of M1 to a previously unoccupied state in the conduction band. The excited electrons can undergo a series of dynamic processes such as thermalization to the conduction band minimum, defect-induced trapping, charge transfer through the interface to M2 to form interfacial excitons, and eventually the electrons relax to the ground state via radiative charge recombination. The probe pulse (hν_2) that impinges after different waiting time Δt can reveal those processes by photoionizing the excited state electrons, and photoemission signals are recorded as a function of delay time to observe the population change.

The attribution of ultrafast dynamics is critically dependent on the characterization of electronic structure, and hence, an energy filtering mechanism is required to preserve the energetic resolution. In time-resolved PEEM, the energy filtering is typically based on a retarding field that essentially acts as a high-pass filter or a hemispherical analyzer. Both methods select electrons of specific energies by filtering out all the other electrons. This filtering mechanism leads to a big disadvantage in TR-PEEM compared to the typical photoelectron spectroscopy, which is inevitably tedious data averaging due to intensity loss. The elongated data acquisition time can, in theory, be reduced by raising the excitation fluence, but then new issues such as the space charge effect, or overpumping the system can emerge that devalue the measurements. Furthermore, the lengthy image collection demands a stricter instrumental as well as sample stability, which adds more experimental stress. This limitation is demonstrated in this thesis, as quantitative analysis of the electronic structure using energy-resolved PEEM data presented in Chapter 5 and Chapter 6 prove to be challenging without sufficient sample lifetime. A time-of-flight detector is a decent solution to overcome electron loss, as it measures all incoming photoelectrons by both position and time. Hence, the total measurement time can be significantly shortened.

1.4 Image formation in PEEM

The understanding of the formation of a PEEM image can be divided into two aspects: (1) how the surface information carried by photoelectrons is transferred from the specimen plane to the image plane, and (2) how the image contrast is generated. The first question concerns the process of focusing the photoelectrons with a properly designed electron lens system. The choice of lens components as well as their geometry eventually determines the best achievable spatial resolution of the PEEM system. The second question leads to discussions on versatile contrast mechanisms stemming from a variety of physical phenomena. Here, we briefly review several of the most common origins of PEEM image contrast that allow the interpretation of physical properties from a diverse range of samples.

Depending on the focal planes governed by different layouts of the electron lenses, information in various domains can be obtained with PEEM. Most experimental results in this thesis detect images in real space, i.e. microscopic imaging. In this mode, photoelectrons from the same points on the sample are focused via a series of electron lenses on a so-called "imaging plane", a representation of the specimen surface with a set magnification is reflected with a camera. Alternatively, in k-space imaging mode, photoelectrons with the same emission angles can be focused at a back focal plane behind the objective, and hence the angular distribution and diffraction patterns can be observed. Another special case is when photoelectrons of the same velocity, i.e. same kinetic energy, are focused together. This resembles a chromatic aberration scenario in itself but allows spectroscopic measurements. Explanations of instrumentation will be covered in more detail in Chapter 2. Here, the discussion on the imaging resolution will be centered on the lateral resolution in real space.

A comprehensive description of photoemission microscopy can be found in the book *Surface Microscopy with Low Energy Electrons* by Ernst Bauer,[46] as well as in a special issue of the journal "Ultramicroscopy" Volume 36, Issues 1-3, 1991.

1.4.1 Resolution limitations

Most PEEM instruments that are currently available in the world detect photoelectrons in transmission geometry, similar to the lens system in a typical transmission electron microscope (TEM) column. The idea behind focusing an electron beam is analogous to the mechanism in an optical system, except that electrostatic fields are utilized for beam manipulation instead of light optics. The heart of an electron lens system is the objective lens, which ultimately determines the resolution and electron transmission of the system (unless the contrast aperture is limited). It is important to remember that the sample is also a part of the objective lens in PEEM, which implies that the surface condition of the specimen impacts the image resolution.

So far, the best reported PEEM resolution that has been achieved is a few nanometers.[48–50] Yet angstrom resolution is theoretically possible, and endeavors have been made by numerous researchers and engineers in both academia and industry to make breakthroughs in this field. Despite that many reasons could influence PEEM image quality, here we provide a few considerations that can make a substantial difference in the spatial resolution and explain the challenges that fundamentally restrict the development.

Electron lenses

The first component of an electron lens system is the objective lens. Normally, a high voltage is applied between the sample plane and the anode of the objective lens to accelerate the photoelectrons into the PEEM column, which naturally turns the specimen into the cathode part of the lens. To a first approximation, the electric field is assumed to be homogeneous, and photoelectrons with a mean initial emission energy E_0 reach a final energy of E. The ultimate resolution δ of the lens system is in general determined by this accelerating field by the relation[51]:

$$\delta \approx \frac{E_0}{eF} \tag{1.4}$$

where F = E/eL is the field strength and L is the length of the field. Based on calculations, the optimal resolution is achieved when the field strength is at 10 kV/mm. Experimentally, this value can be reached in two ways, one is to fix the sample distance and incrementally raise the extractor voltage between the sample and the objective, as it's designed for the FOCUS PEEM system, and the second is to apply a constant voltage but slowly move in the sample distance, as for the ELMITEC PEEM system. The full description of both instruments will be presented in Chapter 2. In principle, once F>10 kV/mm, serious arcing in the vacuum could occur that might cause irreversible damage to the lens components. Hence, the process of increasing the field strength needs to be carefully monitored with the imaging mode and by the pressures of the UHV chamber.

The acceleration field focuses the photoelectrons behind the objective and gives rise to a virtual image that can be further magnified by other electron optics such as projection lenses. Although the functions of other electro-optical components do not relate to the resolution, any imperfections in a specific element may deteriorate the final image quality by deviating the electron beam from rotational symmetry. Astigmatism originating from mechanical defects or misalignment of the optical column can usually be compensated by the octupole stigmators or deflectors placed close to the back focal plane of the objective lens.

Aberrations

As is expected for an optical system, chromatic and spherical aberrations are unavoidable also in an electron lens system. In particular, chromatic aberration in an electron system refers to electrons with different velocities (kinetic energies) deviating from the same trajectory. Typically, slower electrons are more deflected by the same voltage on a lens compared to faster electrons. Spherical aberration occurs when the electrons further away from the optical axis pass through a region with larger electric field strength and are deflected more than electrons closer to the axis. In addition, although a smaller aperture generally helps enhance the resolution, the diffraction effect of the electron beam at small contrast apertures gets more pronounced as the size of the aperture goes down. Thus, the total resolution δ is independently determined by the three terms approximately with the formula[46,51]

$$\delta^2 = \sqrt{\delta_c^2 + \delta_s^2 + \delta_d^2} \tag{1.5}$$

where δ_c, δ_s and δ_d describe chromatic aberration, spherical aberration, and diffraction, respectively. Figure 1.7 graphically summarizes the contribution of each resolution-limiting factor to the total resolution δ as well as aperture radius r for optimum resolution as a function of the initial energy of photoelectrons E_0 for a magnetic triode lens system, as it will be discussed for the design of the ELMITEC PEEM. This information is valuable for the configuration and optimization of a lens system suitable for particular sets of experiments.

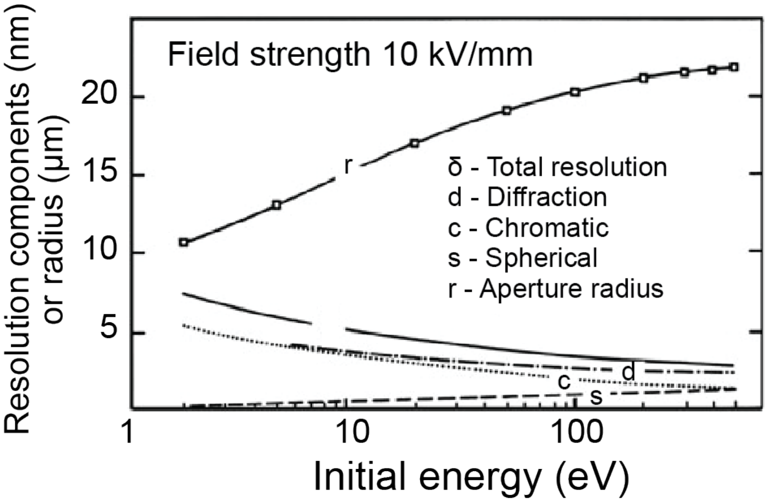

Figure 1.7: Contributions of spherical, chromatic, and diffraction aberrations to the total resolution δ and aperture radius r for optimum resolution as a function of initial energy. The figure is adapted from the book by Bauer.[46]

Samples

So far in this description, we have assumed a homogeneous electrical field within the objective lens for achieving the ideal resolution. However, since the specimen forms an inherent part of the objective, this assumption in the real world is only an approximation, as a perfectly flat sample is unrealistic, and likely also uninteresting. Surface topography (defects, step edges, surface scratches, etc.) distorts the local electrical field, affecting the trajectories of photoelectrons, and ultimately limits the optimum lateral resolution. For samples such as metals or metal oxides, cycles of sputtering and annealing are standard operations for removing contaminants and adsorbates to ensure as clean and flat surfaces as possible. In the past, we have observed a significant resolution enhancement in PEEM images of black phosphorus flakes after heating to remove surface adsorbates.

1.4.2 Contrast mechanisms

The image contrast in PEEM fundamentally results from local differences in photoelectron yields that lead to intensity (or brightness) variations in space. The so-called "features" observed in an image describe changes in photoemission intensity between adjacent pixels. The intensity distribution of a typical PEEM image is usually determined by not one but a complex combination of multiple contrast mechanisms. Here, we introduce several most common mechanisms of contrast generation that help guide the interpretation of PEEM images.

Topographic contrast

The height variations of sample surfaces lead to distortions of the electrical field in the objective lens that modify the electron trajectories. This effect is more pronounced with a light source at grazing incidence. In the PEEM image of a silver grid sample illuminated by a mercury arc lamp (see Figure 1.8(a)), the edges of the geometric structures that are oriented toward the photon source appear brighter than the opposite sides. Interference effects have also been observed along the edges of geometric structures, where interference fringes of incoming light with scattered light off of the edges of a sample are observed both with continuous-wave and pulsed light excitation.

Work function contrast

Differences in chemical compositions or crystallographic orientations cause variations in local work function, and thus the photoelectron yields change across the sample surface. Work function contrast is the dominant mechanism in UV-PEEM involving low-energy electrons, and can be used for mapping materials with different chemical components or crystallographic domains. For example, Figure 1.8(b) shows a relatively thick black phosphorus flake on a silicon (100) substrate (with native oxides). As bulk black phosphorus has a work

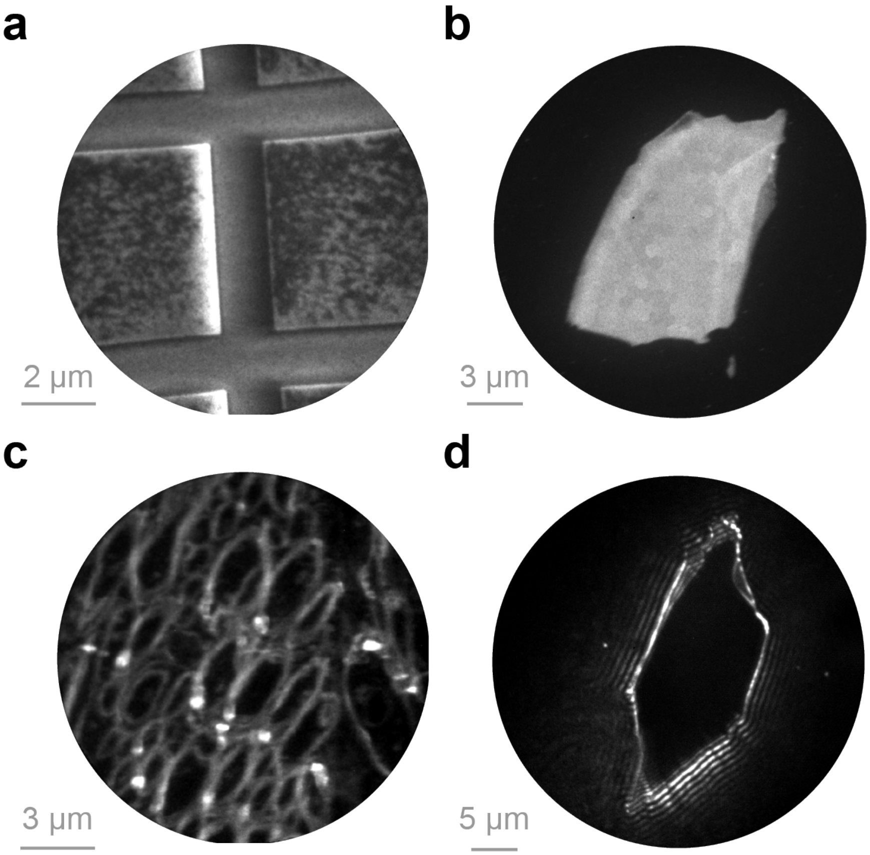

Figure 1.8: PEEM examples of different contrast mechanisms. (a) Topographic contrast: a silver grid sample illuminated by a Hg discharge lamp at gracing incidence. The edges that are towards the light are brighter than the opposite direction. (b) Work function contrast: a black phosphorus flake on a silicon substrate with native oxides. BP has a lower work function than silicon and silicon oxides and thus has stronger photoemission. (c) Density of state contrast: an osmium-stained mouse brain sample with rich myelinated axons. The intensity variations are a result of the difference in density of states modulated by the osmium compounds. The details of this contrast mechanism will be demonstrated in Chapter 7. (d) An example of other contrast mechanisms: a black phosphorus flake on a polycrystalline graphene substrate imaged by an 800 nm femtosecond laser. Strong fringes are observed along the edges of the BP flake. The origin of the fringes is still to be investigated.

function of <4.5 eV[52,52], whereas the work function of Si(100) is about 4.8 eV[53], and for SiO_2 is 5 eV[54], black phosphorus has significantly higher photoemission intensity than the background and thus allows for resolving the sharp edges.

Density of state contrast

Materials possessing different electronic structures have different amounts of available electrons in the occupied states upon photoexcitation, and the distribution of the density of states is reflected by varying brightness in the PEEM image. With low-energy UV photons, the contrast originates mostly from the density of states around the Fermi level. This is exemplified by determining the oxidation states of osmium for biological staining in Chapter 7 (Figure 1.8(c)). Elemental mapping is achievable with X-ray light sources where core-level electrons can be accessed as a result of characteristic absorption from occupied core levels.

Other contrast mechanisms

Additional physical phenomena that alter the local electrostatic microfield can give rise to distinct image contrast in PEEM. For example, the distribution of dipole moment, due to the anisotropic optical selection rule, differences in ferroelectric domains, or variations in magnetization, can create areas of higher or lower electron flux in the sample plane with a polarized excitation source. Furthermore, surface plasmon polaritons, an oscillatory electric field due to the coupling of excited charge carriers and photons, can launch periodic fringe patterns at step edges or terraces (Figure 1.8(d)). These contrast mechanisms are beyond the scope of the experiments described in the thesis, but the purpose here is to showcase the versatility of PEEM applications.

1.5 PEEM applications in surface science

As discussed above, PEEM can be utilized to probe a diverse category of physical properties. In this section, we illustrate the applications in surface science primarily with low-energy UV-PEEM that are mostly relevant to the work in this thesis. We are also going to briefly review a few other practical cases that demonstrate the great potential of PEEM in those fields. Each method has strengths and limitations and usually complementary characterizations are necessary for a complete interpretation of a physical phenomenon. Nevertheless, PEEM provides unique contributions for materials or scientific questions that are suited to this method.

1.5.1 Surface microstructure

Imaging the morphology of a material surface is one of the first applications of PEEM. A UV photon directly probes the electrons in the valence band, and the contrast mechanism is dominant by work function contrast. For surfaces with complex topography such as step edges, facets, etch pits, and intersections of different planes, light diffraction also contributes to the image contrast, and surface microstructure can be resolved. A common example is PEEM imaging of polycrystalline metals based on work function differences.[55]

Another aspect of morphology characterization is to determine crystal orientation based on the manipulation of optical excitation rather than the intrinsic work function difference. This is realized by employing a polarized light source, which allows the determination of the orientation of molecular or inorganic crystals that are subject to selective absorption. We have successfully implemented this technique (polarization-dependent PEEM) by varying the linear polarization of a pulsed laser to map the orientation of 2D black phosphorus (Chapter 4) and a single crystalline molecular film (Chapter 5). Circularly polarized light has also been utilized to resolve magnetic domains that are spin-sensitive.[50,51]

1.5.2 Ultrafast dynamics

Short-lived electronic states can be probed by time-resolved PEEM. We have discussed the basic principles of time-resolved PEEM in Section 1.3.3. Here we briefly introduced a few scenarios where time-resolved PEEM showcases the unique capability of resolving ultrafast dynamics with high spatial resolution. In particular, we provide results that focus on the study of carrier dynamics of layered materials which fundamentally govern the characteristics of semiconductor devices, and those studies that are intimately related to the work presented in Chapter 5.

The early development of time-resolved PEEM extensively probed plasmon dynamics utilizing an interferometric configuration. The interactions of surface plasmon and light waves can be resolved as fringy patterns by precise control of the phase between two identical pump pulses, and the interferometric-TR-PEEM has been successfully applied to visualize surface plasmon polaritons in a series of silver and gold nanostructures.[56,57] However, those studies were mostly limited to metallic samples.

The evolution of the technique continues to push for imaging more complex samples and investigating more sophisticated physical processes. Koshihara et al[58] and Dani et al[59] later reported using time-resolved PEEM to directly image the electron motions on the surface of GaAs or an InSe/GaAs semiconductor lateral heterojunction. The electron movements within a flake as well as the transport process between the heterojunction can be resolved at different time steps. Further modeling of the intensity profile allows the analysis of electron diffusion, where the diffusion velocity and gradient potential can be calculated from the position deviation from the original population. Within a decade, TR-PEEM has progressed to investigate the ultrafast dynamics of complicated materials including Cd_3As_2 semimetal,[60] $CsPbBr_3$ perovskite,[61] single layer WS_2,[62] single layer WSe_2,[63] multilayer WSe_2[64] and the newly emerging material MXene.[65] The results of TR-PEEM reveal local variations of electron dynamics typically reflected by the differences in relaxation time over space due to surface inhomogeneity. The correlation between material morphology and ultrafast carrier dynamics provides important insights into the interpretation of optical spectroscopy where nanoscale sample variations are buried in the ensemble-averaged measurements.

A full exploitation of the energy resolution and momentum resolution of TR-PEEM enables its unprecedented potential in interrogating fundamental questions in material systems. Several groups have reported spectroscopic TR-PEEM, but those experiments are restricted to a narrow k-space near the Γ point as a UV source of a few eV is unable to access higher momentum space. TR-PEEM experiments utilizing extreme UV (XUV) photons via high-harmonics generation (HHG) and a time-of-flight detector successfully observed the exciton formation process in a monolayer WS_2[66] and WSe_2/MoS_2[67] moiré superlattices on the femtosecond timescale in both real space and momentum space. The experimental realization of multi-dimensional PEEM in space, time, energy and momentum, holds great promise for exploring the rich charge carrier landscape in complex layered material systems.

1.5.3 Biological imaging

While PEEM and related imaging techniques have been used extensively in the field of material science, biologically focused PEEM has not received equally significant attention. The initial attempts to apply PEEM to biological samples date back to the early 80s[68–71]. At that point, whether biological samples could be imaged and how image contrast was generated was a general question for the early researchers in this field. The first question naturally arises from how to incorporate biological tissues or cells, typically soft and non-conductive, into a cathode lens system while preserving good imaging conditions. A few issues needed to be addressed to have the biological samples compatible with PEEM: (1) the biological specimens need to be dried to accommodate the ultra-high vacuum (UHV) environment, (2) the samples need to be as flat as possible to ensure high-quality imaging, and (3) the samples need to be conductive, or in good electrical contact with a conductive substrate. There has been tremendous improvement in sample preparation of biological materials since the early stage of bio-imaging with PEEM, and a great deal of ideas were borrowed from scanning electron microscopy (SEM) imaging of biological samples, where mature and robust protocols are well established. Now the standard treatment is that biological samples are first dehydrated sufficiently by either freeze-drying or by replacing water by passing the sample through organic solutions with gradient concentrations. The preparation of intact samples also requires fixation to preserve the biological structure.

Most cellular specimens have three-dimensional profiles rather than being flat. As a result, topographical contrast can predominantly contribute to cell images with PEEM. Typically, the cell edges usually display a remarkably bright feature, whereas regions that correspond to steep slopes appear shadowed. Although fine topographical details are expected to be properly resolved, the ultimate resolution is fundamentally limited due to the unevenly distributed electrical field between the sample and the anode of the objective lens, as discussed in Section 1.4.1. An alternative method takes advantage of biological sections that are thinly sliced from resin-embedded tissues. Appropriately cut sections typically form a surface with a flatness of a few nanometers and can be transferred to a solid substrate that's easily compatible with a PEEM sample holder. This modified sample preparation provides great potential in resolving cross-sections of biological tissues for the understanding of their physical or chemical structures[72] and sets the basis for doing connectomics, or inherently 3D tomography, with electron microscopy, as we will cover in more detail in Chapter 6.

The last but also most important concern is the charging issue for non-conductive biological specimens. If there are insufficient electrons to replenish the emitted photoelectrons, a positive charge will build on the sample surface that severely distorts the spatial resolution. A general treatment in SEM, which also requires conductive samples, is to coat the sample surface with a conductive layer of metal or carbon that is transparent to electron beams. Thin film coating has been applied to X-ray PEEM, as the mean free path of photoelectrons can be as deep as >10 nm, and the biological contrast below the surface is not disturbed.[72] In the case of UV-photon, we have not achieved success with metal coating largely due to the surface sensitivity of photoemission. The other solution, which is what we adopted in Chapter 6, is to use a conductive substrate. Intuitively, having the conductive medium below the insulating sections may not seem as effective, as the edges of the sections don't necessarily form sufficient electrical contact with the substrate. However, we have not observed any charging effect from this configuration over tens of imaging sessions, indicating the effectiveness and consistency of this method.

Additives to the biological specimens can potentially give rise to enhanced sample performance, which is the second question we are going to discuss: the contrast mechanism. We realize that topography forms the primary contrast for the non-flat samples. For flat samples (thin sections), or flat regions in non-flat cellular samples, the photoemission intensity variations are small, and detailed features cannot be readily resolved. This is interpreted as a direct result of similarities of the biological substances in the electronic structure around the Fermi level that can't be distinguished using UV excitation. To overcome this challenge, biological stains have been applied to enhance the image contrast. Originally, colloidal gold or silver nanoparticles were used by Griffith and his team for labeling, which simultaneously increases the biological contrast. Nowadays, biological specimens are more effectively stained with heavy metals and one of the most common ones is osmium, which has demonstrated improved contrast both for conventional SEM/TEM imaging and for PEEM. Phenomenologically, the addition of staining reagents leads to a modified electronic structure of the biological samples, and the metallic particles have the complementary effect of boosting the overall sample conductivity. We will provide a comprehensive understanding of the contrast mechanism, particularly on why and how osmium staining is beneficial in general to biological imaging in PEEM in Chapter 6. A more recent field of using X-ray PEEM for bio-imaging has been developing rapidly. PEEM can be combined with X-ray spectroscopy (XPEEM) which allows chemical imaging of biological objects based on selective X-ray absorption of core-level electrons. This technique has been applied to elemental mapping of biominerals[72] and medically important distribution of elemental chemical states.[72,73]

1.6 Summary of the systems studied

2D black phosphorus

In Chapter 4, we use polarization-dependent PEEM to elucidate the critical relationship between the morphology and electronic structure of few-layer black phosphorus. Orthorhombic, corrugated van der Waals materials are demonstrably anisotropic in their electronic and phonon transport, making them crucial for integrating intrinsic directionality into 2D material-based applications. In addition, the most well-known of these materials, black phosphorus, supports anisotropic charge, phonon, plasmonic, and polaritonic behaviors, making it well-suited for the development of polarization-dependent photodetectors and thermoelectrics, as well as directional waveguides and light emitters. However, black phosphorus is also rich in nanoscale structural morphological features - edges, defects, grain boundaries, wrinkles - which strongly modulate the intrinsic behavior. This spatially dependent variation is typically on the 10-100 nm scale, well beyond the reach of conventional optical microscopy (>200 nm) and too large for the field of view of techniques such as TEM and STM (<20 nm). By investigating the polarization-dependent differential absorbance between the armchair and zigzag directions of the lattice, we find that the edges of few-layer black phosphorus flakes show a significant phase shift of ± 20° in the polarization of maximum absorption with respect to the armchair axis. Our observations suggest a significant spatially dependent modification to optical transitions and to the symmetries of the valence band and conduction band in the vicinity of the edge, which underscores challenges to the current design of black phosphorus nanoscale devices, as well as opportunities for spatially sensitive, directed control of light-matter interactions.

PDI/MoS_2 bilayer heterostructure

In Chapter 5, we detail the polarization-dependent, time-and energy-resolved PEEM imaging of a perylene diimide/MoS_2 bilayer heterostructure to reveal the ultrafast carrier dynamics on the nanoscale. Integrating organic semiconductors with high absorption efficiency with inorganic layered materials with superior carrier mobility enables enhanced performance in optoelectronic devices. In particular, the advancements in the synthetic growth of large-scale monolayer molecular crystals on atomically flat monolayer 2D materials, namely transition metal dichalcogenides, offer an excellent model system to study charge carrier behavior at a well-defined interface. However, the relationship between ultrafast dynamics and molecular ordering has not been fully investigated, due to a lack of simultaneous availability of femtosecond temporal resolution and nanoscale spatial resolution. Combining linearly polarized ultrafast pulses with photoelectron imaging, we identify the molecular orientations within each single crystalline domain and find a consistent reduction in dichroism, thus lower crystallinity, at crystal edges. By analyzing the nanoscale film morphology with the corresponding carrier dynamics, we reveal that molecular film has an insignificant effect on the overall decay dynamics of the heterostructure, and energy-resolved measurements suggest a hybrid state formation at the initial excited electronic states. Our results provide important insights into the role of disorder in integrated organic/inorganic hybrid systems, as well as inspire intentional control of 2D architecture to promote chemically flexible solutions for desired functionalities.

Ultra-thin mouse brain sections

In Chapter 6, we demonstrate that osmium (IV) is the chemical species present in lipid bilayers of biological tissues upon osmium tetroxide staining and identify the likely generation mechanism. Osmium tetroxide(OsO_4) is ubiquitously used to selectively stain lipid membranes for subcellular imaging using electron microscopes. Despite the prevalent success of osmium staining in the past few decades, until now we have not known the chemical speciation that provides this imaging contrast and why it enhances the conductivity of biological materials. This has directly inhibited our ability to develop chemical reactions for high-contrast, high-resolution images using non-toxic staining methods. Using the imaging technique of PEEM for complex biological tissue with nanometer resolution, we show that osmium dioxide (OsO_2) nanoaggregates form at lipid membranes via a series of redox reactions during the staining process. The resulting Os (IV) nanoparticles have a metallic electronic structure that not only provides sample conductivity but also strongly modifies the electron density of states of the stained biological materials, leading to a substantial photoemission intensity difference between the lipid-rich and lipid-free regions.

CHAPTER 2

EXPERIMENTAL APPARATUS

2.1 Overview

This chapter includes a lengthy discussion of various instrumentation that has been implemented in the King lab since the beginning. These experimental apparatus not only benefited the research work presented in this thesis but also set the foundation for numerous exploratory directions for future experiments. First, a high power, high repetition rate ultrafast laser system that's specialized for photoemission will be introduced. Next, two types of photoemission microscopes will be discussed with more information on the electron lens components. Lastly, the setups combining the laser and electron microscopes for specific experimental goals will be described. For practical strategies for optimal alignment, details for components of vacuum chambers as well as instructions on software operations, the reader should refer to Appendix A.1 and A.2.

2.2 Femtosecond laser system

2.2.1 Optical layout

Ultrashort laser pulses are required for polarization-dependent PEEM measurements that involve multi-photon processes (described in Chapter 4) as well as time-resolved PEEM experiments to observe femtosecond dynamics (described in Chapter 5). Here, we employ a commercial femtosecond laser system from Class 5 Photonics, consisting of a pump laser, an optical parametric chirped pulse amplifier (OPCPA), and the second/third harmonic generation. A schematic overview of the laser system is shown in Figure 2.1, which is comprised of one compartment for fundamental outputs (top) and a second one for the harmonic generations (bottom).

An OPCPA merges the advantages of both laser chirped-pulse amplification (CPA) with the scheme of optical parametric amplification (OPA). As a result, femtosecond pulses can be

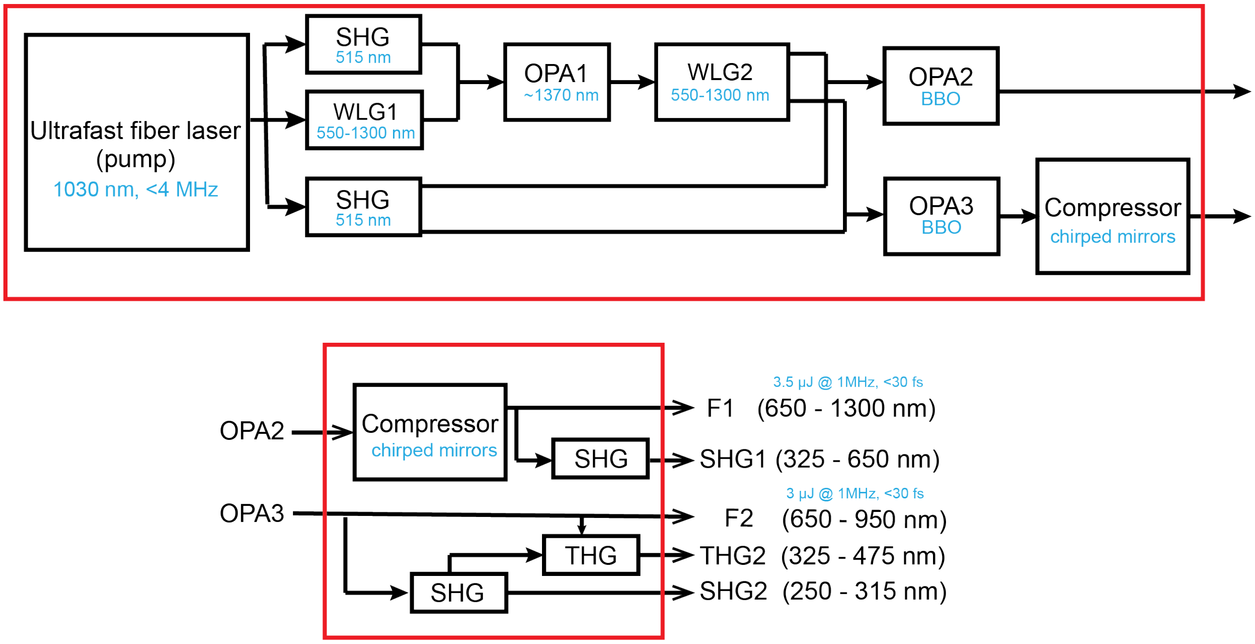

Figure 2.1: Schematic overview of the Class 5 OPCPA system (Drawing isn't to scale). Top: pump laser and the OPCPA process for generating two fundamental outputs. Bottom: the harmonic generations.

amplified to high peak energy at high repetition rates, ideal for PEEM imaging. A Yb-based Coherent Monaco fiber laser (60 W at 1030 nm, $<$350 fs) acts as the pump source for the OPCPA process. The strong near-IR beam is split to generate photons for seed generation and amplification in the OPCPA. The broadband seed pulse (550-1300 nm) is generated via a two-step white light generation (WLG1 & WLG2) process, both using a 5 mm Yttrium aluminum garnet (YAG) crystal. The pump pulse (515 nm) is frequency-doubled from a portion of the 1030 nm beam via a beta barium borate (BBO) crystal. Two fundamental outputs (OPA2 & OPA3) are generated by double-pass amplification processes. By tuning time delay and phase matching, spectral ranges of 650-1300 nm and 650-950 nm are obtained from OPA2 and OPA3, respectively. At full performance, both outputs have $>$2 W power at 800 nm with overnight root-mean-square (rms) stability of under 1%. The wide wavelength range enables us to pump specific optical transitions.

To access a broader spectral range in the visible and ultraviolet (UV), the two fundamental outputs go through separate nonlinear processes to double or triple the frequencies via BBO crystals. The SHG of OPA2 covers 350-650 nm, and the SHG and THG of OPA3 cover 325-475 nm, and 250-315 nm, respectively. The conversion efficiency for the SHGs at 800 nm is up to 50-60% with <1% rms stability. For the THG $\sim$ 5% conversion (>100 mW) has been possible with an rms stability is <2.5%.

The repetition rate of the pump laser was originally tunable from 100 kHz to 1 MHz. After the service visit in April 2022, the system was upgraded to 4 MHz, with additional lenses to accommodate the difference in beam focusing. A high repetition rate with high peak energy enables fast data acquisition while avoiding space charging. In this thesis, the BP experiments (Chapter 4) were conducted at 1 MHz, and the PDI/MoS_2 work (Chapter 5) was conducted at 4 MHz.

2.2.2 Pulse compression

Chirped mirror (CM) pairs are used as optical compressors to compensate for the positive group-delay velocity (GDD) dispersion from transmissive optics. Two sets of CMs are used for the visible (650-950 nm) and near-IR (950-1300 nm) ranges of OPA2, respectively. They are both installed in the harmonics generation box and the alignment is interchangeable with a flip mirror. The compressor for OPA3 is installed in the same box as the OPCPA system and covers the entire spectral range. All compressors use the double-pass design with a folding mirror to make up for the restricted length on the CMs. The best compression result at around 800 nm is achieved with ~28 bounces for the visible compressors for OPA2 and OPA3 and ~20 bounces for the IR compressor of OPA2, and the adjustment of bouncing numbers is required to accommodate different wavelengths and variable laser status, such as the filament position for WLG2.

The pulse duration of the fundamental outputs of the amplifiers is determined by a home-built frequency-resolved optical gating (FROG, Newport) setup. FROG measures the auto-correlation of the fundamental beam in the time domain as well as in the frequency domain simultaneously, which resolves the full properties of the beam.

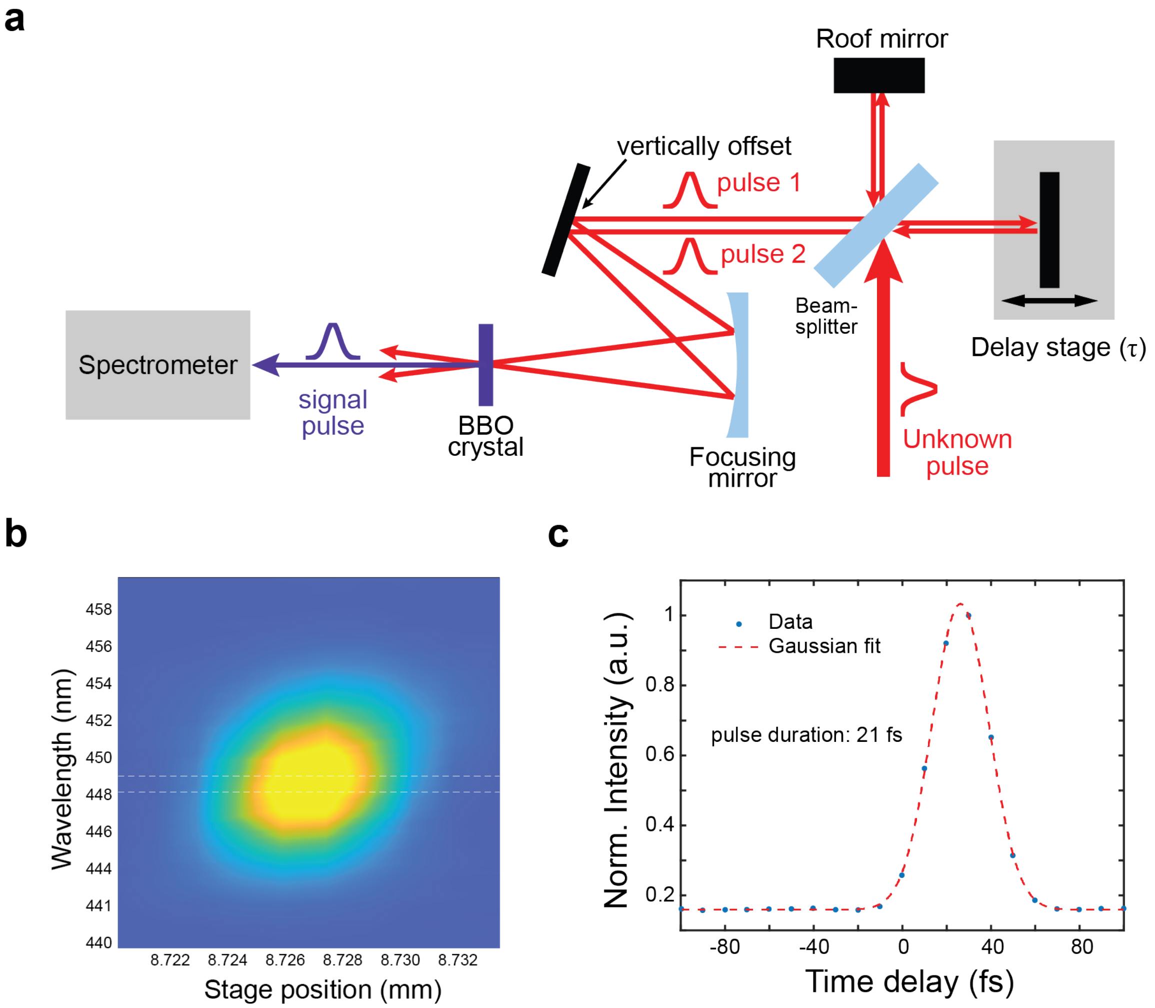

Figure 2.2: (a) Schematic of the FROG setup. (b) A representative FROG trace of a 900 nm beam. (c) The Gaussian fit of the normalized intensity integrated from the spectral window defined by the dashed lines in (b).

A simplified schematic of the FROG setup is shown in Figure 2.2(a), where the incoming unknown pulse is split into two identical arms, and the cross-correlation of the two pulses is recorded by the intensity variation of the second harmonic generation (by a BBO crystal) in time and frequency. A representative FROG trace of a 900 nm beam from one of the fundamental outputs is displayed in Figure 2.2(b) which shows a symmetric profile in both axes. Assuming the incoming beam is Gaussian, the spectrally integrated intensity profile in the time domain can be fitted to obtain the width of the cross-correlation (Figure 2.2(c)). The pulse duration is extracted based on the relation:

$$\sigma_{cc}^2 = \sigma_1^2 + \sigma_2^2 \tag{2.1}$$

We define the pulse duration of the incoming beam as the full width at half maximum (FWHM) of the Gaussian profile, which can be calculated from

$$\mathrm{FWHM} = 2\sqrt{2\ln 2}\,\sigma \tag{2.2}$$

where σ is the standard deviation of the Gaussian function. Thus, the pulse duration of the 900 nm is determined to be 21 fs. To achieve the best compression result, an optimal amount of fused silica (for visible) or SF11 (for near-IR) windows need to be inserted in the beam path to compensate for excess negative GDD from the CM compressors. For bluer wavelengths (<700 nm) where appropriate BBO crystals are costly and less accessible, cross-correlation measurements using photoemission are used for determining pulse durations, which will be discussed below in Section 2.4.1.

2.3 Photoemission electron microscopes

Photoemission experiments have to be performed in an ultra-high vacuum (UHV) environment, typically in the range of 10^{-6}-10^{-11} mbar. The harsh vacuum condition is to avoid surface contamination due to the surface sensitivity of the technique, to preserve the mean free path of electrons as well as to prevent possible arcing at high electrical voltages. For electron microscopy, UHV chambers are required additionally to prevent image distortion from electron collisions. The King lab has two available PEEM systems manufactured by FOCUS GmbH and ELMITEC GmbH, respectively. The FOCUS PEEM is a commercially purchased system with an attached preparation chamber for sample preparation, and the new instrument was installed in November 2019. The majority of the work presented in the thesis, except for some portion of the biological imaging results in Chapter 6, was conducted in this system. The ELMITEC PEEM was a free loan from the Gilbert Lab at the University of Wisconsin and was transported from the Argonne National Laboratory in May 2023. This PEEM was renovated with assistance from ELMITEC in November 2023. At this end of the service visit, base pressures of 10^{-11} mbar was achieved and the imaging functionalities were recovered. Here, we provide descriptions of the two distinct PEEM systems and introduce the differences in electron lens designs for realizing specific experimental goals.

2.3.1 The FOCUS system

The FOCUS PEEM is comprised of an electrostatic lens system and an image acquisition assembly. The layout of the FOCUS PEEM is depicted in Figure 2.3. The sample is uniformly illuminated by a Hg lamp or laser, as explained above. Through a one-photon process with UV light or a multi-photon process with pulsed lasers at visible or near-IR wavelengths, photoelectrons are ejected from the sample surface with kinetic energies typically of a few eV. Up to 16 kV extractor voltage (normally 12 kV is used for operation) is applied to focus the photoelectrons through an electrostatic tetrode. A contrast aperture that is piezo-driven and size-adjustable (30 μm, 70 μm, 150 μm, 500 μm, 1750 μm) is positioned at the back-focal plane of the objective lens to enhance the image resolution. An octopole stigmator/deflector is placed right behind the contrast aperture for correcting axial astigmatism from all orientations. A transfer lens collimates the diverging beam through a second stigmator/deflector to correct non-spherical aberrations of the angular distribution. A continuously variable iris aperture is installed at the first image plane to further enhance the image resolution and contrast. Two projective lenses magnify and focus the images onto a pair of chevron-stacked micro-channel plates (MCP), and the photoelectrons are converted to visible light by a phosphor screen, eventually imaged by a complementary metal oxide semiconductor (CMOS) camera (Hamamatsu). The lens power supplies and data acquisition are controlled by the ProNanoESCA software designed by FOCUS, and details for operational instructions during image acquisition are provided in Section A.2.

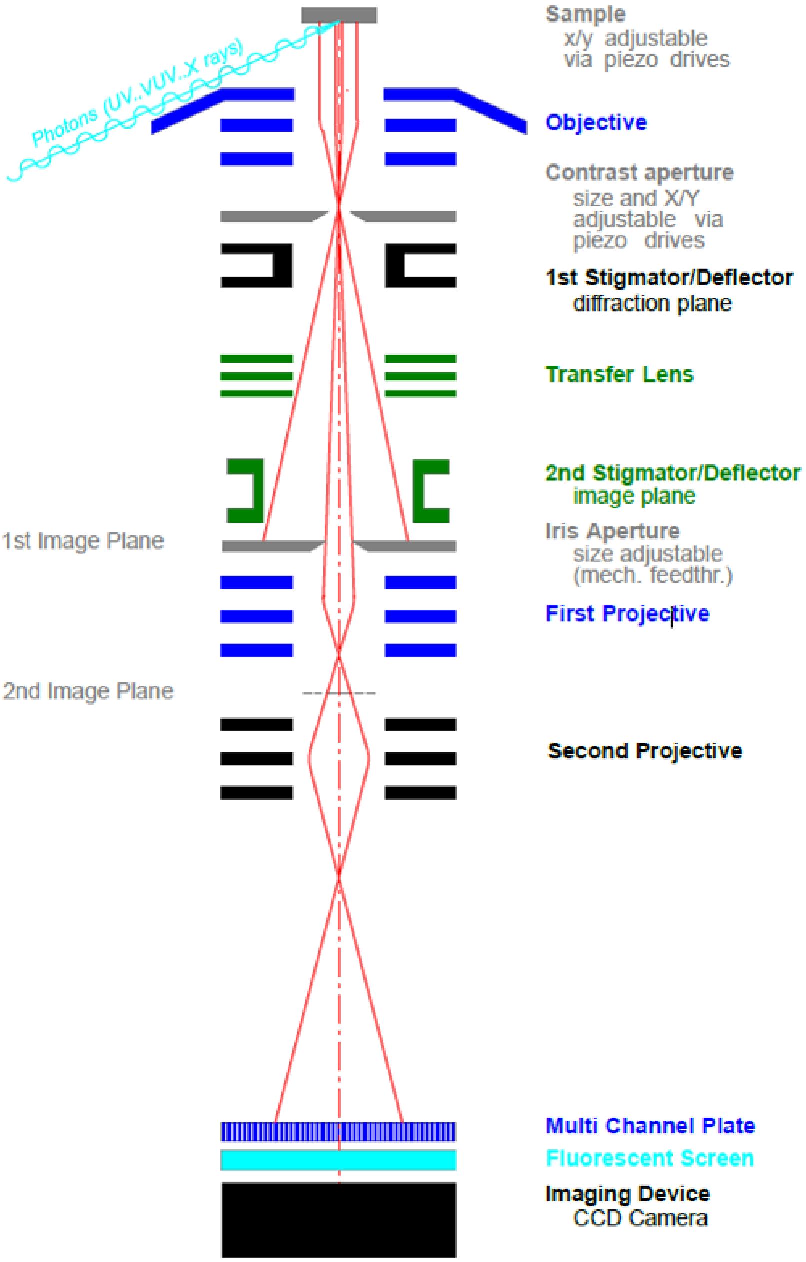

Figure 2.3: The layout of the FOCUS PEEM imaging system. Adapted from the FOCUS PEEM manual.

Several UV-grade quartz viewports are available at the analysis chamber for excitation sources. For all experiments in this thesis, either a Mercury (Hg) lamp or the Class 5 ultrafast laser system was used. A Hg lamp is an unpolarized broadband UV continuous-wave (CW) light source that produces the highest photon energy around 5.0 eV (247 nm). Most of the materials studied have work functions below 5 eV and can therefore be directly imaged via a one-photon photoemission process. The water-cooled HBO 103W/2 mercury short-arc light bulb is secured in a well-sealed housing to prevent UV leaks as well as potential mercury exposure, and the housing is mounted at a viewport at a glancing incident angle (65°). With proper alignment of the focusing mirror and the condenser in the housing, the UV beam is collimated at the output. The beam is directed into a heater filter, which essentially is a dichroic mirror that deflects light components at a cutoff wavelength of ∼280 nm. The full spectrum of the lamp measured by the lab spectrometer (Ocean Insight Maya 2000 Pro) is shown in Figure 2.4. It's worth pointing out that a significant amount of signal persists in the visible region, implying that IR filtering isn't efficient. The spectrum indicates that non-UV photoexcitation needs into taken into consideration for photoemission processes with Hg lamp illumination.

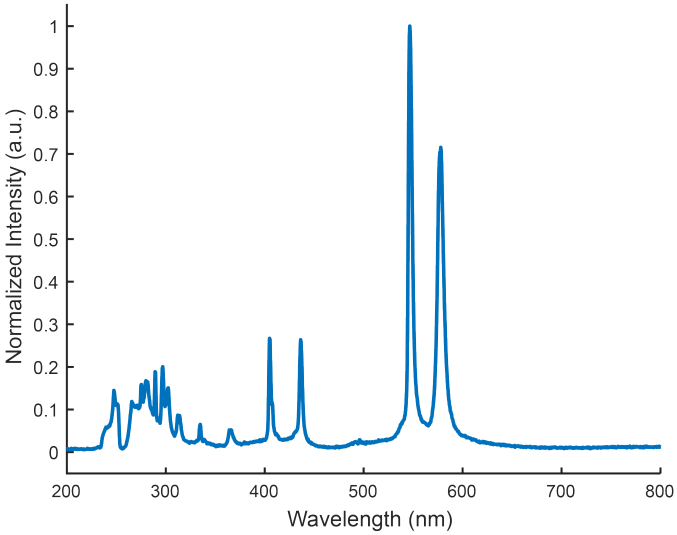

Figure 2.4: Optical spectrum of the Hg arc lamp. Intensity is normalized to the highest peak.

In addition, the Hg lamp housing is compatible with the standard 30 mm optical cage system, allowing installations of additional optical components such as filters, an iris, or a shutter, to modify the light characteristics. A protection tube covering the cage system is provided to contain the UV radiation. Finally, the UV beam is focused onto the sample on the PEEM stage through an in-vacuum lens.

PEEM experiments with laser illumination are conducted with more manipulation of the light sources. We will introduce a few experimental schemes by coupling the Class 5 system into the PEEM column in the later Section 2.4.1.

The resolution of the FOCUS PEEM is determined by a patterned silver (Ag) grid sample. The sample is imaged at the smallest field of view possible. A line profile is usually extracted from the edges and fit to an error function. In the PEEM community, the resolution is typically defined as the 84/16 width of the error function. Figure 2.5 illustrates an example of the resolution cut from a patterned silver grid sample and a spatial resolution of around 20-30 nm has been achieved. The ultimate resolution of this instrument is fundamentally limited by both the nature of electrostatic lenses and sample unevenness. For a practical sample, the typical resolution is around 50-100 nm, which can in principle be improved by perfecting sample cleanness and flatness.

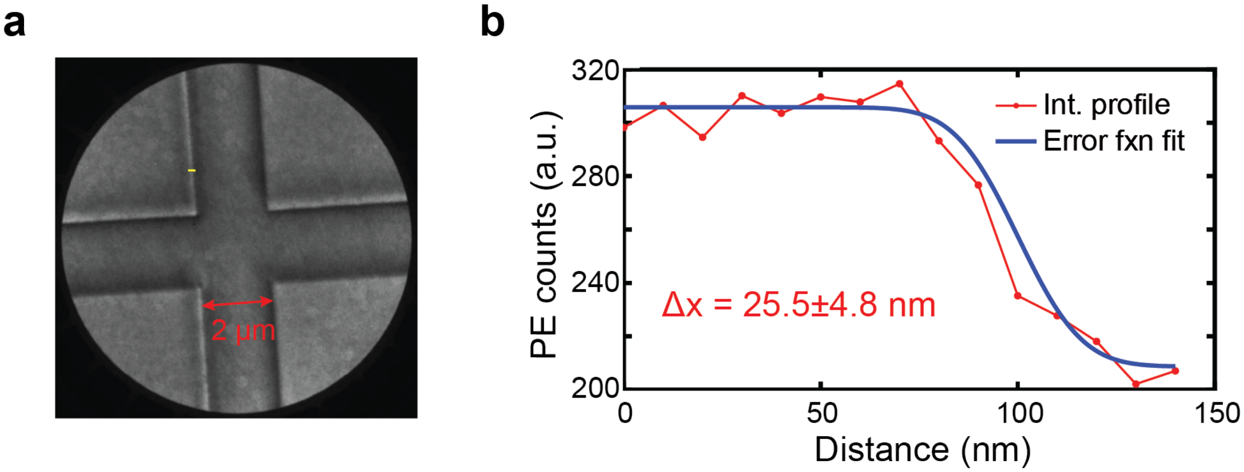

Figure 2.5: (a) Static PEEM image of patterned Ag grids illuminated by the Hg arc lamp. (b) Intensity profile of the yellow segment in (a). The width between 16% and 84% of the maximum of the error function indicates a spatial resolution of 25.5±4.8 nm.

The FOCUS PEEM is also incorporated with a high-pass energy filter that enables energy-filtered imaging and spectroscopic measurements. In practice, an additional component of a retarding field analyzer consisting of a preretardation lens and two retardation grids is available in the electron lens column. The retardation grids shape a homogeneous electrostatic field that acts as a high-energy filter, and only photoelectrons that pass this filter can enter the imaging unit. The strength of the retardation determines the energy resolution of the instrument, and so far, the best achievable energy resolution of the instrument is ∼50 meV. For energy-resolved PEEM experiments, a series of energy-filtered images of the same ROI can be collected by incrementally cutting out photoelectrons with kinetic energies lower than a given energy threshold. Thus, an energy distribution of the electron density can be computed by performing a numerical differentiation of the energy-resolved images. This energy band-pass filtering is automated in the ProNanoESCA software, and can also be done by MATLAB processing of the raw image series. The data analysis for extracting energy distribution curves is provided in Section A.6.2.

2.3.2 ELMITEC system

The ELMITEC PEEM has a distinct electron optics system from the FOCUS system described in Section 2.3.1. Instead of an electrostatic lens system for the FOCUS PEEM, ELMITEC uses electromagnetic lenses in a straight column for imaging. The major difference between the two systems is that the control and adjustments for magnetic lenses are realized by applying currents instead of voltages. As shown in the schematic of the imaging system (Figure 2.6), the sample is mounted on the manipulator with x, y, and z translation as well as tilt control. The sample is constantly held at -20 kV voltage and serves as the cathode of the objective lens. The distance between the sample the the magnetic diode is 2 mm to keep the electrical field at 10 kV/mm for optimal imaging resolution. The objective lens focuses the image before the micro-valve, and the transfer lens images the back focal plane of the objective lens in front of the intermediate plane to image the specimen in real space. A contrast aperture is positioned at the field lens with adjustable diameters of 100 μm, 70

μm, and 30 μm, which can further boost the resolution and image contrast. The image plane is projected between the field lens and the intermediate lens, and the intermediate lens can be essentially shifted laterally with respect to the image plane by the deflectors to alter the magnification of the real image. A pair of projective lenses are placed after the intermediate lens to adjust the magnification of the image projected on the MCP although they don't improve the image quality. The second projective lens (P2) is set to a fixed current of 4000 mA and is water-cooled as the current value is particularly high and would otherwise introduce thermal instability to the imaging system. All lenses are equipped with electromagnetic deflectors for fine-tuning the image resolution. There isn't an energy filter for the ELMITEC PEEM system, and thus the PEEM images produced by this equipment contain information on photoelectrons of all kinetic energies.

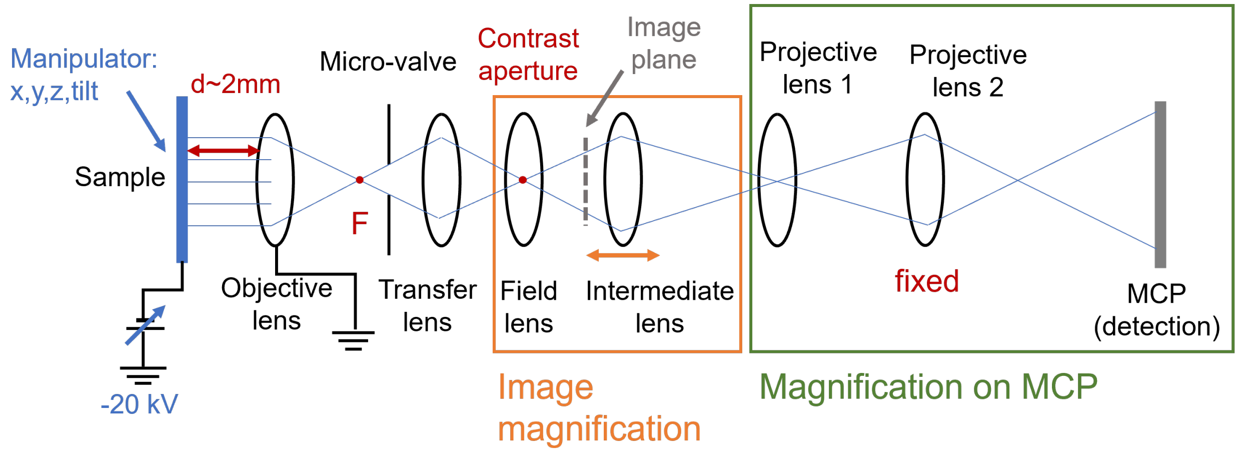

Figure 2.6: The electron optics in the Elimtec PEEM imaging column.

The detection scheme is comprised of a double MCP and a phosphor screen assembly that amplifies and makes visible the photoelectron signals. Finally, the images are captured by a charge-coupled device (CCD) camera (Teledyne). The microscope control is by the LEEM2000 software that allows individual control of all LEEM power supplies. The camera control and image acquisition are achieved by the UVIEW software that is interfaced with the microscope control. The UVIEW software is programmed to continuously capture images with a tunable camera exposure time and a set of fixed average numbers. In addition, videos of a series of images can be collected to monitor intensity evolution over time. Due to the nature of magnetic lenses, the images rotate as the field of view is switched. Thus, the camera is pre-calibrated with a Si grid sample to correct for the rotation angles.

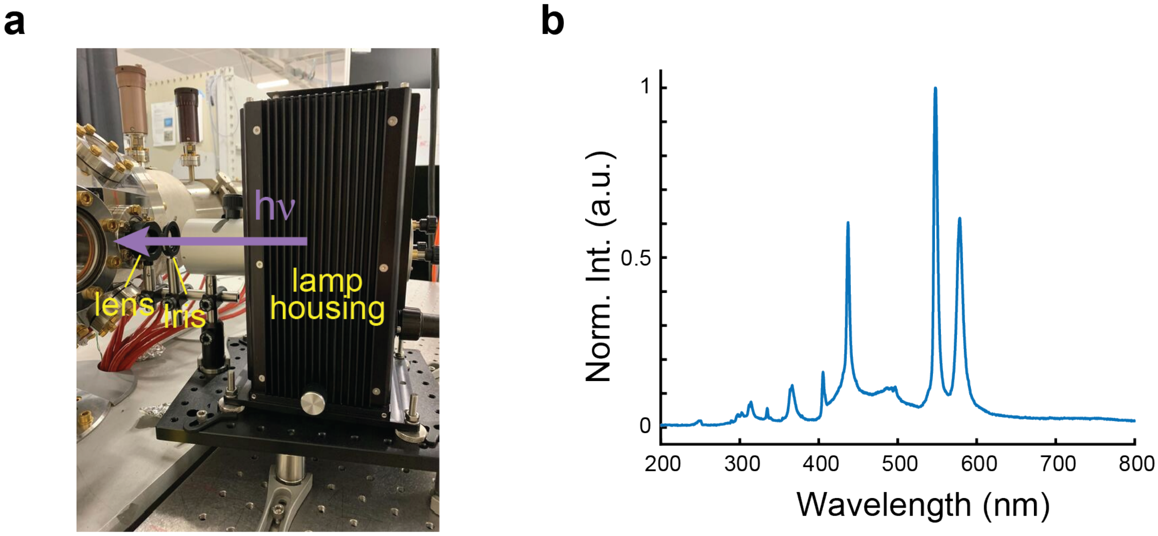

Figure 2.7: (a) A photo of the QD lamp housing and the home-built optical system. (b) The optical spectrum of the Hg lamp. Intensity of normalized.

The primary excitation source for ELMITEC PEEM is also a UV Hg discharge lamp (Quantum Design). The lamp has a different housing design, as depicted in the photography in Figure 2.8 but shares the same bulb as the one installed on the FOCUS system. although there are slight variations in the spectrum (Figure 2.8). The output power is 1.8 W, higher than the other model. Similarly, the UV light is focused onto the sample surface with an optical lens with a focal length of 175 mm. The focused beam size is hard to estimate but the illumination can cover the largest available FoV with this PEEM, which is 175 μm.

The lateral resolution for the ELMITEC PEEM is determined by using a Si sample with Pb islands. Pb has a lower work function than Si and thus is more photoemissive, showing a bright contrast on the Si background. At 2.5 μm FoV, intensity drops from 84% to 16% are measured at a variety of sample positions and the average resolution is 8.3 nm.

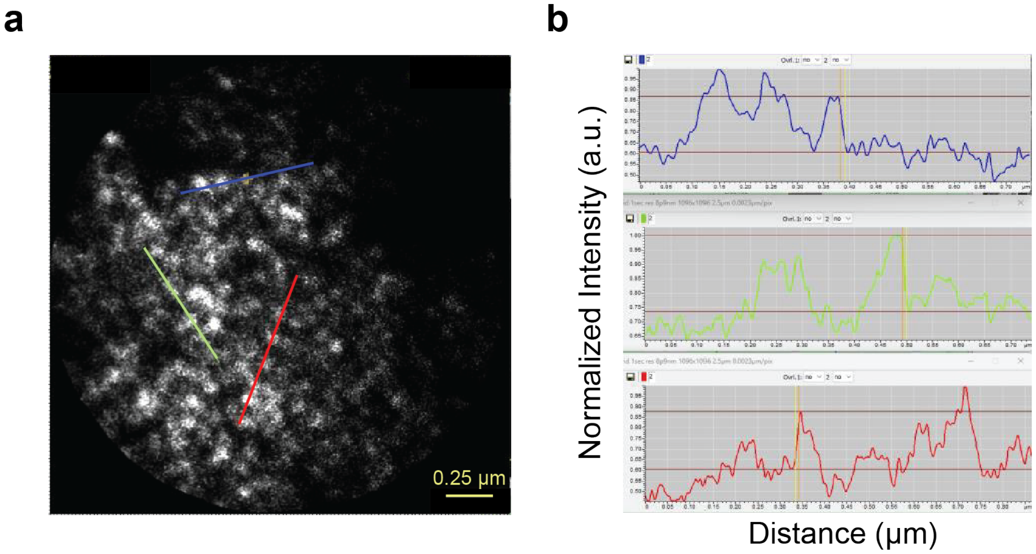

Figure 2.8: (a) PEEM image of Si sample with Pb islands. (b) Intensity profiles corresponding to multiple lines in (a). Intensity drops from 84% to 16% are measured for three positions, yielding an average resolution of 8.3 nm. The data are adapted from ELMITEC service notes from November 2024.

2.4 Technical realization of PEEM experiments

2.4.1 Polarization-dependent PEEM

The Class 5 laser was coupled into the FOCUS PEEM chamber for all the polarization-dependent (PD-PEEM) experiments in this work. In general, the beams are routed across from the laser table built next to the vacuum system. A custom-designed optical breadboard (Minitec) is mounted on the UHV bench for extra optics before the beams are focused into the chamber. Two UV quartz viewports on the vacuum chamber are available for beam coupling: one directly couples the beam onto the sample at 65° incident angle, and the other allows near-normal incidence (NNI, $\sim 4^\circ$) via an in-vacuum Rhodium (Rh) reflector onto the sample surface, allowing the laser polarization to be in-plane with respect to the sample at all polarization angles.

The critical components for the polarization-dependent setup are built on the breadboard next to the vacuum chamber. Figure 2.9 shows a top view of the optical layout for the PD experiments. Typically, the laser beam with polarization parallel to the tabletop is directed from the main laser table onto steering Ag mirrors (for visible beams) on the breadboard. To ensure polarization purity, a Brewster angle thin film polarizer (Eskma) is installed to only allow light polarization that's parallel to the breadboard to pass through. The polarization purity is confirmed by the power distribution of s-and p-polarization separated using a polarization beamsplitter cube (Thorlabs). A $\lambda/2$ waveplate (Thorlabs) mounted on a motorized rotational stage (Newport) is placed after the polarizer to rotate the light polarization. The motor can be interfaced by Python scripts that enable automated serial experiments with controlled steps and rotation speed. Finally, the beam is focused into the chamber using a 200-mm focusing length UVFS plano-convex lens (Thorlabs). A typical beam size of 30-50 μm can be achieved. An attenuator can be placed in the beam path for power modulation, and this is also useful for fluence-dependent experiments. The laser power is measured right before the beam goes into the chamber (after the lens) to ensure the accuracy of the fluence calculation. The process for locating the beam on the sample is usually done at a relatively high laser power for easier visualization. To avoid potential damage, a robust sample such as graphene or polycrystalline gold is used for the search procedure.

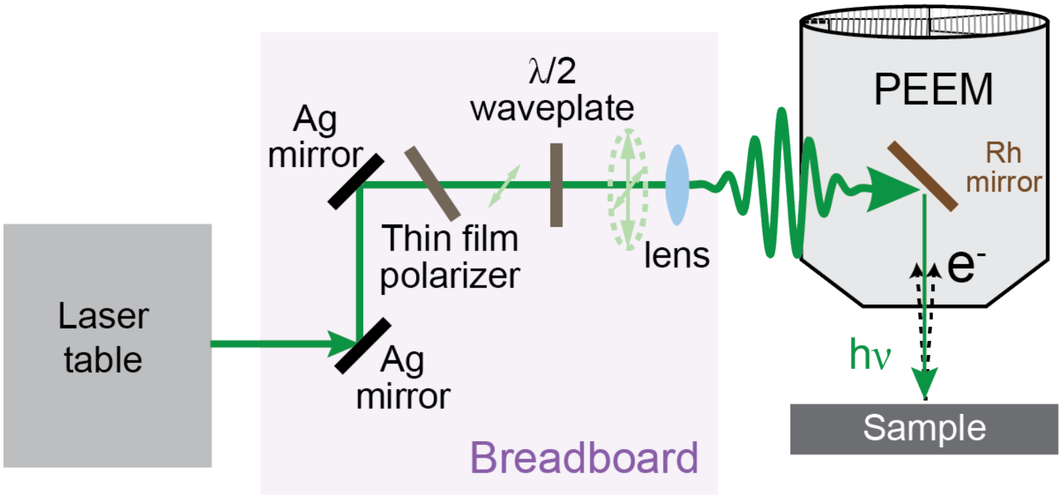

Figure 2.9: Optical diagram for polarization-dependent PEEM experiment.

Since the reflectivity of rhodium is polarization-dependent, an intensity correction must be applied to avoid artifacts for the analysis of polarization-related PE response. The correction can be conducted in two ways: (1) the polarization-dependent reflectivity of the Rh mirror is measured on an isotropic material, and this intensity modulation will be normalized and divided from the raw PEEM data. (2) the PE intensity is integrated across the entire field and the absence of net polarization-dependent absorption is used to determine the total photoelectrons emitted from the sample as a function of laser polarization, which quantitatively describes the polarization-dependent reflectivity of the Rh mirror. The detailed analysis for the first method is provided in Section A.9, and the second method is described in the Supporting Information of previous work from our lab[74] and is adopted for the experiments in Chapter 5.

2.4.2 Time-resolved PEEM

Time-resolved PEEM (TR-PEEM) imaging employs an ultrafast pump-probe configuration using the Class 5 laser system. A visible beam, generated from either the fundamental output, or the SHG, is typically used for selectively pumping the material to a resonant molecular level or a virtual intermediate state. A UV beam, generated by the frequency tripling of the fundamental pulse, photoionizes the excited electrons at a delayed time. The optical setup of a visible pump (SHG) and a UV probe (THG) is demonstrated in Figure 2.10. In this design, the pump pulse is delayed by a linear translation stage (Newport) via a retroreflector, and impinges the sample surface via the NNI viewport. The polarization of the visible beam can be tuned by the $\lambda/2$ waveplate outside the vacuum chamber depending, similar to the PD-PEEM experiments. The UV probe passes through an adjustable fold to compensate for the difference in the beam path in order to temporally overlap with the visible beam. The probe pulse incidents on the sample at the glancing angle (65°) with a fixed polarization. Both beams are focused onto the sample via convex lenses before the UV-grade quartz viewports on the vacuum chamber. The typical size for the visible beam is 30-50 μm in diameter. The beam profile for the UV beam is elliptical due to the angled incidence, and the typical dimension is about 50×100 μm^2. Representative beam profiles can be found in Figure A.32, measured on a polycrystalline graphene sample with PEEM.

Transmissive optics in the beam path, including lenses, waveplates, beamsplitters, dichroic mirrors, and BBO crystals, introduce temporal chirps due to positive group-velocity dispersion (GVD) and can significantly stretch pulses in the time domain. In order to observe ultrafast dynamics occurring on the femtosecond time scale, both the SHG and THG beams need to be properly compressed to compensate for transmission through dispersive media. Chirped mirrors with coatings for UV wavelengths are challenging to manufacture and are costly. Here, two-prism pulse compressors constructed with UV fused silica (UVFS) prism pairs (Altechna) are utilized for optimizing the pulse durations of both beams. The compressors are divided into one for the visible range ($>$450 nm) and the other for the UV ($<$450 nm), depending on the optimal reflection ranges of the metallic mirrors (Ag mirrors for visible beam and Al mirrors for UV beam). The geometry of the prism-pair compressors is also included in Figure 2.10. Contrary to the conventional four-prism compressor, the two-prism setup uses a roof mirror for double passes through the prisms with a height offset. A folding mirror is added between the two prisms to minimize the space. The optimal compression cannot be achieved without careful configuration and alignment of the compressor setup. Details for how to properly align the prism compressor are elaborated in Section A.1.

The pulse durations of the SHG and THG are characterized by the cross-correlation on a poly-crystalline monolayer graphene chip on Si/300 nm SiO_2 (University Wafer, G2047) in PEEM. Graphene is metallic and has a transient response within 30 fs upon photoexcitation,[75–77] and therefore can be used to characterize femtosecond pulses. The characterization is conducted in the following manner: first, the cross-correlation of the UV pulse and a near-IR pulse from a fundamental output is measured. The pulse duration of the near-IR beam has been previously determined by FROG. The cross-correlation is collected by setting an energy filter to detect the highest energy photoelectrons that have the shortest

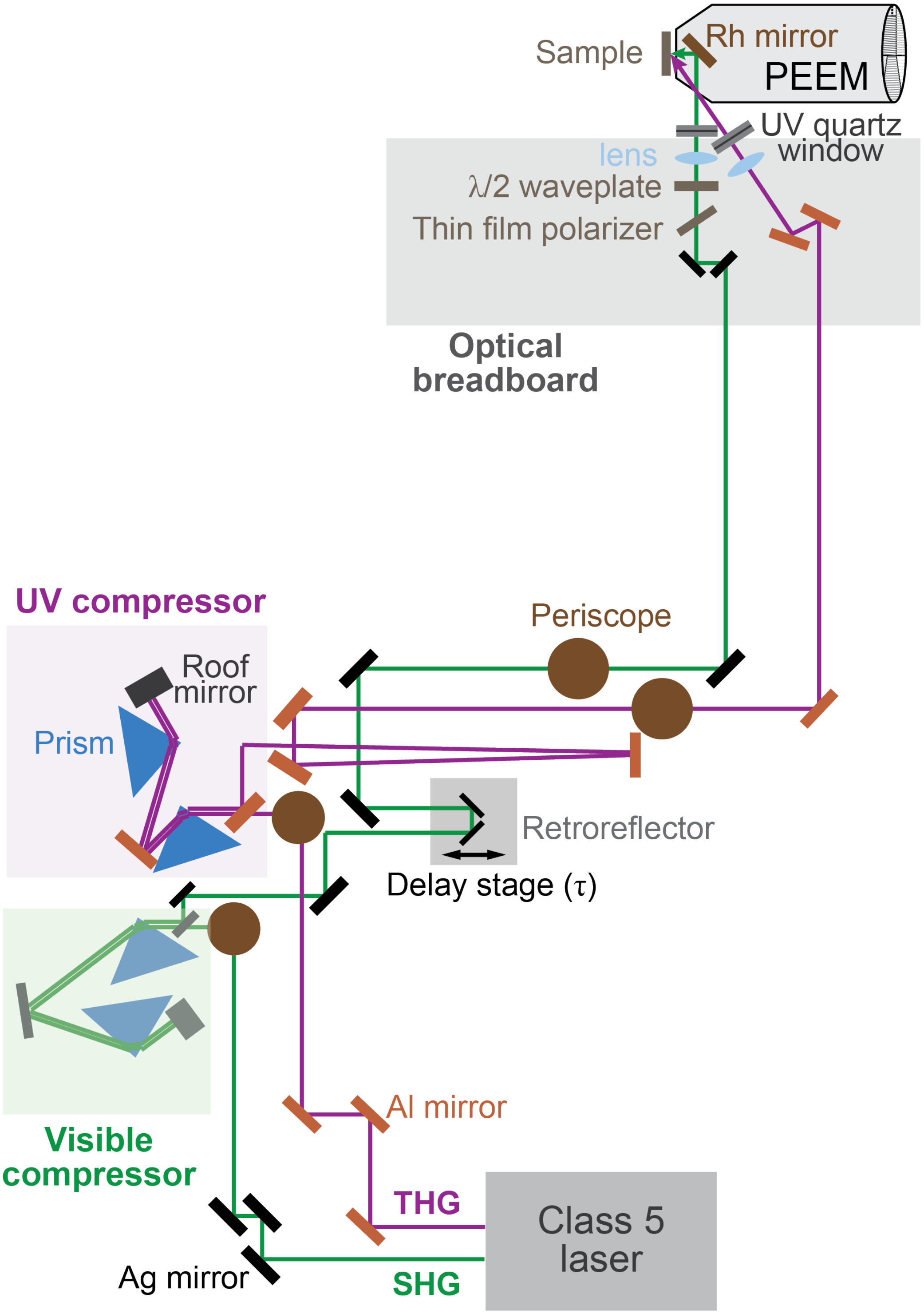

Figure 2.10: Optical diagram for time-resolved PEEM experiment with visible and UV prism compressors.

intrinsic lifetime. The width of the Gaussian cross-correlation can be extracted from fitting and the pulse duration of σ_{300nm} can be calculated based on Equation 2.1 To shorten the optimization time, the prism compressor is often finely tuned to maximize the PE intensity at time zero, which indicates the shortest UV pulse duration has been achieved. Next, the cross-correlation of the UV pulse with the visible pulse is measured in the same fashion to determine the pulse duration of the SHG beam. A representative example of finding the pulse durations of a 575 nm and a 300 nm beam, used for the TR-PEEM experiments in Chapter 5, is presented in Section A.5.3.

CHAPTER 3

PREPARATION AND CHARACTERIZATIONS OF 2D MATERIALS

3.1 Overview

This chapter introduces the fabrication and characterization method of a series of 2D materials that have been investigated in the King Lab. The primary preparation method adopted for works in this thesis is mechanical exfoliation. We will discuss the experimental details of this method, as well as a few modifications to optimize this technique. We will also describe the challenges we have experienced with sample preparation and suggest possible steps for future improvement. Furthermore, we will review three types of microscopy that are commonly used to characterize the morphology and optical properties of 2D materials and demonstrate how those simple techniques can be immensely useful for understanding the underlying physical properties of the samples.

3.2 Mechanical exfoliation

3.2.1 Tape exfoliation

The idea behind exfoliation is based on that the applied vertical mechanical stress overcomes the weak van der Waals (vdW) force between layers of 2D materials. Therefore the layers can be cleaved from bulk crystals and produce single-crystal sheets.[78] This method had its first success by isolating monolayer graphene from a bulk highly oriented pyrolytic graphite (HOPG) crystal simply using Scotch tape in 2004,[79] and graphene was later awarded with a Nobel Prize in 2010. Subsequently, such practice rapidly expanded to the broader 2D community, and modified tape exfoliation techniques were created to accommodate materials with varying strengths of interlayer interactions. Liquid exfoliation, including ultrasonication[80] and ionic intercatalation[81], has also been successfully applied to some 2D materials but those methods were not explored for the work in the thesis.

While synthetic approaches such as chemical vapor deposition (CVD) tend to produce polycrystalline samples with relatively high defect density,[16] 2D materials isolated from bulk crystals (commercially purchased or homegrown) by mechanical exfoliation generally create low-defect single crystalline domains. The drawback of mechanical exfoliation is also clear: achieving monolayers can be laborious and time-consuming, involving lots of trial and error, particularly for materials with relatively stronger interlayer interactions. Furthermore, this technique is unlikely to be able to scale up for industrial applications, and the flake sizes are limited by the dimension of the bulk crystals, usually on the millimeter scale. Nevertheless, mechanical exfoliation is still one of the most popular ways to obtain few-layer 2D materials for extensive research purposes.

Figure 3.1 illustrates the steps of exfoliating HOPG for monolayer graphene,[5] and a text description of the procedure is as follows:

First, a piece of clean tape is cut to about 20 cm long. The two ends can be folded by 3-5 cm for handling. The tape cleaves a bulk crystal from the top surface, and the thick crystal left on the tape will be the starting point of the exfoliation. The tape is then folded onto an adjacent region of the thin crystal, rubbed and pressed for a few seconds, and slowly peeled the tape off to obtain a thinner crystal spot. This fold-and-peel process is repeated several times until the resulting flakes are close to transparent. Lastly, The flakes are transferred to a desired substrate, where a solid chip can be pressed on a target area against the tape and very carefully lifted off for the best transfer yield. Notice that the required times of folding are sample-dependent and experimenter-dependent. Generally, materials with stronger vdW forces, such as black phosphorus, need more folding times to isolate to the 2D regime. On the other hand, thin flakes of a few layers are typically smaller in size and suffer from low transfer efficiency to a substrate. Thus, the optimal folding protocol needs to be explored individually.

The exfoliation results are usually examined by optical images and other characterization tools, as shown in the last two panels of Figure 3.1. We will discuss sample characterization in more detail in Section 3.3.

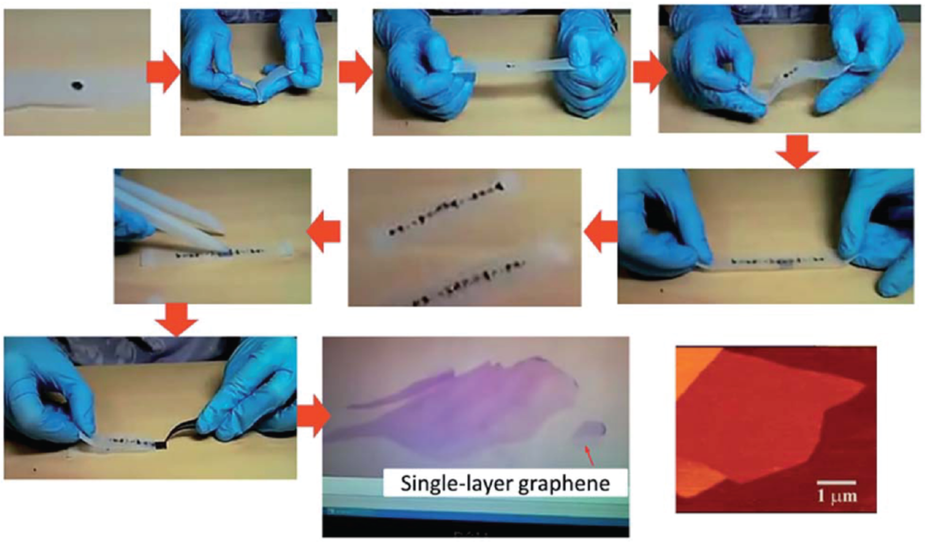

Figure 3.1: Illustration of mechanical exfoliation procedure exemplified by Scotch-tape cleavage of HOPG for monolayer graphene. The figure is adapted from the work by Yi *et al.*[5]

Various adhesive tapes have also been explored in the literature for the most efficient exfoliation. A popular one is a type of PVC-based blue tape, often called Nitto tape, that has slightly lower adhesion. The biggest advantage is that the blue tape leaves significantly less residue on the substrate, yielding cleaner samples, with the downside of reduced efficiency compared to the conventional Scotch tape. Thermal release tape (TRT) is another type of adhesive tape. TRT is sticky at room temperature but loses adhesion in a few seconds with an observable discoloration once heated to the designed releasing temperature. However, the TRT is stiff and hard to have a flexible control for folding and peeling. Practically it is rarely used for the exfoliation of 2D materials, but it is a great tool for transferring the exfoliated thin flakes with minimum introduction of contamination or mechanical stress, which will be discussed later in Section 3.2.4.

The surface condition of substrates, including the cleanness, roughness, and surface material, has a considerable impact on the sample quality by affecting the physisorption of the

2D flakes. Silicon (Si) (100) wafers (with ~2 nm native oxides) are used for most PEEM experiments in this thesis. A pre-cleaning process is required to remove surface adsorbates that might reduce the transfer efficiency. Wet cleaning involving ultrasonication in organic solvents is usually adopted to effectively clean off oil contaminants.[82] More rigorous cleaning procedures such as plasma etching, can be applied to obtain high-quality substrate for device fabrication. This process involves UV-induced oxygen or argon ions sputtering onto the etched material to "kick out" surface contaminants. We didn't find a significant improvement in using plasma-treated substrate for 2D material transfer and PEEM experiments, and thus this cleaning setup is not regularly practiced. It is also reported that a hot transfer procedure can improve the density and size of the resulting 2D flakes by helping push out the trapped gasses at the interface to bring the materials to closer contact with the substrate. We did observe a positive effect on the overall yield of transferred materials with the downside of increased tape residues, which isn't ideal for vacuum experiments. The tape residue can in principle be cleaned by organic solvents but the impact of tape residue on 2D flakes needs careful consideration.

3.2.2 Stamp-assisted exfoliation and transfer

When it comes to constructing more complicated 2D heterostructures, the Scotch tape method lacks the flexibility and precision to manipulate the exfoliated flakes. To overcome this difficulty, viscoelastic stamps, usually with adhesive polymers, are employed to facilitate effective transfer as well as flake positioning.[83] As shown in Figure 3.2, the polymer stamp is pressed against the exfoliated flakes on the tape and then the stamp is carefully lifted from the tape. An optical microscope can be used in this step for a better survey of the desired flakes. Once the flakes are identified, the stamp is positioned relative to the center of a target substrate, pressed, and peeled off very slowly, releasing the flakes onto the acceptor surface. As the polymer stamps are typically transparent, this process can be monitored under a long working distance objective for fine control of flake position and rotation. This is particularly useful for stacking 2D heterostructures with accurate lateral and angular alignment such as magic-angle graphene and Moiré heterostructures. Other advantages of stamp-assisted exfoliation include increased transfer efficiency and cleaner sample surfaces.

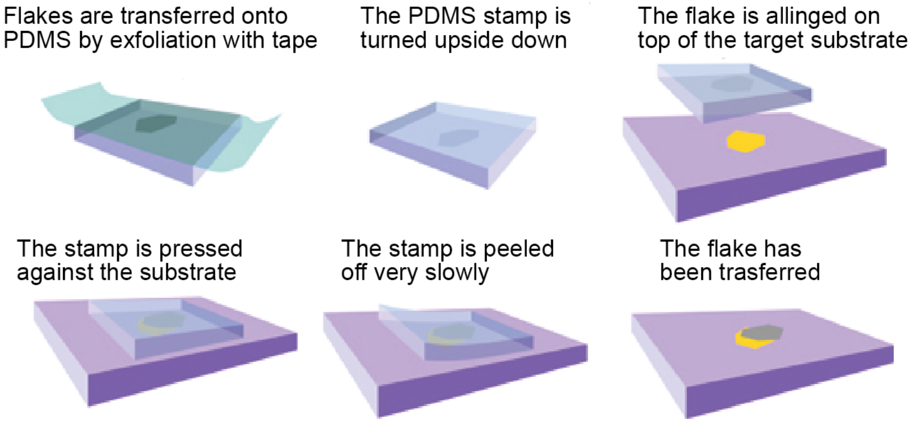

Figure 3.2: Diagram for viscoelastic stamp-involved deterministic transfer of 2D thin flake onto a user-defined location (for instance, another atomically thin flake). The figure is adapted from the work of Castellanos-Gomez *et al.*[83]

The choice of polymer stamps depends on the viscosity and flexibility of the polymers. Polydimethylsiloxane, or PMDS, is a polymer that's heavily adopted for 2D material handling. It can be either purchased commercially (Gelfilm from Gel-Pak) or homemade. In this thesis, all PMDS stamps were custom-made following a fairly simple procedure. Commercial silicone elastomer kit (Electron Microscopy Sciences, Sylgard$^{\mathrm{TM}}$ 184) consisting of the polymer base and the curing agent is mixed and stirred with a given ratio (10:1 for PDMS), and the rigidness of the stamp can be tuned by slightly adjusting the percentages. The liquid mixture is degassed in a vacuum desiccator and then poured into a more such as a glass petri dish. The bubble-free liquid is cured in air to achieve a uniform and thin ($\sim$ 1-2 mm) PMDS sheet, and the curing time depends on the temperature (15 minutes at 150 $^{\circ}$ and 24 hours for room temperature). The large PMDS can be cut into small squares that suit the substrate dimension. It's worth noting that the stamp-assisted transfer using PDMS is not completely residue-free, and surface contamination can be improved by a better selection of the polymer material such as poly(methyl methacrylate) (PMMA) or polycarbonate (PC), which has been reported to yield cleaner sample surfaces.[84]

3.2.3 Gold-assisted exfoliation

Tape exfoliation is a simple sample preparation technique that allows obtaining thin-layer 2D materials ubiquitously. However, due to limited control of the vertical force in the peeling process, this method can be inconsistent, and the resulting flakes usually suffer from non-uniform thickness and small size, which fundamentally hampers the development of large-scale optoelectronics. More recently, the strong affinity of 2D materials to metals has encouraged researchers to use metals as alternative substrates to isolate large, uniform monolayers. It has been revealed by theory and supported by experiments that metals such as gold, adhere strongly to 2D materials due to covalent-like interactions.[85] The strong adsorption overcomes the interlayer van der Waals force, and therefore the out-most layer of 2D bulk crystals is expected to peel off from the surface.

A huge experimental process that implemented this idea is gold-assisted exfoliation, which has been successfully demonstrated by Liu.[78,86]. Since then, researchers have universally applied this method to isolate 40 types of high-quality single-crystalline monolayers with millimeter-size.[85] These large-area monolayers support studies for the fundamental properties and potential applications. There are slightly different variations of the gold-assisted exfoliation. The major distinction is whether the gold layer acts as a substrate, or a "metal tape" for cleavage. We will discuss the considerations for both practices and describe our preliminary efforts in trying to obtain large monolayer black phosphorus and MoS_2 using gold-assisted exfoliation.

Au film as a substrate

Following the protocol of Huang *et al.*,[87] we first tried to exfoliate black phosphorus using the gold film as a substrate. Thin gold films were deposited onto silicon wafers using an E-beam evaporator (AJA E-beam evaporator) at base pressure 10^{-8} torr in the clean room.

After evaporation, the decorated silicon wafers were removed from the vacuum chamber, and the gold films were exposed to air. A 10 nm pure gold film and a 2 nm gold film with 2 nm Ti as an adhesion layer[85] were prepared on separate Si wafers. Atomic force microscopy (AFM) images show that the pure gold film forms patterned islands, whereas the Au/Ti film appears to be featureless at μm scale (Figure 3.3) The root mean square (RMS) roughnesses for the two films are 1.643 nm and 353.2 pm, respectively, indicating the adhesion layer is necessary for a flatter surface that is beneficial for higher exfoliation quality.

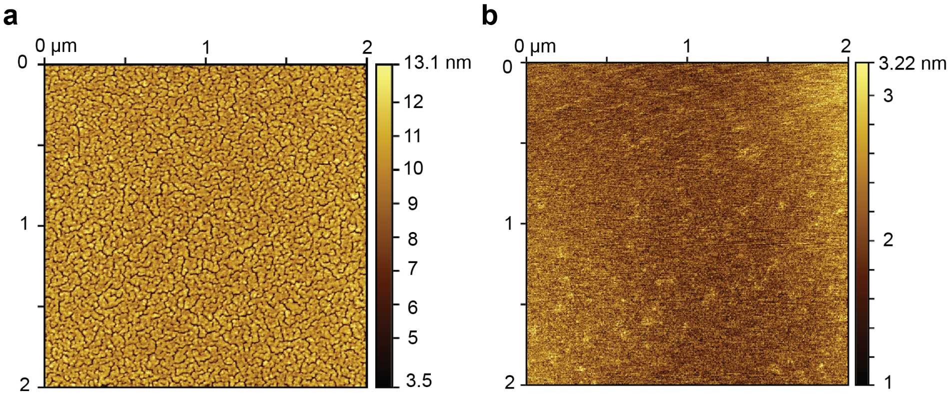

Figure 3.3: AFM images of gold films. (a) 10 nm gold/Si. (b) 2 nm gold/2 nm Ti/Si.

Black phosphorus was initially cleaved 2-3 times in a N_2 glovebox (O_2<1 ppm) using Scotch tap, blue Nitto tape, or Scotch tape assisted with PMDS, as described in Section 3.2.1 and Section 3.2.2. The tapes were pressed gently onto the Au/Ti surface and peeled off slowly. Optical images show that Scotch tape, unsurprisingly, left a large amount of tape residue, but the number of thin flakes was not significantly increased compared to that on a regular silicon chip (Figure 3.4(a)). We did not succeed in obtaining a higher density of flakes with the blue tape either. In addition, portions of the gold film were peeled off from the silicon surface as the tape was removed from the surface (Figure 3.4(b)), introducing extra difficulty in preserving the intact surface. PMDS transfer yielded a cleaner surface, and areas of low optical contrast could be observed from the edges of relatively larger BP flakes, as shown in Figure 3.4(c). AFM measurements show that those flakes could be as thin as 7 nm (8-14 layers, Figure 3.4(d)). Without going to the step of etching off the gold layer, we have not achieved monolayer 2D flakes using this method. The low exfoliation efficiency could be due to the extended air exposure to the gold surface, where surface contaminations weaken the affinity of gold with the 2D materials.[88] A modified gold-assisted exfoliation is used, as will be discussed in the next section, to further improve the results of mechanical cleavage.

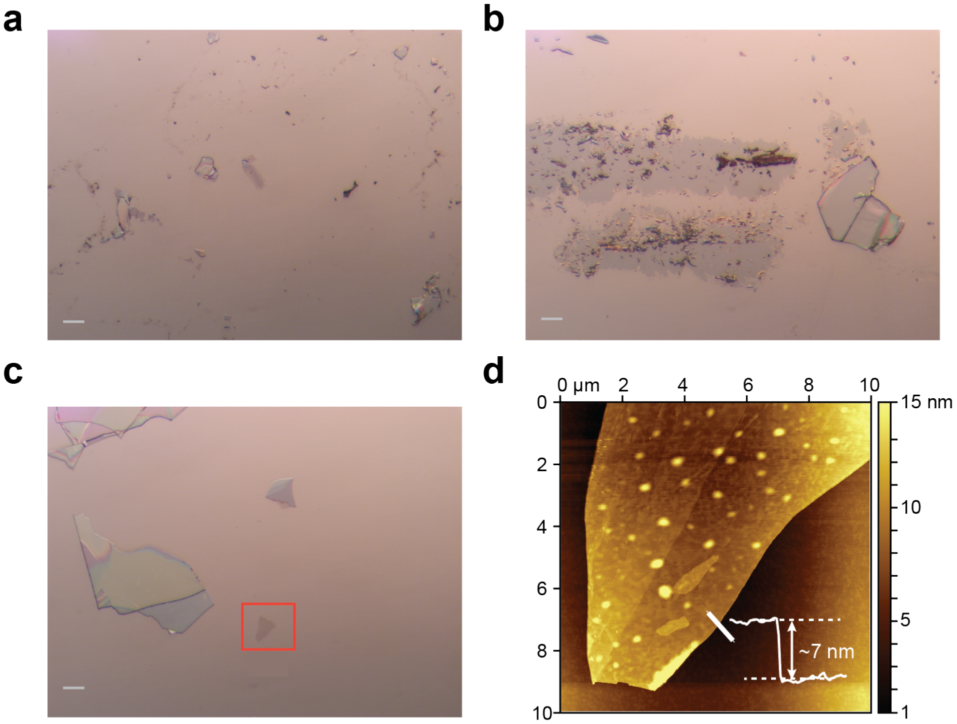

Figure 3.4: Exfoliation results on Au/Ti/Si substrates (a) only Scotch tape. (b) blue Nitto tape. (c) Scotch tape exfoliation and PMDS stamp transfer. Scale bars are all 10 μm (d) AFM image of the flake labeled by the red box in (c).

Au film as a metal tape

Liu's protocol has consistently produced mm-size molybdenum disulfide (MoS_2) on Si/SiO_2 chips, as schematically illustrated in Figure 3.5.[86] Typically, a thick polycrystalline gold 150 nm is deposited onto a Si wafer using the same E-beam evaporator. The wafer is cut into 1 mm×1 mm squares and a layer of polyvinylpyrrolidone (PVP) solution (Sigma-Aldrich, mw 40000, 10% wt in ethanol/acetonitrile wt 1/1) is spin-coated on the Au film (3000 rpm, acceleration 1000rpm/s, 2min) to prevent residue contamination from the tape. The PVP/Au assembly can be easily peeled off from the silicon substrate using a piece of thermal release tape, and the interface of the gold film and silicon is revealed. Although the top of the gold film was exposed to air after evaporation and therefore is rough due to particle adsorption, the as-obtained gold surface preserved the flatness of the silicon substrate and is fresh. The immediate use the the "gold tape" in principle adheres effectively to 2D materials.

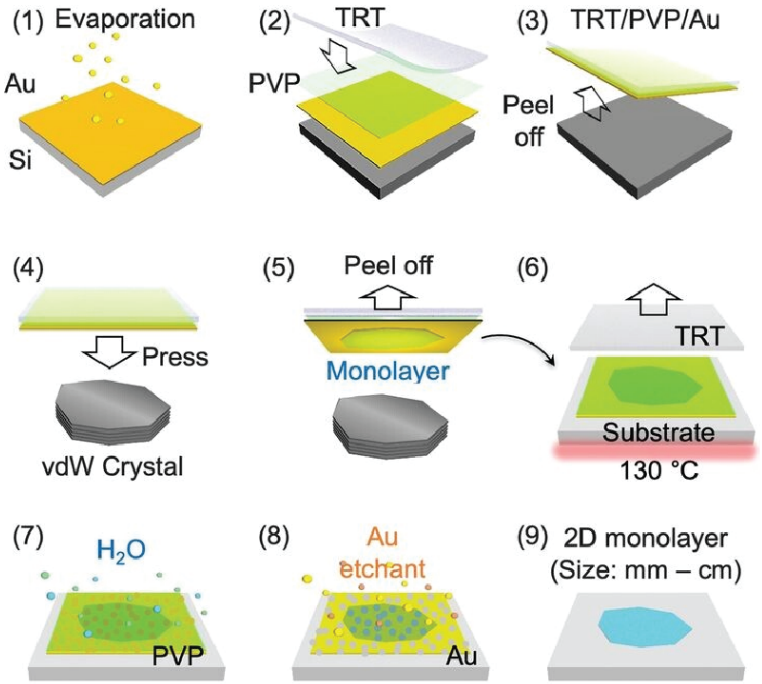

Figure 3.5: Schematic illustration of gold-assisted exfoliation of vdW single crystals. The figure is adapted from the work by Liu *et al.*[86]

We used MoS_2 as the proof-of-principle sample to try to replicate this technique. A piece of bulk crystal was set on the fresh gold tape and slowly lifted off. The first issue was that no visible flake could be readily observed. Subsequently, the TRT/PVP/Au/MoS_2 stack was attached to a pre-cleaned Si chip (with native oxides) and the whole assembly was heated by a hot plate to $\sim 130\ ^\circ$ until the TRT discolored and lost adhesion. The second challenge occurred as we could not release the gold film from the tape effectively. The film either still stuck to the tape/polymer assembly, or it curled up which prevented it from lying uniformly on the Si chip. As a result, the thin flakes that presumably had been exfoliated by gold had trouble attaching to the substrate surface which halted the steps thereafter.

Several modifications could be made to improve the protocol. First, instead of setting the crystals directly on the gold film, the top layer of bulk crystals should be cleaved off by regular tape (Scotch tape) to create a flatter surface. Second, the as-peeled gold film on the TRT needs to be immediately applied onto the flat crystal to perverse the intact gold surface. Pressing and rubbing for a little longer time would also help the crystal stick better to the gold layer. Finally, a pre-treatment of the Si wafer could help the gold film stick onto the substrate. For example, a self-assembled monolayer (SAM) of 1-dodecanol could decrease the wettability of the Si substrate and enhance the adhesion.

Unfortunately, we did not continue to pursue gold-assisted exfoliation for large-scale monolayer 2D materials, since they were not yet necessary for the experiments in the thesis. However, in the future, this method is worthy of serious attention as once successfully implemented, it will open the door to assembling nanoscale to macroscale material for desired physical properties.

3.2.4 Transfer techniques for TEM

So far, we have developed a reliable protocol for isolating and transferring 2D thin flakes on solid substrates, which permits a large variety of measurements including optical spectroscopy/microscopy as well as PEEM. For other techniques, special sample holders are required to facilitate the measurements. In order to carry out ultrafast electron microscopy (UEM) experiments, which couples ultrafast laser with transmission electron microscopy (TEM), flakes must be added to TEM grids. In our group, this technique has been applied to study phonon dynamics in black phosphorus[89]. Here we will describe the protocol that has been developed to transfer mechanically exfoliated BP flakes onto copper grids to enable TEM measurements.

Unlike silicon chips, copper grids are typically 3 mm-diameter disks with fine meshes that allow electrons to transmit through while also providing enough support for samples. The handling of the copper grids is particularly tricky, as the the grids are approximately 25 μm thin and the material is soft. Despite that a perfectly flat grid is favored for reliable TEM measurements, copper grids are fragile and subject to folding and curling, especially when tweezers are used to handle solid-state samples. Therefore, one needs to be extremely careful and patient when transferring 2D flakes, and the transfer procedure should minimize mechanical stress to the grids as much as possible.

The sample preparation procedure was adapted from previously reported transfer methods for TEM samples.[90–92] To prevent oxidation of black phosphorus, all steps were conducted in a N_2 glovebox (O_2<1 ppm). 2D BP flakes were mechanically exfoliated with Scotch tape from bulk crystals (Smart Elements) and transferred onto a PMMA film on thermal release tape (TRT). The PMMA film was prepared by drop casting 15 μL of PMMA solution (wt 2% in anisole) onto a glass slide. The film is then peeled off the slide with TRT to obtain a flat polymer surface. We have also tried other template substrates such as silicon, but the adhesion of PMMA to silicon is stronger than a glass slide and TRT couldn't peel the film off from the surface.

The mechanically exfoliated BP flakes were then transferred to the PMMA/TRT stack, and a 2000-mesh Cu TEM grid (Ted Pella) was placed on top of the BP/PMMA/TRT stack. The grid/BP/PMMA/TRT stack was flipped onto a coverslip and heated at 130 °C to remove the TRT. The coverslip/grid/BP/PMMA assembly was soaked in an anhydrous acetone bath for at least 20 minutes. This washing step was repeated at least twice until the PMMA residue was no longer visible under the optical microscope. The full procedure is schematically summarized in Figure 3.6. Since the samples needed to be later transported to the TEM facility at Argonne National Laboratory, we stored the TEM grids in a vacuum desiccator and pumped the carrier down to 10^{-3} mbar inside the glovebox before taking it out. The grids would then be stored in a high vacuum chamber (10^{-6} mbar) before being introduced to the TEM column (10^{-6} mbar). The thicknesses of the BP flakes were not measured via AFM but estimation from optical contrast indicates that the flakes are on the order of tens of layers (last panel of Figure 3.6).

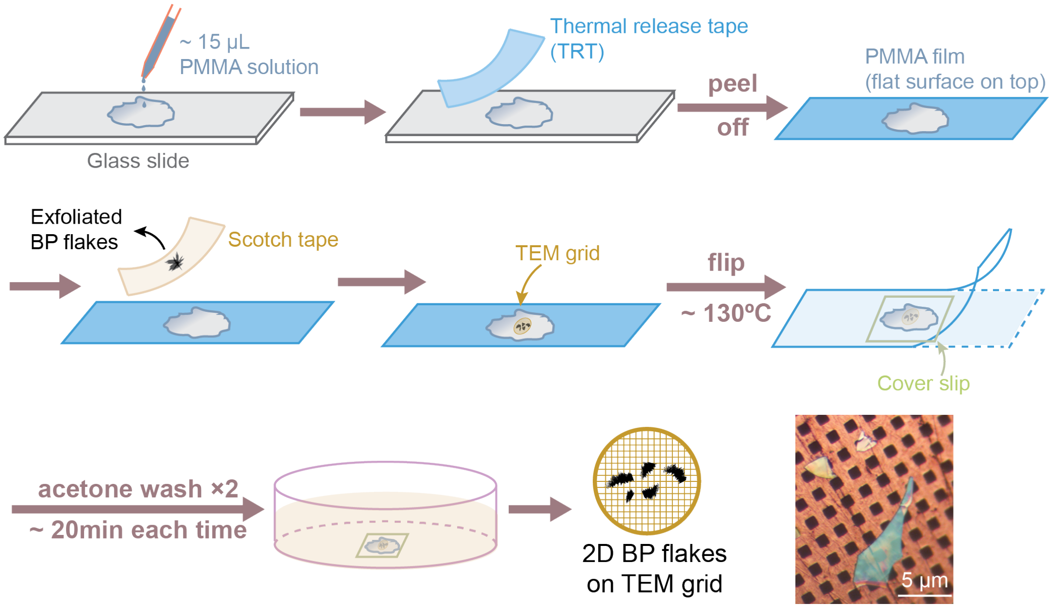

Figure 3.6: Schematic of 2D materials transfer to TEM grids.

3.3 Sample characterization

3.3.1 Optical microscopy

Optical microscopy is a direct, simple, and efficient way to assess the exfoliation results. At appropriate magnifications, optical images provide immediate information on the density, size, positions, and estimated thickness of the exfoliated flakes. Furthermore, by selecting proper illumination sources and incorporating polarizing optics, materials with optical anisotropy can be uncovered at the microscale, and thus the crystal alignment could in principle be identified without advanced instrumentation. This subsection uses mechanical exfoliation of black phosphorus as an example to demonstrate 1) substrate effect on image contrast, 2) optical contrast as an estimation for layer number, and 3) polarization dependence of optical images.

Due to the air sensitivity of black phosphorus, the optical images of exfoliated flakes were collected with a microscope (Amscope) that's installed inside a glovebox, primarily using a 50x objective. The light source is a halogen lamp that produces white light and illuminates from the back of the microscope to reflect from the sample surface, and the reflection intensity was captured by a CMOS camera (Amscope, MU1803-HS).

The optical contrast of 2D flakes on a solid substrate originates from distinct reflections of different materials due to changes in absorption coefficient and optical path. In particular, silicon wafers with thick oxides (e.g. 100 nm or thicker) have interference effects from the multilayer that strongly enhance the background contrast.[93] In comparison, the optical contrast of BP on pure Si substrate (with native oxides) is very poor, making thin flakes extremely difficult to pick up by eye. Figure 3.7 compares images of thin BP flakes transferred on Si/90 nm SiO_2 and Si chips, respectively. BP flakes show sharp contrast on SiO_2 whereas they are hard to locate on Si substrate, particularly for thin flakes that are in the few-layer regime.

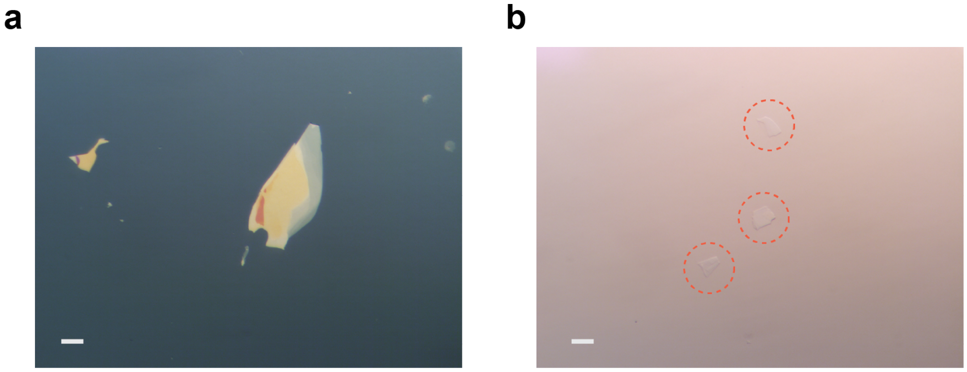

Figure 3.7: Exfoliated thin black phosphorus flakes on different substrates. (a) Si/100 nm SiO_2. (b) Bare Si with native oxides. The circles are the guide to the eye for three low-contrast BP flakes. Scale bars are both 10 μm.

The big flake in the left image not only shows contrast variations at the edges but also depicts color differences. As verified by Raman and AFM, only thicker flakes or flakes with thicker portions display coloration. The appearance of different colors could be related to the thickness-dependent bandgap of black phosphorus, which varies from 2 eV to 0.3 eV from monolayer to bulk crystals.[94] This varying bandgap indicates that the thicker the flake, the absorption is to the infrared (IR), and thus the reflection is more visible. In practice, there isn't necessarily a linear correlation between the color wavelength and layer numbers, as the flake color also depends on the interfacial interference within black phosphorus layers, or between black phosphorus and the substrate. For instance, on a different substrate such as a glass slide, or Si with oxides of different thicknesses, the color of the 2D materials with identical thickness will appear a different color.

At the few-layer limit, the flakes exhibit a similar color as the substrate but with a higher reflection intensity. This contradicts with literature reports where the thin BP flakes show a darker contrast than the Si/SiO_2 substrate.[95] The difference could be due to 1) the light source spectrum and the angle of incidence, 2) the correction for the white balance of the camera, and 3) the difference in SiO_2 thickness that modifies the interference effect. The total reflection intensity be used to estimate flake thickness. Qualitatively, in the thin regime where the flake color appears more transparent, a lower intensity corresponds to a thinner flake. The exact thickness needs to be measured by a quantitative method such as AFM, which will be discussed in Section 3.3.3.

For anisotropic materials such as black phosphorus, variations of flake orientations can be revealed by alternating the polarization of the incident light due to anisotropic optical absorption along different crystal axes. Linear polarizers and analyzers are available to install in the incoming and reflected beam paths of the microscope. As shown in Figure 3.8, the same BP flake was imaged at the same position with perpendicular light polarization in the incoming beam. Drastic color differences can be observed, suggesting changes in optical absorption. In particular, the flake center switches from light green to faint pink, indicating that BP absorbs much stronger when the crystal is aligned with one of the polarizations. The exact crystal direction needs to be determined via a full polarization-dependent measurement with controlled rotation, which isn't accessible on this particular microscope. Quantitative measurements are accessible with a different microscope (Olympus BXFM) in the King Lab by installing a polarizer with a rotational mount. Angular-dependent absorption of materials including In_2Se_3 have been detected to resolve domains on the microscopic level.[89]

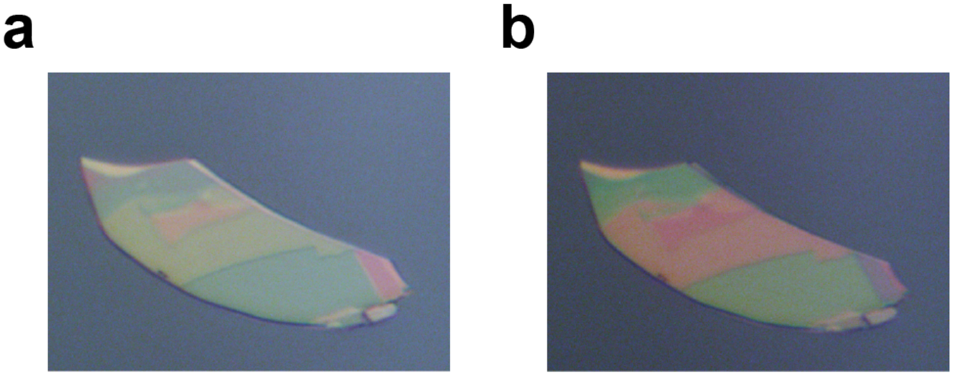

Figure 3.8: Optical images of the same BP flake illuminated by visible light with perpendicular polarizations. Drastic color difference can be found, indicative of varying absorption upon different crystal alignments with light polarization.

3.3.2 Raman spectroscopy/microscopy

Raman spectroscopy, coupled with optical microscopy, is a fast and non-destructive technique to characterize the lattice vibration (phonons) for a wide variety of 2D materials with high spectral and spatial resolution. The peak position, linewidth (FWHM), as well as intensity, are encoded with rich information on chemical compositions, crystal structure, and electronic properties.[96] Raman spectroscopy is extremely sensitive even for detecting an atomically thin 2D layer[97] and therefore is always used as the first evidence to distinguish exfoliated BP flakes from surface contamination (such as tape residue) on the substrate. The phonon modes in 2D materials are strongly subject to external perturbations, providing opportunities to investigate a broad range of properties using Raman spectroscopy, including but not limited to polarization dependence, thickness dependence, temperature dependence, defect concentration, strain characterization, and edge effect.[22,97–101] Among all the fundamental properties, polarization-dependent Raman responses and thickness-dependent Raman spectroscopy have been explored for 2D BP characterizations.

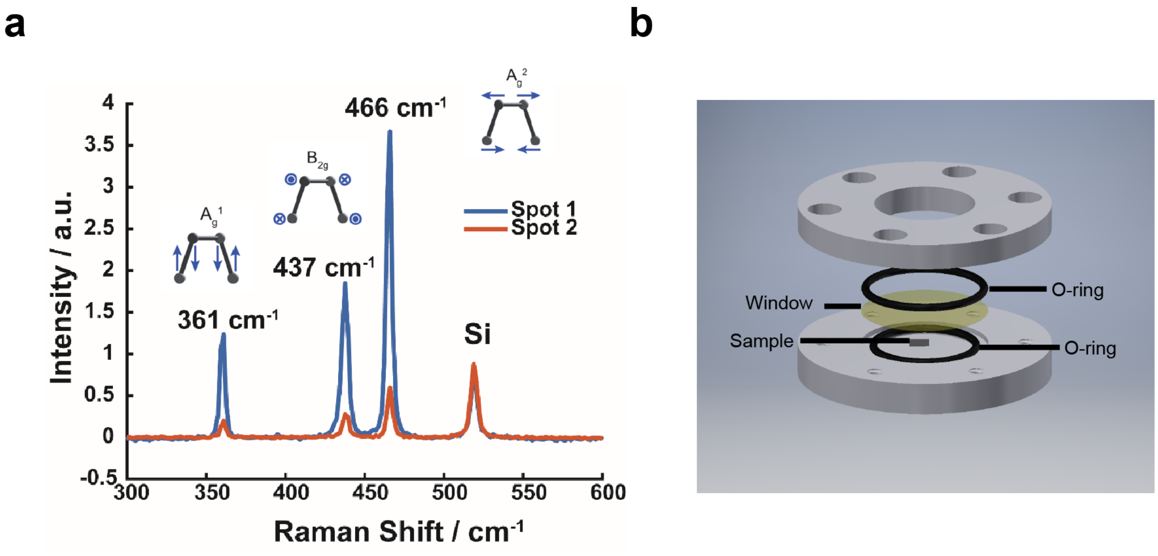

Figure 3.9: (a) Representative Raman spectra of a BP, measured at two different spots, showing characteristic peaks at 362 cm^{-1}, 437 cm^{-1}, and 466 cm^{-1}. The different peak amplitude could be due to different crystal orientations with respect to light polarization. (b) The 3D-printed air-tight transfer cell for Raman microscopy measurements of air-sensitive samples.

For all Raman results presented here, BP flakes on Si/SiO$_2$ were excited by a 532 nm continuous-wave (CW) laser with tunable powers, and Raman scattering was collected by a spectrometer in backscattering configuration with an 1800 gr/mm grating (Horiba LabRAM HR Evolution). The optical image was collected by an LED wide-field illumination and the flake was magnified with a 100x objective and captured with a CCD camera. All experiments were conducted at room temperature. Black phosphorus has three prominent Raman peaks 362 cm^{-1}, 437 cm^{-1}, and 466 cm^{-1}. They represent the three Raman-active vibrational modes A$_g^1$, B$_{2g}$, and A$_g^1$, and the atomic displacements for the lattice vibrations are depicted in Figure 3.9(a).[25,102]

To minimize air exposure during sample transfer and data acquisition, we custom-designed a 3D-printed transfer cell to store the exfoliated BP in an air-free environment for Raman measurements. Compared to machined metal sample holders, 3D printing provides an easier and faster approach to modify the designed models and resin-based materials are less costly to manufacture. The 3D model was designed in AutoDesk Inventor and a Formlabs printer (Form 2 - Flowery Yeti) was used for fabrication. The exploded cell assembly is displayed in Figure 3.9(b). The cap and the base are made of clear resin, with an opening in the cap to conform with the objective diameter and a dip in the base as the sample chamber. A chip is stored in the chamber with a 1 mm UVFS window (Thorlabs) on top for optical access and the window is sandwiched between rubber two O-rings (McMaster-Carr). Six tapped holes are available for closing the cell with plastic screws and the air-tightness was tested by measuring the Raman peaks of a BP sample and the features retained on the same spot after two hours. The transfer cell is typically assembled inside the glovebox where BP flakes are freshly exfoliated to keep the sample in an inert atmosphere.

Thickness-dependent phonon modes of BP have been extensively investigated both experimentally and theoretically. We have tried to use Raman spectroscopy to determine BP layer numbers by measuring Raman spectra on multiple spots on a BP flake with varying thicknesses based on optical contrast, and a representative result is shown in Figure 3.10(a) and (b). The exact thicknesses were determined by AFM (Figure 3.10(c)). The bulk reference was measured from a different thick flake. A few variations can be observed from bulk to thinner layers, including slight frequency shifts, non-monotonic peak broadenings, and possible new emerging modes. In terms of distinguishing new vibrational modes, the deconvolution of the broadened peak can add errors and complexity to spectral analysis.[102] For BP flakes that are above 10 layers, the difference in Raman shift is hardly resolvable, limited by the resolution of the optical grating in the detector. Hence, AFM is a more accurate tool to measure the thicker flakes whereas Raman spectroscopy can be used as a qualitative confirmation for flake thickness.

Nevertheless, Raman spectroscopy still has unique advantages for studying material systems such as graphene and TMDs, where monolayer flakes are easier to obtain, and the

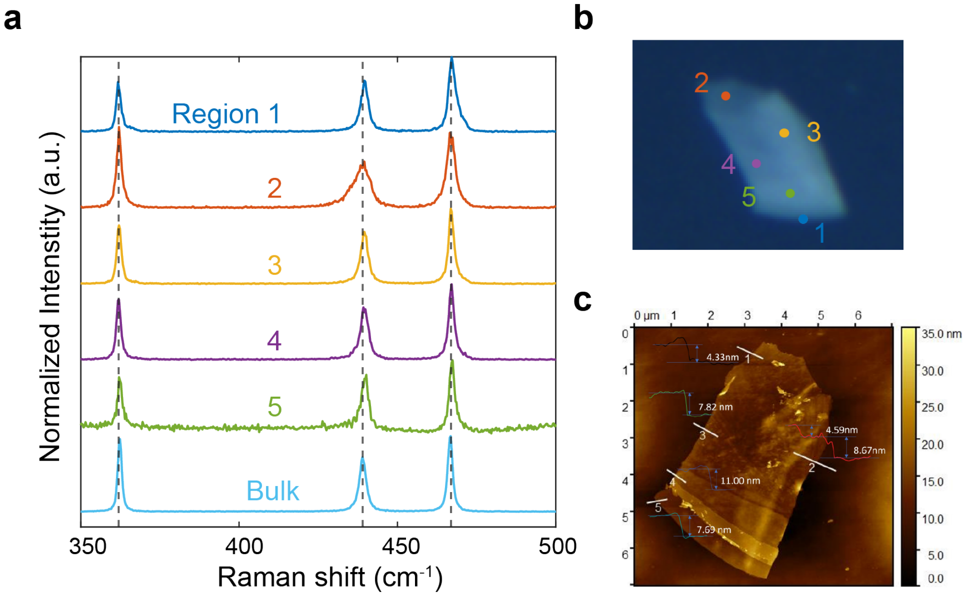

Figure 3.10: (a) Raman spectra collected from five different regions of a flake with varying thicknesses. The bulk spectrum is measured from a different thick flake. (b) Optical image of the BP indicating detection spots. (c) AFM image that shows the thicknesses of the detected areas.

frequency variations in the few-layer region are more prominent.[97,103] Alternatively, low-frequency Raman spectroscopy, exploring the vibrational modes below 200 cm^{-1},[104], provides an additional route to characterize layered crystals as it probes the interlayer interactions. Zeng *et al.* proved that the optical phonon in MoS_2 exhibits as large as 10 cm^{-1} difference with increasing thickness, allowing precise determination of the number of atomic layers.[105] The same group showed a few years after that the shift in low wavenumber modes of BP is even more drastic and can be as large as 32 cm^{-1}.[106] However, low-frequency Raman is hard to observe in most commercial apparatus due to the extremely strong Rayleigh scattering around 0 cm^{-1}.

3.3.3 Atomic force microscopy

Atomic force microscopy is one of the most common probe-scanning microscopy techniques. The sample surface is pixel-by-pixel scanned by a tip that's mounted on a piezo-driven cantilever spring. The force between the probe and the sample is maintained by a feedback loop (usually laser deflection from the cantilever) by adjusting the scanner height and thus a height profile vs. sample position can be obtained.[107] AFM can detect surface height differences down to below 1 nm resolution and therefore is a reliable tool for precisely determining the thickness of layered materials. Tapping mode is the most frequently used operation type for measuring the number of layers in this thesis. In this operation mode, the tip is constantly attracted and repulsed from the surface at a given frequency and the oscillation amplitude is collected at the contact point as the feedback, which can be correlated to the surface height profile. AFM is a powerful tool to characterize few-layer 2D flakes. Besides measuring the layer thickness from a flake edge as shown in the previous sections, surface profiles such as step edges, grain boundaries, and nanostructures can be visualized clearly from exfoliated materials, which reveals the destructive nature of mechanical peeling. In ambient conditions, AFM can capture surface adsorbates and defects. In particular, for air-sensitive materials e.g. black phosphorus, during a 2-hour AFM session, visible nanoscale smooth bumps show up on the ultraflat flakes, implying water or oxygen is gradually degrading the sample by adsorbing on the surface, as indicated in Figure 3.11. On the other hand, surface roughness can be quantified by doing statistical analysis on AFM images. One example is the characterization of gold films as demonstrated in Section 3.2.3 and Figure 3.3.

There are several practical challenges in using AFM for exfoliated materials. First, locating the micrometer-size flakes within the limited translation distance requires prior knowledge of the sample surface. An optical survey at a low magnification is needed before engaging the tip, and it is desirable to transfer target flakes in the substrate center for better positioning. When imaging air-sensitive samples such as BP, it is difficult to avoid O_2 and water absorption during the long acquisition time (1-2 hours). The ideal solution is to conduct the experiments in an insert environment, and there are several available AFM vendors that provide sample cells for environmental control. The other option is to use UHV AFM but

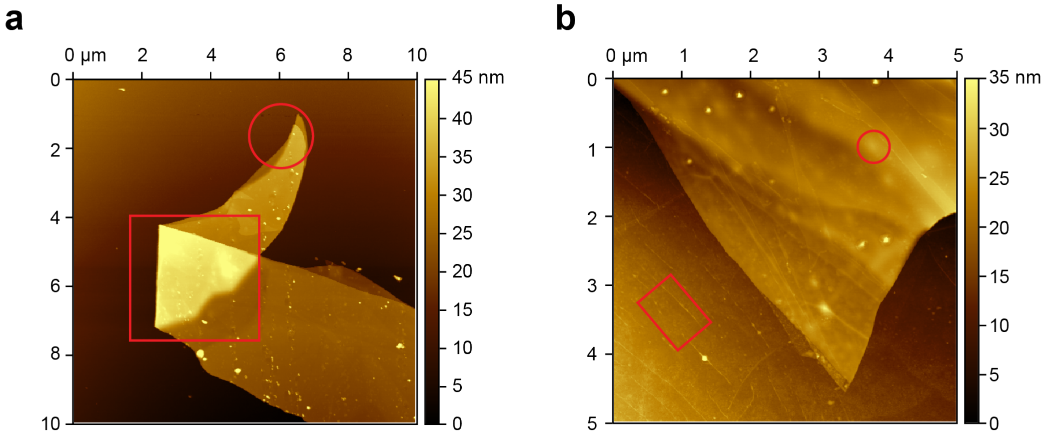

Figure 3.11: (a) A representative AFM image of a thin black phosphorus flake on Si, where terraces can be observed clearly at the flake edges (circled). The bright triangle (boxed) with a smooth bottom edge implies the end of the long BP piece folded under the flake body. The smaller nanoscale bright spots are indicative of surface adsorbates on the BP flake as well as on the substrate. (b) An AFM image of a BP flake on polycrystalline graphene. The circled area is an example of a smooth surface bump that is likely due to water-induced degradation. Additionally, the grain boundaries of graphene can be visualized as sharp nanostripes.

we were limited by the instrument accessibility. Nonetheless, black phosphorus flakes perverse the thickness upon exposure to air for several hours, as degradation typically initiates from the scattered sites in the flake interior. Therefore, the height profiles in the ambient condition can still reliably reflect the real thickness of 2D materials.

CHAPTER 4

NANOIMAGING OF THE EDGE-DEPENDENT OPTICAL POLARIZATION ANISOTROPY OF BLACK PHOSPHORUS

4.1 Abstract

The electronic structure and functionality of 2D materials is highly sensitive to structural morphology, opening the possibility for manipulating material properties, but also making predictable and reproducible functionality challenging. Black phosphorus (BP), a corrugated orthorhombic 2D material, has in-plane optical absorption anisotropy critical for applications such as directional photonics, plasmonics, and waveguides. Here, we use polarization-dependent photoemission electron microscopy to visualize the anisotropic optical absorption of BP with 54 nm spatial resolution. We find the edges of BP flakes have a shift in their optical polarization anisotropy from the flake interior due to the 1D confinement and symmetry reduction at flake edges that alter the electronic charge distributions and transition dipole moments of edge electronic states, confirmed with first-principles calculations. These results uncover previously hidden modifications of the polarization-dependent absorbance at the edges of BP, highlighting the opportunity for selective excitation of edge states of 2D materials with polarized light.[a]

4.2 Introduction

Black phosphorus (BP) is an allotrope of elemental phosphorus with a layered crystal structure, high carrier mobility rivaling that of graphene, and a thickness-dependent band gap spanning the visible to the mid-infrared.[108] With a corrugated orthorhombic crystal structure, BP also has strong in-plane structural, electronic, and optical anisotropy along the

---

[a] Adapted with permission from Joshi, P.P.*, **Li, R.***, Spellberg, J.L., Liang, L. and King, S.B. Nanoimaging of the edge-dependent optical polarization anisotropy of black phosphorus. *Nano Lett.*, **22**, 8 (2022), 3180-3186. * indicates indicates equal author contribution.

two principal in-plane crystal directions, armchair (AC) and zig-zag (ZZ), shown schematically in Figure 4.1(b).[109] Similar to other emerging corrugated orthorhombic materials, particularly GeSe, the symmetries and dispersion of the BP conduction and valence bands cause the dielectric function and conductivity tensor for BP to vary significantly along these two crystal directions.[110–112] As a result, optical absorption is highly dependent upon the direction of the incident electric field, and plasmons and polaritons of BP are predicted to be highly directional and possibly hyperbolic.[110,111,113] These anisotropic optical, plasmonic, and polaritonic properties of BP make it promising for the development of directional waveguides, plasmonic devices, and light emitters, as well as polarization-dependent photodetectors and thermoelectrics.[24,114–118]

Morphological features have been observed or predicted to modify the electronic and phononic properties of BP on the nanoscale.[14,101,119,120] Like other 2D materials prepared via mechanical exfoliation from polycrystalline bulk, few-layer BP can have uncontrolled structural morphology such as grain boundaries, variations in layer thickness, edges, defects, and strain that varies over 10s to 100s of nanometers, which interrupt the properties predicted for defect-free lattices of BP.[13–15,101,119–124] While some structural morphology can be mitigated by "bottom-up" preparation methods,[125] morphological features such as edges are omnipresent in many functional applications. In BP nanoribbons, predicted to support anisotropic plasmons and surface plasmon polaritons, edge effects could readily dominate the system's behavior.[126–129] Edge reconstructions of BP occur readily due to the corrugated orthorhombic lattice and are associated with unique in-gap edge electronic states and phonon modes;[120,130] metallic edge states of BP have been predicted theoretically.[131,132] However, distinguishing the critical interplay of edge and interior electronic behaviors and their effect on the direction-dependent dielectric function and optical properties of BP is not accessible with the limited spatial resolution of near-IR and visible optical microscopies, and is currently unknown.

Here we use photoemission electron microscopy (PEEM) to probe the morphology-dependent polarized light absorption of BP with 54 nm spatial resolution, a 4-8x improvement over the spatial resolution of near-IR and visible optical microscopies. PEEM circumvents the optical diffraction limit by imaging the electrons emitted from a material by light.[133] By using two or more photons for photoemission, instead of one, the contrast observed with PEEM images reflects not only the occupied electronic structure and material work function but also the normally unoccupied electronic structure and optical selection rules for optical absorption, similar to how two-photon photoemission spectroscopy probes the unoccupied electronic structure and dynamics of materials.[134] In contrast to other electron microscopy techniques such as SEM and TEM, no harsh electron beam is required for PEEM, and all of the advantageous properties of light for probing a material (well-resolved photon energies, few femtosecond pulse duration, facile manipulation of focusing and polarization with light optics) are maintained. PEEM with tabletop laser sources has been used previously to image the dynamics of plasmonic fields at metal/vacuum interfaces,[133,135] ultrafast dynamics in halide perovskites and at p/n junctions,[59,136] and the packing and alignment of polymers,[137] to name a few.

In this paper we show that the edges of black phosphorous flakes have a pronounced difference in their polarization-dependent absorption compared to the main body of a BP flake, displaying ± 20° shift in the polarization angle associated with maximum absorption and photoemission intensity. Through first-principles density functional theory (DFT) calculations, we attribute the edge shift to the modification of the electronic charge distributions, and subsequently the optical selection rules, in the near-edge region. Edge-specific optical absorption anisotropy could provide a way to selectively excite the edges of BP, tuning the distribution of charge carriers on the nanoscale even with unfocused light. The reduction in electronic state symmetry that causes the edge-specific absorption in black phosphorus suggests that edge states and properties could be exploited in a wider range of 2D materials, particularly in the design of devices using emerging corrugated orthorhombic 2D materials such as GeSe, arsenene, and GeS.

4.3 Experimental

4.3.1 Sample Preparation

Few-layer BP is mechanically exfoliated onto a Si substrate with an approximately 2 nm thick native oxide layer[138] in a glove box under N_2 atmosphere. The BP samples are transferred into ultra-high vacuum (< 20 s exposure to ambient conditions) and investigated with PEEM under ultra-high vacuum conditions (UHV, 10^{-10} mbar). AFM and Raman microscopy, found in the Figure A.6, Figure A.7 and Figure A.8, confirm the samples are few-layer BP with thicknesses ranging from ∼4 nm to 58 nm (8 to 116 layers) and characteristic Raman peaks, A_g^1, B_{2g}, and A_g^2.[139] Further details are described in the Appendix A.4.

4.3.2 Polarization dependent photoemission electron microscopy

Figure 4.1(a) shows a schematic of the experiment. Linearly polarized laser light is directed at near-normal incidence (NNI) via a Rh mirror onto a BP sample in a UHV PEEM microscope chamber (FOCUS GmbH). The angle of incidence is 4° from normal, allowing the polarization of the laser to be in-plane with respect to the sample at all polarizations. The laser polarization is rotated with a $\lambda/2$ waveplate outside of the UHV chamber, rotating the laser electric field in the sample plane to different angles θ, depicted in Figure 4.1(d). The laser photon energies used in this experiment are 1.55 eV (800 nm) and 2.4 eV (515 nm). These photon energies require 3-photon and 2-photon photoemission (3PPE and 2PPE, Figure S5) to overcome the > 4.0 eV work function of few-layer BP.[140] The first photon excites an electron across the band gap of BP (≈ 0.3 eV for > 5 layers) and the subsequent photon(s) within the same laser pulse photoionize the electron, as shown in in Figure 4.1(b). Time-resolved polarization-dependent experiments, described in the Section A.4.3 and Figure A.18, confirm that the polarization-dependent photoemission intensity is due to the across-band gap absorption rather than the subsequent photo-ionization photon(s). Photoemitted

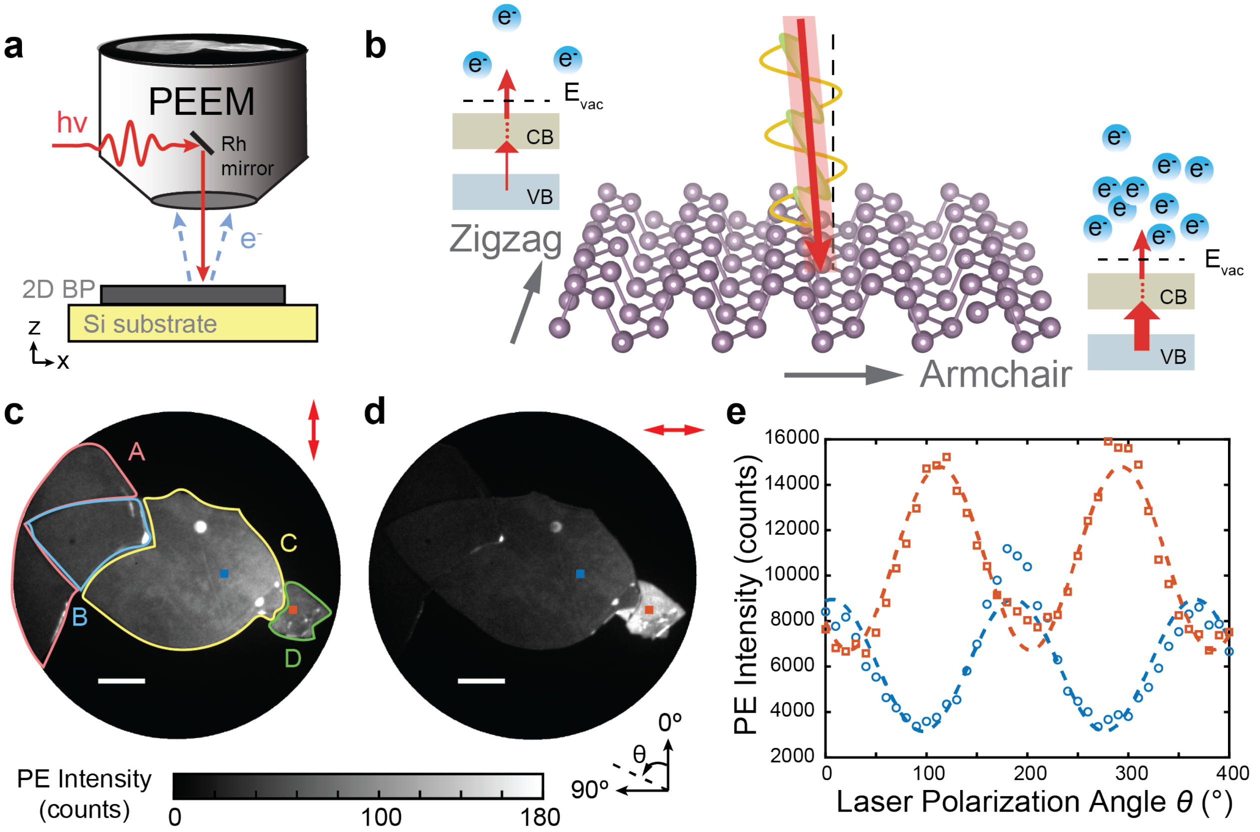

Figure 4.1: (a) Schematic of NNI PEEM. (b) Crystal structure of monolayer BP crystal. Optical absorption is higher when laser polarization is parallel with armchair direction, leading to increased photoemission efficiency, as shown in the energy diagrams of nPPE processes. (c) PEEM images illuminated by 2.4 eV laser at 0° and (d) 90° indicated by the red arrows in the upper right corners; Scale bar: 5 μm. The laser polarization θ is rotated counterclockwise and shown in the inset. (e) Intensity of the red and blue integrated regions shown by the squares in (c) and (d) as a function of θ fit to equation 4.1 (dashed lines).

electrons are accelerated and steered by a set of electron lenses in the PEEM, amplified by a double microchannel plate (MCP)/phosphor screen detector, and imaged by a time-integrated CCD camera. A PEEM image of BP is shown in Figure 4.1(c).

4.3.3 Theory

Plane-wave DFT calculations were carried out using the Vienna *ab initio* simulation package (VASP, version 5.4.4)[141]. The projector augmented wave (PAW) pseudopotentials were used with a cutoff energy of 400 eV, and the Perdew-Burke-Ernzerhof (PBE) exchange-correlation functional was used.[142] To study optical transitions from the BP edges, a monolayer BP nanoribbon with a (1,3) reconstructed edge was selected.[120] A vacuum region of 14 Å in the y and z directions were used to avoid spurious interactions with replicas. The whole structure was optimized until the residual forces were below 0.02 eV/Å with a Γ-centered k-point sampling of $20 \times 1 \times 1$. After the structural relaxation, we computed the electronic band structure, and the electronic wavefunctions corresponding to each band at each k-point to be post-processed by the VASPKIT code for obtaining the transition dipole moments.[143]

4.4 Results and Discussion

Figure 4.1(c) and (d) show PEEM images of the BP flake taken with 2.4 eV illumination and the angle of polarization, θ (shown schematically in Figure 4.1(d)), set to 0° and 90°, respectively. The intensity of the PEEM images are all corrected for the polarization-dependent reflectivity of the Rh NNI mirror, as described in Section A.4.2 and by Neff *et. al.*[137] Four general regions are identified in Figure 4.1(c). Region A is ∼80 layers thick, B is ∼116 layers at the overlap between A and C, C is ∼36 layers, and D is ∼8 layers, as determined by AFM.

By taking a series of PEEM images as a function of θ, we map out the nanoscale polarization dependence of BP. Figure 4.1(e) shows the polarization dependence for the integrated photoemission intensity of the 10-by-10 pixel blue and red squares marked on Figure 4.1(c) and (d) as a function of θ in increments of 10°. The photoemission responses of both regions are periodic with respect to θ and phase-shifted with respect to each other. The polarization-dependent photoemission response is fit well by a cosine-squared fit of the form

$$I_{BP}(\theta) = A\cos^2(\theta - \beta) + C \tag{4.1}$$

where A is the amplitude of the modulation, β is the phase shift, and C is the baseline offset of the fit.[137] These fits are shown in Figure 4.1(e) by the red and blue dashed lines. The goodness of fit is evaluated by the R^2, which in Figure 4.1(e) is 0.86 and 0.95 for the blue and red regions, respectively. We evaluate the magnitude of the polarization anisotropy by the dichroism,

$$\rho = \frac{I_{max} - I_{min}}{I_{max} + I_{min}} = \frac{A}{A + 2C}. \tag{4.2}$$

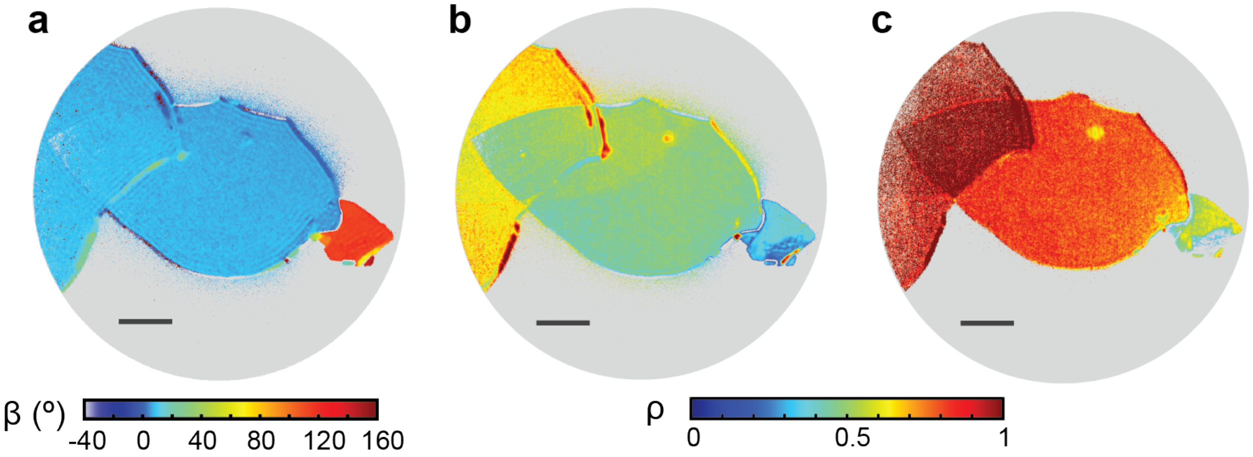

Figure 4.2: (a) 2.4 eV β mapping. (b) 2.4 eV ρ mapping. (c) 1.55 eV ρ mapping. All maps are median-filtered with a 3×3 pixel neighborhood and only pixels with an $\mathrm{R}^2 > 0.6$ are shown. Scale bar: 5 μm.

4.4.1 Pixel-by-Pixel Mapping

In order to evaluate the spatial variation of the polarization anisotropy, we perform pixel-by-pixel analysis on the polarization-dependent PEEM images. I(θ) for each pixel is normalized, fit with equation 4.1, and the resulting β and ρ values are extracted and calculated for each pixel. Figure 4.2(a) shows the resulting β map for 2.4 eV excitation. Maps of ρ for 2.4 eV and 1.55 eV are shown in Figure 4.2(b) and (c), respectively. All maps are median-filtered with a 3-by-3 pixel neighborhood to improve signal-to-noise, and only pixels with a goodness-of-fit $R^2 > 0.6$ are shown. The goodness-of-fit and unfiltered maps can be found in Figure A.13 for comparison. The spatial resolution of Figure 4.2(b) is approximately 120 nm, limited by the comparatively large 35 μm field of view. Figure 4.3 shows line cuts of a PEEM image, β map, and ρ map (Figure A.14(a) and (b)) from a flake with a smaller field of view. The reported resolution is the width between 16% and

84% of the error function. The smallest features we can measure in this image are 73 nm, 85 nm, and 54 nm for the raw PEEM images, the β maps, and the ρ maps respectively and can likely be improved as the spatial resolution of the instrument is approximately 30 nm. This is an approximately 4-8x improvement over conventional visible and near-IR optical microscopy.[144]

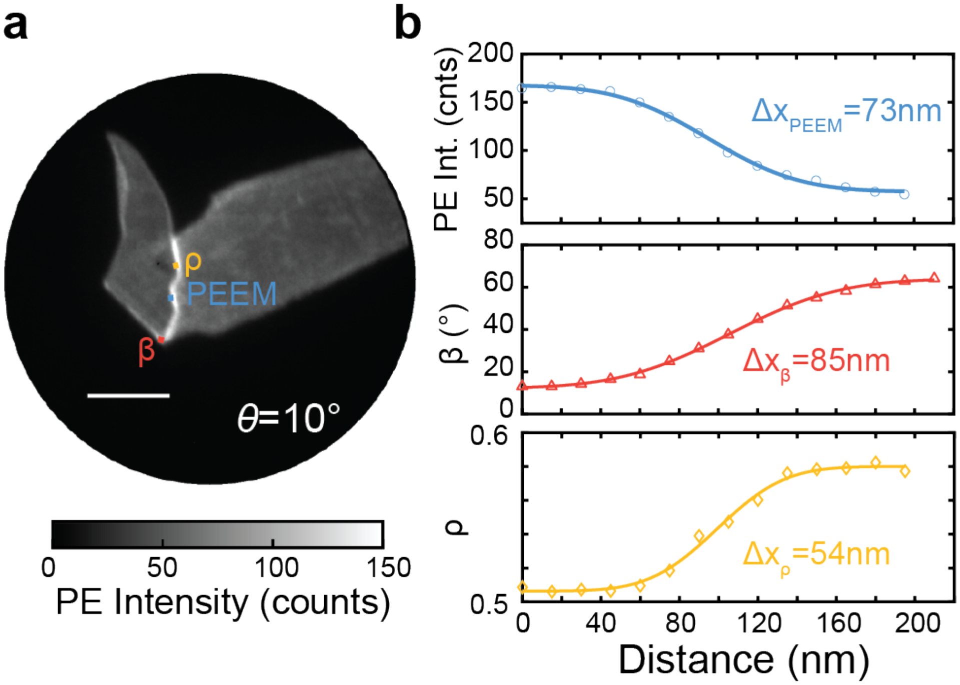

Figure 4.3: (a) 2.4 eV laser-illuminated PEEM image, taken at $\theta = 10°$, where the yellow, blue and red line cuts were taken from the PEEM image, β map and ρ map, respectively. Scale bar: 3 μm. (b) Scatter plots show the line profiles from each image or map, fitted with an error function.

4.4.2 Interpretation of β and ρ

The β values for the interiors of regions A, B, and C are qualitatively similar, however, region D is phase shifted by $-50°$ to $80°$ compared to A, B, and C (Figure 4.2(a)). The anisotropic optical response of BP is well known; for $h\nu < 3$ eV the absorption coefficient for an electric field polarized along the armchair (AC) direction of the lattice exceeds that of the zigzag (ZZ) direction by ~1-2 orders of magnitude.[139] Therefore, more electrons will be excited across the band gap when the laser polarization is aligned with the armchair axis of the BP flake, resulting in the highest photoemission intensity, shown schematically in Figure 4.1(b). From equation 4.1, therefore, $\theta = \beta$ is the angle where the laser polarization is aligned with the armchair axis. As the β values of A, B, and C are approximately the same, we conclude that these are regions of different thicknesses of the same crystalline piece rather than regions with mismatched lattice parameters. However, the measured β of the majority of region D is rotated with respect to A, B, and C by approximately 50 degrees, suggesting it is non-contiguous with the rest of the flake. Comparison to the corresponding AFM image (Figure A.6(a)-(c)) indeed shows that region D is a flake broken off from the A, B, and C regions with folded and/or overlapping areas at the bottom of region D. While the β maps are largely photon energy independent, comparison of Figure 4.2(b) and (c) shows that the dichroism maps, ρ, are photon energy dependent. The dichroism, ρ, is a measure of the contrast between the photoemission intensity at AC (maximum intensity) and at ZZ (minimum intensity), reflecting the differential optical absorbance between the AC and ZZ directions for a particular BP thickness and excitation energy. This differential optical absorption varies as a function of layer thickness and photon energy,[139,145] explaining the difference in the ρ maps for 1.55 and 2.4 eV.

4.4.3 Edge-dependent optical anisotropy

At both photon energies (Figure 4.2(a) and Figure A.12), the edges of regions A, B, and C have β values that are phase shifted by approximately -20° to 20° relative to the interiors of the flakes, where the armchair direction is $\beta = 7^\circ$. Edge-dependent phase shifts are not readily observed in region D, which is significantly thinner (8 layers) than regions A-C, nor are they observed at monolayer edges intentionally introduced through sublimation (Figure A.23).[146–148] Further information regarding the intentionally created edges can be found in Section A.4.4.

Not all edges of the flake have the same phase shift compared to the armchair direction, but along an entire edge segment, the phase shift remains predominantly the same. These

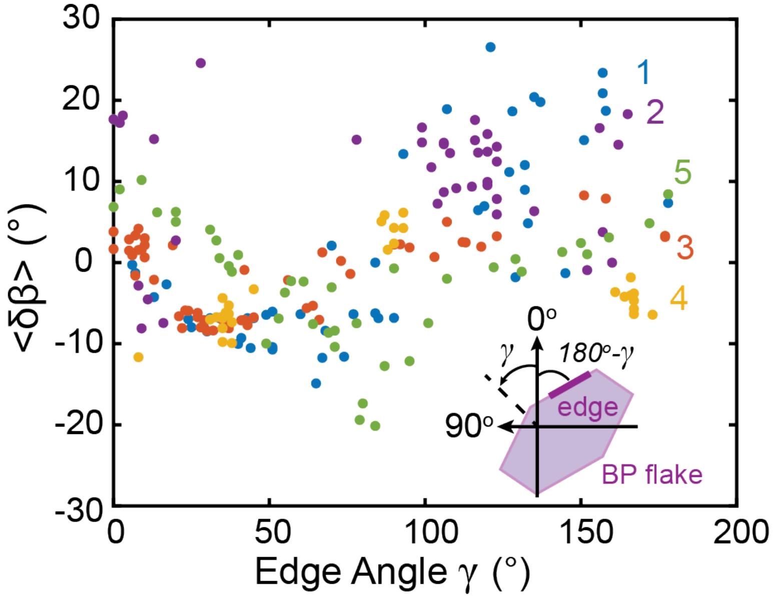

Figure 4.4: Average phase shift $\langle \delta\beta \rangle$ as a function of edge orientation γ, shown schematically in the inset, for five different black phosphorus flakes.

phase shifts are reproducible across different BP flakes and samples. We analyzed the average phase shift of the edge from the flake interior ($\langle \delta\beta \rangle$) for short line segments versus the angle γ of the edge for five different BP flakes (β maps showing these segments can be found in Figure A.17) and find a persistent phase shift of up to $\pm$ 20° at flake edges despite the varied γ for different segments and armchair directions of the flake interiors ranging from 7° to 156° (Figure 4.4).

The phase-shifted optical anisotropy of the edges of regions A, B, and C is independent of folds, wrinkles, and oxides as verified by AFM (Figure A.6) and experiments performed before and after annealing of the samples to 350 °C (Figure A.16), the temperature required to achieve a pristine oxide-free surface.[147–150] We also exclude near-field modification of the incident EM fields as the source of the edge phase shifts. With near-field modifications we would expect a correlation between the β values at flake edges and the angle of the edge defined in the laboratory frame, regardless of the orientation of the AC and ZZ directions of the flake, causing phase shifts to be very large with some flakes and small with others depending on the flake orientation. This is not observed in Figure 4.4, the phase shifts relative to AC orientation are up to ± 20° regardless of the interior flake orientation with respect to the laboratory frame.

To understand the experimentally observed phase-shifted behavior at the edges of BP flakes, we carried out proof-of-principle DFT calculations on a (1,3) reconstructed edge of monolayer BP; calculations on multilayer BP are computationally too expensive. The AC direction is defined as (1,0) while the ZZ direction corresponds to (0,1). Figure 4.5(a) shows the calculated electronic band structure of the BP nanoribbon with the (1,3) edge. By computing the contribution of the edge atoms to each band state (indicated by the size of the red circles), we can identify the two bands at approximately -0.1 eV as edge bands.

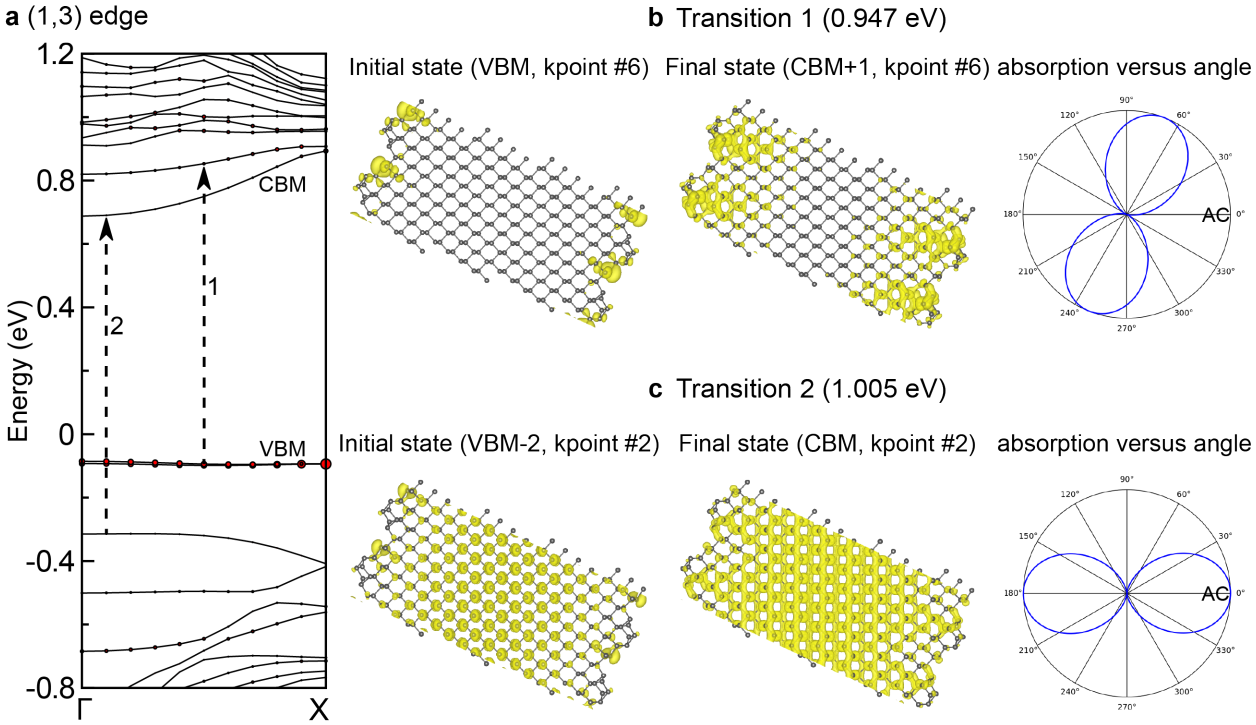

Figure 4.5: (a) Electronic band structure of a monolayer BP nanoribbon with a (1,3) edge with the valence band maximum (VBM) and conduction band minimum (CBM) labeled where the Fermi level is Energy = 0 eV. Red circles superimposed on the bands correspond to the contribution from the edge atoms. For two representative optical transitions (indicated by the arrows), spatial distributions of the charge densities of the initial and final states, and polarization-angle-dependent absorption profiles are shown in (b) and (c).

Mechanically exfoliated BP flakes consist of a mixture of edges with multiple directions. Those edges can be generalized into (1,0) armchair edge (along the AC direction), (0,1) zigzag edge (along the ZZ direction), and (1,3) edge, which represents the predominant experimentally-created BP edge. These different edge geometries form distinct edge bands via edge reconstruction to release the excess energy from dangling bonds, as verified by scanning tunneling spectroscopy and previous theory studies.[120] In particular, DFT calculations predict that due to variations in dangling bond configurations of the AC and (1,3) edge in BP nanoribbons, the reconstructed AC-edged band is above the Fermi level, whereas the edge band is relaxed to below the Fermi level in the (1,3) geometry.[120] This result leads to a large difference in the allowed optical transitions when AC or (1,3) edge states are excited by linearly polarized light. Here, we discuss two edge state transitions that demonstrate large variations in the rotation of transition dipole moments. Note that experimentally, the total amount of rotation angle is an average of all possible optical transitions, depending on the contributions of each edge state that's present in the sample.

Two representative transitions with different transition energies, approximately 0.95 eV and 1.0 eV, are indicated by the arrows in Figure 4.5(a). It is important to note that because of the limitations of obtaining accurate energies in DFT, the energies and momenta of the transitions are illustrative rather than for quantitative comparison to experiment. Figure 4.5(b) and (c) show the spatial distributions of charge densities of the initial valence state and final conduction state for the two transitions. In transition 1, shown in Figure 4.5(b), the charge densities of the initial (VBM) and final (CBM+1) states are largely confined at the edges of BP that have a symmetry reduction compared to the interior atomic structure. Therefore, their spatial distributions and symmetries are significantly modified compared to those of transition 2, where the charge densities of the initial and final states are largely in the interior of BP, shown in Figure 4.5(c). Consequently, the transition dipole moment of transition 1 is notably rotated away from the AC direction, changing the optical selection rules. This is evident in the polarization-angle-dependent optical absorption profile shown on the right of Figure 4.5(b) where the angle of maximum absorption is 69° (more details regarding the selection rules can be found in the Figure A.24 and Figure A.25). These results are in stark contrast to typical optical transitions that occur in the interior of BP shown in Figure 4.5(c) where the transition dipole moment and the maximum absorption are along the AC direction (i.e., 0.0°), as expected for 2D BP.[12,139] In short, our calculations demonstrate that the optical selection rule is modified at the edges of BP due to the 1D confinement and symmetry reduction in comparison with 2D BP, leading to orientation changes of the transition dipole moments at the edges and the experimentally observed phase variations in the maximum absorption direction between the edges and interior. More details for all of the transitions for a range of photon energies can be found in the Appendix A.4 (Figure A.26, Table A.2 and Table A.3)

Our calculations are focused on monolayer BP due to the computational cost, and indicate that edge phase shifts should occur in BP monolayers. However, edge phase shifts are not detected in our experiments on 8-layer, or thinner, regions. As discussed in Section A.4.5, transitions originating from the interior often show stronger intensities than edge-related transitions. Even with the excellent spatial resolution of these experiments, there is inevitably a mixture of edge and interior contributions observed at the edges of our images. With extremely thin BP flakes, when accounting for our spatial resolution, the comparative contribution from the edges and the interior leads to very small computed phase shifts in the monolayer BP nanoribbon, on the order of 2°. We expect that with increasing flake thickness the contribution from the edges compared to the interior increases, leading to the larger phase shifts that we can detect experimentally. Similar thickness dependence is observed in edge-dependent Raman modes, which appear in thick BP samples but disappear with decreasing thickness due to the signal reduction of edge Raman modes with decreasing thickness.[101]

4.5 Conclusion

In conclusion, we have used photoemission electron microscopy (PEEM) to image the nanoscale variation in the polarization-dependent photoemission response of black phosphorus. Enabled by our 54 nm spatial resolution, we observe that the edges of BP flakes have a phase shift in their polarization-dependent absorption of ±20° compared to the interior of the flake. Through comparison with DFT calculations, we assign these phase shifts to modification of the symmetry of the occupied and unoccupied wavefunctions at and in the vicinity of BP edges, due to the 1D confinement and symmetry reduction of BP edges. The unique absorption properties of BP edges mean that the extinction coefficients and complex dielectric function of BP edges are also unique from flake interiors, determining the functionality of BP in photonics-on-chip, waveguides, and directional plasmonic applications. Edge-specific optical absorption could also enable selective excitation of nanoscale BP edges even with far-field optical excitation, controlling the spatial distribution of excited charge carriers on the nanoscale. This work highlights how structural morphology can modify 2D material properties as simple as optical absorption, providing challenges and opportunities for material control.

CHAPTER 5

NANOSCALE DYNAMICS OF PDI/MOS$_2$ BILAYER HETEROSTRUCTURES REVEALED BY ULTRAFAST PEEM

5.1 Abstract

Synthesizing and constructing organic-inorganic 2D van der Waals heterostructures promise the modular design of 2D material properties enabled by the chemical tunability of molecular building blocks. However, spatial variations in these heterostructures have been shown to modify the interfacial electronic structure and ultrafast dynamics, impacting material functionality. Towards establishing a nanoscale structure-property relationship for organic-inorganic 2D heterostructures, we investigated how the ultrafast dynamics of a perylene diimide (PDI)/MoS$_2$ bilayer varies on the nanoscale using time-and energy-resolved photoemission electron microscopy (PEEM). While the crystallinity of the PDI monolayer is reduced at the edges of MoS$_2$ flakes, the dynamics of the bilayer are dominated by MoS$_2$ and are only weakly modified by molecular disorder. Probing the electronic structure of the bilayer as a function of space at different pump-probe time delays shows an instantaneous work function shift at time zero which suggests that the electronic structure of the bilayer system is at least partially hybridized even while being resistant to the impacts of molecular disorder. Our results highlight the possibilities of such molecular/inorganic 2D systems for optical and electronic applications where we see that the concerns regarding the impact of molecular disorder on material excited state properties may not be universal. [a]

---

[a] Adapted with permission from **Li, R.**, Chowdhury, T., Liang, C., Joshi, P., Park, J. and King, S.B. Nanoscale dynamics of PDI/MoS$_2$ bilayer heterostructures revealed by ultrafast photoemission electron microscopy. *In preparation.*

5.2 Introduction

Van der Waals (vdW) heterostructures created by artificially stacking 2D layers provide attractive platforms to engineer material electronic properties. Previous research has largely focused on the stacking of 2D inorganic monolayers, such as graphene and transition metal dichalcogenides (TMDs).[2] Efforts toward careful tuning of material electronic structure and excited state dynamics have focused on tuning relative crystal angles but this process is painstaking and can be hard to control.[151–155] Expanding the library for modification of vdW heterostructures to include organic molecules opens a huge design space for materials, where organic thin films are already used for a wide range of optoelectronic applications.[156–160] The combination of the high mobility of inorganic semiconductors with the tunability of organic counterparts is highly promising for accessing adaptive architectures for advanced optoelectronic devices.

Recently, the ultrafast dynamics of organic/TMD heterostructures, including tetracene/WS_2,[161] C_{60}/WSe,[162] pentacene/MoS_2,[163,164] and 2D polymer/MoS_2,[165] have been investigated using transient absorption (TA) spectroscopy and photoluminescence (PL) spectroscopy. However, these systems exhibit large variations in thickness and crystallinity of the molecular layer, resulting in nanoscale heterogeneity that has been challenging to disentangle from the observed dynamics due to both insufficient spatial resolution and poor control of the molecular/TMD heterostructure. Recent studies discussed the impact of molecular ordering in the charge transfer processes to TMD layers,[166,167] but a simultaneous characterization of molecular film and carrier dynamics has not been achieved. A fundamental understanding of the relationship between material morphology and electronic structure is crucial to realizing the intentional and reliable manipulation of functional devices.

Photoemission electron microscopy, or PEEM, is a wide-field, surface-sensitive imaging technique that enables the scheme of electron detection for optical perturbation. PEEM can be effectively coupled to ultra-short pulsed laser sources, allowing for a pump-probe detection configuration. The unique capability of combining spatial and temporal measurements with requisite resolution makes PEEM well-suited for visualizing the local evolution of charge carriers, as exemplified by metals[168,169], semiconductors[170–172] as well as inorganic materials[61,65,173]. The versatile imaging tool reveals spatially varying physical properties on the nanoscale, including dipole moment distribution[137,174], surface plasmon propagation,[57,133,175–177] electron transport,[58,59] exciton formation,[66,67,178] and excited state dynamics,[62–64] demonstrating its remarkable power in investigating complex heterogeneous solid-state systems.

In this paper we use a novel molecular-MoS_2 heterostructure consisting of a crystalline monolayer of perylene diimide (PDI), a conjugated dye molecule with strong visible absorption,[179,180] and a monolayer (ML) of MoS_2 that also serves as an atomically flat platform for the growth of the highly crystalline molecular film.[35] These heterostructures are a model system that provides a clean interface for investigating interlayer interactions and the impact of molecular disorder. Leveraging the simultaneous energy-, space- and time-resolution of ultrafast electron microscopy, we are able to simultaneously resolve the impact of molecular film crystallinity on the ultrafast excited state dynamics of the heterostructure on the nanoscale. Correlating the nanoscale film morphology with carrier dynamics, we elucidate that the presence of the molecular crystal has a surprisingly weak influence on the overall decay dynamics of the heterostructure, and energy-resolved measurements suggest that the initially formed excited electronic state is a hybrid electronic state of the PDI film and MoS_2. These results provide important insights into the coupling mechanisms of integrated organic/inorganic hybrid systems and the role of disorder in the considerations of coupling inorganic-organic materials.

5.3 Methods

5.3.1 Material preparation

A bilayer heterostructure of perylene diimide and MoS_2 was prepared by depositing a sin-

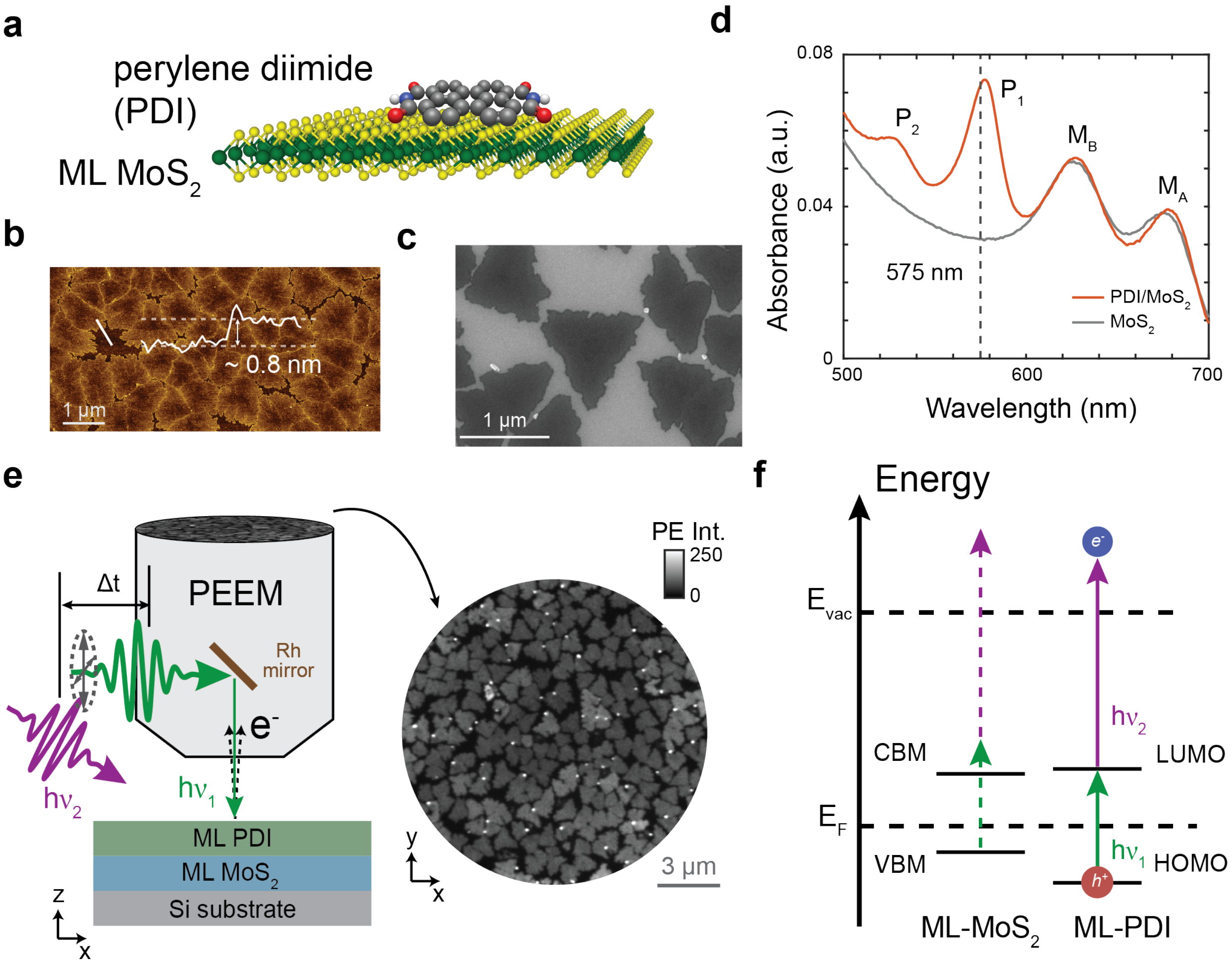

Figure 5.1: (a) A schematic of monolayer perylene diimide (PDI)/monolayer (ML) MoS$_2$ heterostructure. (b) SEM image of bare MoS$_2$. (c) AFM image of the heterostructure, showing the thickness is approximately 0.8 nm. (d) UV-vis static absorption of bare MoS$_2$ and the heterostructure. P$_1$ and P$_2$ correspond to the first two vibronic bands of perylene. M$_A$ and M$_B$ indicate the A and B exciton peaks of monolayer MoS$_2$. (e) A schematic of polarization-dependent and time-resolved PEEM experiment on PDI/MoS$_2$ heterostructure. The green pulse (575 nm) is the near-normal incidence (NNI) polarization-tunable pump, and the purple is the UV probe. A representative image of the bilayer, illuminated by a Hg arc lamp, is obtained with the detector. Time-resolved photoemission images are collected by stepping the time delays between the pump and probe pulses, and energy-resolved images are measured by applying high-pass energy filters. (f) Energy diagram of PDI and MoS$_2$, showing a type I alignment. The pump pulse excites at a molecular resonance to promote electrons from the highest occupied molecular orbital (HOMO) to the lowest unoccupied molecular orbital (LUMO) of PDI, and the UV probe photoionizes the electrons to above the vacuum level (E$_F$). Scattered electrons from MoS$_2$ can also be excited and photoemitted.

gle layer of perylene diimide (PDI) via physical vapor deposition (PVD), on a single layer of CVD-grown MoS_2 on a substrate of single crystalline silicon (111) with native oxide (University Wafer), shown schematically in Figure 5.1(a). The triangular crystal growth of the bare MoS_2 was first verified by scanning electron microscopy (SEM) (Figure 5.1(b)). Increased surface roughness of Si with native oxides results in the slightly irregular edge growth of MoS_2. Small bright features at the edges of certain crystals are overgrown bulk crystals.[10] An atomic force microscopy (AFM, BrukerMultiMode 8) image of the heterostructure (Figure 5.1(c)) shows similar triangles with a consistent domain size of ~1 μm compared to bare MoS_2. There is no height variation within a single MoS_2 triangular domain, implying uniform molecular adsorption. The thickness of the heterostructure of approximately 0.8 nm which is larger than 0.4 nm for single layer PDI,[35], or 0.7 nm for monolayer MoS_2.[181], verifying the sample is indeed a bilayer. The discrepancies could be sample variations in the growth of MoS_2 flakes, or the flakes experienced different interactions with AFM tips during the imaging measurements.

Bare MoS_2 and the heterostructure samples were transferred separately to transparent substrates (fused silica) for UV-vis absorption measurements (Cary 5000 Spectrophotometer), shown in Figure 5.1(d). Both spectra show the three exciton peaks of MoS_2 at 675 nm (1.8 eV, A exciton), 625 nm (2.0 eV, B excitons).[182] The heterostructure has two additional absorption peaks around 527 nm and 575 nm, corresponding to the first two vibronic bands of the S_0-S_1 transition of the PDI.[183] There is a minor ~1 nm shift in MoS_2 peaks in the heterostructure compared to bare MoS_2, suggesting the addition of PDI molecules has a weak impact on the electronic structure of MoS_2.

5.3.2 PEEM experiment system

A schematic of the PEEM experimental apparatus is shown in Figure 5.1(e). The photoemission experiments were conducted on a PEEM manufactured by FOCUS GmbH. The PEEM operates in an ultra-high vacuum (UHV) chamber with a base pressure of $\sim 1 \times 10^{-10}$

mbar. The principle of PEEM is described in great detail elsewhere[74,174,184], but a brief discussion is as follows. PEEM is based on the photoelectric effect, where electrons are excited by photons from the occupied electronic states below the Fermi level to the final states above the vacuum level. The photoemitted electrons are imaged via an electrostatic lens system, and amplified by double micro-channel plates (MCP). The electrons are converted to visible light by a phosphor screen, and eventually imaged by a CMOS camera.

A mercury arc lamp and an ultrafast laser system are used as the light source for photoemission experiments. The Hg lamp is an incoherent UV photon source with the highest accessible wavelength at 247 nm (5.02 eV) and can directly image MoS_2/PDI heterostructure via a one-photon process. A full spectrum of the lamp has been reported in our previous work[184]. Polarization-dependent (PD) and time-resolved (TR) experiments were conducted using a 4 MHz optical parametric chirped pulse amplifier (OPCPA) laser (Class 5 Photonics) that produces two fundamental outputs from 650-950 nm and 650-1300 nm, respectively, with pulse duration of 20-30 fs. One output was frequency-doubled to generate visible photons of 575 nm (2.16 eV), and the other output was frequency-tripled to generate UV photons of 300 nm (4.13 eV). Both photon energies were re-compressed using prism pairs, where the pulse duration of the 575 nm and 300 nm pulses are 27±1 and 27±1 fs, respectively. The full-width at half maximum (FWHM) of cross-correlation of the pump/probe pulses is 99±2 fs, measured on a commercial polycrystalline graphene/300 nm-SiO_2/Si sample (University Wafer) (Figure A.28).

The details of PD measurements have been reported by our group previously.[74,174] In short, 575 nm photons (2.14 eV, fluence 99.5 $\mu J/cm^2$) are linearly polarized and impinge on the sample surface at near-normal incidence ($\sim 4^\circ$) via a rhodium (Rh) mirror in the microscope column. Photoemission with 575 nm is a three-photon (3PPE) process from PDI/MoS_2 as verified by power series measurements (Figure A.27). The laser polarization of the beam is controlled by rotating a $\lambda/2$ waveplate (Thorlabs) via a motorized rotation stage (Newport).

In the TR-PEEM experiments, one 575 nm photon (fluence 99.5 μJ/cm^2) excites the heterostructure at a PDI molecular resonance, creating an excited state. A 300 nm probe (4.13 eV, fluence 3.0 μJ/cm^2) pulse, incident at 65°, photoemits the resulting excited states at a variable time delay after the pump pulse, probing the non-equilibrium electron distribution as a function of time. The probe wavelength was chosen to minimize the 1PPE background as the photon energy is insufficient for direct single photoemission. Both the pump pulse and probe pulse are incident with a polarization parallel with respect to the sample plane. Both beams were focused onto the sample via optical lenses placed just before the UV-grade quartz viewports on the vacuum chamber on the sample. The visible beam is approximately 40 μm in diameter. The UV beam is elliptical due to angled incidence and is around 65 μm by 40 μm in diameters (Figure A.32). Both beam profiles fully cover the FoV used in the work (15 or 20 μm).

The PEEM is also equipped with a high-pass energy filter that enables energy-filtered imaging and spectroscopy. Energy-filtered images of the same region of interest (ROI) are collected by incrementally cutting out photoelectrons with kinetic energies lower than an energy threshold. Thus, an energy distribution curve (EDC) of the photoelectron intensity of a certain ROI is computed by performing a numerical differentiation of the energy-resolved images. The calculation for difference spectra can be found in our previous work.[184] The energy resolution is ~50 meV, and the scans were collected using a 100 meV step size.

5.4 Results

5.4.1 Polarization-dependent PEEM imaging

Figure 5.1(e) shows a PEEM image of the PDI/MoS$_2$ heterostructure illuminated by the Hg lamp. Clear triangular domains can be resolved with higher photoemission intensities than the Si substrate (dark background), and the 1-2 μm domain size is consistent with the AFM and SEM images. The high-quality image shows that PEEM is a successful technique for visualizing molecule/TMD nanostructures. The spots with strikingly bright contrast at the edges of some triangular flakes are bulk MoS_2 crystals also observed in the SEM image. Overall, no variation in morphology within any of the heterostructural domains can be resolved by the unpolarized Hg lamp.

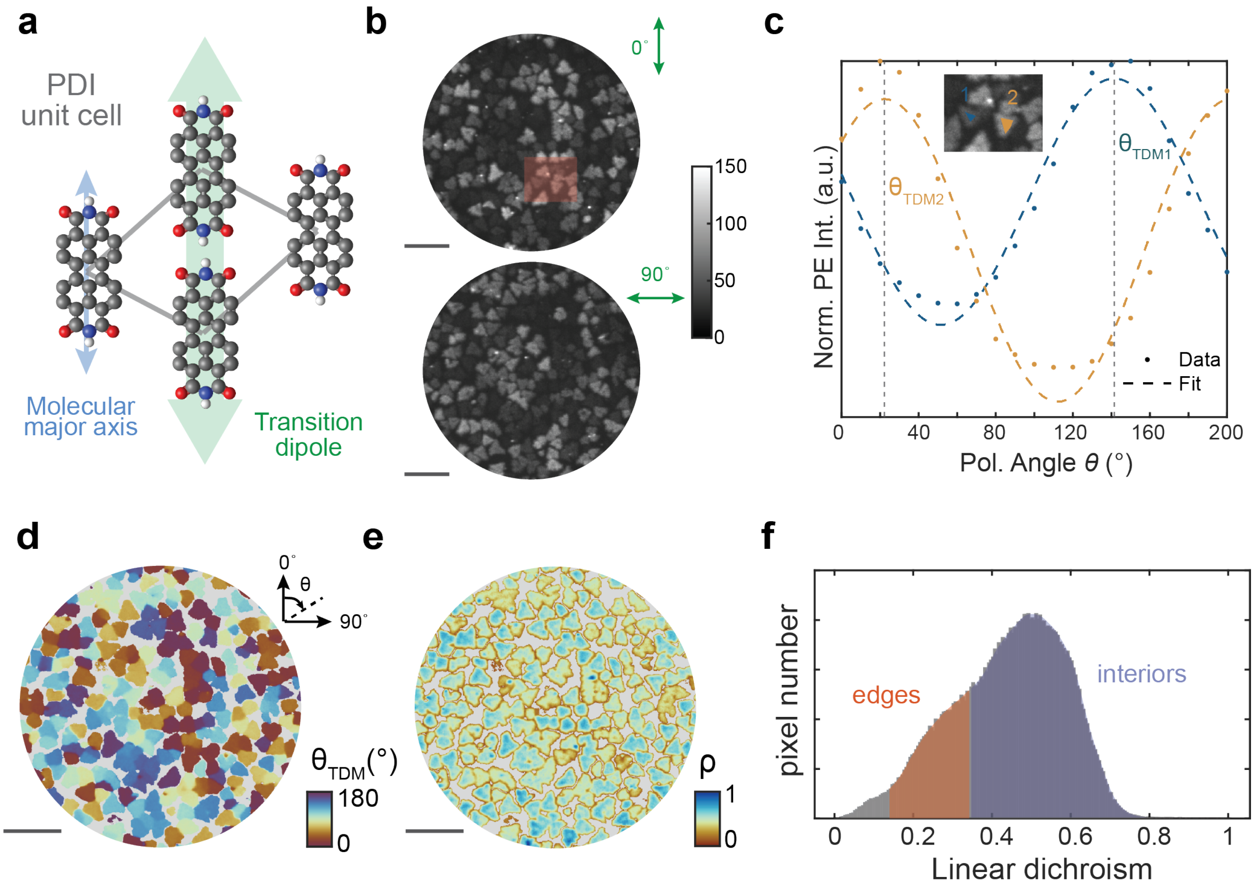

Figure 5.2: (a) Molecular structure of PDI, where the blue thin arrow indicates the major axis along the molecular backbone, and the unit cell, where the green thick arrow shows the transition dipole of a unit cell, in parallel with the major axis. (b) Heterostructure images taken at 575 nm laser polarization angles 0° and 90°, respectively. Scale bar is 3μm. (c) Polarization-dependent photoemission intensities integrated from two ROIs (inset, zooming in from the red box in (b)), and fitted to a $\cos^2$ function. The angles corresponding to the peak intensities show distinct molecular orientation θ_{TDM}. (d) θ_{TDM} map. (e) ρ map. Scale bars are 3 μm in both maps. (f) The histogram of the dichroism values, where the orange and blue shaded regions roughly represent the edges and interiors.

As shown schematically in Figure 5.2(a), the unit cell of the PDI on MoS_2 has a transition dipole moment (TDM) aligned along the major axis (backbone) of the PDI molecules verified by STM.[35] Therefore, a single crystalline PDI film exhibits an anisotropic dielectric tensor that selectively interacts with linearly polarized light, as verified with optical microscopy (see Figure A.31 for a polarized photoluminescence image). We performed PEEM imaging of the heterostructures using a polarized laser as the light source. Figure 5.2(b) shows two PEEM images on the same region of the PDI/MoS_2 heterostructures, illuminated with 575 nm light at two perpendicular polarization angles, $\theta = 0°$ and $\theta = 90°$, as indicated by the arrows in the graph. Compared to the Hg lamp image, the bilayers show substantial variation in photoemission intensities from flake to flake, and the intensity is uniform within each domain.

We performed PD-PEEM measurements using 575 nm photons to determine the orientations of PDI films on MoS_2. A series of PEEM images of the same ROI are acquired at each polarization angle from 0° to 200° with a step size of 10°. We extract the photoemission intensity of crystalline domains as a function of laser polarization angle by integrating the signal counts of selected areas in each frame (Figure 5.2(c)). After a correction for polarization-dependent reflectance of the Rh mirror[74], the modulated intensities can be described by a cosine-squared function in the form of

$$I(\theta) = A\, cos^2(\theta - \theta_{TDM}) + I_0 \tag{5.1}$$

where A is the amplitude of the modulation, θ_{TDM} is the phase shift, which corresponds to the polarization angle with the highest photoemission intensity, and I_0 is the baseline offset. The fit results are shown in Figure 5.2(c). Based on the anisotropic absorption of the PDI molecule, θ_{TDM} represents the transition dipole moment, therefore the molecular orientation of a single crystalline domain. In this case, θ_{TDM1} and θ_{TDM2} were determined from the the fit as 141 ± 2° and 22 ± 3°. The amplitude of the optical anisotropy, or linear dichroism, can be evaluated by

$$\rho = \frac{\mathrm{I_{max} - I_{min}}}{\mathrm{I_{max} + I_{min}}} = \frac{\mathrm{A}}{\mathrm{A + 2I_0}} \tag{5.2}$$

Thus, ρ ranges from 0 to 1.

We evaluated the spatial inhomogeneity of the molecular film by applying pixel-by-pixel fitting to the whole image stack and mapped out the molecular orientation and dichroism, as shown in Figure 5.2. Details for image processing are described in the Supplementary Materials. The color map is chosen such that 0° and 180° are identical, and the angle gets larger in the clockwise direction as illustrated graphically. With a spatial resolution as high as 41±10 nm using PEEM (Figure A.30), we can definitively determine the high uniformity of the molecular crystal within individual $\mathrm{MoS_2}$ domains. We found that for triangular grains that merge into a continuous domain, a well-studied phenomenon during the CVD growth of single-layer TMD crystals,[185,186] the PDI molecules align in the same direction.

In contrast, the dichroism of the PDI molecule shows strong spatial variations from the interior to the edge, as depicted in Figure 5.2(b). The flake interiors tend to have larger ρ (yellow and red) values, whereas there is a consistent reduction in dichroism at the edges of the triangles (green and blue). The histogram in Figure 5.2(b) plots ρ all pixel values. The smaller and larger dichroism values are enhanced by the shaded areas, where pixels of ρ values approximately less than 0.35 primarily reside at the edges, and a large portion of the pixels with ρ>0.35 are dominated by the interior areas (see Figure A.35 for partitioned ρ maps of different ranges).

5.4.2 Nanoscale excited state dynamics of the heterostructure To investigate the spatially dependent charge carrier dynamics of the heterostructure, we performed TR-PEEM measurements. The heterostructure was first pumped by a 575 nm pulse to the unoccupied intermediate states. The relaxation of the excited states was probed by the 300 nm UV beam as a function of delay time after photoexcitation. The heterostructure sample exhibits a rapid decay after photoexcitation within the first few picoseconds and is completely relaxed within 5 ps. The time evolution can be fit by a sum of a Gaussian function and a bi-exponential function convoluted with an instrumental response function, where the first Gaussian function describes the photo-enhancement of emission during pump-probe overlap. The physical processes associated with the two time constants will be analyzed in more detail in Section 5.5.

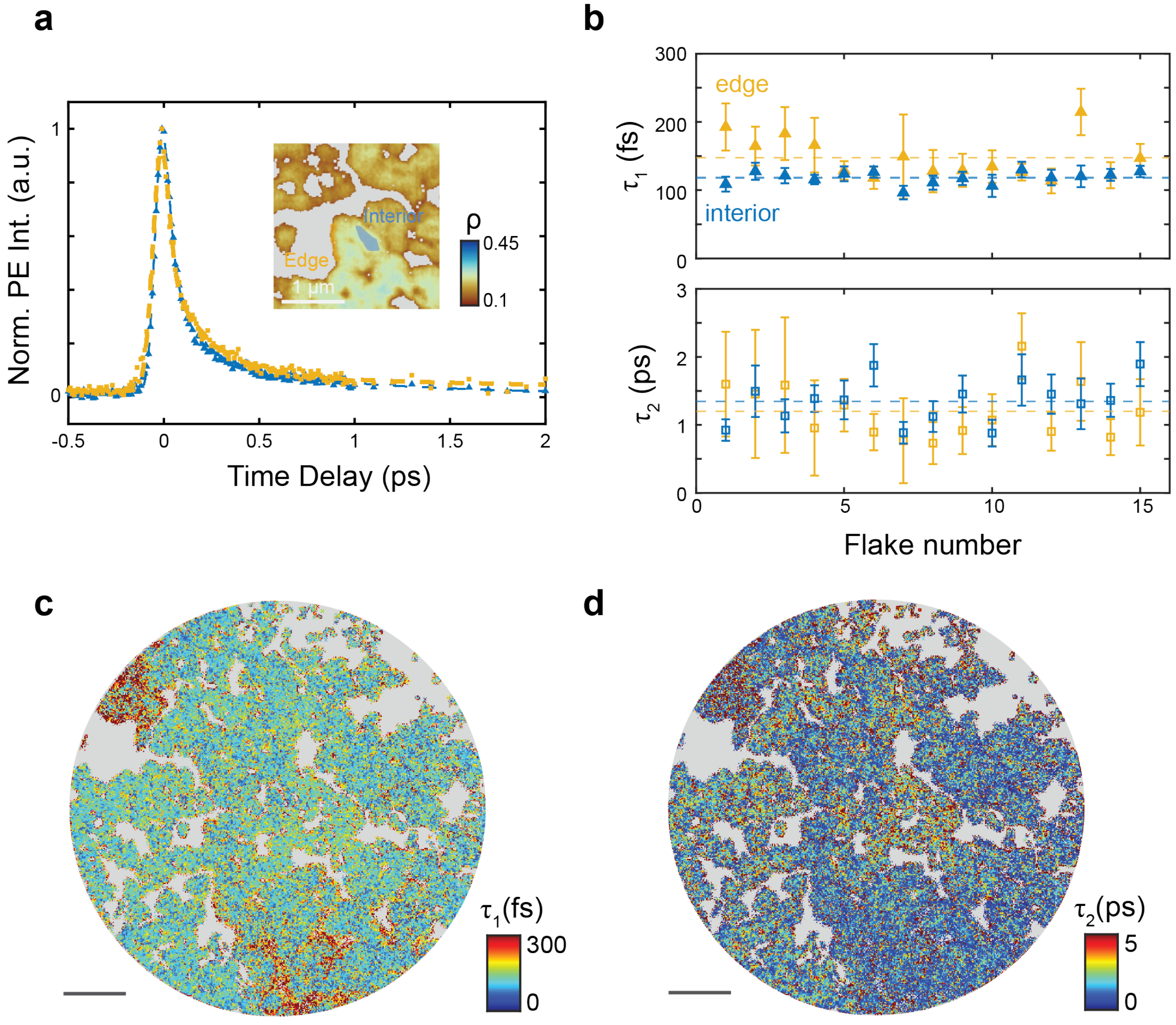

Figure 5.3: (a) Time-resolved photoemission intensities integrated from the interior and edge of the same flake. Inset is the dichroism map, showing the selection of interior vs. edge areas. (b) Statistical comparison of time constants derived from the interiors and edges. (c) τ_1 map. (d) τ_2 map. Scale bars are both 3 μm.

We mapped out the time constants pixel-by-pixel to inspect the flake-to-flake variations in the excited state dynamics. Due to the low S/N of a single pixel, 2×2 binning was applied to the raw images, and an R^2 threshold was applied to remove the poorly fitted pixels. The full details of image analysis can be found in A.5.4. Figure 5.3(c) and (d) show the resulting τ_1 and τ_2 maps, respectively. The shorter lifetime exhibits a relatively uniform distribution across the majority of the flakes, ranging from 100-200 fs, with a negligible difference from the edges to the interior. We observe heterostructures at the upper right and bottom left corners display a slightly longer lifetime. We attribute this to a reduced goodness of fit possible owing to lower photoemission intensities of this particular region, and thus the fitted results are less convincing (Figure A.33). On the other hand, τ_2 values have a larger range across the ROI. While the majority of the pixels have a fitted value of <5 ps, longer lifetimes were measured in the range of 10-30 ps as well. The slight spatial variations in the τ_2 map from flake to flake could be a result of sample variations during synthesis that modify the electronic structure and hence the ultrafast dynamics, such as differences in atomic defect densities in the MoS_2,[17,62] or strain profile modulation.[187,188]. Direct evidence of those morphological differences requires corroboration with techniques allowing atomic resolution, such as scanning tunneling microscopy (STM) or transmission electron microscopy (TEM).

To examine the edge difference in excited state dynamics, we compared the time evolution of the photoemission intensities originating from the interior and the edge of the same flake. The edge areas were selected based on the ρ map where the dichroism is noticeably decreased. To our surprise, there's no substantial difference in the dynamics between the two areas, as demonstrated by Figure 5.3. To verify the consistency of this observation, we additionally examined the fitted lifetimes of a series of flakes, and the result is plotted in Figure 5.3. It appears that τ_1 of the edge regions are overall slightly longer than the interiors, typically less than 100 fs. For the τ_2 process, the difference is minimal, and there is no obvious trend of whether the edges have a reliably longer or shorter process.

5.4.3 Time-resolved electronic structure

Next, we studied the time-and space-dependent spectra of the bilayers upon photoexcitation. A series of energy-filtered PEEM images of the same ROI were collected at various pump-probe time delays (-1, 0, 0.1, 0.2, 1, 50, 100 ps). We survey a series of bilayer domains and construct the EDCs of each triangle as a function of time delay. The time-dependent EDCs of a representative sample area are plotted in Figure 5.4(a). The EDCs can be well fit by the sum of a Heaviside step function plus an exponential convoluted with a Gaussian function, and a second independent Gaussian function:

$$\mathrm{I_{PE}(E)} \propto \mathrm{A_1}\, \mathrm{e}^{-(\mathrm{E}-\mathrm{E_1})/\sigma_1^2} * \mathrm{e}^{-(\mathrm{E}-\mathrm{E_1})/\mathrm{b}} + \mathrm{A_2}\, \mathrm{e}^{-(\mathrm{E}-\mathrm{E_2})/\sigma_2^2} \tag{5.3}$$

$\mathrm{E_1}$ and $\mathrm{E_2}$ describes the peak positions of the secondary electron and the extra peak, $\mathrm{A_1}$ and $\mathrm{A_2}$ are the amplitudes of each peak. σ_1 and σ_2 is the widths of the peaks. The two Gaussian components are separately presented by the dashed line in Figure 5.4(a) and the overall fit is shown by the solid lines. The energy cutoff, i.e. the half of the maximum magnitude of the secondary edge, can be used to determine the relative work function of the material surface to the instrument,[189] as indicated by the black dotted lines.

Compared to negative time delays, there's a noticeable increase in energy of the secondary edge, corresponding to an increase in the work function of the heterostructure, immediately after pump excitation of approximately 100 meV. An additional peak emerges at time zero at around 4.4 eV, suggesting the emergence of a previously unoccupied electronic state. At later time delays, the work function gradually decreases. After about 1 ps, the secondary edge recovers to about its original position before time zero, implying the work function of the surface is mostly recovered. By 100 ps, the work function recovers to its equilibrium position within the instrumental resolution. We plot the relative work function values versus the time delay in Figure 5.3(b) which clearly illustrates the rise-and-dip trend of the work function over time. To confirm that the secondary edge shifting is unique to the heterostructures, we

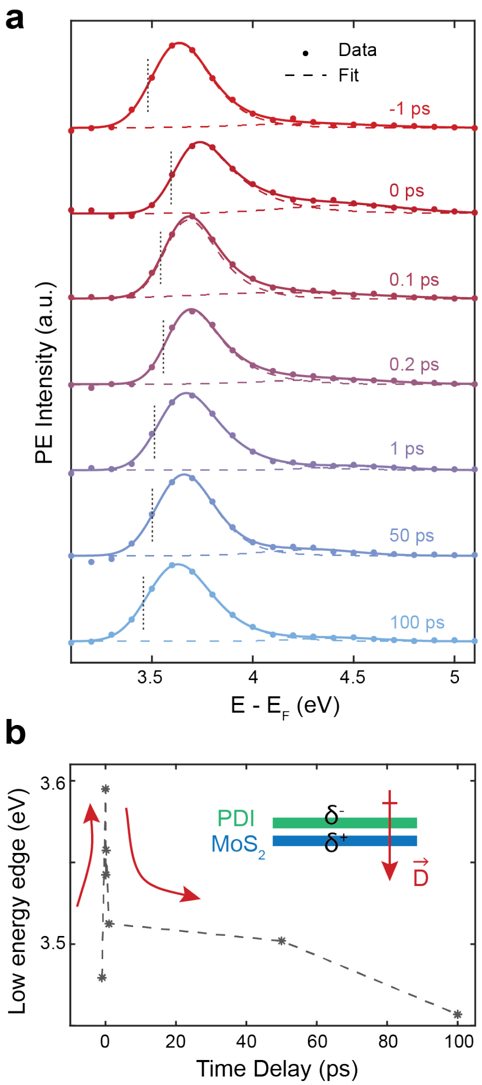

Figure 5.4: (a) Time-dependent energy distribution curves (EDC) and the corresponding fitting. The dots show the raw data. The solid lines are the overall fit functional whereas the dashed lines represent the two Gaussian components. The vertical dotted lines indicate the relative work function at each time delay. (b) Relative work function vs. time delay. The inset shows the schematic of the induced transition dipole at the interface of the bilayer due to partial charge density.

further examined the time-dependent spectra of the bare Si substrate and found that the spectra overlapped at each pump-probe time delay (Figure A.39).

5.5 Discussion

Combining the mapping of crystal orientation, optical dichroism, and ultrafast dynamics with nanoscale spatial resolution, we can provide a comprehensive understanding of the role of the molecular layer in the modification of the physical properties of ML $\mathrm{MoS_2}$. The molecular crystal orientation mapping (θ_{TDM} map) confirms the single crystalline nature of the PDI film inside $\mathrm{MoS_2}$ domains. By plotting the histogram of the crystal angles, we found that the crystal directions are relatively randomly distributed (Figure A.34), suggesting the initiation and growth of the molecular film is not epitaxial to the buried TMD crystals.

The dichroism distinction at edges compared to the interiors could be due to either (1) reduction in PDI coverage or density at the edges of $\mathrm{MoS_2}$, or (2) reduced local crystallinity of the PDI layer at the edges of $\mathrm{MoS_2}$. For quantitative analysis, Equation 5.2 can be rewritten as $\rho = \frac{\mathrm{I_{max}/I_{min}}-1}{\mathrm{I_{max}/I_{min}}+1} = 1 - \frac{2}{\mathrm{I_{max}/I_{min}}+1}$. A reduction in dichroism means that the ratio of $\mathrm{I_{max}/I_{min}}$ is decreased. We can approximate that the photoemission intensity in a given region is proportional to the total number of molecules from Beer's law. Molecular adsorption on $\mathrm{MoS_2}$ results in a significant increase in photoemission compared to bare $\mathrm{MoS_2}$. We do not observe PE intensity reduction at the edges in the original PEEM images (Figure 5.1(e) and Figure 5.2(b)). Furthermore, any change in molecular density would modify $\mathrm{I_{max}}$ and $\mathrm{I_{min}}$ in the same way, keeping the ratio, and thus the dichroism, the same. This makes mechanism (1) unlikely to be the cause of the dichroism reduction we observe experimentally. However, it is well known that TMDs tend to form dangling bonds at grain boundaries, resulting in higher defect densities at the edges during chemical deposition.[190] A reduction in $\mathrm{MoS_2}$ crystallinity will disrupt the physical adsorption of PDI, making mechanism (2), reduced crystallinity at the edges, the primary reason for the reduced dichroism at flake edges.

Now we discuss the likely mechanisms of the observed ultrafast dynamics. The measured time constants are all below the 10s of ps timescales that would be comparable to typical organic semiconductors.[159,191] In contrast, the 100s of femtosecond and few ps lifetimes of the excited states are notably similar to the reported photophysics of MoS_2 and other TMD systems.[62,63,163,192] This suggests that the molecular layer is fairly innocent in altering the carrier dynamics that are inherent to monolayer MoS_2, and the dynamics of the heterostructure are dominated by MoS_2. We note here that, the probe photon energy should not be able to access photoelectrons photoemitted from the K point of monolayer MoS_2 the location of the valence band maximum (VBM) and conduction band minimum (CVB).[193] Therefore, we assign the initial 100-200 fs process to hot electron cooling process via intervalley scattering in MoS_2,[194,195] and the <5 ps process is electron decay via a defect trapping path,[62,196] similar to what has been observed in other experiments on MoS_2 as well as other TMD systems. It is important to highlight that there appears to be little statistical significance of the edge regions in the ultrafast dynamics of the heterostructure, unlike the polarization-dependent measurements. This implies that the crystallinity of PDI plays a minor role in determining the dynamics of the heterostructure, and suggesting that the dynamics of the heterostructure are tolerant of molecular disorder.

The rapid increase in the work function within the cross-correlation of the pump and probe pulses seen in energy-resolved PEEM suggests an extremely rapid modification in the chemistry or charge distribution at the heterostructure surface, and there are several mechanisms that could be operative.[197] Previous studies on molecule/TMD systems have revealed interfacial charge transfer processes. However, these charge transfer excitons are typically formed on the timescales of a few to tens of picoseconds in molecular/TMD heterostructures and primarily occur with type II band alignment, making this mechanism unlikely.[161–163,166,167,198,199] Theory predicts instead that the PDI/MoS_2 heterostructure adopts type I alignment, with an energy difference of less than 100 meV between the LUMO of PDI and the CBM of MoS_2, making the formation of charge transfer excitons unlikely but possibly promoting the hybridization of the PDI LUMO with the MoS_2 CB.

Transient surface photovoltage (SPV) is another common reason for work function shifts as a function of pump-probe time delay.[200–202] SPV occurs at the surfaces of semiconductors when photogenerated electrons and holes are spatially separated due to interfacial band bending, resulting in a transient electrostatic field in the photoactive layer that shifts the surface potential. However, SPV usually results in a rigid shift of the entire electronic structure,[203] and the additional peak in the data that appears at time zero does not shift with the work function, making it unlikely that SPV is the cause of the work function shift here. We also see no work function shift in bare Si areas that were illuminated under the same photon condition (Figure A.39), indicating that the work function shift is unique to the heterostructures.

Lastly, the work function shift could be due to direct excitation into an excited electronic state that has an interfacial dipole with the negative end pointing toward the vacuum. Recent theoretical modeling has shown that because of the small energy difference between the PDI LUMO and the MoS_2 CVB, a hybrid electronic state between PDI molecules and MoS_2 could be formed. Such a hybridization picture of 2D heterostructures has also been proposed in other works.[165,204–206] The excitation into such a state would lead to a partial separation of charge density at the interface with a partial negative charge in the molecular layer and a partial positive charge in the MoS_2 layer shown schematically in the inset of Figure 5.4(b). Such a surface dipole has been shown to result in an increase in the work function of a material.[197] At later time delays, the strength of the surface dipole relaxes as the excited state population decays. PD-PEEM imaging at 670 nm, resonant with the MoS_2 A exciton, still shows strong polarization dependence which would be unexpected in MoS_2 alone (Figure A.38), that suggests that resonances characteristic of MoS_2 still have some properties of the molecular species, and supporting such a hybrid excited state.

5.6 Conclusion

In summary, we use PD-, TR-, and energy-resolved PEEM to extensively explore the spatially-dependent crystal orientation, linear dichroism, and ultrafast carrier dynamics of a PDI/MoS_2 bilayer system. PD-PEEM identifies the directions of molecular alignment within each single crystalline domain and uncovers a consistent reduction in dichroism, thus lower crystallinity, at crystal edges. Through the direct measurements of the electronic structure of the bilayer, we find that MoS_2 primarily determines the carrier dynamics of the heterostructure via the formation of a hybrid state at the interface, whereas the molecular layer plays a less important role. We reveal that the hot electron cooling process via intervalley scattering in the MoS_2 occurs on the timescale of 100-200 fs, and the electron decay process occurs over a few picoseconds. This work suggests that in a non-charge transfer 2D heterostructure, in-plane material morphology has a negligible impact on the overall photophysical properties of the hybrid system, promoting large-scale and disorder-tolerant production of optoelectronics applications based on organic/inorganic 2D semiconductors.

CHAPTER 6

PHOTOEMISSION ELECTRON MICROSCOPY FOR BIOLOGICAL MATERIALS AND THE CONTRAST MECHANISM

6.1 Overview

This chapter introduces an intriguing opportunity for applying PEEM to biology. In particular, PEEM shows an exciting future for volume imaging of neurological tissues in whole mouse brains that overcomes the limited acquisition speed in current electron microscopy development. We first show preliminary results that demonstrate PEEM is a suitable tool for nanoscale neurological imaging. Then, we discuss the contrast mechanism of osmium-stained biological materials that allows the generation of high-resolution, high-contrast PEEM images. Lastly, we discuss concerns over contrast degradation that has been encountered during bio-PEEM imaging, and possible mitigation strategies for improvements in the future.

6.2 Synaptic resolution PEEM mapping for connectomics

6.2.1 Abstract

Detailing the physical basis of neural circuits with large-volume serial electron microscopy (EM), "connectomics", has emerged as an invaluable tool in the neuroscience armamentarium. However, imaging synaptic resolution connectomes is currently limited to either transmission electron microscopy (TEM) or scanning electron microscopy (SEM). Here, we describe a third way, using photoemission electron microscopy (PEEM) which illuminates ultra-thin brain slices collected on solid substrates with UV light and images the photoelectron emission pattern with a wide-field electron microscope. PEEM works with existing sample preparations for EM and routinely provides sufficient resolution and contrast to reveal myelinated axons, somata, dendrites, and sub-cellular organelles. Under optimized

conditions, PEEM provides synaptic resolution; and simulation and experiments show that PEEM can be transformatively fast, at Gigahertz pixel rates. We conclude that PEEM imaging leverages attractive aspects of SEM and TEM, namely reliable sample collection on robust substrates combined with fast wide-field imaging, and could enable faster data acquisition for next-generation circuit mapping. [a]

6.2.2 Introduction

A confluence of advances in 3D EM imaging, sample preparation, and algorithms has enabled the exhaustive mapping of how neurons connect in large volumes of brain – connectomics. Connectomics has emerged as an invaluable tool in the neuroscience toolbox and the analysis of wiring patterns in cortex, hippocampus, retina, songbird sensory motor cortex, zebrafish larvae, and entire fly brains have helped discover principles of brain functions that could not have been revealed in any other way.[41,207–213] These datasets are also inherently valuable as public repositories for future investigations by the broader neuroscience community.[214,215] Thus, there is only increased demand for even larger 3D EM datasets. The next leap in connectomics will be reconstructing full neural circuits in mammalian brains. But to make that leap, large-volume connectomes need to be cheaper and faster. A 50-100 fold drop in the price of a "connectomic voxel" could revolutionize connectomics, similar to the way a 50-100 fold reduction in the cost of DNA sequencing[216] placed large-scale DNA analysis at the core of modern biology. However, all EM connectomic reconstructions use either transmission electron microscopy (TEM) or scanning electron microscopy (SEM),[40] which have limitations in the reliable automated serial pickup of ultrathin brain slices (UTBS), or acquisition costs, respectively.

In this work, we investigated whether photoemission electron microscopy (PEEM) would be a third option. Photoemission electron microscopes are commercially available, and are

---

[a] Adapted with permission from Boergens, K.M., Wildenberg, G., **Li, R.**, Lambert, L., Moradi, A., Stam, G., Tromp, R., van der Molen, S.J., King, S.B. and Kasthuri, N. Photoemission electron microscopy for connectomics. *BioRxiv* (2023).

routinely used in chemistry and surface physics[174,217–220] and have been used since the 1970s for biological imaging,[48,221,222] and even to image neurons in culture.[223] PEEM uses wide-field illumination (such as UV light) to emit photoelectrons from materials and captures variations in the resulting photoemission pattern with standard electron optics.[224] Photoemitted electrons are accelerated and projected with electrostatic and electromagnetic lenses onto an electron detector. Commercial PEEMs can have resolution capabilities of less than 15 nm, which is suitable for synaptic connectomics.[225] There are also cameras available that capture PEEM data at multi-GHz pixel rates, making a fast PEEM for connectomics plausible. Here, we report the first study of PEEM imaging of ultrathin brain slices prepared using standard connectomics sample preparation methods.[226]

6.2.3 Methods

Sample Preparation

Mouse brain sections are prepared for PEEM imaging following the same protocol used for standard SEM preparation using multiple rounds of osmium tetroxide staining.[226] In brief, the mouse was perfused transcardially to preserve the ultrastructure. The mouse brain is surgically removed, post-fixed, and a vibratome-sectioned brain slice ($200 \times 300\,\mu\text{m}^2$) is stained with successive rounds of osmium tetroxide, potassium ferrocyanide, uranyl acetate, and lead nitrate, before ethanol dehydration and embedding with EPON resin. The resin-encapsulated brain is then sliced using an ultramicrotome to 40-80 nm-thick UTBS. The majority of the sections in this work are picked up on a Si substrate (with native oxide) coated with 50 nm of gold and glow-discharged unless otherwise stated.

Photoemission electron microscopy

The UTBS on the substrate is illuminated using a broadband mercury arc lamp with a short-pass filter allowing photons with energies greater than 4.43 eV (280 nm) to focus on the sample. The resulting photoelectrons are imaged with a photoemission electron microscope manufactured by FOCUS GmbH (Figure 6.4), ELMITEC GmbH (Figure 6.1) and Figure

6.2) and SPECS GmbH (Figure 6.5 and Figure 6.3). The typical exposure time for one image is hundreds of seconds. High-resolution images are obtained by integrating the same region of interest (ROI) to improve signal-to-noise. To estimate how many photons would be required to elicit an electron, we used a pulsed laser with a wavelength of 244 nm and known flux, and acquired a PEEM image of a 60 nm brain slice deposited on gold. We estimate the amount of electrons collected by measuring the SNR ratio and calculating from that shot noise measurement back to the number of electrons collected. The images in this work are shown with inverted grayscale (dark is bright in the original PEEM images) to keep a consistent display with typical SEM imaging.

Image processing

2D image montaging is performed in FIJI (ImageJ) using the Grid/Collection stitching plugin. PEEM image stacks are 3D-aligned using AlignTK (https://mmbios.pitt.edu/aligntk-home). To achieve the necessary contrast of UTBS in PEEM, multiple images of the same ROI are captured which introduced drift to the set of images, presumably from instabilities in the stage. Therefore, two people (G.W. and K.M.B.) independently visually inspected the series of images to estimate the pixel drift which was corrected by shifting the images by the estimated pixel drift. Lastly, a maximum intensity projection is generated from the drift-corrected series to produce the final PEEM images. Manual 3D annotation was done using VAST.[227]

Space charging simulations

Electrons are simulated to be emitted from a 40×40 μm^2 substrate with a spatial distribution according to an existing low-noise EM image (10 nm pixel size) from a UTBS of neuropil. They are given an isotropic energy distribution with a standard deviation of 2 eV. Through simulation, we determine that suppression of emission due to space charging had a negligible effect even at the highest sample current densities investigated. After emission, the electrons are subjected to a homogeneous electric field of 15 kV/mm. In each 10 fs time step of the simulation, the Coulomb interaction of each pair of in-flight electrons is calculated and applied to the electrons. Once an electron has a distance greater than 1 mm from the sample, it is removed from the simulation. For each job, this process is repeated until 5000 electrons have been removed that were not affected by simulation ramp-up effects. Then, using their final position and angle, each electron is back-projected to the virtual image plane, located 1 mm behind the sample,[228] and the electron location in this virtual image plane is compared to the actual emission location. Throughput is calculated using the Rose contrast criterion.[229] All in all 400,000 jobs were executed.

6.2.4 Results

PEEM compatible specimen processing

In order to achieve consistent imaging while avoiding sample charging, we first explored the sample preparation method to ensure the typically soft, nonconductive MB sample compatible with PEEM. The 40-60 nm brain sections that had been prepared for EM-based connectomics[226] were first picked up on a square-centimeter-sized silicon chip that was coated with a 50 nm layer of metal (gold or platinum), shown in Figure 6.1(a). The chip was typically treated with glow discharge to increase hydrophilicity and adhesiveness of brain sections. A representative image is shown in 6.1(c). We are able to identify biological features readily observed in standard connectomic datasets including cellular features (e.g., somata, blood vessels, dendrites, and myelinated axons) and sub-cellular features (e.g., mitochondria, endoplasmic reticulum, nuclear membrane, and nucleolus). We repeated tens of UTBS samples prepared following the same protocol and over 90% of the time, high-quality images could be obtained successfully, demonstrating the consistency and robustness of this method. The exceptions mostly arise from a puzzling sample degradation issue, which will be discussed further in Section 6.4.

The drawback of this method, however, lies in the challenge of systematically collecting several or more sections in a sequential order, and preferably in controlled orientations. This

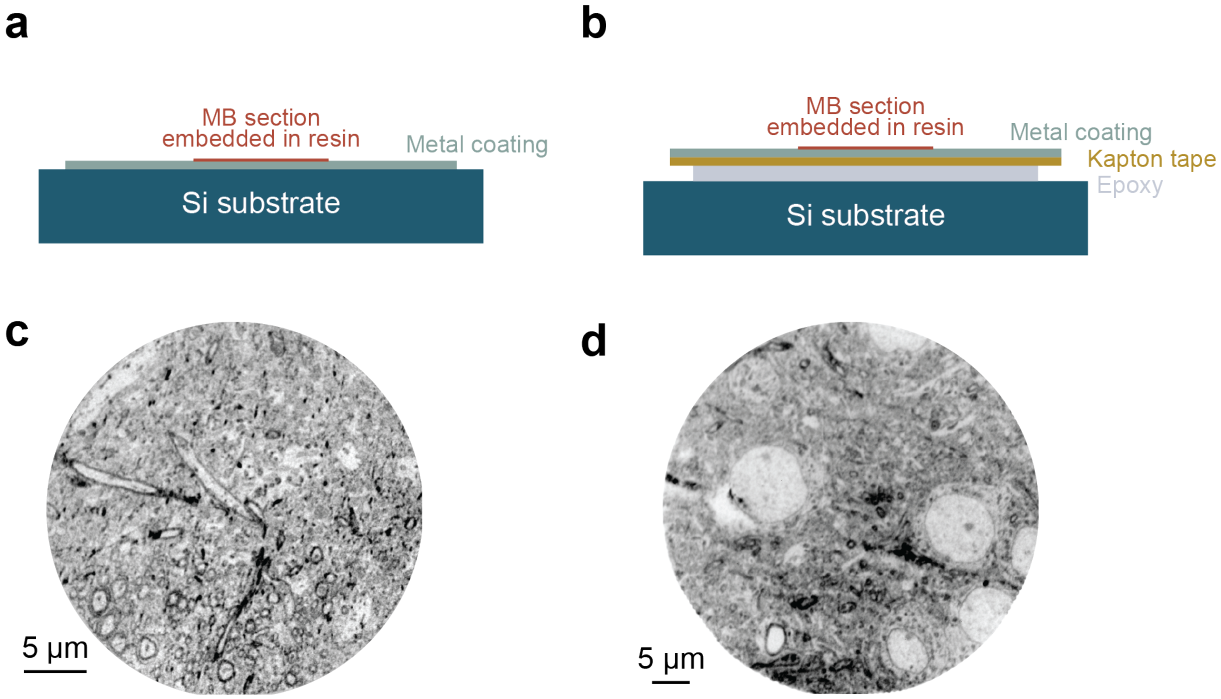

Figure 6.1: Sample configurations of MB samples for PEEM imaging. (a) MB sections are picked up by a metal-coated Si substrate. (b) MB sections are picked up on metal-coated Kapton tape, and adhered to Si substrate using epoxy. (c)(d) Resulting PEEM images corresponding to (a) and (b). The metal coatings are Pt in both cases.

is of vital importance, as the reconstruction of a 3D image stack involves acquiring hundreds or even thousands of images in order to establish a precise correlation of an image stack.[41] Not only does the manual pick-up method limit the number of sections that can be imaged at one time, but also the process of exchanging a large volume of chips is laborious and time-inefficient.

Inspired by the automated tape-collecting ultramicrotome (ATUM) method that has been successfully applied in the SEM connectomics community,[41] we pick up a series of UTBS samples on a metal-coated Kapton tape. The as-picked-up sections are cut into pieces with the approximate dimension as the substrate, and epoxy is used to stick the tapes (with MB sections on them) on a clean Si chip. The flatness of the epoxy layer is achieved by applying an even force on the surface while the epoxy is still fluidic, and 24-48 hours of curing at 60°C is followed to solidify the sample assembly. A schematic of the eventual sample configuration is shown in Figure 6.1(b). This type of sample has been imaged with PEEM, and Figure 6.1(d) is a representative image where the MB section was picked up on a Pt-coated tape. Similar ultrastructures can be observed, and no significant sample charging or arcing was observed during the imaging process. However, we do notice that the overall image resolution and contrast are slightly reduced compared to the first sample configuration, and variations from sample to sample indicate that this approach needs further improvement. One possible reason could be the sample flatness since it has been untested with any characterization metrics to this date. Nevertheless, the tape method provides great potential for automating sample preparation in the long-term development of connectomics with PEEM.

Efforts on synaptic resolution

It is crucial to prove that PEEM is capable of providing resolution on the synaptic level to fully describe the neuronal network structure. Below 10 nm spatial resolution is typically required to evidently resolve a synapse in a mouse brain, which is close to the achievable PEEM resolution that has been reported in the literature.[49] Efforts have been made by utilizing PEEM instruments configured with different electron lens designs that aim to overcome the resolution limit. The ELMITEC PEEM in the King lab has a magnetic lens system that in theory has an overall higher resolution than the FOCUS PEEM which uses only electrostatic lenses, and has reached 7-8 nm resolution in the past.

Unusually thick mouse brain sections of hundreds of nanometers are used for the resolution tests, as thicker biological samples allows higher photoemission yields according to the universal curve (Figure 1.4). Stronger PE intensities further enable optimization at a relatively small FoV, which is essential for attaining the best possible resolution. Figure 6.2(a) is an optical image for an MB section of ∼400 nm thick sitting on a gold-coated Si chip, where the cellular structure can already observed with a clear contrast. The PEEM image of the section is shown in Figure 6.2(b), and as expected, the stronger photoemission response is immediately observed. Upon further inspection, the area indicated by the red box shows

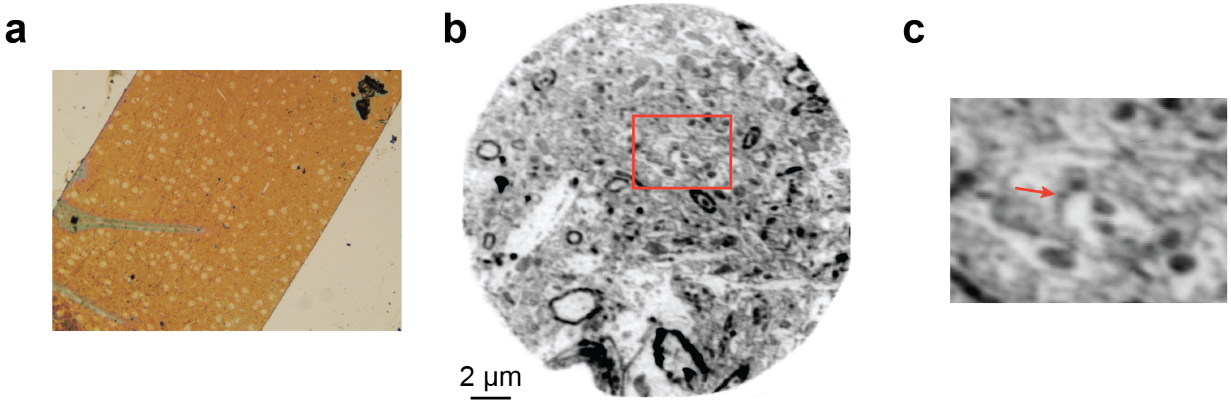

Figure 6.2: PEEM imaging of 400 nm-thick MB section. (a) Optical image of the thick section. (b) A representative PEEM image of the thick section. (c) An area from (b) that could likely be a synapse.

evidence of a neuronal synapse, as indicated by the arrow in the zoom-in view is magnified in Figure 6.2(c). Although the features are still not unsatisfyingly convincing at this level of resolution, we can argue that pre-synaptic vesicle clouds can be roughly distinguished by the thickened cell membrane.

We further sought a third PEEM instrument manufactured by SPECS that intentionally handles the aberrations by design (aberration correction). Finally, a high-resolution resolution PEEM image by Hg lamp is acquired at 20 μm FoV, averaging over 20 images (Figure 6.3(a)). Synapses can be clearly identified with individual, putative ∼40 nm diameter, synaptic vesicles, as demonstrated by the magnified images in Figure 6.3(b) and (c). This result reveals the groundbreaking evidence that PEEMs can deliver sufficient resolution for full connectomic circuit reconstruction.

Serial imaging for 2D and 3D tracking

PEEM imaging is also relatively free of distortions with well-stabilized environmental control, and we demonstrated this point by performing (1) 2D montaging of tiled images, and (2) 3D stacking of a continuous series of images. The first point was realized by collecting nine PEEM images in adjacent ROIs at a relatively large FoV (50 μm) with minimum adjustment on the lens parameters except for the lateral position of the sample. Figure

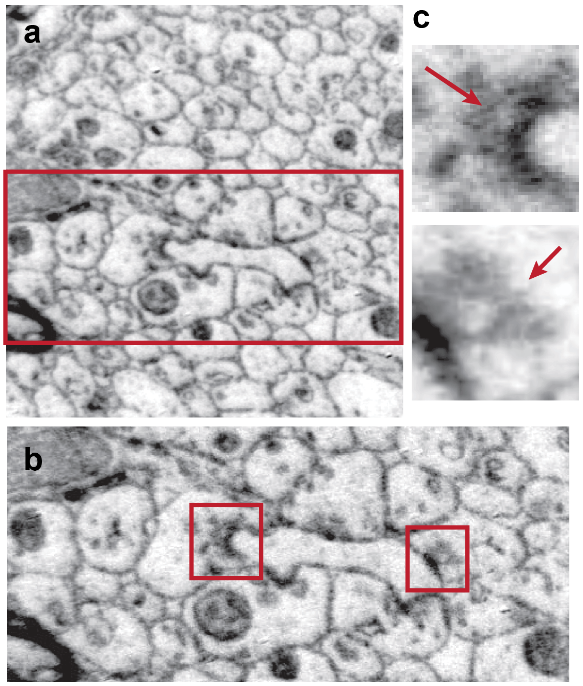

Figure 6.3: PEEM can achieve synaptic resolution. (a) High-resolution PEEM image of a UTBS. (b) Zoom in from A (red rectangle) showing multiple synapses (red squares) as evidenced by the presence of post-synaptic densities (PSD) and pre-synaptic vesicle clouds. (c) Zoom in from b (red squares) of two synapses with individual pre-synaptic vesicles visible (red arrowheads).

6.4(a) shows the overview of a 2D montage of the stitched images. The boundaries of the individual images are relatively closely connected with negligible position offset, and different neurological features such as somata, blood vessels, dendrites, and myelinated axons can be clearly distinguished at this magnification. The zoom-in views of the neurological components are further displayed in Figure 6.4(b)-(e). This visually astonishing picture shows PEEM's ability to easily reconstruct a relatively large in-plane image of the sample surface while preserving sufficient resolution. A global view with fast acquisition allows for the rapid identification of an ROI, and is particularly beneficial for the inspection of synapses across a UTBS.

We address the second point by tiling multiple overlapping PEEM fields of view (FOV). Six samples consisting of a series of sequentially cut MB sections are imaged and aligned in

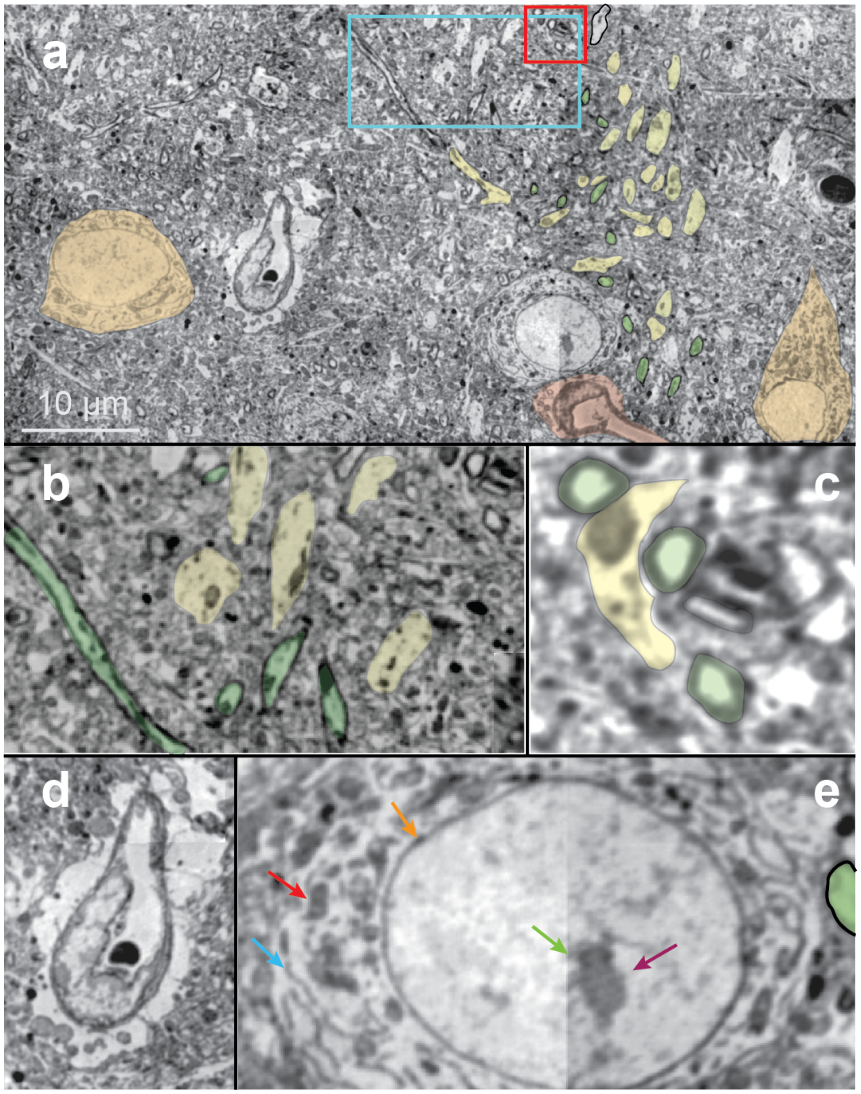

Figure 6.4: 2D PEEM montage of adjacent ROIs. (a) a 60 nm UTBS was imaged over 9 overlapping fields of view (FOV) spanning $72 \times 37\,\mu\text{m}^2$ and algorithmically stitched together, showing different neurological features commonly found in EM datasets including somata (orange), blood vessels (red), dendrites (yellow), and individual myelinated axons (green). (b) Zoom in from (a) (light blue box) showing a close-up of individual dendrites (yellow) and myelinated axons (green). (c) Zoom in from (b) (red box) showing further detail of individual dendrites (yellow) and myelinated axons (green). (d) Representative example of a blood vessel with the processes of an astrocyte making a putative neurovascular unit. (e) Representative example of a neuronal soma with mitochondria (red arrowhead), endoplasmic reticulum (light blue arrowhead), nucleolus (purple arrowhead), and nuclear membrane (orange arrowhead). The green arrowhead shows a stitch line between two FOVs.

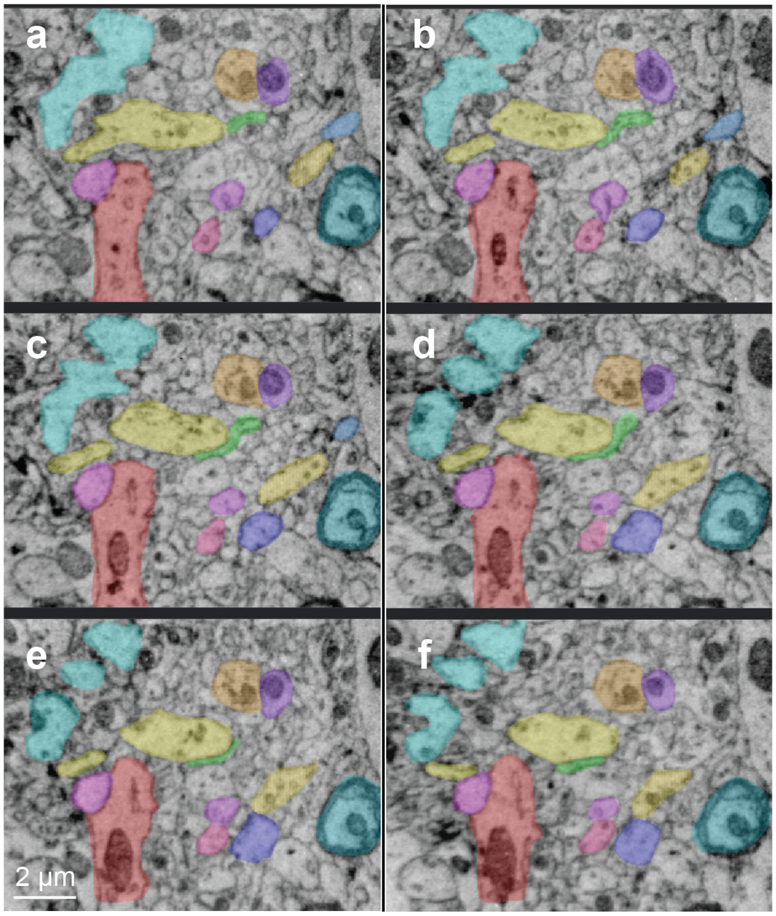

Figure 6.5: 3D stack of PEEM images that allows tracing neurites in a serial stack of UTBS imaged. (a)-(f) are images of a serial stack of UTBS, 40 nm thick, imaged with medium-resolution PEEM. Multiple neurological features can be manually traced through the stack including dendrites of varying size, myelinated axons, and glia across 6 sections.

a stack. Neurological features including myelinated axons, dendrites, and glia are identified, as individually color-masked in Figure 6.5. We are able to trace the evolution of each type of cellular component based on the varying size and shape, and obtain a basic interpretation of the directionality of the neuronal network progression. The preliminary result of 3D PEEM image stacking implies the great prospects of PEEM for 3D volume electron microscopy (vEM) and opens the opportunities to use PEEM to reconstruct fast projectomes.[230]

6.2.5 Discussion

Here we have described the first successful imaging of UTBS using PEEM at synaptic resolution and serial image acquisition at projectomic resolution. Furthermore, we'd like to discuss the plausibility of achieving fast acquisition for large-volume connectomics and projectomic of a whole mouse brain with PEEM.

We explore whether PEEM imaging could be fast, potentially at Gigahertz acquisition rates. For the results shown in this study, mercury arc lamps were used to illuminate the sample but the low photon flux necessitates long integration times (i.e., minutes) which is too slow to image large volumes with PEEM. An obvious upgrade would be to illuminate instead with continuous wave (CW) UV lasers which produce a photon flux over 10,000 times higher than arc lamps. Thus, we investigate the compatibility of UTBS with laser-based illumination.

We conservatively estimate that at most 3 million photons are needed to elicit an electron (see Section 6.2.3 for the simulation details). We then measure the emissivity ratio between the sample regions with the lightest and heaviest osmium-stained structures, i.e. the cytoplasm versus mitochondria in Figure 6.4, and find a ratio of 2.7±0.2. A 0.5 W 244 nm laser produces a flux of 6.1×10^{17} photons per second and using the Rose contrast criterion,[229] and thus we conclude that such a laser would provide enough signal to support connectomic resolution imaging at a pixel rate of over 2 GHz. Notably, such lasers are commercially available.

An adult mouse brain, conservatively estimated to be 1 cm^3, imaged at 15 nm isotropic resolution, as tentatively demonstrated above, would result in a dataset of 2.96×10^{17} voxels. A single PEEM with a CW UV laser, imaging non-stop at 2 Gigahertz pixel rate, would take approximately five years to finish that acquisition. UTBS can be easily distributed across multiple PEEMs, decreasing the time to map a mouse brain proportionately to the number of PEEMs used. A 2 GHz PEEM is feasible given the analyses above and would be faster than current approaches using TEMs or SEMs with a potentially significant price reduction.

In addition, another application of PEEMs would be to map, at a lower resolution, projectomes of entire mouse brains, with imaging times of a few months. We found imaging at 40 nm projectomic resolution to work reliably; and such mapping makes good use of the large field of view of PEEM setups, which can be up to 800 μm^2. Finally, we found preliminary evidence that SOA machine learning algorithms for identifying objects in scenes could be easily trained to identify cell boundaries in PEEM datasets (Segment Anything from Meta[231], Supplementary Figure 3). While not surprising, given the similarity of PEEM brain images to SEM and TEM, such preliminary data suggests that a PEEM mouse projectome can be both quickly acquired and reconstructed in the near future.

The ultimate PEEM for connectomics, or more broadly, volume electron microscopy applications, that can surpass SEM and TEM demands considerate improvements in sample preparation, instrumental engineering as well as algorithm development for image analysis. Ideally, the 3D reconstruction of nanometer biological structures is not limited to mouse brain tissues. The potential of applying PEEM to wider biological substances including cells, other tissues, and small organisms will be explored. Experimentally, high-throughput ultrastructural imaging relies on reproducible sample collection for large-volume thin sections. As one of the resolutions, further optimization of the automatic tape-collecting ultramicrotomy method that is compatible with PEEM imaging is required to achieve a spatial resolution comparable to SEM. In addition, mechanical modifications to the PEEM sample cartridge are desired to accommodate large-area substrates (i.e., a 4" silicon wafer), where serial sections acquired on the tape can be mounted and imaged to substantially reduce the transfer time into the vacuum. Furthermore, preprogrammed software packages are necessary to minimize imaging time, which allows automated tracking and focusing of regions of interest with drift correction and orientation matching. This development requires significant joint efforts from industrial factories and academic research laboratories to promote PEEM to be commercially competitive with other well-established EM techniques. Finally, the construction of serial individual images into an image volume requires rigorous data processing. This step typically involves alignment of the same region of interest from adjacent images for a single volume, and stitching multiple volumes to recover the original size of the sample.[232] We have shown the successful implementation of image registration and local feature segmentation for a small volume of PEEM image stack, where the approaches are similar to SEM image analysis. Thus, we expect the optimization of the analysis techniques to be carried out concurrently with the ongoing research for SEM. Overall, PEEM holds great promise to exceed the state-of-the-art techniques despite the foreseeable non-trivial investment to overcome the current obstacles.

We end by noting that illuminating UTBS with photons instead of electrons opens up the space of sample preparation for PEEM imaging. It is plausible that different sample preparations could be even more suitable for PEEM and that combinations of existing EM stains or entirely new stains could increase contrast. Also, for each contrast agent candidate, higher throughput could be achieved by identifying the optimal excitation wavelength. In summary, further exploration of PEEM as a connectomic or projectomic mapping technique can only increase its capabilities and open new pathways for providing large-volume circuit mapping.

6.2.6 Conclusion

In summary, we have demonstrated exploratory work on exploiting a new electron microscopy technique, PEEM, for large-volume serial neurological imaging. A robust sample preparation technique was successfully applied to produce consistently high-resolution, high-contrast PEEM images of ultra-thin mouse brain sections. With PEEM instruments with a magnetic lens system or aberration correction apparatus, we were able to identify synapse structures with sufficiently high spatial resolution, indicating the capability of PEEM to capture critical neuronal components. Furthermore, serial image reconstruction of small sample quantities was achieved with the assistance of vision algorithms for both 2D image stitching and 3D neurite tracing. Additionally, our simulation illustrates another attractive advantage of PEEM for fast-speed, high-throughput image acquisition by a proper selection of illumination sources. All in all, the exploration of PEEM as a connectomic technique can only increase its capability and open new pathways for large-volume circuit mapping with fast data acquisition.

6.3 Contrast mechanism of Os-stained biological samples

6.3.1 Abstract

Electron imaging of biological samples stained with heavy metals has enabled visualization of subcellular structures critical in chemical-, structural-, and neuro-biology. In particular, osmium tetroxide (OsO_4) has been widely adopted for selective lipid imaging. Despite the ubiquity of its use, the osmium speciation in lipid membranes and the process for contrast generation in electron microscopy (EM) have continued to be open questions, limiting efforts to improve staining protocols and therefore high-resolution nanoscale imaging of biological samples. Following our recent success using photoemission electron microscopy (PEEM) to image mouse brain tissues with synaptic resolution, we have used PEEM to determine the nanoscale electronic structure of Os-stained biological samples. Os(IV), in the form of OsO_2, generates nanoaggregates in lipid membranes, leading to a strong spatial variation in the electronic structure and electron density of states. OsO_2 has a metallic electronic structure that drastically increases the electron density of states near the Fermi level. Depositing metallic OsO_2 in lipid membranes allows for strongly enhanced EM signals and conductivity of biological materials. The identification of the chemical species and understanding of the membrane contrast mechanism of Os-stained biological specimens provides a new opportunity for the development of staining protocols for high-resolution, high-contrast EM imaging. [b]

---

[b] Adapted with permission from **Li, R.**, Wildenberg, G., Boergens, K., Yang, Y., Weber, K., Rieger, J.,

6.3.2 Introduction

Osmium tetroxide (OsO_4) has been extensively used for enhancing membrane contrast in electron microscopy (EM) for the last several decades due to its lipid-selective chemical reactivity.[226,233–239]. Conventional understanding of the mechanism of Os contrast generally focuses on the identity of Os as a "heavy metal", with a high atomic number.[240] However, the oxidation state and bonding of osmium in lipid membranes, and the reactions occurring during the staining process are surprisingly unknown. This has left puzzling questions for the broad community that uses OsO_4 chemistry for electron microscopy, such as why osmium staining improves the conductivity of biological samples and facilitates EM imaging without severe charging problems. The question of the chemical identity and formation mechanism of osmium compounds in lipid membranes has also hampered efforts to modify staining protocols of biological materials for EM to improve chemical uptake in large tissue samples, improve image contrast, or develop chemistries that don't require highly toxic osmium tetroxide. Reaction development has relied on exhaustive search rather than rational design.

Historically, the biological literature suggested that osmate esters are formed in the tails of unsaturated fatty acids in lipid membranes, as facilitated by the well-understood reaction of OsO_4 with alkenes.[241] The Os nuclei of the osmate esters present in regions with high lipid concentrations were suggested to be the source of improved electron scattering in SEM and TEM.[233] More recently, research on improving the staining of whole brain samples hypothesized the osmium species responsible for EM contrast is osmium(IV) (OsO_2), rather than the previously proposed osmium(VIII). Upon staining, the biological material underwent an observable color change in an *ex-situ* model experiment, suggestive of the formation of Os(IV).[226] However, the presence of OsO_2 was not confirmed, and it was unclear how OsO_2 would impact the SEM contrast. X-ray photoelectron spectroscopy (XPS) of stained

---

Arcidiacono, A., Klie, R., Kasthuri, N. and King, S.B. OsO_2 as the Contrast-Generating Chemical Species of Osmium-Stained Biological Tissues in Electron Microscopy. *In reivew.*

specimens showed the presence of a mixture of low Os oxidation states, but lacked the spatial resolution needed to determine the locations of different Os oxidation states.[242] Therefore, it is of vital importance to determine the local electronic structure of Os-stained biological materials on the nanoscale and unravel the reaction scheme of the osmium staining process.

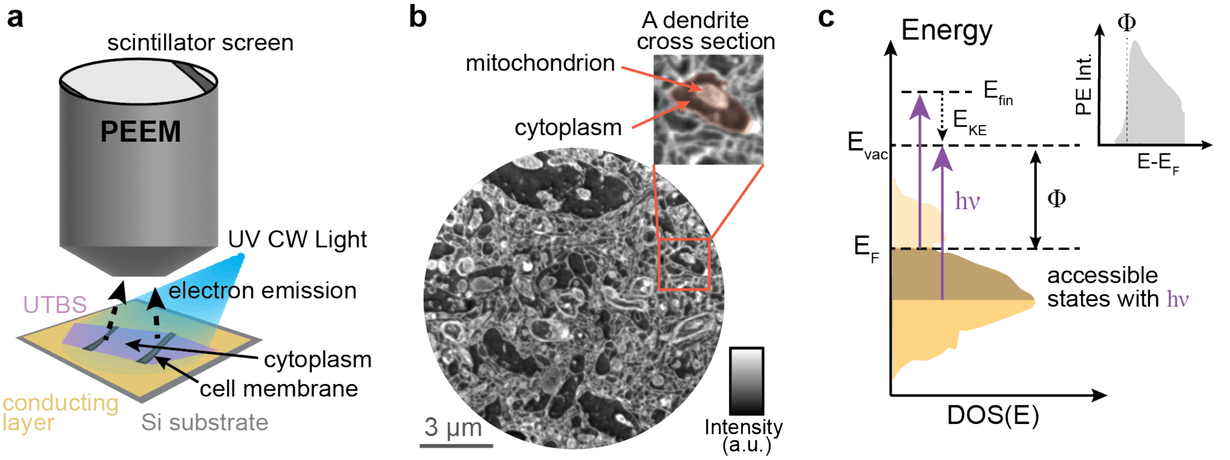

Figure 6.6: (a) A schematic of PEEM. An ultra-thin brain slice (UTBS) is placed on a gold-coated Si substrate, illuminated by a Hg lamp ultra-violet (UV) continuous-wave (CW) light source. (b) A representative PEEM image of mouse brain tissue. The bright contours indicate the cell membranes stained with osmium, and the dark features are the unstained cytoplasm. Ultrastructure can be clearly revealed, such as the neural dendrite and the mitochondrion in the shaded area in the inset. (c) Energy diagram of photoemission process, where electrons in occupied states below the Fermi level (E_F) are photoexcited with UV light of photon energy $h\nu$ to final states (E_{fin}) above the vacuum level (E_{vac}) with kinetic energy E_{KE}. The work function, Φ, is the energy difference between E_F and E_{vac}. The inset shows a schematic of the obtained photoemission spectrum from the accessible density of states (DOS) as a function of the kinetic energy of photoelectrons.

We have recently demonstrated wide-field imaging of ultra-thin brain slices (UTBS) stained with OsO_4 and $K_4Fe(CN)_6$ with synaptic resolution using photoemission electron microscopy (PEEM).[243] PEEM is based on the photoelectric effect where a photon with energy greater than the work function of a material causes the emission of electrons with a spatial distribution that is magnified and mapped to a detector via electron lenses, as shown in Figure 6.6(a). PEEM probes the local electronic structure of imaged materials and has illustrated the potential for detailed surface mapping of biological materials at a submicrometer resolution.[72,222,244–246] Therefore, this technique facilitates the identification of the electronic structure of osmium compounds used in biological staining, shedding light on how and why osmium staining improves sample conductivity and image contrast in electron microscopy.

In this paper, we show that biological materials stained with OsO_4 and $K_4Fe(CN)_6$ form OsO_2 nanoaggregates in the lipid membranes. OsO_2 behaves like a metal, possessing a high electron density of states (DOS) that crosses the Fermi level, and provides the needed conductivity and electron DOS for successful PEEM imaging of biological tissues. We propose a full mechanistic picture leading to OsO_2 formation, discuss possibilities for a likely slow step, and pinpoint specific routes for contrast improvement. As the speciation of osmium also plays an important role in the contrast and conductivity of samples for SEM and TEM that share the same staining protocol, the mechanism of Os staining and image contrast described here is equally critical for improving image quality of biological materials in the broader EM field.

6.3.3 Experimental Methods

Sample Preparation

Mouse brain sections were prepared for PEEM imaging following the same protocol used for SEM[226] and for PEEM imaging in our previous work using the "reduced osmium" staining protocol[243]. Briefly, the mouse was perfused transcardially to preserve tissue ultrastructure. The mouse brain was surgically removed and fixed, and a vibratome sectioned brain slice (200-300 μm) was stained with successive rounds of osmium tetroxide and potassium ferrocyanide before ethanol dehydration and embedding with EPON resin. Resin encapsulated brain was then sectioned using an ultramicrotome to a 40-80 nm-thick UTBS which was picked up on a Si substrate with native oxide (n-SiO_2/Si) coated with 50 nm of polycrystalline gold. The additional conductive layer was used to prevent sample charging during photoemission[247]. Further details of sample preparation can be found in A.6.1

PEEM Imaging

The UTBS on the Au/n-SiO_2/Si substrate was illuminated using a broadband Hg arc lamp that generates UV continuous-wave (CW) light. The lamp is mounted with a high-pass optical filter allowing photons with energies greater than 4.43 eV (280 nm) to impinge on the sample, and the highest photon energy is approximately 5.0 eV (247 nm) (see full spectrum in Supporting Information Fig. S4). The resulting photoelectrons are imaged with a photoemission electron microscope manufactured by Focus GmbH. The PEEM operates at ultra-high vacuum (base pressure $\sim 5 \times 10^{-11}$ mbar). Photoexcited electrons are projected, via an electrostatic lens system, onto a double micro-channel plate (MCP), converted to visible light by a phosphor screen, and eventually imaged by a CMOS camera. The typical exposure time for one image is 10 seconds. High-resolution images were obtained by averaging the same regions of interest (ROI) to improve the signal-to-noise ratio. The PEEM is equipped with a high-pass energy filter where only photoelectrons with kinetic energies higher than a given energy threshold can pass and be detected, enabling energy-resolved PEEM images. The energy resolution of the instrument is approximately 50 meV and scans were collected using 100 meV steps.

STEM-EDS and EELS Measurements

Additional characterizations were done using scanning transmission electron microscopy (STEM, JEOL ARM200-CF). The chemical composition of the Os-stained regions was analyzed with energy dispersive spectroscopy (EDS, Oxford XMAX100TLE) to determine the Os:O ratio. A total exposure time of up to 15 minutes was used during EDS measurements due to the thin nature of the specimens. Electron energy-loss spectroscopy (EELS, post-columns Gatan Continuum GIF ER spectrometer) measurements were conducted on osmium-rich regions as well, with an electron probe semi-convergence angle of 17.8 mrad and a collection angle of 53.4 mrad.

6.3.4 Results and Discussion

Energy-Resolved PEEM Imaging

Figure 6.6(b) shows a PEEM image of a UTBS on a Au/n-SiO_2/Si substrate. Photoelectrons are emitted from the UTBS via a one-photon photoemission process using a broadband Hg arc lamp that generates ultraviolet (UV) photons. Brighter regions of Figure 6.6(b) indicate more photoemissive components whereas darker regions are biomaterials that have low photoemission yield. Based on comparison to SEM images of similar samples, the bright outlines depict neuron or organelle membranes that selectively bind osmium. The darker background consists of unstained regions of biological tissues, such as cytoplasm, that do not contain lipid bilayers. More specifically, the inset of Figure 6.6(b) is the zoom-in of the red box. The shaded region is the cross-section of a neural dendrite, and the bright solid spot within the cytoplasm is a mitochondrion. The difference in signal intensities allows us to visually distinguish the ultrastructure of biological material with subcellular resolution, and the features are comparable to what has been previously collected using SEM[41].

The contrast observed in PEEM is due to stained and non-stained regions generating different intensities of photoelectrons. To understand why photoemission intensity varies spatially in the brain tissue, we performed energy-resolved PEEM to measure the local electronic structure of the UTBS. We used a high-pass energy filter to incrementally cut out photoelectrons with kinetic energy lower than an energy threshold and obtained a series of PEEM images at the same sample position. The photoemission intensity of an ROI is extracted as a function of photoelectron energy with respect to the Fermi level of the analyzer (E-E_F), and we compute the energy distribution of the photoelectrons by performing a numerical differentiation of the energy-resolved images (see Section A.6.2). The low energy edge of this distribution, termed the secondary edge in the photoemission spectroscopy literature, can be used to determine the work function (Φ) of the material.[189,248] This value is the energy difference between the vacuum level and the Fermi level (Φ=E_{vac}-E_F), as depicted in the energy diagram in Figure 6.6(c).

Figure 6.7(a, inset) shows three ROIs of varying signal intensities and their corresponding photoemission spectra. All three curves have been normalized to the peak intensities and offset vertically for clarity. Despite variation in the total photoemission counts, the three spectra display almost identical photoemission spectra. We estimated the relative values of the work function ($\Delta\Phi$) of each region by shifting the energy axis with respect to the secondary edge of the top spectrum ($\Delta(\mathrm{E}-\mathrm{E_F})$). The relative work function was found by fitting each photoemission spectrum with an exponentially modified Gaussian function and looking for the energy cutoff corresponding to half of the maximum magnitude (see more details on data processing in Section A.6.2). The dashed line in Figure 6.7(a) marks the secondary edges of the three spectra. As $\Delta\Phi_{\mathrm{bright}} = 0$, the relative work functions for the gray and dark regions are 0.011 eV and 0.021 eV, respectively, which are smaller than $\pm$ 0.05 eV (instrument resolution). This result indicates that there is no measurable work function variation across the sample even with the existence of heavy metal stains. Therefore, the image contrast that is observed with UTBS in PEEM cannot be due to sample work function variation, but must be due to a variation in the sample electronic structure.

The high energy sides of the photoemission spectra in Figure 6.7(a) are virtually identical within the energy resolution. No additional peaks can be identified in the spectra from the bright ROI, which would indicate distinctive electronic states in this region. The similarity in spectra makes it unlikely that there is a difference in contrast-generating chemical species across the sample. It is instead more likely that there exists a concentration gradient of a singular chemical species, resulting in variation in photoemission intensities as a function of space. As shown schematically in Figure 6.7(b), biological tissues, such as unstained cytoplasm, are typically considered to be insulating materials. For example, proteins commonly have optical absorption around 4.43 eV (280 nm)[249], and have a high ionization energy[250]. Therefore, the photon source used in this work can not photoemit efficiently from the oc-

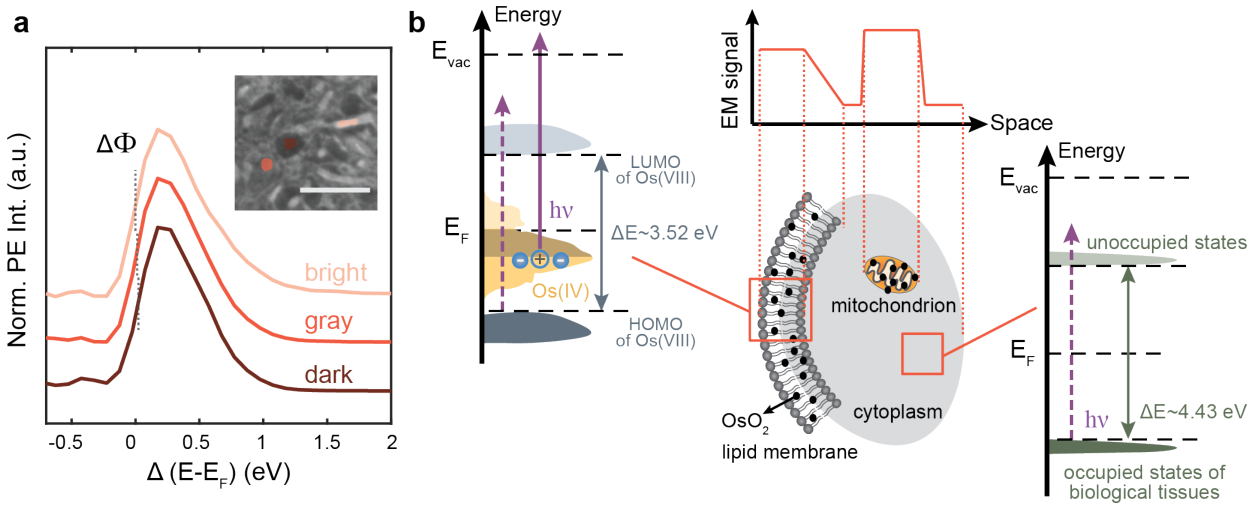

Figure 6.7: (a) Photoemission spectra of bright, gray, and dark ROIs (corresponding different blue shades) shown in the inset. Dashed lines indicate work function relative to the secondary edge of the top spectrum (corresponds to the brightest region). The scale bar is 2 μm. (b) Energy diagrams comparing electron densities of osmium(IV) near the Fermi level with HOMO-LUMO gaps of Os(VIII) and biological tissues. Lipid membranes of cells and organelles such as mitochondria efficiently bind to osmium, generating stronger signals in EM images, whereas unstained regions such as cytoplasm generally yield low EM intensity.

cupied electronic states of pure biological tissues, resulting in low photoemission intensities. Similarly OsO_4 and Os(VIII) compounds are also insulators with large HOMO-LUMO gaps of about 3.52 eV (352 nm)[251] and large ionization potentials[252], resulting in low photoemission yield. However, OsO_2 is known to have metallic properties[253–255], providing OsO_2 with the requisite electronic structure for high photoemission yield.

Elemental Characterizations of Osmium Species

Similar to its well-studied Group 8 analog RuO_2, OsO_2 tends to form metal oxide aggregates[253,255,256]. Figure 6.8(a) shows a high-angle annular dark-field transmission electron microscopy (HAADF-STEM) image of UTBS on a TEM grid, where the bright contrast corresponds to atomic columns containing elements with high atomic numbers. Bright contrast in the HAADF image shows aggregates clustering along cell membranes. Energy dispersive spectroscopy (EDS) mapping of the same ROI (Figure 6.8(b)) shows that the bright aggregates are osmium-rich, confirming that osmium has indeed been deposited specifically

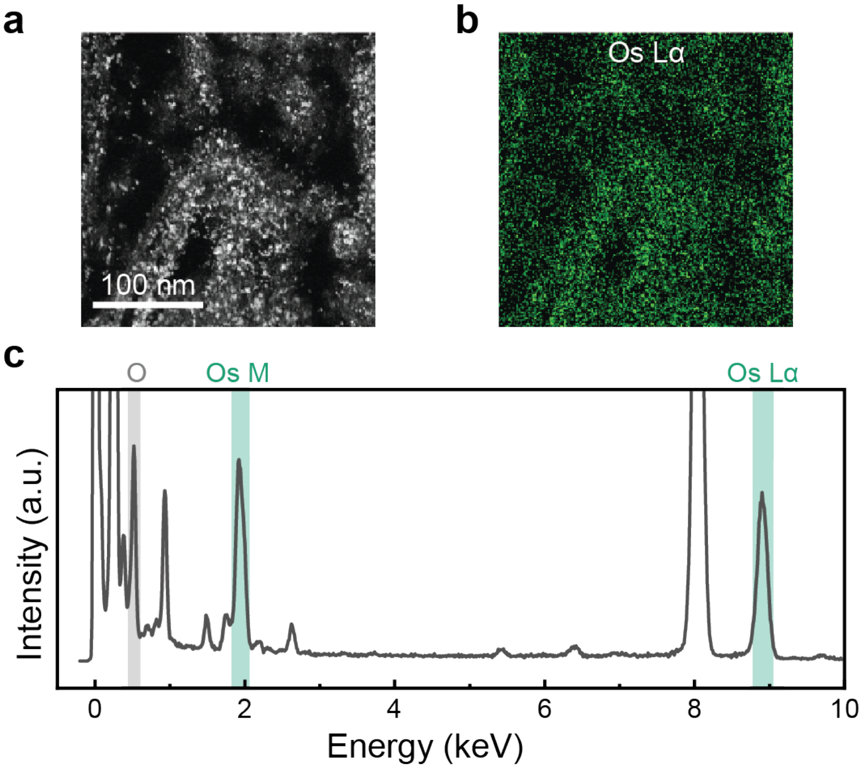

Figure 6.8: (a) A high-angle annular dark-field transmission electron microscopy (HAADF-STEM) image of an area with clear contrast of aggregates along cell membranes. (b) Energy dispersive spectroscopy (EDS) map from the Os Lα signal of the mapped area. (c) EDS spectrum of the elements detected, where the grey band highlights the O K signal at 0.525 keV, and green bands highlight Os M and Lα peaks at 1.91 keV and 8.91 keV, respectively. Note that other elements were also detected in the spectrum, but were disregarded for the purpose of the analysis. The full EDS spectrum can be found in Figure A.42.

in the lipid membranes. Figure 6.8(c) shows the corresponding EDS spectrum. Characteristic peaks of osmium M and Lα lines at 1.91 keV and 8.91 keV, respectively, can be clearly observed, and oxygen Kα signal is also confirmed at 0.53 keV. The average elemental ratio of Os:O from the Os-rich areas is calculated to be between 1:2 to 1:3, corroborating OsO_2 as the main osmium species. It is important to note that O signal is also detected in background areas where there is limited contrast from the bright clusters, indicating the likely overestimation of O composition in Os-O compounds. Furthermore, electron energy loss spectroscopy (EELS) was used to additionally verify the existence of both Os and O (see more discussion in Section A.6.5). The combination of the EDS and EELS results indicates that Os most likely takes the valence state of IV, despite that some mixture of higher and lower states of osmium persists[242,257].

Chemical Reactions for OsO_2 Formation

Hua *et al.* studied the formation of OsO_2 in tissue stains using color comparisons in a test tube experiment. From this result, they proposed a simple reaction scheme that invited future experiments to support the contributions of low-oxidation state osmium in EM staining[226]. Here, having confirmed OsO_2 and Os(IV) compounds as primary chemical species that provide PEEM contrast, we aim to deliver a more detailed and accessible description of the staining mechanism.

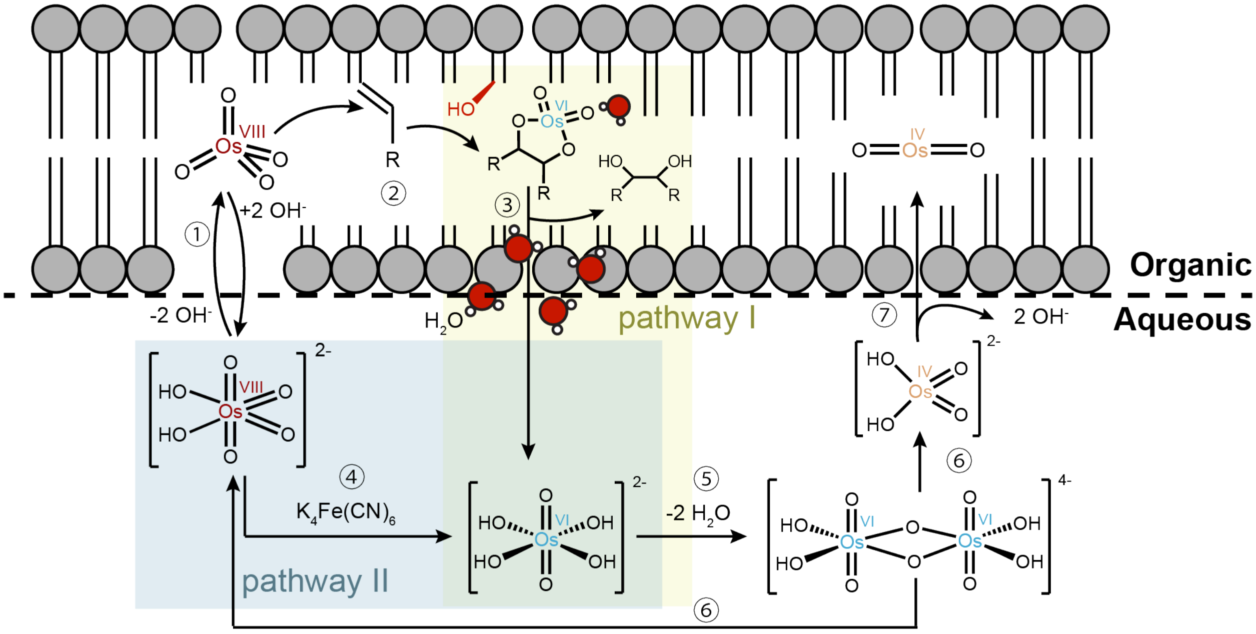

Figure 6.9: Schematic illustration of the formation and deposition of OsO_2 in the lipid membrane during the staining process.

Buffered OsO_4 is introduced to biological tissue in its ionic water-soluble form, $[OsO_4(OH)_2]^{2-}$, see Step 1 in Figure 6.9. To ensure homogeneous staining across 100s μm-thick tissue block, osmium compounds passively diffuse through various layers of membranes to penetrate cells and organelles. This process is facilitated by $[OsO_4(OH)_2]^{2-}$ switching back and forth with its non-polar lipophilic form OsO_4[258,259]. In this reaction, Os(VIII) loses or gains two hydroxyl groups at the membrane-cytoplasm interface, resulting in an even distribution of Os(VIII) in the cell lipid phase.

In the next step (Step 2), OsO_4 selectively couples to specific sites in the lipid membranes to form bound osmium. It is widely accepted that this process is realized via Sharpless dehydroxylation, where C=C bonds in unsaturated fatty acids attack an electropositive osmium center of the Os=O, resulting in the formation of an intermediate cyclic osmate ester (Os(VI))[242,257,260]. This ultimately leads to the reduction of Os(VIII) to Os(VI), as verified previously by XPS measurements[242].

The transiently generated Os(VI) in Step 2 can be accessed through two different pathways, either via the migration of the osmate ester to the hydrophilic head of the lipids for spontaneous hydroxylation (Pathway I in Figure 6.9), or via reduction, initiated by additive $K_4Fe(CN)_6$, producing water-soluble $[OsO_2(OH)_4]^{2-}$ in the aqueous phase (Pathway II). In Pathway I, nearby water molecules or hydroxyl groups are necessary to promote hydroxylation (Step 3), but their origin in the lipid phase has not been well discussed in the literature. It is known that water can passively diffuse across lipid membranes to allow for osmotic equilibrium; this small population of water may serve as a potential −OH source in the membrane[261]. Additionally, it has been observed that osmium can migrate towards the membrane-water interface, resulting in a higher concentration of osmium complexes at the hydrophilic heads[242,262]. This may be in part due to interfacial water facilitating the ring-opening reaction. Finally, hydroxyl groups in the phospholipids can also be utilized to form $[OsO_2(OH)_4]^{2-}$.

In the second pathway, Os (VIII) can be reduced via the addition of a reducing agent, in this work, potassium ferrocyanide ($K_4Fe(CN)_6$). $[OsO_4(OH)_2]^{2-}$ is directly reduced outside the lipid bilayer to Os(VI) (Step 4) in parallel with the spontaneous hydroxylation that occurs in Pathway I. This reduction step circumvents the osmate ester formation between the bilayer and greatly accelerates the generation of Os(VI) in the aqueous phase.

Lastly, the formation of OsO_2 occurs via a disproportionation reaction of Os(VI) under biological pH conditions (buffer pH=7.4)[242,263]. Previous X-ray studies of model systems suggested the presence of a dimeric Os(VI) crystal structure with a double oxo bridge[242,264]. Herein, we assume that the same dioxo-bridged osmium species is being formed (Step 5)[256]. There are debates regarding the possibility of a tri-osmium product emerging, although this needs future experimental evidence[256,265]. The osmium(VI) dimer is known to be unstable and undergoes asymmetric Os−O bond cleavage. This results in the oxidation of one Os(VI), regenerating Os(VIII), and the reduction of the other Os(VI) center, finally forming $[OsO_2(OH)_2]^{2-}$ in water (Step 6)[266]. The dehydroxylation of $[OsO_2(OH)_2]^{2-}$ can readily deposit the lipid-soluble OsO_2 into the bilayer membranes as aggregates (Step 7). The production of OsO_2 contributes to the primary contrast observed in EM images.

Our determination of the source of the contrast in the reduced osmium staining protocol has implications beyond PEEM. Other EM techniques that are commonly used for biological imaging, such as SEM and TEM, adopt the same staining method and will significantly benefit from the proposed contrast mechanism. With the understanding of the speciation of osmium, efforts can be made towards the deposition of a higher concentration of OsO_2 into the lipid membranes. For example, the possibilities to initiate Pathway I in Figure 6.9 suggest that finding new ways to introduce −OH in proximity to membrane heads could potentially increase the production of $[OsO_4(OH)_2]^{2-}$ for the eventual generation of the contrast relevant OsO_2. Overall, the understanding of the chemical identity of osmium staining promotes intentional modifications for protocol development rather than improvements based upon exhaustive search.

6.3.5 Conclusion

In summary, this work provides a detailed description of the chemical species responsible for obtaining high-contrast images of Os-stained ultra-thin brain slices in electron microscopy. Nanoscale imaging of biological complexes using PEEM enables us to characterize the spatially varying electronic structure of stained UTBS. OsO_2 nanoaggregates are formed in lipid membranes and provide the needed conductivity and contrast due to the metallic electronic structure of OsO_2. We propose a full and detailed scheme of the reactions and pathways necessary for the formation of OsO_2 in the lipid membranes. The determination of the source of contrast, as well as the relevant pathways for OsO_2 generation suggested herein, challenges the long-adopted understanding of Os-staining in biological tissue. Our knowledge of the chemical origin of EM contrast sets the foundation for modifying staining protocols by intentionally engineering the electronic structure of chemical and biological structures on the nanoscale, ultimately achieving sensitive and selective visualization of nanoscale biological components.

6.4 Investigations on contrast degradation

6.4.1 Introduction

Despite the consistent generation of high-resolution PEEM images, contrast degradation has been a challenging issue for long-term imaging and fundamentally restricts the experimental time for investigating the EPON-embedded samples. The degradation mainly manifests in two aspects. First, the intensity of the whole FOV gradually increases upon illumination. Second, the intensity difference between the originally bright features (e.g. mitochondria) and dark areas (cytoplasm) decays over time, and eventually, typically in 40 minutes to 2 hours, the biological tissues become indistinguishable. An example demonstrating the effect is shown in Figure 6.10. Optical microscopy has been employed to visualize the changes in the sample before and after PEEM imaging with the Hg lamp. The major distinction in the sample is that the color of the resin changes significantly from pale gray to amber, a typical sign of polymer degradation under UV light.[267] However, using a high NA objective, the neurons can still be optically observed, indicating no matter what substances that have degraded the PEEM image quality, there is no damage to biological tissues. This is additionally verified by scanning electron microscopy (SEM) images of the illuminated sample, and high-resolution images show that the ultrastructure is retained. A variety of control experiments have been performed to determine the source of the degradation. The potential sources include sample preparation protocols, embedding materials, sample storage to surface condition, excitation source, and imaging temperature. Some parameters have been shown to slow down the degradation process, however, to this date, consistently preserving the image contrast for a time frame longer than two hours is still an obstacle to the development of bio-PEEM technology.

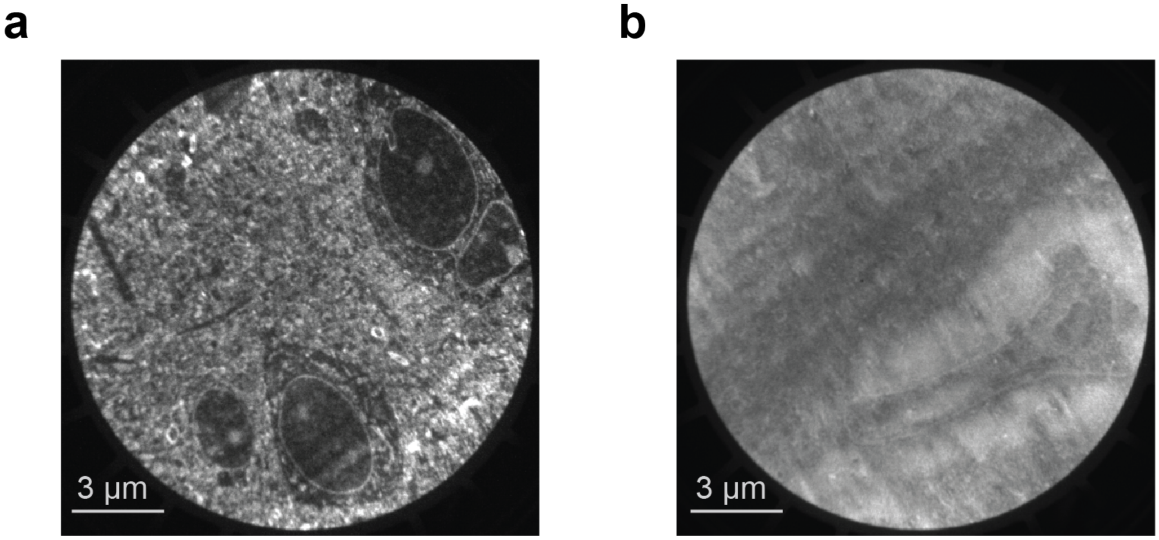

Figure 6.10: (a) A PEEM image of a mouse brain section on a gold substrate. (b) A PEEM image of the same sample after 30 minutes of continuous imaging time. Scale bar: 3 μm.

6.4.2 Sources of the degradation

Comparison with other imaging techniques

The conditions of the mouse brain sections that have been imaged with PEEM and have shown degraded contrast are investigated with optical microscopy and SEM. Figure 6.11(a) is an optical image of a 40 nm thick mouse brain section that has been previously imaged with PEEM. Although the cellular structures were barely resolved by PEEM, neurons, and organisms with clear color contrast can still be observed in the optical images. This result shows that the biological tissues were not disintegrated due to high vacuum or light illumination. To further visualize the ultrastructure on the nanoscale, PEEM-degraded samples were imaged with SEM with high magnifications. Similarly, individual neurons and organisms whose lipid membranes were stained with heavy metals show strong intensities while the unstained background has dark contrast (Figure 6.11(b)), as expected for typical SEM images of brain tissues. Both methods confirmed that the biological structures were preserved after the photoemission experiments. This indicates that the PEEM contrast decay isn't a consequence of the disappearance of the soft tissues, but rather global modifications of certain components continuously diminish the photoemission yields from the osmium stains. This is also consistent with the observation that the entire sample becomes brighter during imaging contrary to a local effect.

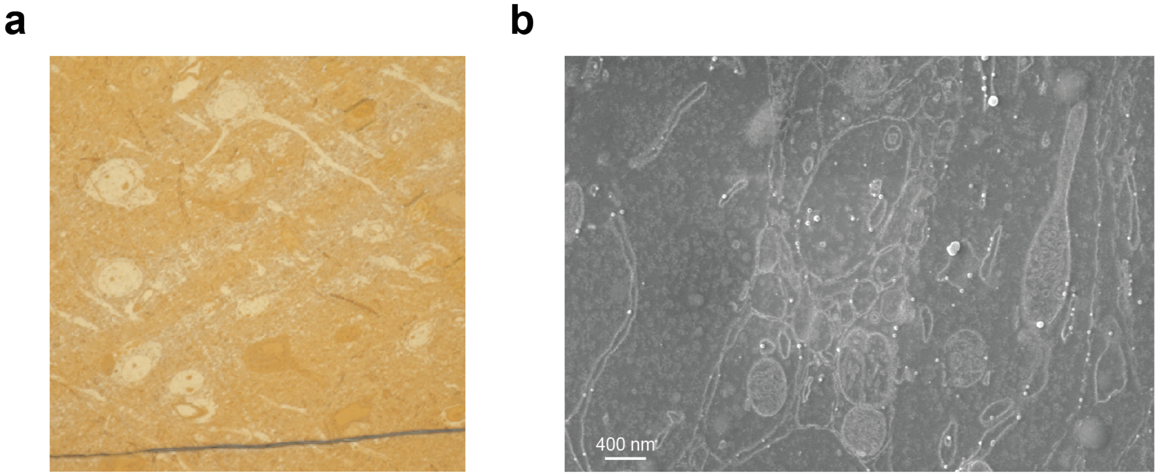

Figure 6.11: (a) An optical image of a 40 nm thick mouse brain section on a gold substrate that has been imaged with PEEM. (need a scale bar) (b) An SEM image of a different mouse brain section on a Si substrate whose contrast has degraded in PEEM.

Instrument variations

To understand that the success of PEEM imaging of biological tissues isn't unique to one instrument, as well as to eliminate the possibility that the degradation issue is induced by the local environment of the FOCUS PEEM chamber at UChicago, we carried out imaging of mouse brains prepared with the same protocol with four different PEEM instruments/manufacturers at multiple countries and institutions. Comparisons of the images are displayed in Figure 6.12.

Figure 6.12(a) is a representative PEEM image collected using the FOCUS system in the King lab, and the details for image acquisition have been illustrated in Section 6.2.3. For the sample specifically, the mouse brain section is ∼60 nm thick, which shows an enhanced contrast than the standard 40 nm section. A FoV of 15 μm was selected and averaged 50 times with a camera exposure time of 10 seconds for each frame. This image was collected in the first 20 minutes of the measurements where the sample had not shown evidence of significant degradation.

Mouse brain sections of 40 nm thickness were transferred onto gold substrates at UChicago and carried to the LEEM/PEEM facility at Leiden University in the Netherlands. The image acquisition was conducted on an aberration-corrected PEEM system manufactured by SPECS GmbH, Berlin. The excitation source was a Hg discharge lamp, and the photoemission signal was collected by an electron detector that has a better detector resolution than the conventional MCP-based detection system.[268] Figure 6.12(b) shows the best quality image from the trip, where the FOV is 5.7 μm, and the image was averaged for 10 frames and the dwell time is 5 seconds. The final image was processed by subtracting the camera noise from the background and correcting the lateral drift due to instrument instability. Using the 84%/16% lateral separation standard, the optimal resolution achieved is around 23 nm. The contrast degradation issue, however, seems to be less dramatic in this instrument. For some samples, the contrast can be retained for several hours and the features of the biological tissues can be vaguely seen toward the end of an imaging session. A close look at the long exposure image stacks shows that over 100 image frames, there are clear increases in sample intensities, which aligns with the observation in the FOCUS PEEM. This test strongly demonstrates the reproducibility of bio-imaging with PEEM, further confirming the robustness of the experimental design. At the same time, it also supports disconnection of the degradation issue and experimental apparatus as well as the location.

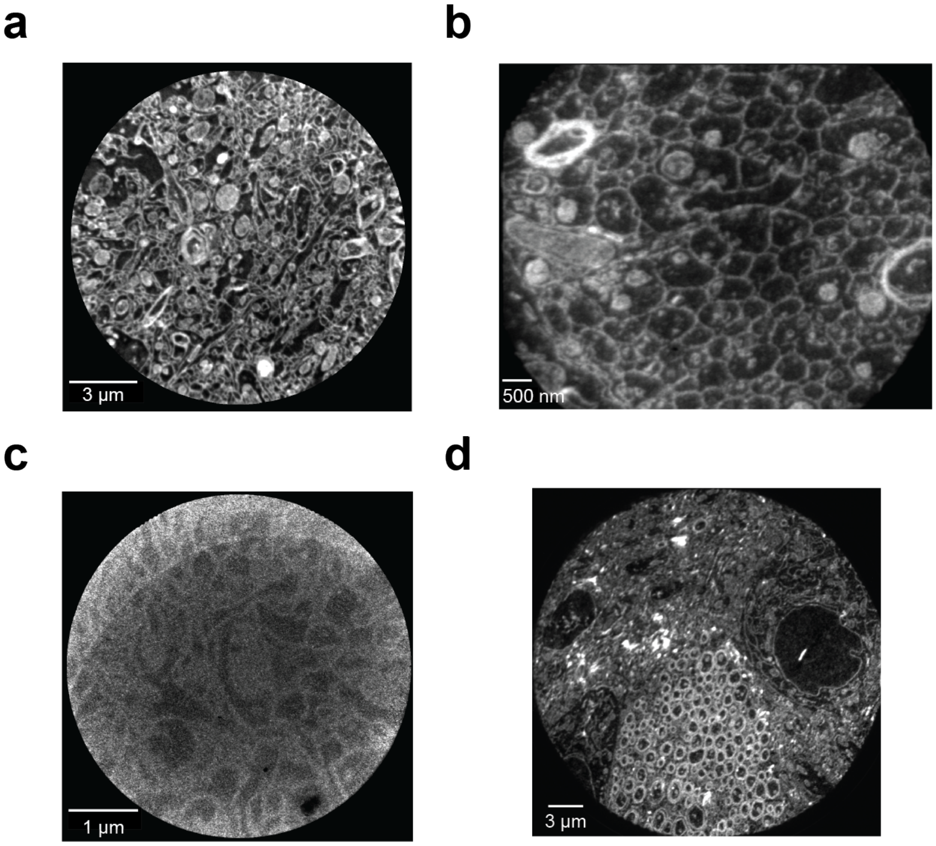

Figure 6.12: PEEM images of mouse brain sections collected by different instruments. (a) FOCUS PEEM in the King lab at UChicago. (b) SPECS PEEM at Leiden University in the Netherlands. (c) ELMITEC PEEM in the German factory site. (d) ELMITEC PEEM in the King lab at UChicago.

To triple-check the consistency of bio-imaging and push for the resolution limit, we were able to bring mouse brain samples to ELMITEC Elektronenmikroskopie GmbH, a third PEEM manufacturer based in Germany and with expertise in developing PEEM systems configured with magnetic lenses. The samples were prepared in the same way in the US and imaged with a Hg lamp in the factory. Unfortunately, the samples were poorly stored before being transferred into the vacuum, and as a result, the image quality wasn't as excellent as with other PEEMs. Figure 6.12(c) shows an example from the German visit. The arc on the top left side of the ROI and the black spot at the bottom right are damaged regions on the

MCP/camera that are challenging to remove from the original image via image processing. Regardless, the cellular features can still be resolved, but the photoemission efficiency and the contrast are much reduced in comparison to other test experiments. Since a high-contrast image was not able to be produced from this batch of samples, it is difficult to assess how the contrast evolved throughout data collection.

Owing to the successful refurbishment of the ELMITEC system inherited from Wisconsin (see Section 2.3.2), we had the opportunity to test more mouse brain samples with a similar ELMITEC PEEM in the King Lab. As displayed in Figure 6.12(d), the mouse brain sections that were carefully stored have been imaged with a Hg discharge lamp (Quantum Design) and have consistently provided comparable contrast to images taken with the other manufacturers. This test alleviated the concern that bio-imaging is only applicable to limited instrument types. Typically after one hour or two of continuous imaging on the same section, evidence of contrast degradation starts to get more pronounced. On the positive side, the overall effective imaging time is longer on average than that in the FOCUS system, meaning that in principle, we can afford to run experiments that require longer sample lifetimes.

To sum up, the quality and reliability of imaging resin-embedded biological tissues are broadly verified with a variety of PEEM configurations. The decay of image contrast has unexceptionally occurred in almost all situations, although the time frame and the level of degradation are not necessarily agreeable. For the following investigations on the persisting issue, the choice of the PEEM instrument is not the decisive factor.

Surface conditions

From the imaging mechanism perspective, surface contamination from air or in the vacuum environment, such as adsorbed water, oxygen, or charged particles, can alter the imaging quality from the biological tissue given that photoemission is extremely sensitive to surface variations.[269] In addition, the choice of substrates may impact the imaged objects by affecting the conductivity and, ultimately the density of states via physical contact. Several control experiments on surface conditions have been carried out to explore how surface cleanness relates to contrast difference.

(1) Substrate morphology. The first concern is whether weak adhesion between the mouse brain section and the substrate might have led to poor electrical contact, causing sample charging and worsening the image quality. Although gold is chemically inert and rarely reacts with air molecules under normal conditions, it has been well studied that gold atoms diffuse into vacancy sites of silicon over time.[270] The morphology of various thin polycrystalline gold films was inspected by AFM (Bruker MultiMode 8) in terms of substrate age and thickness Figure 6.13 compares the topography of four gold films. The first three were freshly deposited on Si substrate within a day with thicknesses of 10 nm, 50 nm, and 100 nm, and the last one is a 50 nm thick film that had been stored in the air for approximately a month. Visually, the thin films show overall homogeneous distributions of grains with different grain sizes, where the grains of the 10 nm gold film are on average less than 10 nm, and the 100 nm and old 50 nm films have grain sizes of ∼50 nm. Areas of 1×2 μm^2 were selected for statistical analysis of representative regions, and the rms roughness of each film was calculated using the software Gwyddion, and the results are 1.246 nm, 1.398 nm, 1.204 nm, and 1.043 nm, respectively, as indicated under each image. It was expected that the oxygen and surface contaminants would accumulate more old gold film, but those were not captured necessarily by the height profile and would require other more chemically sensitive techniques such as X-ray photoemission spectroscopy (XPS). Nevertheless, the characterizations suggest that despite the slight variations in the gold nanostructure, there's no significant correlation between surface roughness and film thickness/freshness.

(2) Substrate materials. Although we have confirmed that gold is a good substrate material, it has rich density of states around the Fermi level and is strongly photoemissive when illuminated by UV light. There are considerations concerning whether photoelectrons originating from the substrate can propagate through the thin biological sections and even-

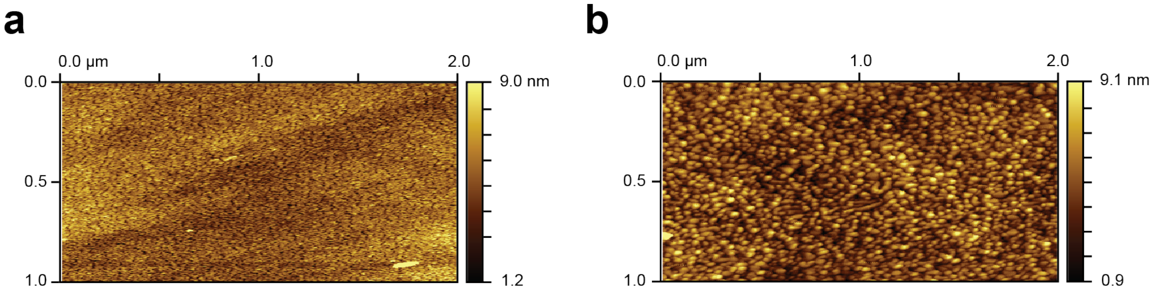

10 nm, 1 d, roughness *1.246 nm*

100 nm, 1 d, roughness *1.398 nm*

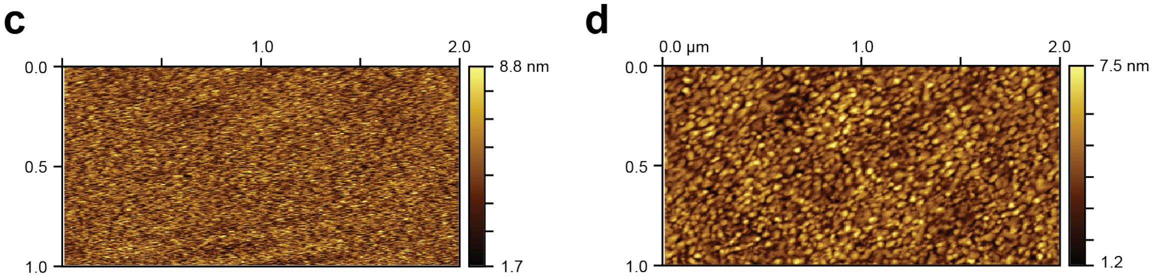

50 nm, 1 d, roughness *1.204 nm*

50 nm, 1 mon, roughness *1.043 nm*

Figure 6.13: AFM images of gold films of various thicknesses and ages.

tually overwhelm the sample signal and weaken the contrast. To test this possibility, we compared the contrast of mouse brain tissues on three different substrate materials: 1) 10 nm polycrystalline gold deposited on Si, 2) 10 nm polycrystalline platinum (Pt) deposited on Si, and 3) bare Si with native oxides. The control experiments were all measured by the ELMITEC PEEM at UChicago, and each substrate was imaged with at least two samples. The rationale for choosing the other two substrate materials is that the substrates need to both provide sufficient conductivity to prevent charging of the insulating plastics and have lower photoemission signals in contrast to the photoemission response from the tissues. The work function of polycrystalline Au is around 5.1 eV, and for Pt, the work function is about 5.65 eV.[271]. Based on the spectrum of the Hg lamp (Figure 2.8), a great number of photoelectrons can be emitted from the gold substrate but not from the Pt due to insufficient photon energy, allowing Pt to provide a dark background underneath the biosamples. Silicon, on the other hand, is a semiconductor and has limited electron densities around the Fermi level and thus the photoemission intensity is much weaker than the metals. In terms of whether the Si substrate is conductive enough to maintain the sample at a constant high voltage, especially in the presence of a thin layer of oxides, we experimented by coating a 1 nm layer of Pt/Pd (80/20) film on the entire sample following Gilbert's methods[72] to prevent potential sample charging.

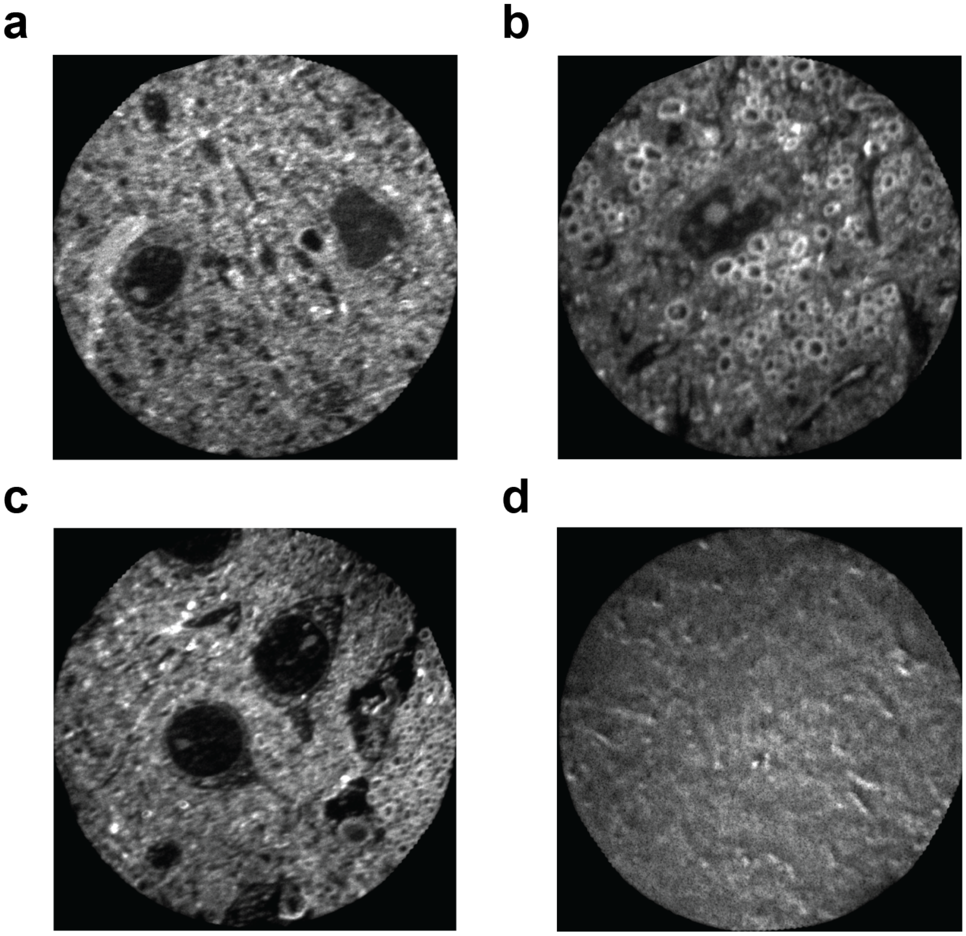

Figure 6.14: PEEM images of mouse brain sections picked up on different substrates. (a) 10 nm Au. (b) 10 nm Pt. (c) Si with native oxides. (d) Si with native oxides, with 1 nm Pt/Pd (80/20) coating. The fields of view are 30 μm.

To verify the hypothesis of the difference in photoemission, the samples were moved to the edge of the sections to compare the relative intensity with each substrate. Gold unsurprisingly has a much higher photoemission yield than resin. Interestingly, the Pt substrate is brighter than the section, contrary to the assumption that Pt is barely photoemissive with the current excitation source. This can be explained by the higher chemical activity of

Pt that leads to the formation of oxides on the surface. Since no rigorous cleaning procedures (annealing and sputtering) were carried out before the measurements, it's reasonable to assume that the real work function is lower than the reported value. As expected, the photoemission intensity of silicon didn't exceed the sections, and we did not observe substantial charging occurring on the sample, indicating that Si can support appropriate electrical contact with the tissue sections, although the heavy metal stains additionally supply the conductivity.

High-contrast images were obtained from all three substrates, as summarized in Figure 6.14. Initially, the three different types of samples exhibit comparably vivid quality. Qualitatively, the Pt sample shows a moderately finer contrast. We further tested the image stability over a long exposure time on each sample and observed a rapid increase of the photoemission intensity on the Au substrate within 40 minutes, substantially deteriorating the image quality. In contrast, after two hours of imaging on the Pt and Si samples, the contrast experienced severe decay but the cellular features could still be captured. The reason why the gold substrates consistently show shorter imaging time frames in both instruments is not fully understood. One possibility is that water and oxygen have a higher tendency to attach to the gold surface. The illumination of the UV lamp continuously heats the surface throughout imaging and the adsorbed molecules are gradually released from the surface, changing the surface composites and thus the photoemission intensity. More experiments regarding the outgassing effect will be discussed later.

Conversely, additional metal coating on the Si substrate fails to enhance the imaging results, and a representative example is illustrated in Figure 6.14(d). Other than the island features that are likely induced by the non-uniform coating process, the image displays invariable photoemission intensity across the surface, meaning that the coating layer, rather than the osmium-modified tissues, primarily contributes to the PEEM contrast. This outcome further demonstrates the superior surface sensitivity of the photoemission process initiated by a UV excitation source. Another factor to consider is that the presence of palladium in the coating material may have lowered the work function of the surface ($\Phi_{\mathrm{Pd(100)}} \approx 5.0$ eV[272]), and as a result, the strong photoemission from the entire top layer dominates the spatially varying osmium signals.

(3) Surface adsorbates. Outgassing is a phenomenon where the trapped gas molecules desorb from the surface and it constantly occurs in high vacuum systems.[273] Outgassing from the epoxy as the embedding material has been reported to cause artifacts and lower the image contrast in SEM imaging of biological tissues.[274] Since photoemission is subjective to changes in surface substances, the concentrations of adsorbed molecules, as well as the evolution of the concentrations, can be easily reflected in the change in image quality. Water vapor is one of the major species that can shift the electronic structure of the surface.[275] We first carried out experiments by varying the moisture level of the sample storage conditions. One set of samples was stored in a vacuum desiccator, and before imaging, the chip was kept in the loadlock (base pressure $\sim 10^{-8}$ mbar) overnight to minimize water vapor collected from the air during the transfer process. The other set was stored in a N_2 desiccator where the hygrometer constantly indicates a moisture level of 30%. Before PEEM imaging, the chip was only pumped down in the load lock for about 20 minutes. Figure 6.15(a) and (b) are the PEEM images of the two chips after continuous imaging. The sample with better moisture control still experienced decreasing contrast and in 50 minutes, the image quality was beyond satisfactory. The second sample, while in principle possessed a higher water content on the surface, showed a similar decay rate as the previous one, and the neuronal structures were barely observable in 50 minutes. This result implies that the biological sections are not necessarily sensitive to the storage environment. Water adsorption/desorption may still play a role as no characterizations were conducted to confirm the reduction of water concentration.

It has been verified in previous testing that heating a single crystalline copper sample helps remove surface contaminants and lower the work function. Consequently, the sample

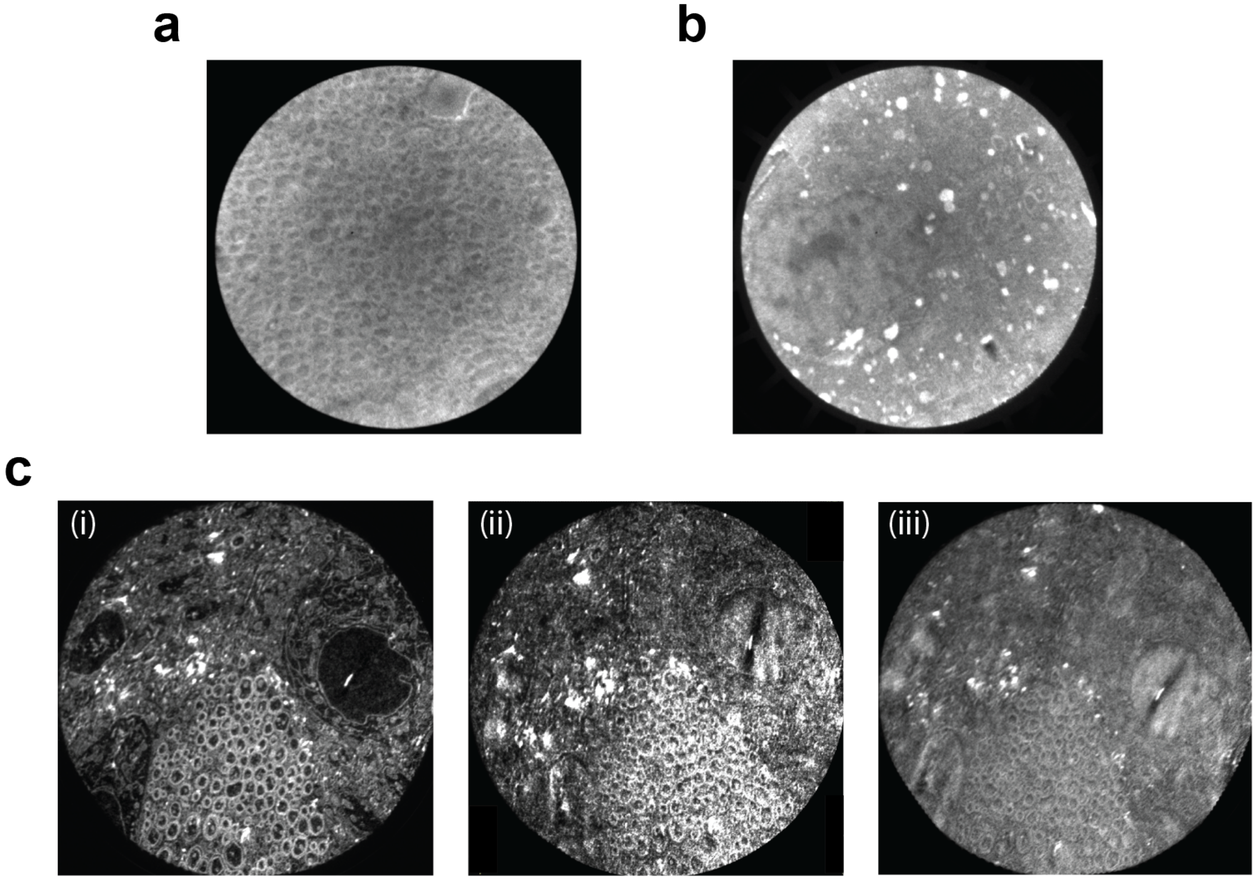

Figure 6.15: Control experiments studying the surface adsorbate effect on PEEM images. (a) PEEM image of a mouse brain section on a gold substrate after 50 minutes of continuous Hg lamp illumination. The sample was previously stored in a vacuum desiccator and was pumped in the load lock overnight before being placed into PEEM. (b) PEEM image of a mouse brain section on gold substrate after 40 minutes of continuous illumination. The sample was previously stored in a N_2 desiccator with poor moisture control and was pumped in the load lock for 20 minutes before imaging. (c) The evolution of PEEM image of a mouse brain section on Pt substrate. (i) sample was freshly imaged after being heated at $\sim$100 °C for minutes. (ii) sample after one hour of continuous imaging. The overall photoemission intensity drastically increased. (iii) sample was heated again at $\sim$100 °C for minutes after contrast degradation. The contrast does not recover. Note that the dynamic range of the last image has been adjusted.

work function is reduced, yielding a high photoemission S/N, and the scratches on the surface can be imaged with high resolution (see Appendix). Following this logic, we tried heating the mouse brain sample and looking to remove water from the surface more effectively. Figure 6.15(c) lays out the evolution of the image quality of the same area as a function of time. In this case, a mouse brain section was set on a Pt substrate. The chip was first heated in the sample holder at 100 °C for 5 minutes in the ELMITEC system, and the immediate results visibly demonstrated excellent contrast. Though a reference to the image quality before heating was lacking, we were able to continuously image the sample for at least one hour and the contrast was largely retained, which seemed to be an improvement of the sample life span compared to previous tests. When focusing on the same ROI to monitor image quality for another 20 minutes, we noticed again, the brightening of the entire sample as well as the worsening of the contrast. In particular, areas that were originally dark, such as the cytoplasm of a large cross-section of a neuron, Assuming that the re-adsorption of water or other gas molecules slowly altered the surface properties, we tried heating the sample once again with the same parameters (100 °C for 5 minutes). However, the desorption of adsorbates did not recover the image contrast. To understand if the degradation was only induced at the ROI that had been imaged, we scanned across the sample by moving the manipulator and found the image quality had been distorted on the rest of the surface. The lessons learned from this test is that gently heating samples is in general a good practice to remove surface impurities and is beneficial for good image quality, but the contrast degradation isn't reversible by further cleaning off surface adsorbates.

UV degradation

Having eliminated the essence of the biological samples, the instruments, and the surface properties from the sources of PEEM contrast degradation, we have narrowed down the possibility to constant exposure to the excitation source. One consistent phenomenon we have been seeing in every imaged section is the change in the color of the embedding medium for biological tissues, i.e. the epoxy resin. An example showing the color difference of the plastics before and after PEEM imaging is shown in Figure 6.16. Notice that here the embedded samples are HeLa cells for the comparison on the same sections, but the same observations also apply to the mouse brain samples, suggesting changes in the chemical and physical substances of the polymer.

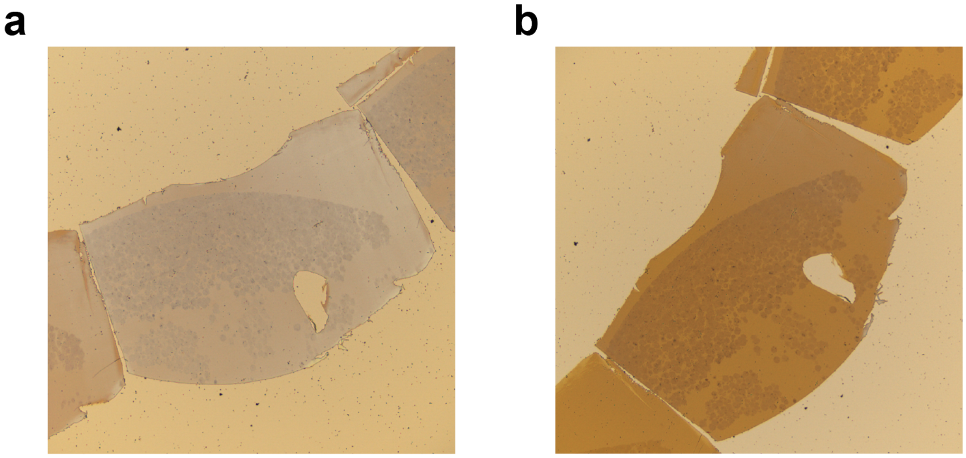

Figure 6.16: Discoloration of the epoxy resin from the same section. (a) Before UV exposure. (b) After UV exposure.

The embedding resin for preparing most mouse brain samples here is LX 112, a substitute for the classic EPON 812 formulation established by Lufts in 1961.[276]. The chemical nature of the embedding media is (poly-glycidyl) ether of glycerol, which essentially is a mixture of tri-glycidyl and di-glycidyl ethers of glycerol[277]. The chemical structure of tri-glycidyl of glycerol is illustrated in Figure 6.17. It is well known that polymer materials are vulnerable to UV radiation, a photodegradation effect where UV light produces free radicals in the polymer matrix which initiates chain reactions and can eventually break polymer bonding.[267,278–280] Epoxy polymers, as well as other categories of polymers such as polystyrene (PS), have been repeatedly reported to undergo rapid yellowing upon exposure to UV light, which is consistent with our observations. Over prolonged exposure, irreversible deterioration of mechanical properties occurs, leading to embrittlement of the materials, which we haven't necessarily experienced or been able to image in the PEEM experiments so far.

UV-vis spectroscopy was used to characterize the optical absorption properties of the pure resin samples, as well as the resin with embedded brain tissues as shown in Figure 6.17(b). Although the assignment for the transition isn't well interpreted given the heterogeneous system, the strong absorption around 230-240 nm overlaps with the spectrum of the Hg

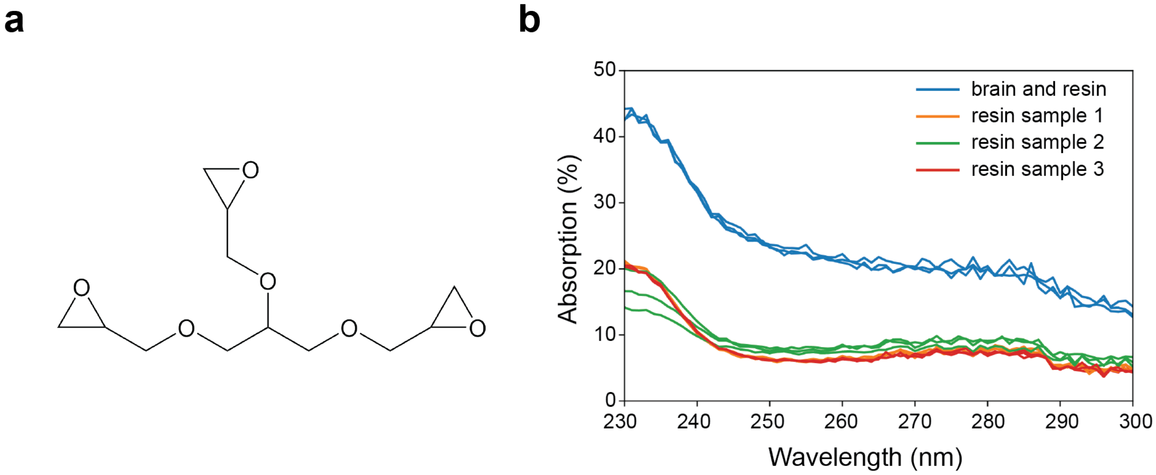

Figure 6.17: (a) Chemical structure of tri-glycidyl ether of glycerol. (b) The absorption spectra for multiple resin samples and resin with mouse brain.

lamp in the UV regime, indicating that UV light is effectively utilized for gradual chemical changes in the system and thus the photoemission behavior.

To establish a better correlation of how the degradation of the embedding media affects the PEEM image quality, we used a UV lamp to illuminate the mouse brain section outside the PEEM chamber to intentionally degrade the polymers and check the PEEM images after the damage. Figure 6.18(a) shows a photograph of the setup for the test experiment. Optical microscopy was employed to monitor the color change of the resin. The Hg lamp is the same one that was used for imaging in the ELMITEC system, where the housing in the current tests is elevated to couple the beam into the microscope. A cube beamsplitter was installed to deflect the incoming UV beam vertically down onto the sample surface. An LED white light source was originally installed from the back of the microscope body to provide wide-field illumination. Both the reflected UV light and the LED light are collected in the upright direction by a CMOS camera (Amscope). Admittedly, there are several flaws in the design of the test experiments. First, a UV-grade beamsplitter was unfortunately not available at the point of the experiments. As a consequence, the ~1.8 W incoming beam is severely cut to only about 30 mW before the sample is, significantly reducing the resemblance to the real PEEM imaging situation. Second, the focusing conditions are not consistent in both scenarios. A 150 mm uncoated concave lens (Thorlabs) focuses the UV beam onto the sample on the PEEM manipulator and the illumination area covers the entire chip (a circular opening with ∼7 mm diameter). In the optical microscope setup, the utilization of a 20x objective (NA 0.25) focuses the beam much higher. Figure 6.18(b) depicts the Hg lamp beam profile captured by the optical system, where the beam adopts a donut shape with the most intense center of ∼50 μm in diameter. Third, despite the much-decreased power, the UV light still almost saturates the camera dynamics limit even at the lowest exposure time. Ideally, a UV filter should be installed to remove the lamp contribution in the optical image to achieve better visualization of the sample. However, instead, a neutral-density (ND, optical density=2) filter is inserted before the camera to reduce the intensity of both the UV and the white light. By adjusting the image contrast, the areas that are illuminated can be seen better, such as at the ring of the beam profile, but overall, live tracking the discoloration of the section remains difficult.

Two trials were carried out and videos of continuous illumination were recorded for one hour (ROI1) and three hours (ROI2) on two separate regions of a mouse brain section on a gold substrate. Figure 6.18(c) shows the two areas after UV radiation, where yellow ring patterns mirroring the beam profile appeared on both ROIs, and the regions that were away from the beam retained the same color. This result strongly suggests that even with relatively low power, UV light can create local damage to the epoxy resin within a short time frame.

We then used PEEM to check the image contrast of the discolored section, and we were able to locate the ROIs that correspond to the yellow areas. The PEEM images, however, didn't necessarily reflect the degraded ring shapes in the optical image, shown in Figure 6.19. Nevertheless, we found a great number of bright patches that weren't present in fresh samples showed up in the proximity of the directly exposed regions, which is similar to the brightening effect on previous samples where the entire surface was under wide-

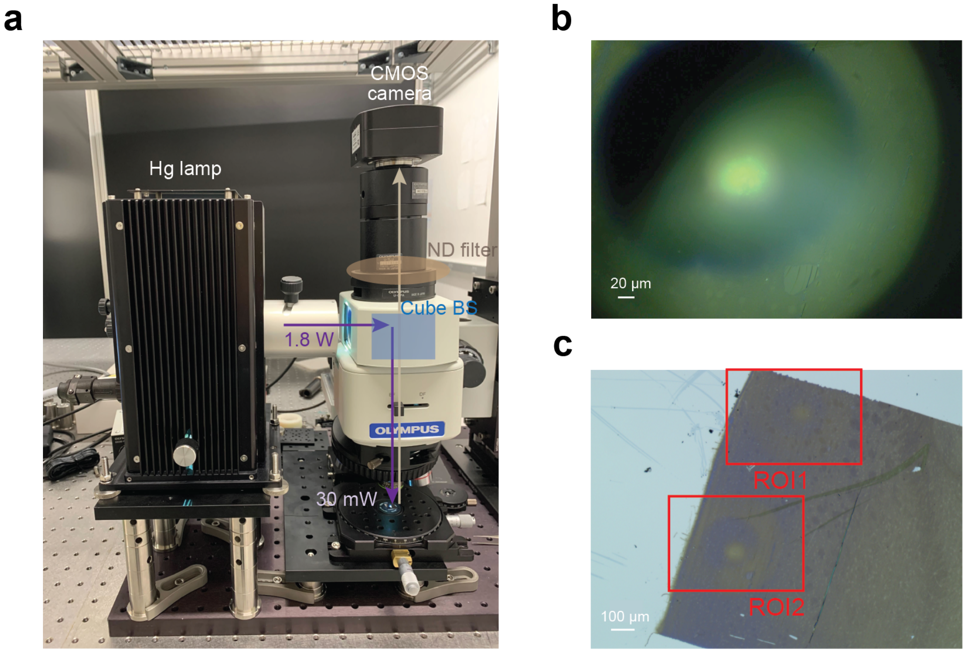

Figure 6.18: Test experiments for intentional degradation of the epoxy resin. (a) A photo of the microscope setup. BS: beamsplitter (b) An optical image of the Hg lamp beam profile with representative components labeled. (c) A 10x optical image of two areas after UV illumination for 1 hour and 3 hours, respectively.

field UV illumination in PEEM. The contrast in those patches is qualitatively lower than in the adjacent areas where the background is still dark. A possible explanation is that the *ex-situ* experiments only reached an intermediate state of the chemical reaction due to different fluence and illumination time, resulting in partial degradation in the PEEM image. Careful repeats with a modified experimental design are required to fully reveal targeted degradation. Regardless, the test results support the working hypothesis that irreversible photodegradation of the embedding material due to overexposure to UV light is likely to be the major source of the reduced PEEM contrast.

6.4.3 Mitigation of UV degradation

As this project focuses less on the exact mechanism of the polymer degradation process, we didn't survey the full characterizations of the epoxy resin regarding changes in chemical bonds or mechanical performances. Rather, we explicitly invested in ways to mitigate the

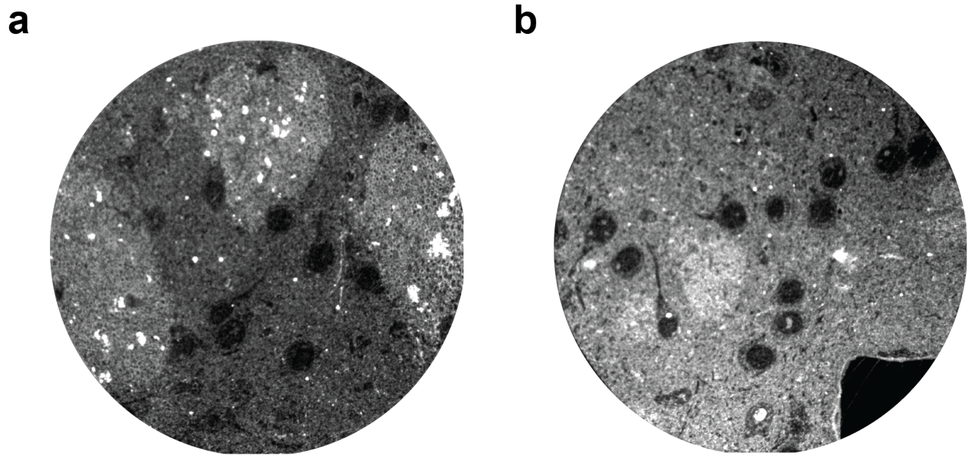

Figure 6.19: PEEM images of the intentionally degraded section. (a) ROI1. (b) ROI2.

light-induced polymer damage aiming to lengthen the PEEM imaging lifespan for biological samples that are fabricated with the same embedding technique. Several aspects of mitigation strategy are discussed here, including chemical modifications on the sample or re-design of the instrumentation, to slow down or eventually prevent the degradation process. While most approaches proved to be unsatisfying, some methods have shown improved sample performance, inspiring future exploration to ultimately overcome the light instability issue.

UV stabilizers

The first attempt to address the UV stability problem is to use chemical designs to interrupt the reactions that could lead to polymer decomposition. We first tried switching to a type of UV-curable resin as the embedding material that has been reported to show more robustness against UV irradiation.[281] The imaging results showed promises, where clear image contrast lasted for over an hour, a minor extension of the imaging lifespan, although the image quality still underwent noticeable degradation over the course of 2-3 hours of continuous illumination. The same section was left in the vacuum chamber overnight and imaged again the next day, the sharp feature didn't recover, implying that UV light is detrimental to the UV-cured resin. The comparison of the fresh image and the day after is displayed in Figure 6.20(a). The curing, i.e. the solidification process of polymer utilizing

UV light is often based on the principle that the absorption of the UV photon initiates the chain reaction in the polymeric system which usually happens rather rapidly.[282] However, the curing process will stop once there is no photoactive monomer left and the role of an initiator doesn't necessarily indicate that UV light is non-destructive on the chemical bonds, and the kinetics of photodegradation depends on the spectrum, intensity, and the illumination period. In the case of PEEM imaging, the consistent contrast decay pattern suggests that the putative UV stability of the new resin imposes a positive effect but overall cannot survive the required imaging condition.

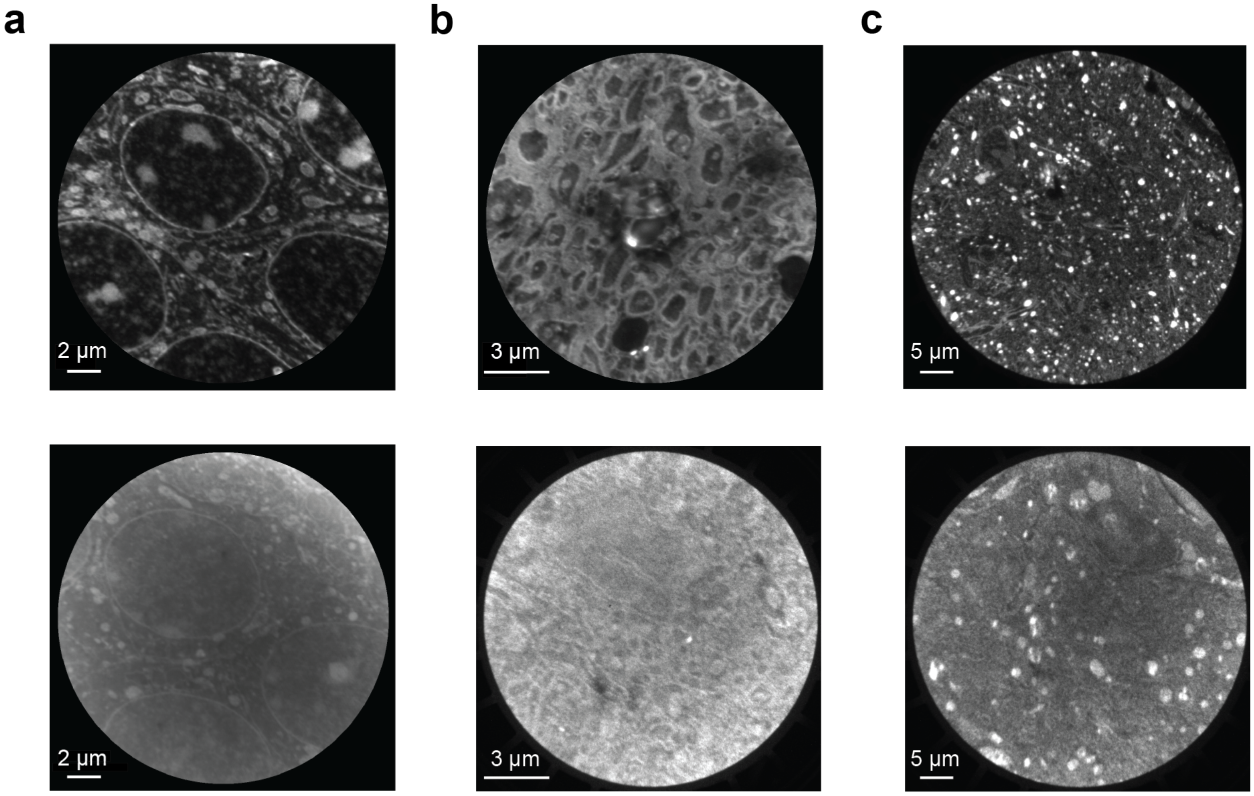

Figure 6.20: Comparisons of PEEM images before and after UV exposure. Top: images that are collected within the first 20 minutes of Hg lamp illumination. Bottom: images of the same sections with degraded contrast. (a) Using UV-curable resin as the embedding medium. (b) Adding free radical scavenger TEMPO in the resin. (c) Adding free radical scavenger in the staining solutions.

Other developments to reduce the photodamage of polymers involve using UV stabilizer additives in the polymer matrices with varying stabilization mechanisms. We have adopted two frequently used strategies here: one is using free radical scavengers, which function by interfering with the propagation step in the oxidative chain.[280] 2,2,6,6-tetramethylpiperidinyloxy, commonly known as TEMPO, was added to the formulation of the resin during the embedding process. TEMPO has been found to be useful in trapping free radicals and reactive intermediates.[283] Despite the potential utility, the first issue that came along is that the addition of the compound significantly altered the physical properties of the resin and it became difficult to cut for a smooth surface from the polymer block. Consequently, chatters (vibrations during ultramicrotoming) and wrinkles persisted on the ultra-thin sections, lowering the initial image quality. In terms of photostability, we were able to observe that the top graph in Figure 6.20 faded into the bottom image with extremely faint contrast in about 30 minutes, showing little to no effect in stabilizing the image for a longer time frame.

The second method is to use a UV absorber to prevent the UV light from reaching the bulk of polymers and thus delay the bond-breaking reactions.[280] In this case, tannic acid, with a strong absorption in 240-320 nm,[284] was added to the staining reagents. In addition, tannic acid was once used as a stain for enhancing the contrast of subunit structures in cells (such as microtubules and collagen) in SEM in the last century, despite that this compound is no longer popular among modern staining techniques.[285–287] The as-image brain tissue is shown on the top panel of Figure 6.20(c). On top of the regular contrasted membrane structures, additional extraordinarily bright spots appear inside the neural cells. The existence of those spots aligns with our understanding of the properties of tannic acid. First, the resonance excitation in the UV region causes strong photoemission processes. Second, tannic acid tends to certain stain subcellular components. However, this observation also indicates that the UV absorber is not distributed fully within the brain sample due to selective binding, and therefore the protection of the fragile polymer is limited. As anticipated, we observed drastic changes in image contrast after about 35 minutes, again failing to improve the long-lasting performance of the embedded brain samples.

In summary, chemical modifications of sample preparation provide versatile pathways for UV protection of epoxy resin, but the impacts of the additives on the embedding quality and image characteristics need to be taken into careful account.

Cold experiments

Another intuitive step to consider for slowing down chemical relations is to image the biosamples at low temperatures. The FOCUS PEEM system is incorporated with a liquid nitrogen (LN2) cryostat to allow experiments at a wide range of temperatures *in situ*. We were able to image the mouse brain sections, prepared with regular protocols with no additives, at a stable temperature of around 140 K on multiple sets of samples. It is not of surprise that the decay rate of image contrast is decelerated in a cold environment, but at the same time, we have observed variability in the effective imaging time from sample to sample, ranging from over 2 hours to 40 minutes. We believe that in general, cooling is a good way to stabilize the resin, which not only reduces the reaction rate but also diminishes the thermal effect upon light illumination, but phenomenologically it can't consistently acquire sufficient imaging time for serial imaging, and adds experimental complexity.

Excitation sources

Since UV light has been the major concern of the degradation issue, we naturally raised the question of whether we can manipulate the light source for photoemission to achieve similarly high, but more stable, image contrast. An observation that supports this hypothesis is that we have realized the average imaging time is longer in the ELMITEC systems than in the FOCUS system. Given the Hg lamps for both PEEMs share the bulb of the same specifications (Osram HBO 103W/2), the primary differences in the illumination are the power and the focusing condition of the UV light, hence the fluence. This tracks with the fact that the photoemission counts are indeed higher in the FOCUS PEEM. In theory, if we can maintain good S/N for resolution optimization, lowering the fluence by reducing the power or loosely focusing the beam on the sample should extend the useful imaging time.

Furthermore, we considered testing wavelength-dependent image behavior. Since the Hg lamp spectrum is broadband, we employed an ultrafast laser (Class 5 Photonics, 4 MHz) with adjustable photon energies that can be coupled into the PEEM chamber for excitation. Either UV or visible excitation was utilized to test the capability of laser imaging and the pulse durations were not characterized. We could hardly observe any features except for surface contamination when we imaged with 266 nm (4.67 eV) regardless of laser power, and the overall S/N is extremely low (Figure 6.21(a)). Power series implies that the photoemission intensity excited with 266 nm follows a linear trend with laser fluence, indicating 4.67 eV barely reaches the work function of the bio-section and higher photo energies are required for efficient photoemission. At a shorter wavelength of 244 nm (5.08 eV) excitation (fluence $\sim$1.78 nJ/cm^2), we were able to resolve the contours of the stained membranes with good one-on-one correspondence with the same ROI under Hg lamp illumination, see Figure 6.21(b). We further tested PEEM imaging by using a 400 nm (3.10 eV) beam, which is known to be under the work function limit and should follow a two-photon process to generate photoelectrons. Interestingly, we not only saw good contrast with features well matched with the Hg lamp image, but the contrast was inverted, where the membranes with osmium stains were dark and the unstained areas turned out to be bright, as illustrated in Figure 6.21(c). A possible explanation is that the 400 nm light resonantly excited certain components in the stain-free regions, leading to strong enhancement in photoemission, whereas osmium compounds don't have an intermediate state upon excitation of visible light, and thus the photoemission yield is poor. Nevertheless, the success of laser imaging on resin-embedded mouse brain tissues opens up the possibility of manipulating light to reduce possible photodamage on the epoxy.

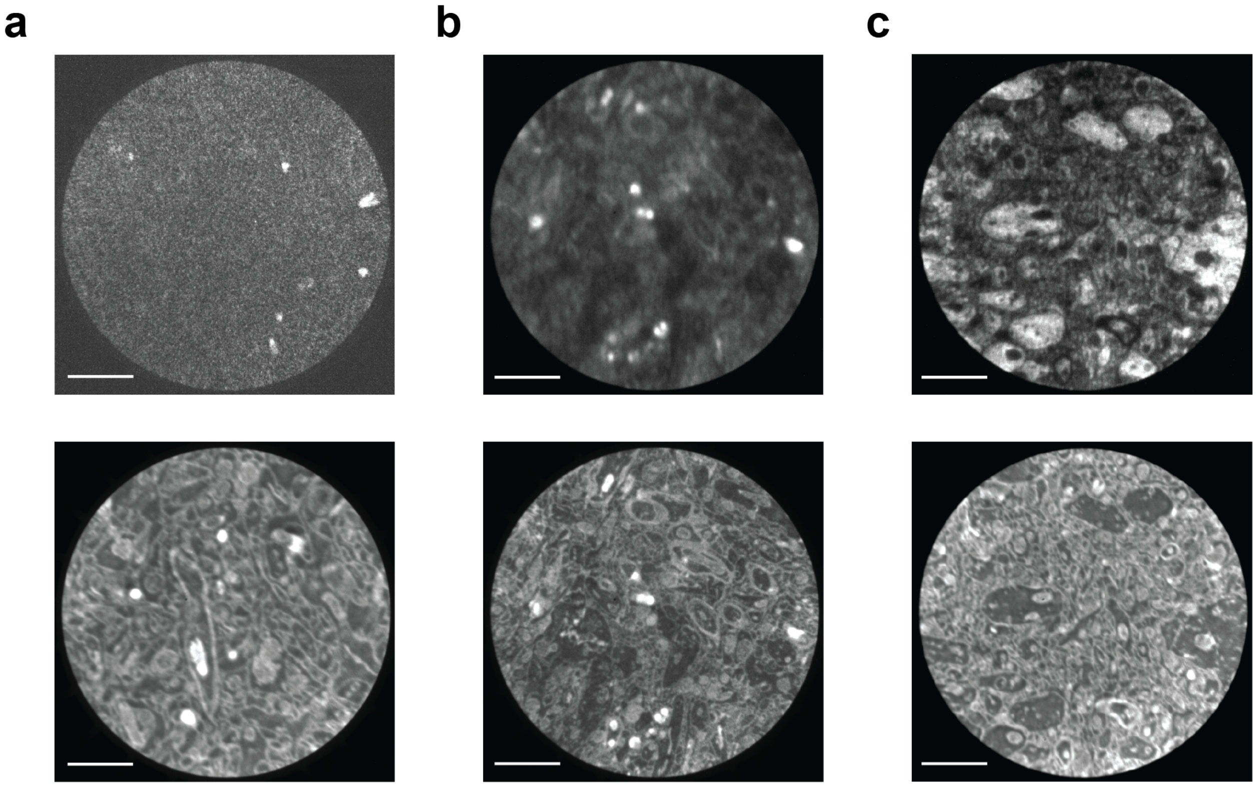

Figure 6.21: Laser imaging of mouse brain samples with varying wavelengths (top) and the comparison of the same ROIs imaged with Hg lamp (bottom). (a) 266 nm (4.67 eV). (b) 244 nm (5.08 eV). (c) 400 nm (3.10 eV). Scale bars are 3μm

6.4.4 Conclusion

We introduce a persisting contrast degradation issue during PEEM imaging of osmium-stained, resin-encapsulated, and thin-sliced mouse brain samples, which have hindered the progress of continuous imaging on the same sample. Efforts towards tracing down the source of the degradation have been made by systematically investigating variables that might have impacted the image quality. Although most controls including the biological samples, the instruments, and the surface properties, don't make a significant difference in the effective imaging time, UV-induced degradation in the embedding media shows evidence of modifications on the chemical substances of the biological sections and thus influences the photoemission response. We survey mitigation strategies to reduce UV damage by chemically modifying the embedding polymer, slowing down the reactions at cold temperatures, or circumventing UV exposure. We show that even though the physics process involving multi-photon photoemission of the osmium-stained specimen requires further fundamental understanding, the employment of a tunable laser excitation source has great potential in preserving high-quality mouse brain images in the long term.

CHAPTER 7

PEEM WITH BRIGHT FUTURE - ONGOING EXPERIMENTS AND FUTURE DIRECTIONS

7.1 Overview

In this chapter, we will discuss the preliminary work we have done in expanding the imaging capabilities of PEEM in complex heterogeneous samples, materials or biological samples, to realize more practical goals. Specifically, we will discuss how PEEM can be beneficial for two schemes of intentional modifications to improve material functionalities. In addition, we will further demonstrate the potential of PEEM for nanoscale 3D image reconstruction in biological as well as inorganic materials. We will examine the limitations that we have experienced and suggest future steps for experimental improvements and data interpretation.

7.2 Towards modular tuning of 2D materials functionalities

With the understanding of material morphology-property correlation, numerous opportunities remain to be explored for intentional modifications of material properties including defect engineering, modulated carrier mobility and guided charge transport. Ultimately, we can think of incorporating the desired properties into functional devices to fully embrace the technological potential of van der Waals layered materials.

7.2.1 Resolving energy landscape in strained 2D hybrids

We have established that PEEM is capable of routinely resolving nanoscale domains in anisotropic systems such as 2D black phosphorus. Furthermore, we demonstrate that PEEM is an excellent tool to study the spatially-dependent electronic structure of an organic-inorganic heterostructure. An attractive direction of PEEM application is to investigate intentionally designed hybrid systems that are subject to modifications in the dielectric environment, which usually result in tailored optical and electrical properties.

Many accessible variables can be the tuning knobs for functional 2D materials, including chemical modification,[288,289] vdW stack integration,[290,291] as well as rotational alignment.[292] In particular, 2D materials typically have flexible mechanical properties and are subject to in-plane strain which modifies their electronic structure and can fundamentally tune their physical properties.[293–296] Despite the surging investigations using macroscopic force to deform 2D sheets, here we have explored the approach of using photoswitchable molecular thin films via van der Waals interactions to achieve nanoscale strain engineering. Specifically, photochromic molecules such as spiropyran (SP) isomerizes reversibly between open and closed ring formations upon exposure to specific wavelengths of light. SP molecules can form self-assembled monolayers (SAM) on 2D material surface and the ring-opening process to MC is proposed to induce an out-of-plane dipole moment creating an interfacial dipole at the 2D material interface (Figure 7.1(a)).[297] The molecular deformation generates mechanical force to the adjacent materials, and this strain effect has been used for nanoscale mechanical control of strain-induced disassembly of nanotubules.[298,299] However, whether the mechanical strain can be transferred to a 2D material underneath the molecular film, and the mechanism of how the light-induced surface modifications alter the electronic structure of 2D materials remain open questions.

We can use PEEM to directly probe the electronic structure landscape of the coupled molecular-2D sample and study modifications on charge carrier dynamics upon the molecular switch. We have conducted preliminary experiments by fabricating SP thin films and characterizing the photoswitching behavior on the surface. SP solution was spin-coated on a quartz substrate with an optimized recipe to form relatively uniform molecular films. Based on the molecular absorption, we used a 365 nm LED light (Thorlabs) to photoswitch the molecular film. The static UV-vis absorption spectra before and after 10 minutes of UV exposure were shown in Figure 7.1(b) (measured by Shimadzu 3600). Clear peak shifting in the UV region can be observed in the photo-induced product, and there is an emerging peak at around 580 nm, confirming the presence of merocyanine.[297].

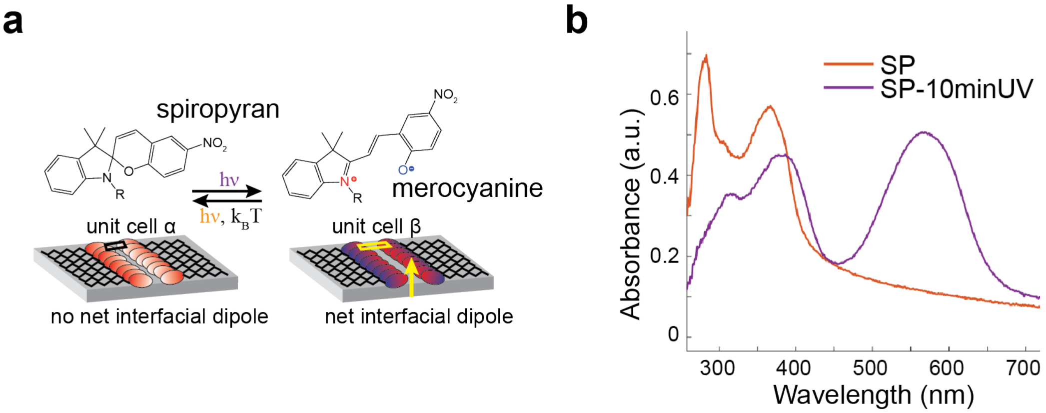

Figure 7.1: (a) A schematic showing that spiropyran molecules undergo reversible structural change to merocyanine upon light irradiation or heating/cooling and modify surface dipole. (b) UV-vis absorption spectra of SP film on quartz before and after UV illumination.

Although we have not actively integrated the molecular film on 2D materials, future efforts can be foreseen in implementing the nanoscale strain tuning on a prototypical sample such as graphene, as the strain-induced effects have been well replicated and extensively characterized using various techniques including photoluminescence microscopy, Raman spectroscopy and electrical measurements.[96,300–302] Strain-induced electronic structure modifications of 2D layers are expected to produce different contrasts in the PEEM images. However, to understand the relative contribution of strain effects in contrast to interfacial dipoles, it is necessary to create a consistent approach to quantifying the amount of mechanical force transferred from the molecular film to the underneath 2D layers. The ability to control and manipulate the electronic structure of 2D materials will ultimately improve the engineering efficiency to realize programmable and adaptive functionalities in van der Waals heterostructures.

7.2.2 Imaging quantum phenomena in strongly coupled systems

Layered materials provide a confined 2D space to suppress electromagnetic fields. Subsequent quantum effects such as strong coupling between light and electronic transition in materials, also known as polaritons, can be used to manipulate charge carrier dynamics on the nanoscale. The use of interferometric time-resolved photoemission electron microscopy (ITR-PEEM) has been a mature field since about 20 years ago, and this technique has achieved remarkable advancements in studying surface plasmon polaritons in plasmonic metal or nanostructures. Plasmons are a collective oscillation of free electrons in a solid-state system, and the plasmonic field can selectively couple to light based on the geometric arrangements of the metal structure or the light polarization. When an ultrafast pulse incidents on a plasmonic surface, the interference of light and the plasmonic wave results in constructive and destructive phase modulation of the optical field, and thus the propagation of the surface plasmon can be visualized as bright and dark fringes in PEEM images.[57,303,304]

In the past, we have consistently observed the fringe patterns in static PEEM images of a BP flake deposited on a polycrystalline graphene substrate (on 300 nm SiO_2/Si) upon pulsed laser excitation. Figure 7.2(a) shows an optical image of a representative BP flake. Based on the optical contrast and transparency (see Section 3.3.1), we estimate that the bottom right corner (light blue) is thinner than the flake body (opaque white). The same flake was imaged in PEEM with 515 nm (Figure 7.2(b)(d)) and 800 nm (7.2(c)(e)) pulsed laser at two perpendicularly in-plane polarizations.

We have shown in Chapter 4 that BP on Si substrate strongly photoemits upon 515 nm photoexcitation, and exhibits intensity modulation upon polarization rotation. Contrary to previous observations, the bulkier flake body appears dark regardless of the light polarization, indicating very weak photoemission responses, whereas the thinner corner shows more photoemission intensity that is polarization-dependent. The thickness-dependent photoemission is evident in the modifications to the electronic structure of BP by a metallic substrate, where the thick BP could be excited to a non-resonant virtual intermediate state that significantly reduces the photoionized electrons. In addition, interferometric patterns can be found in both the bright BP portion as well as on the graphene substrate. The fringes are predominantly aligned along the flake edges and with the light polarization. In contrast, PEEM images excited by the 800 nm beam have a drastically different appearance. The entire BP flake shows strong photoemission signals compared to graphene, despite a crack feature emerging across the flake body, which is surprisingly not observable in the optical image. In either polarization, the PEEM images show strong modulating intensities, and the fringes propagate further into both materials, making it difficult to precisely determine the flake edges. Similarly, the fringes are primarily launched from the flake edges, and interference is stronger at the aligned light polarization.

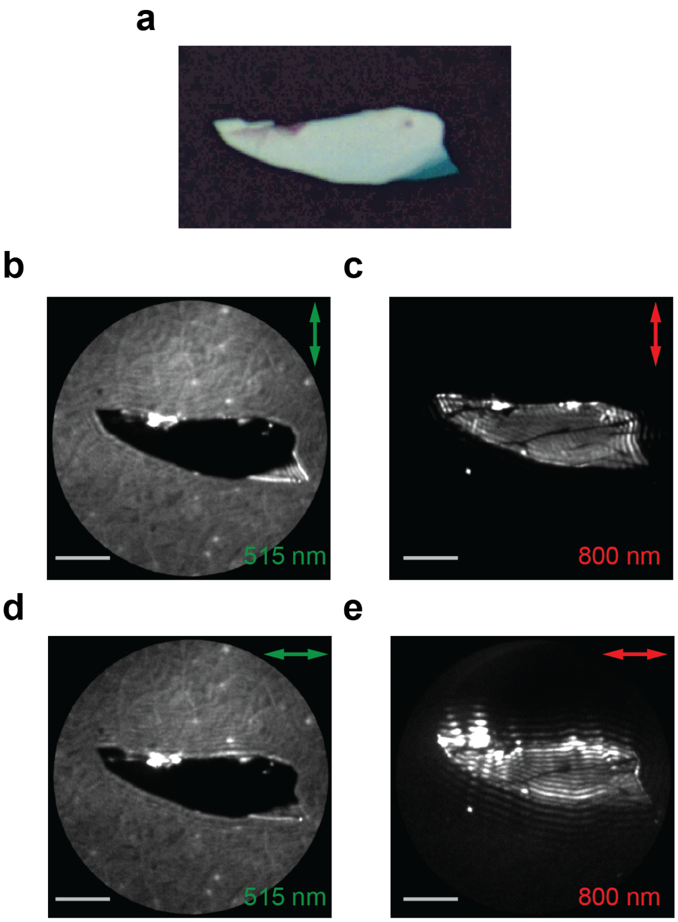

Figure 7.2: (a) An optical image of a BP flake on a polycrystalline graphene substrate. (b)(d) PEEM images of the same flake with 515 nm illumination at two perpendicular light polarizations. (c)(e) PEEM images of the same flake with 800 nm illumination at two perpendicular light polarizations, showing significant enhancements of the fringes.

It is unclear whether the observed features are indeed plasmonic responses, and further experiments and theory modeling are required to understand the physical nature of the fringes. However, this experimental result suggests the potential of expanding the sample library for interferometric PEEM imaging which has been mostly restricted to nanostructured metals.[133] 2D materials or heterostructures that exhibit light-induced plasmonic effects in principle should be captured similarly with PEEM. It would be interesting to explore the interference patterns in terms of excitation wavelength, light polarization as well as the shape of the nanoflakes. The analysis of intensity amplitudes, propagation lengths, and phase separation in different dielectric environments can provide further information on the relationship between sample morphology and the coupling strength of light and matter, if there is any. Moreover, time-resolved experiments could be performed to capture the dynamics of the wave propagation, which will reveal charge transport processes in composite nanomaterials. This research direction will uncover the correlation of the sample geometry with hybrid light-matter interactions, and improve efficient energy generation and energy use in photocatalysis, photovoltaics, and light-emitting devices.

7.3 Development of ultramicrotomed samples for PEEM imaging

We have demonstrated in Chapter 6 that PEEM provides a rapid and reliable opportunity for imaging ultra-thin sections of mouse brain tissue with synaptic resolution. Here, we aim to extend the use case of the technique of ultramicrotome to create a broader range of thin-sliced systems that will benefit from a fast reconstruction of 3D tomography on the nanoscale, ranging from biological systems to inorganic nanoparticles.

7.3.1 PEEM imaging of cellular systems

Having understood the mechanism of why heavy metal-stained biological samples produce contrast in PEEM, we can modify the chemical composites of the samples to achieve more targeted imaging. As a proof of principle, we made attempts to imagine a sample of a HeLa cell embedded with Si nanowires (NW). Utilizing the difference both in work function difference and the density of states, we expect a clear intensity variation between the biological tissues and the silicon. The ability to resolve the contrast between soft organic and hard inorganic materials allows for studying the integration mechanism, which sets the basis for biointerface engineering.

PEEM imaging of unstained cells

The Si NW intercalated HeLa cells were grown by the Tian lab at UChicago. and the protocol can be found in the reference.[305] The preparation for ultramicrotoming the cell samples is as follows:

The as-grown cells are collected from Petri dishes and are centrifuged to form a pellet at the bottom of a centrifuge tube. The pellet is first dehydrated at room temperature in ethanol (EtOH) for about 20 minutes. Then ethanol is removed. For the EPON resin (EMbed 812 Kit, Electron Microscopy Sciences) infiltration process, increasing ratios of EPON/EtOH are added to the dehydrated cell pellet in a sequence of 25% EPON / 75% EtOH, 50% EPON/50% EtOH, 75% EPON/25% EtOH for 24 h each. Notice that in each solution removal process, the cells can disperse into the bulk solution which leads to disaggregation of the cell pellet. At last, the cell pellet is soaked in 100% EPON for 3-4 h. Then remove all EPON in the centrifuge tube. The cell pellet is transferred to a tip-end capsule (Ted Pella) as a mold and filled with EPON. The resin is cured at 60° for at least 48 hours until it is solidified. Longer hours may be required if the resin isn't cured sufficiently.

The resin-embedded cell pellet is cut into 80-100 nm thick slices using an ultramicrotome and the thin layers are picked up on Au-coated silicon substrates, a similar preparation process to mouse brain tissues.

The resulting samples on substrates are imaged in the FOCUS PEEM by a Hg lamp, and an example is shown in Figure 7.3(a). A roughly circular shape can be seen at the right side of the ROI that corresponds to a HeLa cell. Due to the inexperienced biological handling process, the cells are likely already broken during the embedding process, and thus

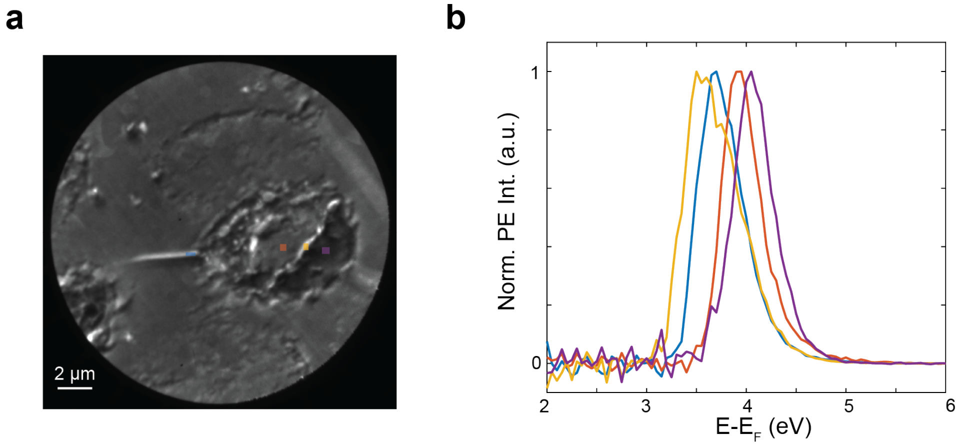

Figure 7.3: (a) PEEM image of the unstained HeLa cell + SiNW. (b) Different spectra of four corresponding ROIs marked in (a), showing different secondary edges.

the image doesn't show a complete regular periphery. The overall contrast is significantly different from the Si substrate. This is because the unstained cell and its organelles have a low electron density of states around the Fermi level, as illustrated in Chapter 6 section xxx [insert reference]. In addition, we also noticed that there are a sharp horizontal feature as well as sparse bright spots around the cells, which could be silicon wires that distribute in random directions in the cell systems. The long sharp stick could be a nanowire cut that was cut completely within a thin section, whereas the bright spots could be nanowires that were cut into cross sections.

We further performed energy-resolved PEEM imaging and measured the photoemission spectra of four areas with varying photoemission intensities, shown in Figure 7.3(b). The secondary edges, representing the work function of the surface, show clear differences. The higher the PE intensity, the lower the work function is, indicating that the contrast results from differences in chemical components rather than the density of states. The reason why the possible Si NW features have enhanced PE intensity from the Si substrate is possibly due to a thin layer of native oxides that cover the bare Si substrate. Although a high-resolution image of the HeLa cell is not obtained from the unstained procedure, the preliminary results show that PEEM has the potential to directly distinguish biointerfaces from inorganic materials.

PEEM imaging of Os-stained cells

To enhance the contrast from cellular structures, we adopt the osmium staining protocol similar to that for mouse brain tissues to incorporate heavy metals in the same HeLa cell + Si NW samples. The cell pellet is obtained using a centrifuge as described above. The staining process is as follows:[226]

The cell pellet is first soaked in 2% OsO_4 aqueous solution for 1 hour. Then remove osmium, and add 2.5% potassium ferrocyanide for 1 hour. Next, remove potassium and add 4% pyrogallol (320 mM) aqueous solution for another hour. Wash the cell with fresh Milli-Q water twice and for 30 minutes each time. Then add 2% OoS_4 solution for 1 hour for the second round of staining. Finally, wash the sample with Milli-Q water twice again and for 30 minutes each time. Note that OsO_4 solution is highly volatile and toxic, so the operations MUST be carefully conducted in a well-ventilated fume hood. After staining, the osmium solution MUST be properly disposed of by the regulations of EHS. All staining process is conducted at room temperature.

The infiltration and ultramicrotome procedures are the same as the unstained cell samples. Lastly, the thinly sliced sections are picked up on Au-coated silicon substrates with thicknesses of approximately 60, 80, and 100 nm.

We imaged the stained samples again using the Hg lamp in the FOCUS PEEM column. Figure 7.4(a) shows an image that demonstrates a higher contrast cell feature. where the cell membranes can be easily recognized as circular lines. It is less clear what the clusters at the outside of the cell membranes are and more biological knowledge would be required for more accurate assignment of the structures. Similar to the observation in Figure 7.3(a), we observe bright, scattered spots around the cell membranes, particularly at the clustering regions. The spots could potentially be cross-sections of the SiNWs. However, the stained cell samples suffered from contrast degradation issues, similar to the effect described in

Section 6.4, that forbids a long scan for energy-resolved imaging. The three images in Figure 7.4 demonstrate the rapid change in the image contrast. The first one is an image of a sample freshly transferred into the PEEM column. In about 10 minutes of UV lamp illumination, the overall intensity of the FoV increases drastically, and the cell features are nearly buried in the background. Interestingly, the contrast between the biological tissues and the substrate reverses after about one hour of continuous imaging (Figure 7.4(c)), where not only the stained lipid membranes but also the cell bodies become much darker compared to the background, suggesting possible modifications in the chemical composites.

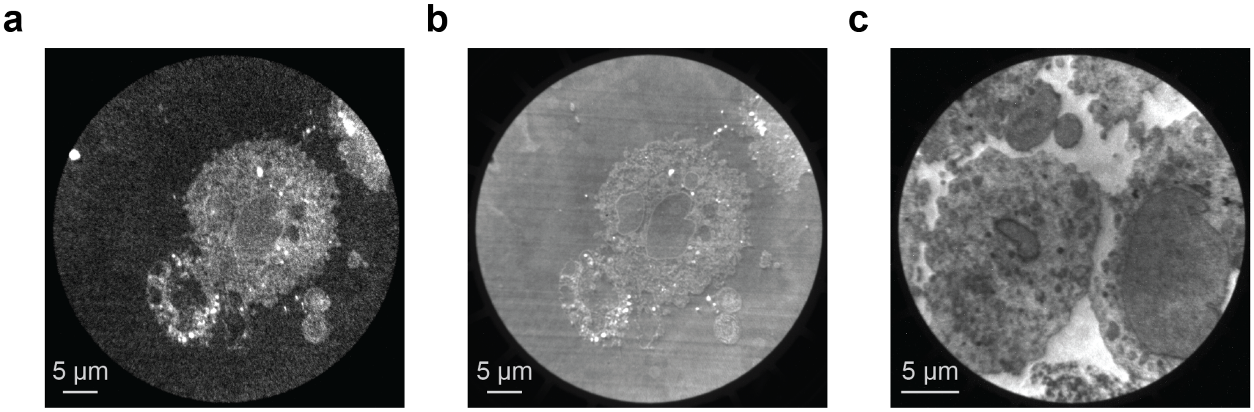

Figure 7.4: PEEM image evolution of the stained HeLa cell + SiNW. (a) Fresh image. (b) Image after 10 minutes of illumination. (c) Image after 1 hour of illumination.

It is unclear what are the causes of the contrast difference over such a short period of time. Possible reasons could be the imperfect biological sample preparation, or the fast UV degradation due to the choice of embedding media, as has been discussed in Section 6.4.2. Additionally, the as-cut cell samples could not be consistently imaged in the FOCUS PEEM due to charging, indicating that more cares are needed to ensure a clean and flat sample surface.

Overall, the imaging tests on a model system consisting of SiNW intercalated HeLa cells prove PEEM is capable of resolving biological samples other than mouse brain tissue. With higher-quality biological sample handling and optimized protocols for ultramicrotomy, we believe that PEEM has great potential in high-speed, wide-field, and high-resolution biological imaging of a broad range of composite samples.

7.3.2 Electrochemical materials

The development of lithium-ion batteries has tremendously grown in the past decades due to the increasing demand for electric vehicles, portable electronics, and stationary energy storage.[306] Understanding how different cations of the battery materials are combined and phase segregate as a function of electrochemical performance is the key aspect for high Li to Na selectivity, particularly in the case of the intercalation of different cations and transition metals in transition metal oxide nanoparticles. Here, we use cobalt oxide nanoparticles, consisting of a Li-rich core, and a Na-rich shell, as a proof-of-principle sample to demonstrate PEEM is able to distinguish different ionic species at the interface based on electronic structure variations. In addition, we aim to provide a new opportunity to more efficiently create cross-sections of the nanoparticles via ultramicrotomy compared to the traditional focused ion beam (FIB) milling. Eventually, we expect to achieve the reconstruction of a full 3D distribution of cation and transition metal species within inorganic nanoparticles.

Cobalt oxide nanoparticles by FIB milling

We made initial attempts at PEEM imaging of the cobalt oxide nanoparticles by using samples that were thinly cut with the convectional FIB milling method. FIB milling is a technique that utilizes charged particles, typically gallium (Ga) ions, to strike a sample and sputter atoms to etch or machine the surface.[307] The sample preparation procedure has been described in previous work.[306] The SEM image in Figure 7.5(a) shows the layered cobalt oxide after ion exchange before FIB milling. The size of the nanoparticles ranges from 5 to 20 μm in diameter. Furthermore, the X-ray diffraction (XRD, Figure 7.5(b)) confirmed a phase mixture of $\mathrm{Li}_0 \cdot 94\,\mathrm{CoO}_2$Li0.94CoO2 and $\mathrm{Na}_0 \cdot 51\,\mathrm{CoO}_2$. At the current vacancy level, we expect a composition of $\mathrm{Li}_0 \cdot 42\,\mathrm{Na}_0 \cdot 28\,\mathrm{CoO}_2$. We selected a particle with ~12 um diameter for the FIB lift out. The selected region is a cross-section lamella from the center of a particle. The particle was carefully milled such that a few nanometers of roughness was achieved.

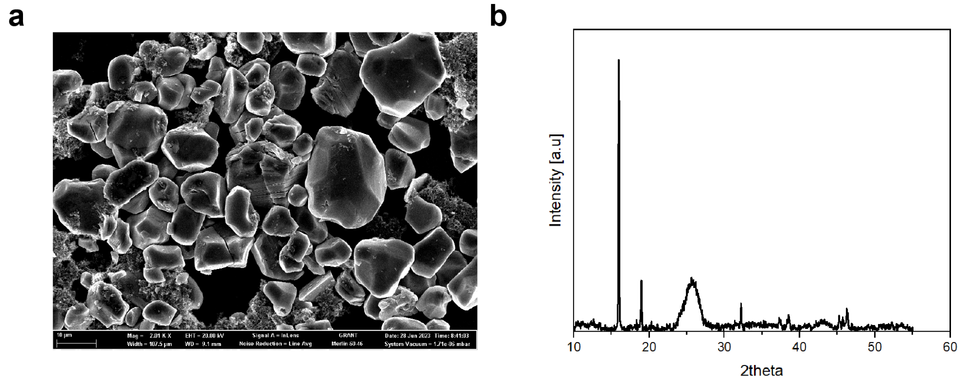

Figure 7.5: Characterizations of the layered cobalt oxide nanocrystals after ion exchange before FIB milling. (a) SEM image. (b) X-ray diffraction (XRD).

The FIB-milled nanoparticle was transferred onto a 7×7 mm^2 Si(111) substrate, and the sample was then imaged in the FOCUS PEEM system using the Hg lamp. A rectangular area is easily located as a mark for the target sample due to continuous electron beam damage during SEM imaging, shown in Figure 7.6(a). Three features are identified within the rectangle: the bottom rectangle is the FIB-thinned sample. The material above is a piece of carbon from the coating process, and the lamella-shaped feature at the top is a cut in the Si. During the imaging process, no sample charging or arcing was observed, and the imaging condition was rather stable, indicating the surface cleanness and flatness were satisfactory for PEEM.

We zoomed in on the region of the milled particle with a FoV of 15 μm. With patience and attentive optimization, we were able to resolve layered features, with alternating bright and dark stripes, in the interior of the sample cross-section, as indicated in Figure 7.6(b). The left and top edges have much higher photoemission intensities, suggesting different chemical substances compared to the rest of the sample. Based on the materials involved in the FIB process, we attribute the bright edges to the carbon coating, which was used to protect the sample from gallium (Ga) damage during the FIB thinning process and to transfer the

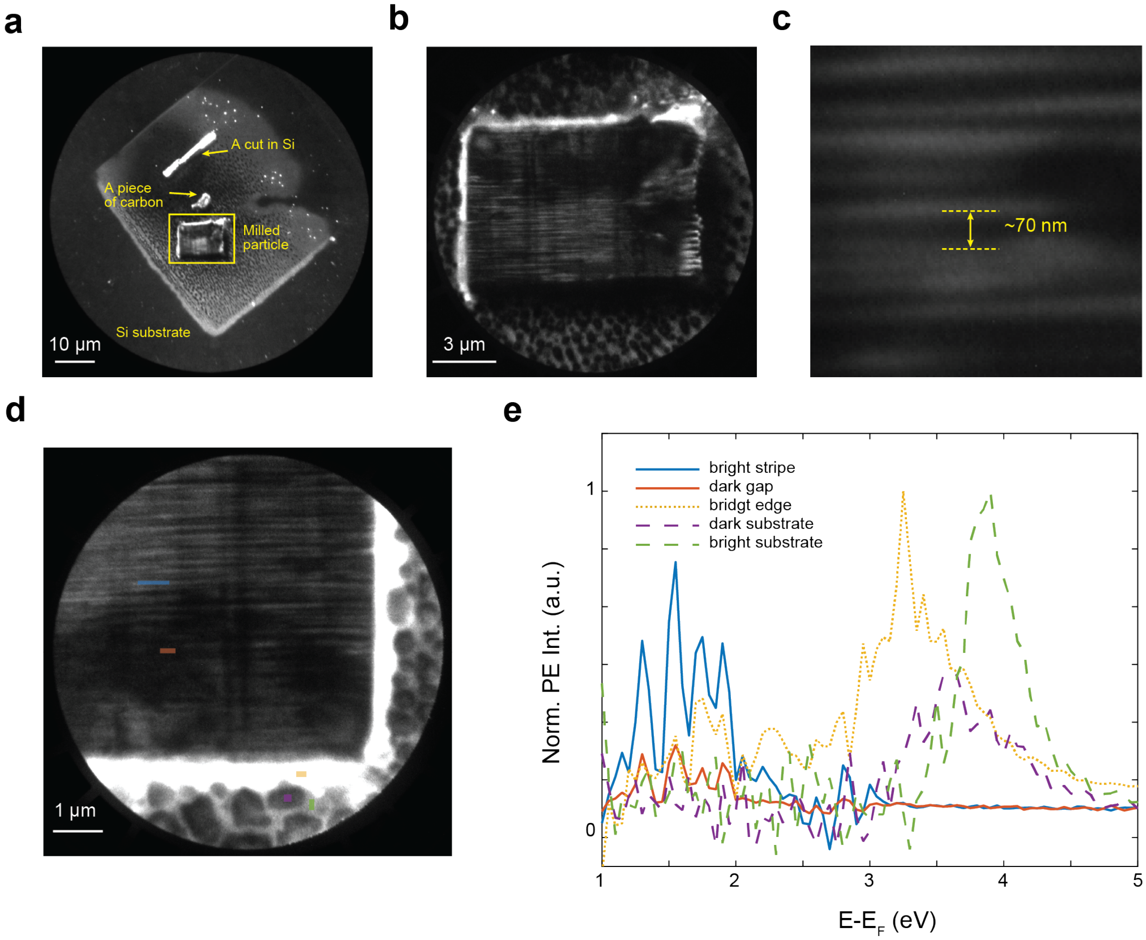

Figure 7.6: PEEM images of the FIB $Li_{0.42}Na_{0.28}CoO_2$ nanoparticles on bare Si susbstrate. (a) An overview of the sample area slightly damaged by the electron beam in SEM, recognized as a brighter rectangular feature due to raster scanning. Three clear features are identified where the milled nanoparticle is the rectangle at the bottom. (b) A zoom-in view of the milled sample, where an alternating layered feature was resolved in the interior. (c) High magnification image of the layers. The gap between the bright strips is around 70 nm. (d)(e) Spatially dependent photoemission spectra of multiple integrate areas boxed in (d), showing varying secondary edges and thus different work functions.

sample with the manipulator tip.

With further magnification of the stripy area, we were able to quantitatively measure the spacing between two bright lines as approximately 70 nm. This distance matches surprisingly well with the low-angle annular dark-field scanning transmission electron microscopy (LAADF-STEM) images in previous work.[306] LAADF STEM of the sample showing differences in the phase contrast in the material. The bright contrast regions had a high sodium (Na) composition according to elemental diffraction energy-dispersive X-ray spectroscopy (EDS) and the dark contrast had a high lithium (Li) composition according to electron energy loss spectroscopy (EELS). Each domain contains multiple layers of either high Li content ($\mathrm{Li_0 \cdot 94\,CoO_2}$) or high Na content ($\mathrm{Na_0 \cdot 51\,CoO_2}$). Thus, the 70 nm region of multiple layers of $\mathrm{Li_0 \cdot 94\,CoO_2}$ phase with multiple layers of Na0.51CoO2 above and below it (or vice versa). The LAADF image here shows that the spacing between domains can vary from ∼5 nm to >50 nm.

To get a better understanding of the elemental characteristics of the nanoparticle, we performed energy-resolved PEEM imaging and obtained energy distribution curves of five representative areas (annotated by different colors in Figure 7.6(d)): (1) a bright layer in the interior, (2) a dark layer in the interior, (3) a bright edge, (4) a darker area on the substrate, and (5) a brighter area on the substrate, and the resulting spectra are plotted in Figure 7.6. Despite the low S/N ratio that is improvable with more averages, the spectra have shown apparent distinctions, particularly the secondary edge cutoffs which reflect the work functions of the measured materials. We first observe the different line shapes of the bright and dark layers within the sample, showing a difference in the electronic structure. Although systematic investigations and repeats are needed for a fine conclusion, the preliminary result signifies great potential in PEEM for elemental characterizations with nanoscale resolution, which has proven to be powerful. We also notice that the spectrum of the edge has a broad line shape and its secondary edge is uniquely separated from the others. This corroborates the previous hypothesis that the bright edges are neither cobalt oxides nor part of the Si substrate. Moreover, the two areas selected from the substrate also show differences. The origin of the differences is not evident but it could be in part due to the SEM process where additional chemical species were introduced onto the substrate that led to the holey structure on the imaged area.

Although we have shown that PEEM has great promise in resolving elemental contrast with the requisite conditions for layered cobalt oxides, the biggest drawback is that the procedure for FIB milling and sample transfer is extremely tedious and inconsistent, which doesn't benefit long-term research that requires more accessible protocols. For example, we were not able to obtain images with a similar quality in the second trial. On the contrary, the second sample experienced charging issues and caused severe arcing that could be risky for the instrument. A more reliable sample preparation method is called for PEEM imaging of electrochemical materials.

Embedded thin sections of nanoparticles by ultramicrotomy

We seek to implement ultramicrotomy, inspired by biological sample preparation for EM, in broader inorganic material systems. This idea has been practiced in 2D materials and lithium-ion batteries,[308,309] but the reliability and application of ultramicrotoming inorganic nanoparticles for PEEM imaging are still to be explored.

Here, we performed the initial trial by using nanoparticles of the same size and density as the ones previously utilized for FIM thinning. The ion-exchanged nanoparticles are mixed with EPON resin and centrifuged to achieve a denser distribution at the bottom of the mold. The resin is then cured to fix the nanoparticles. The as-prepared polymer blocks are ultramicrotomed (Leica EM UC6 at the TEM facility at UChicago) with a diamond knife (DiATOME, Ultra 45, 3.5 mm) to a set thickness of 100 nm thin slices, although depending on the resin quality and the vibrations during cutting, the thickness is usually inaccurate. The as-cut slices are gently picked up with the assistance of a "Perfect Loop" (Ted Pella) from the water boat and transferred to an Au-coated Si substrate. All prepared sections are dried in the air. A gentle heating procedure on a hot plate can speed up the drying process but may leave water marks around the sections.

The surface condition is first inspected using optical microscopy. Representative images are displayed in Figure 7.7(a), imaged with 20x (top) and 100x (bottom) objectives, respectively. The black particles are the cobalt oxides and the grey/yellow irregular pieces are the as-cut resins. There are a few features that indicate the imperfections of the ultramicrotome results. We first notice that the density of the nanoparticles is very high, where the particles cover almost the entire resin section. The nanoparticles also form aggregates, and those clusters could hinder the efforts to visualize structures of individual particle cross-sections. Second, there are plenty of holes and gaps between the nanoparticles and the plastics. This strongly suggests that the cross-linking of the particle and resin is poor. When the diamond knife cuts through the polymer block, chunks of particles pump out of the plane of resin, leading to disconnection in the sections. This is also in part due to the difference in sample preparation compared to biological samples, where an infiltration procedure that requires a few days of increasing resin concentrations ensures the proper penetration of the polymer dendrites into the soft tissues. For inorganic materials that are much harder, the lack of polymer infiltration is the primary reason for the bad contact. The variations in hardness in the resin block are not only a huge risk for damaging the diamond knife, but also give rise to uneven cutting results. Consequently, and also the third observation, the nanoparticles form a very rough surface with drastic height differences, casting a foreseeing focusing issue for PEEM imaging.

The sample is transferred into the FOCUS PEEM column and imaged with the Hg lamp. We very cautiously and slowly ramp up the extractor voltage to prevent possible acring and image the sample at a relatively large FoV, shown in Figure 7.7(b). The bright flakes are the inorganic crystals and the darker background should be the portion of resin. It is not surprising that the image shows different focal planes as we vary the voltages for the focusing lenses, as this is consistent with the height differences observed in the optical images. In addition, the edges of the flakes are not sharply resolved, which could relate to the discontinuity in the resin. Overall, we cannot achieve a similarly high resolution as the FIB milled sample to distinguish the layering feature in the cross-sections, and the sample preparation needs to be strongly modified.

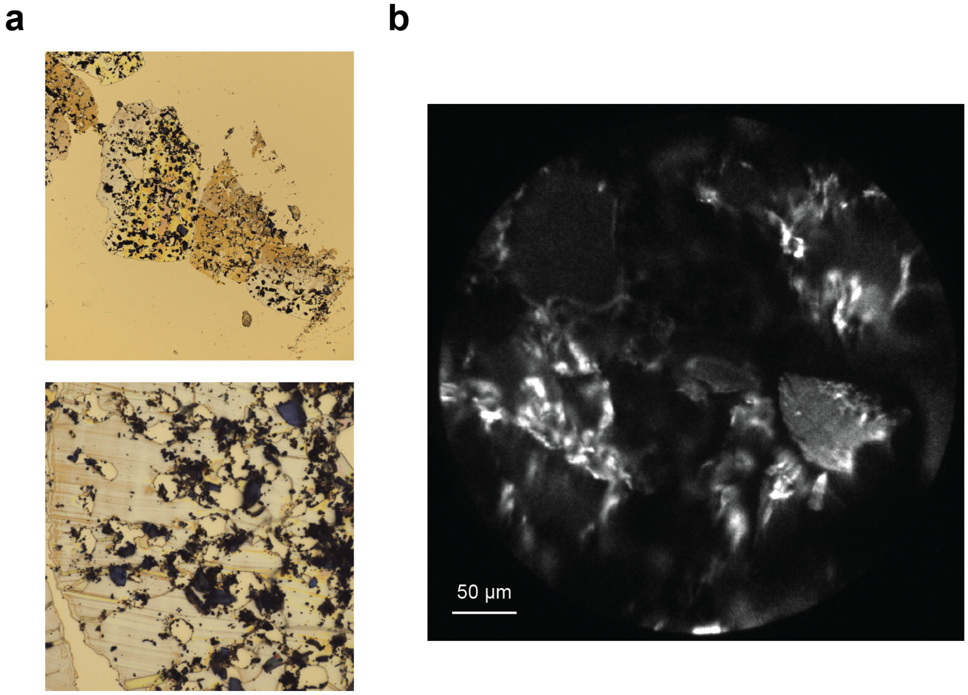

Figure 7.7: (a) Optical images at low (20x) and high (100x) magnification. (b) A PEEM image of the thin section.

The quality of ultramicrotome can be improved from two aspects: (1) lower the concentration of the nanoparticles mixed in the resin, and (2) use particles of smaller sizes. With a lower particle concentration, we observe much less clustering of the sediment in the cured resin block which allows better contact of the diamond knife with the polymer itself. The resulting sections (picked up on a bare Si(111) substrate) look much flatter optically (Figure 7.8(a)), despite the presence of chattering due to the vibrations in the room. However, there are still cracks in the section, as well as small holes that could be due to particles popping out of the cutting surface. In this section particularly, we can't easily observe black particles that represent the embedded materials, indicating the absence, or at least scarcity of cobalt oxides. The corresponding PEEM image is shown in Figure 7.8(c), where a clear hole feature is observed with a sharp focus, and the chatters are also clearly reflected. Surface survey in PEEM similarly doesn't yield strong intensity variation that would be an indication of Co oxides. Reflecting on the ultramicrotome process, it's likely that since the particles are more scattered in the resin, not each section necessarily contains the embedded inorganic crystals depending on the cutting depth. This means that an optimized concentration, as well as an even particle distribution, are crucial to consistent cutting results.

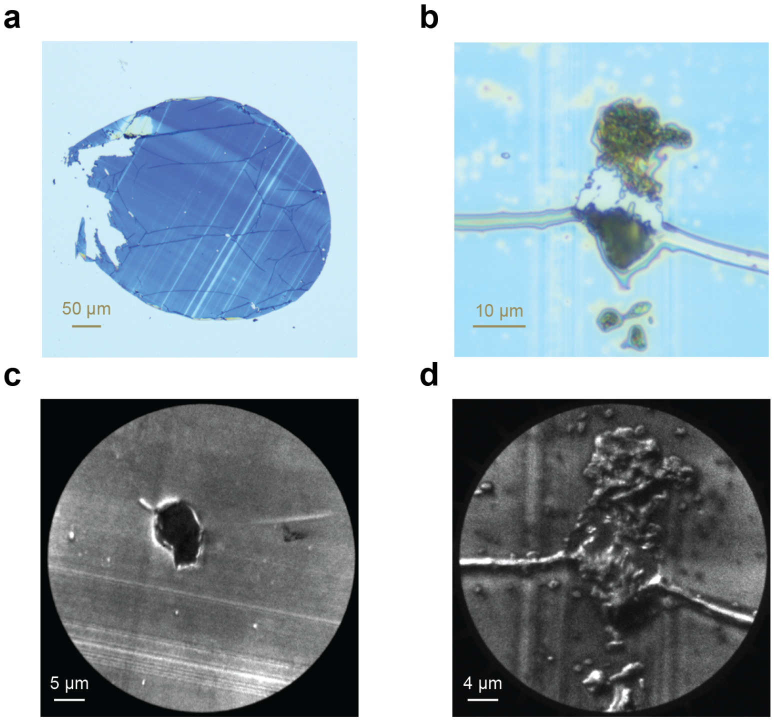

Figure 7.8: (a)(c) Optical and PEEM images of embedded Co-NP of 10 μm diameter and low density in resin. (b)(d) Optical and PEEM images of another set of embedded Co-NP with a better particle distribution on the sections.

The particle diameters can be chemically engineered to be smaller than 10 μm, with a distribution of size variations in each batch. After a few more attempts for ultramicrotomy, we are finally able to observe the presence of black particles in the thin sections with better cutting locations in the polymer blocks, as shown in Figure 7.8(b). The particles are still fully supported by the polymer, as we see a breakage between the two black pieces, but a better connection seems to have been achieved. We are able to locate the same area in PEEM (Figure 7.8(d)), where the two stripes on both sides are more likely to be a result of height contrast. The resolution of the particles is improved, in that the edges are no longer charging, suggesting better electrical contact with the substrate. The as-cut crystals are visually not flat, as verified by different focal planes in PEEM, indicating the cut quality still isn't ideal. Imaging at higher magnification proves to be difficult due to sample instability. During the imaging period, this particular sample was stable at 12 kV extractor voltage for only about 10 minutes before it started to arc badly and cause pressure bumps and thus the imaging had to be halted for the safety of the instrument.

Based on current investigations, we believe there is potential for realizing ultramicrotomy for inorganic nanoparticles, but an optimized protocol to properly expose the cross-sections of layered materials is challenging. Unlike biological tissues, crystalline materials have specific orientations that require specific cutting angles to characterize in-plane and out-of-plane chemical components. In the case of spherical nanoparticles, the orientations of dispersed particles embedded in resin are extremely difficult to predict and manipulate. A cutting angle parallel is favorable for successful ultramicrotome but if the angle is tilted or vertical, CoO_2 bonds must be too hard to break, causing fracturing and roughness.

To sum up, we have shown that PEEM has the advantage of mapping elemental contrast of layered electrochemical materials with nanoscale resolution. However, the development of a robust sample preparation protocol is a strong demand before PEEM can be used for systematic studies for structural and composite information of cross-sectional specimens.

7.4 Conclusion

In summary, we first introduced the idea of engineering the electronic structure of layered systems by integrating functional materials to achieve intentional modification of optical and electrical properties. We discussed two opportunities to realize the nanoscale manipulation, by photo-induced strain effect, or by geometrical control of light-matter coupling. We presented preliminary results for both methodologies and described how PEEM can be an effective technique for resolving the morphological-dependent ultrafast dynamics that are fundamental for device designs. We further suggested control experiments, such as varying excitation sources or material designs, that could help penetrate the underlying physical processes. In the second part, we demonstrate the ongoing experiments that explore a ubiquitous sample preparation method, ultramicrotomy, for both biological samples and inorganic materials, which will allow volume PEEM imaging of thin-sliced cross-sections. We show the great potential of PEEM for a broader range of biological samples based on the success of HeLa cell imaging, and this paves the way for investigations involving nanoscale imaging in biological and medical research.

REFERENCES

[1] Novoselov, K. S. et al. Electric field effect in atomically thin carbon films. *Science*, **306**(5696): 666–669 (2004).

[2] Novoselov, K. S., Mishchenko, A., Carvalho, A., and Neto, A. H. C. 2D materials and van der Waals heterostructures. *Science*, **353**(6298): aac9439 (2016).

[3] Liu, Y. et al. Van der Waals heterostructures and devices. *Nat. Rev. Mater.*, **1** (9): 16042 (2016).

[4] Gao, E. et al. Mechanical exfoliation of two-dimensional materials. *J. Mech. Phys. Solids*, **115**: 248–262 (2018).

[5] Yi, M. and Shen, Z. A review on mechanical exfoliation for the scalable production of graphene. *J. Mater. Chem. A*, **3**(22): 11700–11715 (2015).

[6] Li, H., Wu, J., Yin, Z., and Zhang, H. Preparation and applications of mechanically exfoliated single-layer and multilayer MoS_2 and WSe_2 nanosheets. *Acc. Chem. Res.*, **47**(4): 1067–1075 (2014).

[7] Castellanos-Gomez, A. et al. Isolation and characterization of few-layer black phosphorus. *2d Mater.*, **1**(2): 025001 (2014).

[8] Cai, Z., Liu, B., Zou, X., and Cheng, H.-M. Chemical vapor deposition growth and applications of two-Dimensional materials and their heterostructures. *Chem. Rev.*, **118** (13): 6091–6133 (2018).

[9] Lee, G.-H. et al. High-Strength Chemical-Vapor–Deposited Graphene and Grain Boundaries. *Science*, **340**(6136): 1073–1076 (2013).

[10] Kang, K. et al. High-mobility three-atom-thick semiconducting films with wafer-scale homogeneity. *Nature*, **520**(7549): 656–660 (2015).

[11] Molas, M. R. et al. The optical response of monolayer, few-layer and bulk tungsten disulfide. *Nanoscale*, **9**(35): 13128–13141 (2017).

[12] Tran, V., Soklaski, R., Liang, Y., and Yang, L. Layer-controlled band gap and anisotropic excitons in few-layer black phosphorus. *Phys. Rev. B*, **89**(23): 235319 6 (2014).

[13] Raja, A. et al. Dielectric disorder in two-dimensional materials. *Nat. Nanotechnol.*, **14**(9): 832–837 (2019).

[14] Quereda, J. et al. Strong Modulation of Optical Properties in Black Phosphorus through Strain-Engineered Rippling. *Nano Lett.*, **16**(5): 2931–2937 (2016).

[15] Shi, E. et al. Extrinsic and Dynamic Edge States of Two-Dimensional Lead Halide Perovskites. *ACS Nano*, **13**(2): 1635—1644 (2019).

[16] Rhodes, D., Chae, S. H., Ribeiro-Palau, R., and Hone, J. Disorder in van der Waals heterostructures of 2D materials. *Nat. Mater.*, **18**(6): 541–549 (2019).

[17] He, Z. et al. Defect engineering in single-layer MoS_2 using heavy ion irradiation. *ACS Appl. Mater. Interfaces*, **10**(49): 42524–42533 (2018).

[18] Rivnay, J. et al. Large modulation of carrier transport by grain-boundary molecular packing and microstructure in organic thin films. *Nat. Mater.*, **8**(12): 952–958 (2009).

[19] Peng, Z., Chen, X., Fan, Y., Srolovitz, D. J., and Lei, D. Strain engineering of 2D semiconductors and graphene: from strain fields to band-structure tuning and photonic applications. *Light Sci. Appl.*, **9**(1): 190 (2020).

[20] Qiao, J., Kong, X., Hu, Z.-X., Yang, F., and Ji, W. High-mobility transport anisotropy and linear dichroism in few-layer black phosphorus. *Nat. Commun.*, **5**(1): 4475 (2014).

[21] Li, L. et al. Black phosphorus field-effect transistors. *Nat. Nanotechnol.*, **9** (5): nnano.2014.35 (2014).

[22] Wang, X. et al. Highly anisotropic and robust excitons in monolayer black phosphorus. *Nat. Nanotechnol.*, **10**(6): nnano.2015.71 (2015).

[23] He, J. et al. Exceptional and anisotropic transport properties of photocarriers in black phosphorus. *ACS Nano*, **9**(6): 6436–6442 (2015).

[24] Yuan, H. et al. Polarization-sensitive broadband photodetector using a black phosphorus vertical p–n junction. *Nat. Nanotechnol.*, **10**(8): 707–713 (2015).

[25] Liu, X., Ryder, C. R., Wells, S. A., and Hersam, M. C. Resolving the in-plane anisotropic properties of black phosphorus. *Small Methods*, **1**(6): 1700143 (2017).

[26] Fei, R. et al. Enhanced thermoelectric efficiency via orthogonal electrical and thermal conductances in phosphorene. *Nano Lett.*, **14**(11): 6393–6399 (2014).

[27] Meng, S., Shi, H., Jiang, H., Sun, X., and Gao, B. Anisotropic charge carrier and coherent acoustic phonon dynamics of black phosphorus studied by transient absorption microscopy. *J. Phys. Chem. C*, **123**(32): 20051–20058 (2019).

[28] Castellanos-Gomez, A. Black phosphorus: Narrow gap, wide applications. *J. Phys. Chem. Lett.*, **6**(21): 4280–4291 (2015).

[29] Lin, C., Grassi, R., Low, T., and Helmy, A. S. Multilayer black phosphorus as a versatile mid-infrared electro-optic material. *Nano Lett.*, **16**(3): 1683–1689 (2016).

[30] Li, P., Lu, J., Cui, H., Ruan, S., and Zeng, Y.-J. The development, application, and performance of black phosphorus in energy storage and conversion. *Adv. Mater.*, **2** (8): 2483–2509 (2021).

[31] Kadantsev, E. S. and Hawrylak, P. Electronic structure of a single MoS_2 monolayer. *Solid State Commun.*, **152**(10): 909–913 (2012).

[32] Li, X. and Zhu, H. Two-dimensional MoS_2: Properties, preparation, and applications. *J. Materiomics*, **1**(1): 33–44 (2015).

[33] Zeng, H., Dai, J., Yao, W., Xiao, D., and Cui, X. Valley polarization in MoS_2 monolayers by optical pumping. *Nat. Nanotechnol.*, **7**(8): 490–493 (2012).

[34] Neto, A. H. C. Charge density wave, superconductivity, and anomalous metallic behavior in 2D transition metal dichalcogenides. *Phys. Rev. Lett.*, **86**(19): 4382–4385 (2001).

[35] Mujid, F. *Vapor-Phase Growth of Two-Dimensional Molecular Crystals and Their Structure-Property Relationships*. PhD thesis, Univeristy of Chicago (2022).

[36] Han, Z. and Porter, A. E. In situ electron microscopy of complex biological and nanoscale systems: Challenges and opportunities. *Front. Nanotechnol.*, **2**: 606253 (2020).

[37] Weston, A. E., Armer, H. E. J., and Collinson, L. M. Towards native-state imaging in biological context in the electron microscope. *J. Chem. Biol.*, **3**(3): 101–112 (2010).

[38] de Jonge, N. and Peckys, D. B. Live cell electron microscopy is probably impossible. *ACS Nano*, **10**(10): 9061–9063 (2016).

[39] Kourkoutis, L. F., Plitzko, J. M., and Baumeister, W. Electron microscopy of biological materials at the nanometer scale. *Mater. Res.*, **42**(1): 33–58 (2012).

[40] Collinson, L. M. et al. Volume EM: a quiet revolution takes shape. *Nat. Methods.*, **20** (6): 777–782 (2023).

[41] Kasthuri, N. et al. Saturated reconstruction of a volume of Neocortex. *Cell*, **162** (3): 648–661 (2015).

[42] Boergens, K. M., Kapfer, C., Helmstaedter, M., Denk, W., and Borst, A. Full reconstruction of large lobula plate tangential cells in Drosophila from a 3D EM dataset. *PLoS ONE*, **13**(11): e0207828 (2018).

[43] Einstein, A. Zur Elektrodynamik bewegter Körper. *Ann. Phys.*, **322**(10): 891–921 (1905).

[44] Lenard, P. Ueber die lichtelektrische Wirkung. *Ann. Phys.*, **313**(5): 149–198 (1902).

[45] Seah, M. P. and Dench, W. A. Quantitative electron spectroscopy of surfaces: A standard data base for electron inelastic mean free paths in solids. *Surf. Interface Anal.*, **1**(1): 2–11 (1979).

[46] Bauer, E. *Surface microscopy with low energy electrons*. Springer (2014).

[47] Sibbett, W., Lagatsky, A. A., and Brown, C. T. A. The development and application of femtosecond laser systems. *Opt. Express*, **20**(7): 6989 (2012).

[48] Könenkamp, R. et al. 5.4 nm spatial resolution in biological photoemission electron microscopy. *Ultramicroscopy*, **110**(7): 899–902 (2010).

[49] Sun, Q. et al. Direct imaging of the near field and dynamics of surface plasmon resonance on gold nanostructures using photoemission electron microscopy. *Light Sci. Appl.*, **2**(12): e118 (2013).

[50] Taniuchi, T., Kotani, Y., and Shin, S. Ultrahigh-spatial-resolution chemical and magnetic imaging by laser-based photoemission electron microscopy. *Rev. Sci. Instrum.*, **86**(2): 023701 (2015).

[51] Schneider, C. M. and Schönhense, G. Investigating surface magnetism by means of photoexcitation electron emission microscopy. *Rep. Prog. Phys.*, **65**(12): 1785 (2002).

[52] Cai, Y., Zhang, G., and Zhang, Y.-W. Layer-dependent band alignment and work function of few-Layer phosphorene. *Sci. Rep.*, **4**(1): srep06677 (2015).

[53] Marri, I. et al. Surface chemistry effects on work function, ionization potential and electronic affinity of Si(100), Ge(100) surfaces and SiGe heterostructures. *Phys. Chem. Chem. Phys.*, **22**(44): 25593–25605 (2020).

[54] Guerreiro, A. N., Costa, I. B., Vale, A. B., and Braga, M. H. Distinctive electric properties of Group 14 oxides: SiO_2, SiO, and SnO_2. *Int. J. Mol. Sci.*, **24**(21): 15985 (2023).

[55] Przychowski, M., Marx, G., Fecher, G., and Schönhense, G. A spatially resolved investigation of oxygen adsorption on polycrystalline copper and titanium by means of photoemission electron microscopy. *Surf. Sci.*, **549**(1): 37–51 (2004).

[56] Dai, Y., Dąbrowski, M., Apkarian, V. A., and Petek, H. Ultrafast Microscopy of Spin-Momentum-Locked Surface Plasmon Polaritons. *ACS Nano*, **12**(7): 6588–6596 (2018).

[57] Gong, Y., Joly, A. G., Hu, D., El-Khoury, P. Z., and Hess, W. P. Ultrafast imaging of surface plasmons propagating on a gold surface. *Nano Lett.*, **15**(5): 3472–3478 (2015).

[58] Fukumoto, K., Yamada, Y., Onda, K., and Koshihara, S.-y. Direct imaging of electron recombination and transport on a semiconductor surface by femtosecond time-resolved photoemission electron microscopy. *Appl. Phys. Lett.*, **104**(5): 053117 (2014).

[59] Man, M. K. L. et al. Imaging the motion of electrons across semiconductor heterojunctions. *Nat. Nanotechnol.*, **12**(1): 36–40 (2016).

[60] Xue, Z. et al. Photoexcited electron dynamics in Cd_3As_2 revealed by time- and energy-resolved photoemission electron microscopy. *J. Phys. Chem. C*, **126**(6): 3134–3139 (2022).

[61] Liu, W. et al. Mapping trap dynamics in a $CsPbBr_3$ single-crystal microplate by ultrafast photoemission electron microscopy. *Nano Lett.*, **21**(7): 2932–2938 (2021).

[62] Li, Y. et al. Ultrafast electron cooling and decay in monolayer WS_2 revealed by time- and energy-resolved photoemission electron microscopy. *Nano Lett.*, **20**(5): 3747–3753 (2020).

[63] Wang, L., Xu, C., Li, M.-Y., Li, L.-J., and Loh, Z.-H. Unraveling spatially heterogeneous ultrafast carrier dynamics of single-layer WSe_2 by femtosecond time-resolved photoemission electron microscopy. *Nano Lett.*, **18**(8) (2018).

[64] Xu, C. et al. Ultrafast charge transfer and recombination dynamics in monolayer–multilayer WSe_2 junctions revealed by time-resolved photoemission electron microscopy. *ACS Nano*, **18**(3): 1931–1947 (2024).

[65] Chen, J. et al. Effects of intercalation on the interlayer electron-transfer process in Mo-based multilayered MXene flakes. *J. Phys. Chem. C*, **125**(31): 17232–17240 (2021).

[66] Wallauer, R. et al. Momentum-resolved observation of exciton formation dynamics in monolayer WS_2. *Nano Lett.*, **21**(13): 5867–5873 (2021).

[67] Schmitt, D. et al. Formation of moiré interlayer excitons in space and time. *Nature*, **608**(7923): 499–503 (2022).

[68] Houle, W. A. and Griffith, O. Photoelectron microscopy of viruses. *Ultramicroscopy*, **11**(1): 71–74 (1983).

[69] Birrell, G., Rose, S. M., and Griffith, O. Photoelectron microscopy of erythrocyte ghosts; imaging of lectin binding sites with colloidal gold markers. *Ultramicroscopy*, **12**(3): 213–218 (1984).

[70] Birrell, G. B., Habliston, D. L., Nadakavukaren, K. K., and Griffith, O. H. Immunophotoelectron microscopy: the electron optical analog of immunofluorescence microscopy. *Proc. Natl. Acad. Sci. U.S.A.*, **82**(1): 109–113 (1985).

[71] Birrell, G. B., Hedberg, K. K., and Griffith, O. H. Pitfalls of immunogold labeling: analysis by light microscopy, transmission electron microscopy, and photoelectron microscopy. *J. Histochem. Cytochem.*, **35**(8): 843–853 (1987).

[72] Gilbert, P. U. Polarization-dependent Imaging Contrast (PIC) mapping reveals nanocrystal orientation patterns in carbonate biominerals. *J. Electron Spectros. Relat. Phenomena*, **185**(10): 395–405 (2012).

[73] Gilbert, B. et al. Spectromicroscopy of boron in human glioblastomas following administration of $Na_2B_{12}H_{11}SH$. *Phys. Rev. E*, **62**(1): 1110–1118 (2000).

[74] Spellberg, J. L. et al. Electronic structure orientation as a map of in-plane antiferroelectricity in β'-In_2Se_3. *Sci. Adv.*, **10**(24): eado2136 (2024).

[75] Kampfrath, T., Perfetti, L., Schapper, F., Frischkorn, C., and Wolf, M. Strongly coupled optical phonons in the ultrafast dynamics of the electronic energy and current relaxation in graphite. *Phys. Rev. Lett.*, **95**(18): 187403 (2005).

[76] Breusing, M., Ropers, C., and Elsaesser, T. Ultrafast carrier dynamics in graphite. *Phys. Rev. Lett.*, **102**(8): 086809 (2008).

[77] Lui, C. H., Mak, K. F., Shan, J., and Heinz, T. F. Ultrafast photoluminescence from graphene. *Phys. Rev. Lett.*, **105**(12): 127404 (2010).

[78] Liu, F. Mechanical exfoliation of large area 2D materials from vdW crystals. *Prog. Surf. Sci*, **96**(2): 100626 (2021).

[79] Novoselov, K. S. et al. Two-dimensional atomic crystals. *Proc. Natl. Acad. Sci. U.S.A.*, **102**(30): 10451–10453 (2005).

[80] Yasaei, P. et al. High-quality black phosphorus atomic layers by liquid-Phase exfoliation. *Adv. Mater.*, **27**(11): 1887–1892 (2015).

[81] Kamysbayev, V. et al. Covalent surface modifications and superconductivity of two-dimensional metal carbide MXenes. *Science*, **369**(6506): 979–983 (2020).

[82] Bera, B. Applied nanotechnology silicon wafer cleaning: A fundamental and critical step in semiconductor fabrication process. *Int. J. Appl. Nanotechnol.*, **5**(1): 8–13 (2019).

[83] Castellanos-Gomez, A. et al. Deterministic transfer of two-dimensional materials by all-dry viscoelastic stamping. *2d Mater.*, **1**(1): 011002 (2014).

[84] Watson, A. J., Lu, W., Guimarães, M. H. D., and Stöhr, M. Transfer of large-scale two-dimensional semiconductors: Challenges and developments. *2d Mater.*, **8** (3): 032001 (2021).

[85] Huang, Y. et al. Universal mechanical exfoliation of large-area 2D crystals. *Nat. Commun.*, **11**(1): 2453 (2020).

[86] Liu, F. et al. Disassembling 2D van der Waals crystals into macroscopic monolayers and reassembling into artificial lattices. *Science*, **367**(6480): 903–906 (2020).

[87] Desai, S. B. et al. Gold-mediated exfoliation of ultralarge optoelectronically-perfect monolayers. *Adv. Mater.*, **28**(21): 4053–4058 (2016).

[88] Velicky, M. et al. Mechanism of gold-assisted exfoliation of centimeter-sized transition-metal dichalcogenide monolayers. *ACS Nano*, **12**(10): 10463–10472 (2018).

[89] Joshi, P. P. et al. Anomalous reduction in black phosphorus phonon velocities driven by lattice anisotropy (2023). doi:10.26434/chemrxiv-2023-r0qq2-v2.

[90] McKenna, A. J., Eliason, J. K., and Flannigan, D. J. Spatiotemporal evolution of coherent elastic strain waves in a single MoS_2 Flake. *Nano Lett.*, **17**(6): 3952–3958 (2017).

[91] Cremons, D. R., Plemmons, D. A., and Flannigan, D. J. Femtosecond electron imaging of defect-modulated phonon dynamics. *Nat. Commun.*, **7**(1): 11230 (2016).

[92] Kim, Y.-J., Lee, Y., Kim, K., and Kwon, O.-H. Light-induced anisotropic morphological dynamics of black phosphorus membranes visualized by dark-field ultrafast electron microscopy. *ACS Nano*, **14**(9): 11383–11393 (2020).

[93] Bing, D. et al. Optical contrast for identifying the thickness of two-dimensional materials. *Opt. Commun.*, **406**: 128–138 (2018).

[94] Deng, B. et al. Efficient electrical control of thin-film black phosphorus bandgap. *Nat. Commun.*, **8**(1): 14474 (2017).

[95] Lu, W. et al. Plasma-assisted fabrication of monolayer phosphorene and its Raman characterization. *Nano Res.*, **7**(6): 853–859 (2014).

[96] Huang, M., Yan, H., Heinz, T. F., and Hone, J. Probing strain-induced electronic structure change in graphene by Raman spectroscopy. *Nano Lett.*, **10**(10): 4074–4079 (2010).

[97] Ferrari, A. C. and Basko, D. M. Raman spectroscopy as a versatile tool for studying the properties of graphene. *Nat. Nanotechnol.*, **8**(4): 235–246 (2013).

[98] Cong, X., Liu, X.-L., Lin, M.-L., and Tan, P.-H. Application of Raman spectroscopy to probe fundamental properties of two-dimensional materials. *npj 2D Mater. Appl.*, **4**(1): 13 (2020).

[99] Favron, A. et al. Photooxidation and quantum confinement effects in exfoliated black phosphorus. *Nat. Mater.*, **14**(8): 826–832 (2015).

[100] Abdollah et al. Strain engineering and Raman Spectroscopy of monolayer transition metal dichalcogenides. *Chem. Mater.*, **30**(15): 5148–5155 (2018).

[101] Ribeiro, H. B. et al. Edge phonons in black phosphorus. *Nat. Commun.*, **7** (1): 12191 (2016).

[102] Phaneuf-L'Heureux, A.-L. et al. Polarization-resolved Raman study of bulk-like and Davydov-induced vibrational modes of exfoliated black phosphorus. *Nano Lett.*, **16** (12) (2016).

[103] Li, H. et al. From bulk to monolayer MoS_2: Evolution of Raman scattering. *Adv. Funct. Mater.*, **22**(7): 1385–1390 (2012).

[104] Bartels, R. A., Oron, D., and Rigneault, H. Low frequency coherent Raman spectroscopy. *JPhys Photonics*, **3**(4): 042004 (2021).

[105] Zeng, H. et al. Low-frequency Raman modes and electronic excitations in atomically thin MoS_2 films. *Phys. Rev. B*, **86**(24): 241301 (2012).

[106] Dong, S. et al. Ultralow-frequency collective compression mode and strong interlayer coupling in multilayer black phosphorus. *Phys. Rev. Lett.*, **116**(8): 087401 (2016).

[107] Musumeci, C. Advanced scanning probe microscopy of graphene and other 2D materials. *Crystals*, **7**(7): 216 (2017).

[108] Carvalho, A. et al. Phosphorene: From theory to applications. *Nat. Rev. Mater.*, 08 **1** (11): 16061 (2016).

[109] Ling, X., Wang, H., Huang, S., Xia, F., and Dresselhaus, M. S. The renaissance of black phosphorus. *Proc. Natl. Acad. Sci. U.S.A.*, 04 **112**(15): 4523–4530 (2015).

[110] Li, P. and Appelbaum, I. Electrons and holes in phosphorene. *Phys. Rev. B*, **90** (11): 115439 (2014).

[111] Low, T. et al. Tunable optical properties of multilayer black phosphorus thin films. *Phys. Rev. B*, **90**(7): 075434 (2014).

[112] Low, T. et al. Plasmons and screening in monolayer and multilayer black phosphorus. *Phys. Rev. Lett.*, 09 **113**(10): 106802 (2014).

[113] van Veen, E. et al. Tuning two-dimensional hyperbolic plasmons in black phosphorus. *Phys. Rev. Appl.*, **12**(1): 014011 (2019).

[114] Bullock, J. et al. Polarization-resolved black phosphorus/molybdenum disulfide mid-wave infrared photodiodes with high detectivity at room temperature. *Nat. Photonics*, **12**(10): 601–607 (2018).

[115] Fei, R. et al. Enhanced thermoelectric efficiency via orthogonal electrical and thermal conductances in phosphorene. *Nano Lett.*, 10 **14**(11): 6393–6399 (2014).

[116] Huber, M. A. et al. Femtosecond photo-switching of interface polaritons in black phosphorus heterostructures. *Nat. Nanotechnol.*, **12**(3): 207–211 (2017).

[117] Low, T. et al. Polaritons in layered two-dimensional materials. *Nat. Mater.*, 11 **16** (2): 182–194 (2016).

[118] Biswas, S. et al. Tunable intraband optical conductivity and polarization-dependent epsilon-near-zero behavior in black phosphorus. *Sci. Adv.*, **7**(2): eabd4623 (2021).

[119] San-Jose, P., Parente, V., Guinea, F., Roldán, R., and Prada, E. Inverse funnel effect of excitons in strained black phosphorus. *Phys. Rev. X*, 09 **6**(3): 031046 (2016).

[120] Liang, L. et al. Electronic bandgap and edge reconstruction in phosphorene materials. *Nano Lett.*, **14**(11): 6400–6406 (2014).

[121] Wei, Y. and Long, R. Grain boundaries are Benign and suppress nonradiative electron-hole recombination in monolayer black phosphorus: A time-domain ab initio study. *J. Phys. Chem. Lett.*, **9**(14): 3856–3862 (2018).

[122] Surrente, A. et al. Excitons in atomically thin black phosphorus. *Phys. Rev. B*, 03 **93** (12): 121405 (2016).

[123] Zhu, T. et al. Highly mobile charge-transfer excitons in two-dimensional WS_2/tetracene heterostructures. *Sci. Adv.*, **4**(1): eaao3104 (2018).

[124] Kang, J. et al. Solvent exfoliation of electronic-grade, two-dimensional black phosphorus. *ACS Nano*, **9**(4): 3596–3604 (2015).

[125] Wu, Z. et al. Large-scale growth of few-layer two-dimensional black phosphorus. *Nat. Mater.*, **20**(9): 1203–1209 (2021).

[126] Watts, M. C. et al. Production of phosphorene nanoribbons. *Nature*, **568**(7751): 216–220 (2019).

[127] Das, P. M. et al. Controlled sculpture of black phosphorus nanoribbons. *ACS Nano*, **10**(6): 5687–5695 (2016).

[128] Liu, Z. and Aydin, K. Localized surface plasmons in nanostructured monolayer black phosphorus. *Nano Lett.*, 05 **16**(6): 3457–3462 (2016).

[129] Han, L., Wang, L., Xing, H., and Chen, X. Active tuning of midinfrared surface plasmon resonance and its hybridization in black phosphorus sheet array. *ACS Photonics*, **5**(9): 3828–3837 (2018).

[130] Yao, F. et al. In situ TEM study of edge reconstruction and evolution in monolayer black phosphorus. *Nanoscale*, **13**(7): 4133–4139 (2021).

[131] Peng, X., Copple, A., and Wei, Q. Edge effects on the electronic properties of phosphorene nanoribbons. *J. Appl. Phys.*, **116**(14): 144301 (2014).

[132] Guo, H., Lu, N., Dai, J., Wu, X., and Zeng, X. C. Phosphorene nanoribbons, phosphorus nanotubes, and van der Waals multilayers. *J. Phys. Chem. C*, **118**(25): 14051–14059 (2014).

[133] Dąbrowski, M., Dai, Y., and Petek, H. Ultrafast photoemission electron Microscopy: Imaging plasmons in space and time. *Chem. Rev.*, **120**(13): 6247–6287 (2020).

[134] Ueba, H. and Gumhalter, B. Theory of two-photon photoemission spectroscopy of surfaces. *Prog. Surf. Sci.*, **82**(4-6): 193–223 (2007).

[135] Crampton, K. T., Joly, A. G., and El-Khoury, P. Z. Direct visualization of counter-propagating surface plasmons in real space-time. *J. Phys. Chem. Lett.*, **10**(19): 5694–5699 (2019).

[136] Doherty, T. A. S. et al. Performance-limiting nanoscale trap clusters at grain junctions in halide perovskites. *Nature*, **580**(7803): 360–366 (2020).

[137] Neff, A., Niefind, F., Abel, B., Mannsfeld, S. C. B., and Siefermann, K. R. Imaging nanoscale morphology of semiconducting polymer films with photoemission electron microscopy. *Adv. Mater.*, 05 **29**(29): 1701012 (2017).

[138] Bohling, C. and Sigmund, W. Self-limitation of native oxides explained. *Silicon*, **8** (3): 339–343 (2016).

[139] Ling, X. et al. Anisotropic electron-photon and electron-phonon interactions in black phosphorus. *Nano Lett.*, **16**(4): 2260–2267 (2016).

[140] Cai, Y., Zhang, G., and Zhang, Y.-W. Layer-dependent band alignment and work function of few-layer phosphorene. *Sci. Rep.*, 10 **4**(1): 6677 (2014).

[141] Kresse, G. and Furthmüller, J. Efficient iterative schemes for ab initio total-energy calculations using a plane-wave basis set. *Phys. Rev. B*, Oct **54**: 11169–11186 (1996).

[142] Perdew, J. P., Burke, K., and Ernzerhof, M. Generalized gradient approximation made simple. *Phys. Rev. Lett.*, Oct **77**: 3865–3868 (1996).

[143] Wang, V., Xu, N., Liu, J.-C., Tang, G., and Geng, W.-T. Vaspkit: A user-friendly interface facilitating high-throughput computing and analysis using vasp code. *Comput. Phys. Commun.*, **267**: 108033 (2021).

[144] Hohenester, U. *Nano and quantum optics: An introduction to basic principles and theory.* Springer Nature, Cham, Switzerland (2020).

[145] Lan, S., Rodrigues, S., Kang, L., and Cai, W. Visualizing optical phase anisotropy in black phosphorus. *ACS Photonics*, **3**(7): 1176–1181 (2016).

[146] Fortin-Deschênes, M., Levesque, P. L., Martel, R., and Moutanabbir, O. Dynamics and mechanisms of exfoliated black phosphorus sublimation. *J. Phys. Chem. Lett.*, **7** (9): 1667–1674 (2016).

[147] Liu, X., Wood, J. D., Chen, K.-S., Cho, E., and Hersam, M. C. In situ thermal decomposition of exfoliated two-dimensional black phosphorus. *J. Phys. Chem. Lett.*, **6**(5): 773–778 (2015).

[148] Kumar, A. et al. STM study of exfoliated few layer black phosphorus annealed in ultrahigh vacuum. *2d Mater.*, **6**(1): 015005 (2018).

[149] Edmonds, M. T. et al. Creating a stable oxide at the surface of black phosphorus. *ACS Appl. Mater. Interfaces*, **7**(27): 14557–14562 (2015).

[150] Kuntz, K. L. et al. Control of surface and edge oxidation on phosphorene. *ACS Appl. Mater. Interfaces*, **9**(10): 9126–9135 (2017).

[151] Yoo, H. et al. Atomic and electronic reconstruction at the van der Waals interface in twisted bilayer graphene. *Nat. Mater.*, **18**(5): 448–453 (2019).

[152] Kim, K. et al. Tunable moiré bands and strong correlations in small-twist-angle bilayer graphene. *Proc. Natl. Acad. Sci. U.S.A.*, **114**(13): 3364–3369 (2017).

[153] Rivera, P. et al. Valley-polarized exciton dynamics in a 2D semiconductor heterostructure. *Science*, **351**(6274): 688–691 (2016).

[154] Bai, Y. et al. Excitons in strain-induced one-dimensional moiré potentials at transition metal dichalcogenide heterojunctions. *Nat. Mater.*, **19**(10): 1068–1073 (2020).

[155] Naik, M. H. et al. Intralayer charge-transfer moiré excitons in van der Waals superlattices. *Nature*, **609**(7925): 52–57 (2022).

[156] Lunt, R. R., Benziger, J. B., and Forrest, S. R. Relationship between crystalline order and exciton diffusion length in molecular organic semiconductors. *Adv. Mater.*, **22** (11): 1233–1236 (2010).

[157] Obaidulla, S. M. et al. MoS_2 and perylene derivative based type-II heterostructure: Bandgap engineering and giant photoluminescence enhancement. *Adv. Mater. Interfaces*, **7**(3): 1901197 (2020).

[158] Ji, J. and Choi, J. H. Recent progress in 2D hybrid heterostructures from transition metal dichalcogenides and organic layers: Properties and applications in energy and optoelectronics fields. *Nanoscale*, **14**(30): 10648–10689 (2022).

[159] Sharma, A., Hasan, M. M., and Lu, Y. Exciton dynamics in 2D organic semiconductors. *Mater. futures*, **1**(4): 042001 (2022).

[160] Zeb, J. et al. Ultrafast dynamics of the liquid deposited blend film of porphyrin donor and perylene diimide acceptor. *Chem. Phys.*, **559**: 111547 (2022).

[161] Zhu, T. et al. Highly mobile charge-transfer excitons in two-dimensional WS_2/tetracene heterostructures. *Sci. Adv.*, **4**(1): eaao3104 (2018).

[162] Zhao, C. et al. Ultrafast electron transfer with long-lived charge separation and spin polarization in WSe_2/C_{60} heterojunction. *J. Phys. Chem. Lett.*, **12**(15): 3691–3697 (2021).

[163] Homan, S. B. et al. Ultrafast exciton dissociation and long-lived charge separation in a photovoltaic pentacene–MoS_2 van der Waals heterojunction. *Nano Lett.*, **17**(1): 164–169 (2017).

[164] Xie, X.-Y., Liu, X.-Y., Fang, Q., Fang, W.-H., and Cui, G. Photoinduced carrier dynamics at the interface of pentacene and molybdenum disulfide. *J. Phys. Chem. A*, **123**(36): 7693–7703 (2019).

[165] Balch, H. B. et al. Electronically coupled 2D polymer/MoS_2 heterostructures. *J. Am. Chem. Soc.*, **142**(50): 21131–21139 (2020).

[166] Wang, Z. et al. Long-range hot charge transfer exciton dissociation in an organic/2D semiconductor hybrid excitonic heterostructure. *J. Am. Chem. Soc.*, **145**(20): 11227–11235 (2023).

[167] Clercq, D. M. d. et al. Exciton dissociation, charge transfer, and exciton trapping at the MoS_2/organic semiconductor interface. *J. Phys. Chem. C*, **127**(23): 11260–11267 (2023).

[168] Kubo, A., Jung, Y. S., Kim, H. K., and Petek, H. Femtosecond microscopy of localized and propagating surface plasmons in silver gratings. *J. Phys. B*, **40**(11): S259 (2007).

[169] Sun, Q. et al. Dissecting the few-femtosecond dephasing time of dipole and quadrupole modes in gold nanoparticles using polarized photoemission electron microscopy. *ACS Nano*, **10**(3): 3835–3842 (2016).

[170] Fukumoto, K., Yamada, Y., Koshihara, S.-y., and Onda, K. Lifetimes of photogenerated electrons on a GaAs surface affected by nanostructural defects. *Appl. Phys. Express*, **8**(10): 101201 (2015).

[171] Hu, A. et al. Spectromicroscopy and imaging of photoexcited electron dynamics at in-plane silicon pn junctions. *Nanoscale*, **13**(4): 2626–2631 (2020).

[172] Fukumoto, K. et al. Femtosecond time-resolved photoemission electron microscopy for spatiotemporal imaging of photogenerated carrier dynamics in semiconductors. *Rev. Sci. Instrum.*, **85**(8): 083705 (2014).

[173] Fukumoto, K. et al. Ultrafast electron dynamics in twisted graphene by femtosecond photoemission electron microscopy. *Carbon*, **124**: 49–56 (2017).

[174] Joshi, P. P., Li, R., Spellberg, J. L., Liang, L., and King, S. B. Nanoimaging of the edge-dependent optical polarization anisotropy of black phosphorus. *Nano Lett.*, **22** (8): 3180–3186 (2021).

[175] Crampton, K. T., Joly, A. G., and El-Khoury, P. Z. Uncovering surface plasmon optical resonances in nanohole arrays through interferometric photoemission electron microscopy. *Appl. Phys. Lett.*, **120**(8): 081102 (2022).

[176] Kahl, P. et al. Direct observation of surface plasmon polariton propagation and interference by time-resolved imaging in normal-incidence two photon photoemission microscopy. *Plasmonics*, **13**(1): 239–246 (2018).

[177] Dai, Y. et al. Plasmonic topological quasiparticle on the nanometre and femtosecond scales. *Nature*, **588**(7839): 616–619 (2020).

[178] Bennecke, W. et al. Disentangling the multiorbital contributions of excitons by photoemission exciton tomography. *Nat. Commun.*, **15**(1): 1804 (2024).

[179] Balakrishnan, K. et al. Effect of side-chain substituents on self-assembly of perylene diimide molecules: Morphology control. *J. Am. Chem. Soc.*, **128**(22): 7390–7398 (2006).

[180] Austin, A. et al. Enhanced Davydov splitting in crystals of a perylene diimide derivative. *J. Phys. Chem. Lett.*, **8**(6): 1118–1123 (2017).

[181] Kong, Y. et al. Interlayer exciton emission in a MoS_2/VOPc inorganic/organic van der Waals heterostructure. *Mater. Horiz.*, **9**(4): 1253–1263 (2022).

[182] Zhang, C., Wang, H., Chan, W., Manolatou, C., and Rana, F. Absorption of light by excitons and trions in monolayers of metal dichalcogenide MoS_2: Experiments and theory. *Phys. Rev. B*, **89**(20): 205436 (2014).

[183] Engel, E. et al. Transient absorption spectroscopy and quantum-chemical studies of matrix-isolated perylene derivatives. *Phys. Rev. B*, **73**(24): 245216 (2006).

[184] Li, R. et al. Contrast mechanism of osmium staining in electron microscopy of biological tissues (2023). doi:10.26434/chemrxiv-2023-scskq-v2.

[185] Zande, A. M. v. d. et al. Grains and grain boundaries in highly crystalline monolayer molybdenum disulphide. *Nat. Mater.*, **12**(6): 554–561 (2013).

[186] Cao, D., Shen, T., Liang, P., Chen, X., and Shu, H. Role of chemical potential in flake shape and edge properties of monolayer MoS_2. *J. Phys. Chem. C*, **119**(8): 4294–4301 (2015).

[187] He, K., Poole, C., Mak, K. F., and Shan, J. Experimental demonstration of continuous electronic structure tuning via strain in atomically thin MoS_2. *Nano Lett.*, **13**(6): 2931–2936 (2013).

[188] Castellanos-Gomez, A. et al. Local strain engineering in atomically thin MoS_2. *Nano Lett.*, **13**(11): 5361–5366 (2013).

[189] Hüfner, S., Schmidt, S., and Reinert, F. Photoelectron spectroscopy—An overview. *Nucl. Instrum. Methods Phys. Res. A*, **547**(1): 8–23 (2005).

[190] Zhou, W. et al. Intrinsic structural defects in monolayer molybdenum disulfide. *Nano Lett.*, **13**(6): 2615–2622 (2013).

[191] Park, S. et al. Type-I energy level alignment at the PTCDA—monolayer MoS_2 interface promotes resonance energy transfer and luminescence enhancement. *Adv. Sci*, **8** (12): 2100215 (2021).

[192] Robert, C. et al. Exciton radiative lifetime in transition metal dichalcogenide monolayers. *Phys. Rev. B*, **93**(20): 205423 (2016).

[193] Ryou, J., Kim, Y.-S., KC, S., and Cho, K. Monolayer MoS_2 bandgap modulation by dielectric environments and tunable bandgap transistors. *Sci. Rep.*, **6**(1): 29184 (2016).

[194] Selig, M. et al. Dark and bright exciton formation, thermalization, and photoluminescence in monolayer transition metal dichalcogenides. *2d Mater.*, **5**(3): 035017 (2018).

[195] Dal Conte, S. et al. Ultrafast valley relaxation dynamics in monolayer MoS_2 probed by nonequilibrium optical techniques. *Phys. Rev. B*, **92**(23): 235425 (2015).

[196] Wang, H., Zhang, C., and Rana, F. Ultrafast dynamics of defect-assisted electron-hole recombination in monolayer MoS_2. *Nano Lett.*, **15**(1): 339–345 (2015).

[197] King, S. B., Broch, K., Demling, A., and Stähler, J. Multistep and multiscale electron transfer and localization dynamics at a model electrolyte/metal interface. *J. Chem. Phys.*, **150**(4): 041702 (2019).

[198] Zhong, C. et al. Mechanisms of ultrafast charge separation in a PTB_7/monolayer MoS_2 van der Waals heterojunction. *J. Phys. Chem. Lett.*, **9**(10): 2484–2491 (2018).

[199] Ye, L. et al. Ultrafast singlet energy transfer before fission in a tetracene/WSe_2 type II hybrid heterostructure. *J. Phys. Chem. Lett.*, **12**(34): 8440–8446 (2021).

[200] Kronik, L. and Shapira, Y. Surface photovoltage phenomena: Theory, experiment, and applications. *Surf. Sci. Rep.*, **37**(1-5): 1–206 (1999).

[201] Yang, S.-L., Sobota, J. A., Kirchmann, P. S., and Shen, Z.-X. Electron propagation from a photo-excited surface: Implications for time-resolved photoemission. *Appl. Phys. A*, **116**(1): 85–90 (2014).

[202] Ciocys, S., Morimoto, T., Moore, J. E., and Lanzara, A. Tracking surface photovoltage dipole geometry in Bi_2Se_3 with time-resolved photoemission. *J. Stat. Mech.: Theory Exp.*, **2019**(10): 104008 (2019).

[203] Tanaka, S.-i. Utility and constraint on the use of pump-probe photoelectron spectroscopy for detecting time-resolved surface photovoltage. *J. Electron Spectros. Relat. Phenomena*, **185**(5-7): 152–158 (2012).

[204] Liu, X. et al. Photoresponse of an organic semiconductor/two-dimensional transition metal dichalcogenide heterojunction. *Nano Lett.*, **17**(5): 3176–3181 (2017).

[205] Oliva, I. G., Caruso, F., Pavone, P., and Draxl, C. Hybrid excitations at the interface between a MoS_2 monolayer and organic molecules: A first-principles study. *Phys. Rev. Mater.*, **6**(5): 054004 (2022).

[206] Meneghini, G., Reutzel, M., Mathias, S., Brem, S., and Malic, E. Hybrid Exciton Signatures in ARPES Spectra of van der Waals Materials. *ACS Photonics*, **10**(10): 3570–3575 (2023).

[207] Harris, K. and Stevens, J. Dendritic spines of CA 1 pyramidal cells in the rat hippocampus: Serial electron microscopy with reference to their biophysical characteristics. *J. Neurosci.*, **9**(8): 2982–2997 (1989).

[208] Anderson, J. R. et al. Exploring the retinal connectome. *Mol. Vis.*, **17**: 355 (2011).

[209] Bock, D. D. et al. Network anatomy and in vivo physiology of visual cortical neurons. *Nature*, **471**(7337): 177–182 (2011).

[210] Kornfeld, J. et al. EM connectomics reveals axonal target variation in a sequence-generating network. *eLife*, **6**: e24364 (2017).

[211] Svara, F. et al. Automated synapse-level reconstruction of neural circuits in the larval zebrafish brain. *Nat. Methods*, **19**(11): 1357–1366 (2022).

[212] Winding, M. et al. The connectome of an insect brain. *Science*, **379**(6636): eadd9330–eadd9330 (2023).

[213] Takemura, S.-y. et al. A connectome of the male drosophila ventral nerve cord (2023). doi:10.1101/2023.06.05.543757.

[214] Dorkenwald, S. et al. FlyWire: online community for whole-brain connectomics. *Nat. Methods.*, **19**(1): 119–128 (2022).

[215] Hider, R. et al. The Brain Observatory Storage Service and Database (BossDB): A Cloud-Native Approach for Petascale Neuroscience Discovery. *Front. Neuroinform.*, **16**: 828787 (2022).

[216] von Bubnoff, A. Next-generation sequencing: The race is on. *Cell*, **132**(5): 721–723 (2008).

[217] Dai, Y. et al. Plasmonic topological quasiparticle on the nanometre and femtosecond scales. *Nature*, **588**(7839): 616–619 (2020).

[218] Spektor, G. et al. Revealing the subfemtosecond dynamics of orbital angular momentum in nanoplasmonic vortices. *Science*, **355**(6330): 1187–1191 (2017).

[219] Tromp, R. et al. A new aberration-corrected, energy-filtered LEEM/PEEM instrument. I. Principles and design. *Ultramicroscopy*, **110**(7): 852–861 (2010).

[220] Schmidt, T. et al. Double aberration correction in a low-energy electron microscope. *Ultramicroscopy*, **110**(11): 1358–1361 (2010).

[221] Bauer, E. A brief history of PEEM. *J. Electron Spectros. Relat. Phenomena*, **185** (10): 314–322 (2012).

[222] Skallberg, A., Bunnfors, K., Brommesson, C., and Uvdal, K. New tools for imaging neutrophils: work function mapping and element-specific, label-free imaging of cellular structures. *Nano Lett.*, **21**(1): 222–229 (2020).

[223] Stasio, G. d. et al. High-Resolution Photoelectron Microimaging of Neuron Networks. *EPL*, **16**(4): 411–414 (1991).

[224] Rempfer, G. F., Skoczylas, W. P., and Griffith, O. H. Design and performance of a high-resolution photoelectron microscope. *Ultramicroscopy*, **36**(1-3): 196–221 (1991).

[225] Helmstaedter, M. et al. Connectomic reconstruction of the inner plexiform layer in the mouse retina. *Nature*, **500**(7461): 168–174 (2013).

[226] Hua, Y., Laserstein, P., and Helmstaedter, M. Large-volume en-bloc staining for electron microscopy-based connectomics. *Nat. Commun.*, **6**(1): 7923 (2015).

[227] Berger, D. R., Seung, H. S., and Lichtman, J. W. VAST (Volume Annotation and Segmentation Tool): Efficient manual and semi-automatic labeling of large 3D image stacks. *Front. Neural Circuit.*, **12**: 88 (2018).

[228] Tromp, R., Wan, W., and Schramm, S. Aberrations of the cathode objective lens up to fifth order. *Ultramicroscopy*, **119**: 33–39 (2012).

[229] Rose, A. *Vision: Human and electronic.* Springer US (1974).

[230] Kasthuri, N. and Lichtman, J. W. The rise of the 'projectome'. *Nat. Methods.*, **4** (4): 307–308 (2007).

[231] Kirillov, A. et al. Segment anything (2023). doi:10.48550/arXiv.2304.02643.

[232] Peddie, C. J. et al. Volume electron microscopy. *Nat. Rev. Methods Primers*, **2** (1): 51 (2022).

[233] Wigglesworth, V. B. The use of osmium in the fixation and staining of tissues. *Proc. R. Soc. B: Biol. Sci.*, **147**(927): 185–199 (1957).

[234] Subbaraman, L. R., Subbaraman, J., and Behrman, E. J. Formation and hydrolysis of osmate(VI) esters. *Inorg. Chem.*, **11**(11): 2621–2627 (1972).

[235] Lalaoui, N. et al. Osmium(II) complexes bearing chelating N-heterocyclic carbene and pyrene-modified ligands: surface electrochemistry and electron transfer mediation of oxygen reduction by multicopper enzymes. *Organometallics*, **35**(17): 2987–2992 (2016).

[236] Song, K., Feng, Z., and Helmstaedter, M. High-contrast en bloc staining of mouse whole-brain and human brain samples for EM-based connectomics. *Nat. Methods*, **20** (6): 836–840 (2023).

[237] Wigglesworth, V. B. Histological staining of lipids for the light and electron microscope. *Biol. Rev.*, **63**(3): 417–431 (1988).

[238] Scheller, E. L. et al. Use of osmium tetroxide staining with microcomputerized tomography to visualize and quantify bone marrow adipose tissue in vivo. *Methods Enzymol.*, **537**: 123–139 (2014).

[239] Graham, L. and Orenstein, J. M. Processing tissue and cells for transmission electron microscopy in diagnostic pathology and research. *Nat. Protoc.*, **2**(10): 2439–2450 (2007).

[240] Seligman, A. M., Wasserkrug, H. L., and Hanker, J. S. A new staining method (OTO) for enhancing contrast of lipid-containing membranes and droplets in osmium tetroxide-fixed tissue with osmiophilic thiocarbohydrazide (TCH). *J. Cell Biol.*, **30** (2): 424–432 (1966).

[241] Vollhardt, K. P. C. and Schore, N. E. *Organic Chemistry: Structure and Function*. W. H. Freeman, New York, 6th edition (2011).

[242] White, D. L., Andrews, S., Faller, J., and Barrnett, R. J. The chemical nature of osmium tetroxide fixation and staining of membranes by X-ray photoelectron spectroscopy. *Biochim. Biophys. Acta - Biomembr.*, **436**(3): 577–592 (1976).

[243] Boergens, K. M. et al. Photoemission electron microscopy for connectomics (2024). doi:10.1101/2023.09.05.556423.

[244] Tsutsumi, T. et al. Energy-filtered X-ray photoemission electron microscopy and its applications to surface and organic materials. *Solid State Electron.*, **51**(10): 1360–1366 (2007).

[245] Schmidt, C. A. et al. Myriad Mapping of nanoscale minerals reveals calcium carbonate hemihydrate in forming nacre and coral biominerals. *Nat. Commun.*, **15** (1): 1812 (2024).

[246] Skallberg, A., Bunnfors, K., Brommesson, C., and Uvdal, K. Neutrophils activated by nanoparticles and formation of neutrophil extracellular traps: work function mapping and element specific imaging. *Anal. Chem.*, **91**(21): 13514–13520 (2019).

[247] Birrell, G. B., Hedberg, K. K., Habliston, D. L., and Griffith, O. Biological applications of photoelectron imaging: a practical perspective. *Ultramicroscopy*, **36**(1-3): 235–251 (1991).

[248] Reinert, F. and Hüfner, S. Photoemission spectroscopy—from early days to recent applications. *New J. Phys.*, **7**(1): 97–97 (2005).

[249] Pignataro, M. F., Herrera, M. G., and Dodero, V. I. Evaluation of peptide/protein self-assembly and aggregation by spectroscopic methods. *Molecules*, **25**(20): 4854 (2020).

[250] Close, D. M. Calculated vertical ionization energies of the common α-amino acids in the gas phase and in solution. *J. Phys. Chem. A*, **115**(13): 2900–2912 (2011).

[251] Pershina, V., Bastug, T., Fricke, B., and Varga, S. The electronic structure and properties of group 8 oxides MO_4, where M=Ru, Os, and element 108, Hs. *J. Chem. Phys.*, **115**(2): 792–799 (2001).

[252] Green, J. C., Kaltsoyannis, N., Sze, K. H., and MacDonald, M. A. An investigation of the electronic structure of osmium tetroxide by photoelectron spectroscopy with variable photon energy. *Chem. Phys. Lett.*, **175**(4): 359–363 (1990).

[253] Regoutz, A. et al. Insights into the electronic structure of OsO_2 using soft and hard X-ray photoelectron spectroscopy in combination with density functional theory. *Phys. Rev. Mater.*, **3**(2): 025001 (2019).

[254] Rogers, D. B., Butler, S. R., Shannon, R. D., Wold, A., and Kershaw, R. *Ruthenium and iridium dioxides osmium dioxide tungsten dioxide and β-ruthenium dioxides*, volume 13, pages 135–145. McGraw Hill (1972).

[255] Hayakawa, Y. et al. Electronic structure and electrical properties of amorphous OsO_2. *Phys. Rev. B*, **59**(17): 11125–11127 (1999).

[256] Belazi, D., Solé-Domènech, S., Johansson, B., Schalling, M., and Sjövall, P. Chemical analysis of osmium tetroxide staining in adipose tissue using imaging ToF-SIMS. *Histochem. Cell Biol.*, **132**(1): 105–115 (2009).

[257] Schroeder, M. Osmium tetraoxide cis hydroxylation of unsaturated substrates. *Chem. Rev.*, **80**(2): 187–213 (1980).

[258] Ogino, Y., Chen, H., Kwong, H.-L., and Sharpless, K. B. On the timing of hydrolysis/reoxidation in the osmium-catalyzed asymmetric dihydroxylation of olefins using potassium ferricyanide as the reoxidant. *Tetrahedron Lett.*, **32**(32): 3965–3968 (1991).

[259] Kolb, H. C., VanNieuwenhze, M. S., and Sharpless, K. B. Catalytic asymmetric dihydroxylation. *Chem. Rev.*, **94**(8): 2483–2547 (1994).

[260] Khan, A. A., Riemersma, J. C., and Bbooij, H. L. The reactions of osmium tetroxide with lipids and other compounds. *J. Histochem. Cytochem.*, **9**(5): 560–563 (1961).

[261] Nickels, J. D. and Katsaras, J. Membrane hydration, the role of water in the structure and function of biological membranes. *Subcell. Biochem.*, **71**: 45–67 (2015).

[262] Stoeckenius, W. Electron microscopy of fixed lipids. *Protoplasma*, **63**(1-3): 214–217 (1967).

[263] Cairns, J. F. and Roberts, H. L. Osmium tetroxide-catalysed oxidation of olefins. *J. Chem. Soc. C*, **0**(0): 640–642 (1968).

[264] Cartwright, B. A., Griffith, W. P., Schröder, M., and Skapski, A. C. X-ray molecular structure of the asymmetrically bridged ester complex di--oxo-bis[(cyclohexane-1,2-diolato)oxo(quinuclidine)osmium(VI)], $[OsO_2(O_2C_6H_{10})(C_7H_{13}N)]_2$. *J. Chem. Soc.*, **0**(19): 853–854 (1978).

[265] Ströh, S., Hammerschmith, E. W., Tank, D. W., Seung, H. S., and Wanner, A. A. In situ X-ray-assisted electron microscopy staining for large biological samples. *eLife*, **11**: e72147 (2022).

[266] Korn, E. D. A chromatographic and spectrophotometric study of the products of the reaction of osmium tetroxide with unsaturated lipids. *J. Cell Biol.*, **34**(2): 627–638 (1967).

[267] Naveen, R., Kumar, M., Ramesh, M., Abinaya, R., and Prasath, M. An investigation on effect of ultraviolet (UV) rays on mechanical properties of epoxy laminates. *Mater. Today Proc.*, (2023).

[268] Schramm, S. M., Berghaus, J. K. A., Schaff, O., Tromp, R. M., and Molen, S. J. v. d. Low-energy electron microscopy and spectroscopy with ESCHER: Status and prospects. *IBM J. Res. Dev.*, **55**(4): 1:1–1:7 (2011).

[269] Hüfner, S. *Photoelectron Spectroscopy, Principles and Applications.* Advanced Texts in Physics. Springer Berlin, Heidelberg (2003).

[270] Wilcox, W. R. and LaChapelle, T. J. Mechanism of gold diffusion into silicon. *J. Appl. Phys.*, **35**(1): 240–246 (1964).

[271] DeJarld, M. et al. Surface potential and thin film quality of low work function metals on epitaxial graphene. *Sci. Rep.*, **8**(1): 16487 (2018).

[272] Gay, J. G., Smith, J. R., Arlinghaus, F. J., and Capehart, T. W. Electronic structure of palladium (100). *Phys. Rev. B*, **23**(4): 1559–1566 (1981).

[273] Strong, J. *Procedures in Experimental Physics.* Bradley, IL: Lindsay Publications (1938).

[274] Unger, A.-K., Neujahr, R., Hawes, C., and Hummel, E. *Improving Serial Block Face SEM by Focal Charge Compensation*, pages 165–178. Springer US (2020).

[275] Hodgson, A. and Haq, S. Water adsorption and the wetting of metal surfaces. *Surf. Sci. Rep.*, **64**(9): 381–451 (2009).

[276] Luft, J. H. Improvements in epoxy resin embedding methods. *J. Cell Biol.*, **9**(2): 409–414 (1961).

[277] Ellis, E. A. No more Epon 812: This product does not exist today. *Microsc. Today*, **22**(3): 50–53 (2014).

[278] Grassie, N., Guy, M. I., and Tennent, N. H. Degradation of epoxy polymers. Part 5—Photo-degradation of bisphenol-A diglycidyl ether cured with ethylene diamine. *Polym. Degrad. Stab.*, **14**(3): 209–216 (1986).

[279] Nikafshar, S. et al. The effects of UV light on the chemical and mechanical properties of a transparent epoxy-diamine system in the presence of an organic UV absorber. *Materials*, **10**(2): 180 (2017).

[280] Yousif, E. and Haddad, R. Photodegradation and photostabilization of polymers, especially polystyrene: Review. *Springerplus*, **2**(1): 398 (2013).

[281] Decker, C. and Zahouily, K. Photodegradation and photooxidation of thermoset and UV-cured acrylate polymers. *Polym. Degrad. Stab.*, **64**(2): 293–304 (1999).

[282] Mendes-Felipe, C., Oliveira, J., Etxebarria, I., Vilas-Vilela, J. L., and Lanceros-Mendez, S. State-of-the-art and future challenges of UV curable polymer-based smart materials for printing technologies. *Adv. Mater. Technol.*, **4**(3) (2019).

[283] Montanari, F. et al. *2,2,6,6-Tetramethylpiperidin-1-oxyl*, pages 1–12. John Wiley Sons, Ltd (2016).

[284] Katwa, L. C., Ramakrishna, M., and Rao, M. R. R. Spectrophotometric assay of immobilized tannase. *J. Biosci.*, **3**(2): 135–142 (1981).

[285] Burton, P., Hinkley, R., and Pierson, G. Tannic acid-stained microtubules with 12, 13, and 15 protofilaments. *J. Cell Biol.*, **65**(1): 227–233 (1975).

[286] Mollenhauer, H. H. and Morré, D. J. Some unusual staining properties of tannic acid in plants. *Histochemistry*, **88**(1): 17–22 (1987).

[287] Afzelius, B. A. Section staining for electron microscopy using tannic acid as a mordant: A simple method for visualization of glycogen and collagen. *Microsc. Res. Tech.*, **21** (1): 65–72 (1992).

[288] Wang, H., Yuan, H., Hong, S. S., Li, Y., and Cui, Y. Physical and chemical tuning of two-dimensional transition metal dichalcogenides. *Chem. Soc. Rev.*, **44**(9): 2664–2680 (2014).

[289] Rajapakse, M. et al. Intercalation as a versatile tool for fabrication, property tuning, and phase transitions in 2D materials. *npj 2D Mater. Appl.*, **5**(1): 30 (2021).

[290] Kang, K. et al. Layer-by-layer assembly of two-dimensional materials into wafer-scale heterostructures. *Nature*, **550**(7675): 229 (2017).

[291] Wong, J. et al. High photovoltaic quantum efficiency in ultrathin van der Waals heterostructures. *ACS Nano*, **11**(7): 7230–7240 (2017).

[292] Kim, K. et al. Van der Waals heterostructures with high accuracy rotational alignment. *Nano Lett.*, **16**(3): 1989–1995 (2016).

[293] Dai, Z., Liu, L., and Zhang, Z. Strain engineering of 2D materials: Issues and opportunities at the interface. *Adv. Mater.*, **31**(45): 1805417 (2019).

[294] Tsoukleri, G. et al. Subjecting a graphene monolayer to tension and compression. *Small*, **5**(21): 2397–2402 (2009).

[295] Li, Y., Yang, S., and Li, J. Modulation of the electronic properties of ultrathin black phosphorus by strain and electrical Field. *J. Phys. Chem. C*, **118**(41): 23970–23976 (2014).

[296] Huang, S. et al. Strain-tunable van der Waals interactions in few-layer black phosphorus. *Nat. Commun.*, **10**(1): 2447 (2019).

[297] Gobbi, M. et al. Collective molecular switching in hybrid superlattices for light-modulated two-dimensional electronics. *Nat. Commun.*, **9**(1): 2661 (2018).

[298] Pathem, B. K., Claridge, S. A., Zheng, Y. B., and Weiss, P. S. Molecular switches and motors on surfaces. *Annu. Rev. Phys. Chem.*, **64**(1): 605–630 (2013).

[299] Fredy, J. W. et al. Molecular photoswitches mediating the strain-driven disassembly of supramolecular tubules. *Proc. Natl. Acad. Sci. U.S.A.*, **114**(45): 11850–11855 (2017).

[300] Park, K.-D. et al. Hybrid tip-enhanced nanospectroscopy and nanoimaging of monolayer WSe_2 with local strain control. *Nano Lett.*, **16**(4): 2621–2627 (2016).

[301] Sarwat, S. G. et al. Revealing strain-induced effects in ultrathin heterostructures at the nanoscale. *Nano Lett.*, **18**(4): 2467–2474 (2018).

[302] Ghorbani-Asl, M., Borini, S., Kuc, A., and Heine, T. Strain-dependent modulation of conductivity in single-layer transition-metal dichalcogenides. *Phys. Rev. B*, **87** (23): 235434 (2013).

[303] Kubo, A., Jung, Y. S., Kim, H. K., and Petek, H. Femtosecond microscopy of localized and propagating surface plasmons in silver gratings. *J. Phys. B*, **40**(11): S259 (2007).

[304] Kubo, A. et al. Femtosecond imaging of surface plasmon dynamics in a nanostructured silver film. *Nano Lett.*, **5**(6): 1123–1127 (2005).

[305] Zimmerman, J. F. et al. Free-standing kinked silicon nanowires for probing inter- and intracellular force dynamics. *Nano Lett.*, **15**(8): 5492–5498 (2015).

[306] Hill, G. T., Shi, F., Zhou, H., Han, Y., and Liu, C. Layer spacing gradient $(NaLi)_{1-x}CoO_2$ for electrochemical Li extraction. *Matter*, **4**(5): 1611–1624 (2021).

[307] Giannuzzi, L. and Stevie, F. A review of focused ion beam milling techniques for TEM specimen preparation. *Micron*, **30**(3): 197–204 (1999).

[308] Cichocka, M. O., Bolhuis, M., Heijst, S. E. v., and Conesa-Boj, S. Robust sample preparation of large-area in- and out-of-plane cross sections of layered materials with ultramicrotomy. *ACS Appl. Mater. Interfaces*, **12**(13): 15867–15874 (2020).

[309] Taylor, A. K., Nesvaderani, F., Ovens, J. S., Campbell, S., and Gates, B. D. Enabling a high-throughput characterization of microscale interfaces within coated cathode particles. *ACS Appl. Energy Mater.*, **4**(9): 9731–9741 (2021).

[310] Schlaf, R. Calibration of photoemission spectra and work function determination. `http://rsl.eng.usf.edu/Documents/Tutorials/PEScalibration.pdf` (2013).

[311] Novikov, A. Experimental measurement of work function in doped silicon surfaces. *Solid-State Electron.*, **54**(1): 8–13 (2010).

[312] Yu, Y.-J. et al. Tuning the graphene work function by electric field effect. *Nano Lett.*, **9**(10): 3430–3434 (2009).

[313] Weaver, J. H., Olson, C. G., and Lynch, D. W. Optical investigation of the electronic structure of bulk Rh and Ir. *Phys. Rev. B*, **15**(8): 4115–4118 (1977).

[314] Johannsen, J. C. et al. Direct view of hot carrier dynamics in graphene. *Phys. Rev. Lett.*, **111**(2): 027403 (2013).

[315] Breusing, M. et al. Ultrafast nonequilibrium carrier dynamics in a single graphene layer. *Phys. Rev. B*, **83**(15): 153410 (2011).

APPENDIX A

APPENDIX

A.1 Alignment of prism compressors

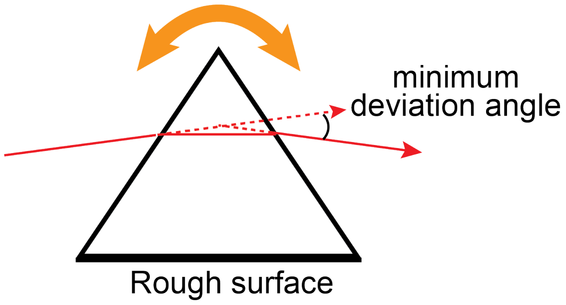

Figure A.1: Diagram showing the minimum deviation angle in a prism. This is achieved when the incident and exiting angles are equal.

The prism compressors need to be configured and aligned carefully to create negative dispersion to compensate for positive dispersion from other optical components, otherwise the prism compressor can introduce its own distortions (i.e. spatial chirp or pulse-front tilting) or higher-order dispersion. In general, three parameters mainly affect the compression efficiency: 1) the angles of incidence (AOI) into both prisms, 2) the separation distance between the two prisms, and 3) the insertion lengths. To achieve all degrees of freedom for optimization, the prisms are typically mounted on a stack of a rotational stage and a linear stage, where the rotational stage should be under the linear stage to preserve the direction of the linear motion given a varying AOI. In principle, the dispersion properties of a compressor vary with the AOI. For ease of alignment, the AOI is usually chosen such that the refracted beam comes out at the same angle as the incident beam at the central wavelength of the spectrum to be compressed, and this angle is named the "angle of minimum deviation", as illustrated in Figure A.1. In practice, this angle is determined by rotating the prism along the normal axis (indicated by the thick arrowhead in Figure A.1) while monitoring the lateral movement of the refracted beam on a card or a beam block. The refracted beam first travels horizontally in one way, hits an endpoint, and returns in the opposite direction. The prism needs to be positioned at the point where the refraction starts to go back, and the same operation applies to both prisms.

The separation distance and prism insertion length depend on the central wavelengths to be compressed as well as the amount dispersion in the system. For the time-resolved PEEM experiments in the thesis, a two-prism compressor geometry was used (see Figure 2.10), and the separation distances of the relevant wavelengths are listed in Table A.1, which could be a good starting point for future optimization. The separation can be adjusted by only moving the folding mirror rather than disassembling the whole prism compressor. Similarly, the optimal insertion lengths of each prism require fine-tuning according to the pulse duration. Typically, the incident beam should be close to the apexes of the prisms for best compression. The linear stage position can be optimized to the strongest intensity of the cross-correlation signal. Finally, the uncompressed beam needs to be coupled to the prism compressor at p-polarization (parallel to the tabletop).

Wavelength (nm)	Tip-to-tip distance (cm)	Achieved pulse duration (fs)
SHG prism compressor		
575	100.5	<30
THG prism compressor		
300	34	<100

Table A.1: Reference of the prism separation distances for SHG and THG compression.

A.2 The UHV systems in detail

A.2.1 Scienta Omicron system

The UHV system for the FOCUS PEEM is manufactured by Scienta Omicron. The preparation chamber is comprised of a load lock, a preparation chamber, and an analysis chamber, isolated by gate valves. Figure A.2 shows a 3D diagram of the UHV chambers and a few key components. The system electronics are interfaced and interlocked with the Mistral System Controller accessible from both the power supply rack and the computer.

The samples to fit into the FOCUS sample holders are typically 7×7 mm^2 chips to cover the 5-mm diameter circular opening. The thicknesses are preferred to be 380 μm or more in

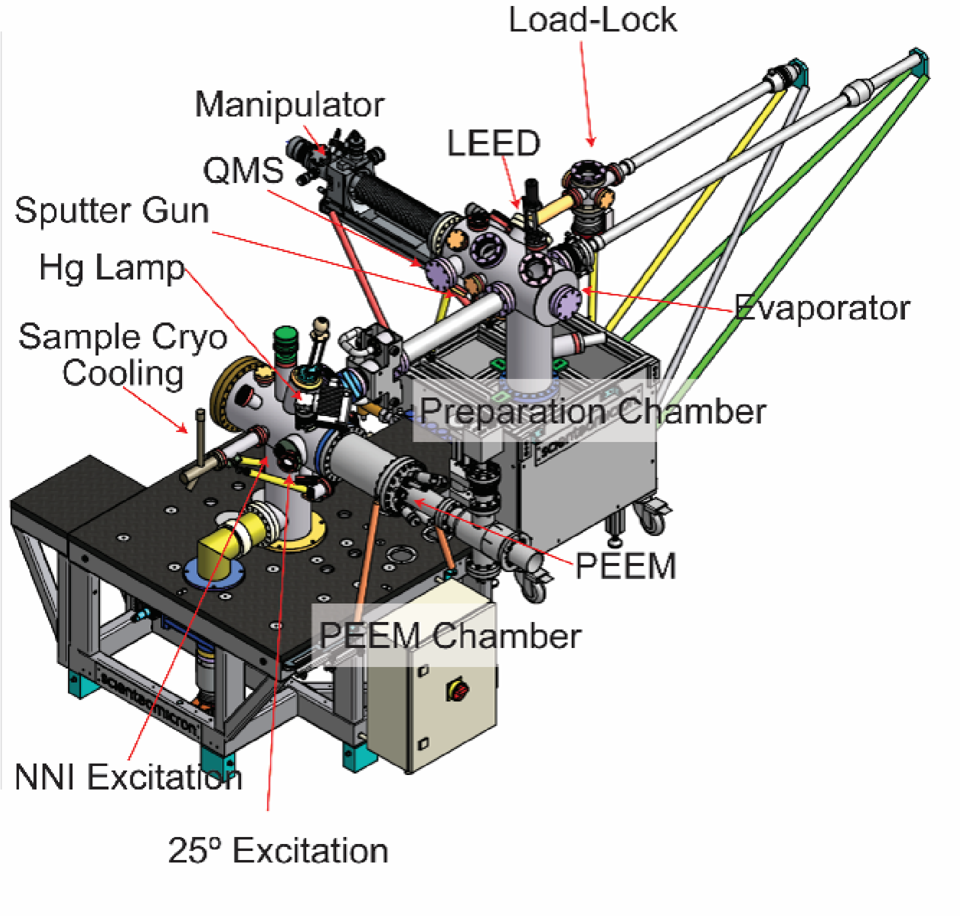

Figure A.2: Overview of the FOCUS UHV system.

order to fit into the grooves of the mount and be clamped firmly by the spring from the back of the holder. A schematic of the sample holder is shown in Figure A.3. Other geometries such as a larger front opening or a 10×10 mm^2 rectangle are also available to adapt to sample varieties. Additionally, thermal couple pins can be attached to the mount for precise measurements of sample temperature.

The load lock is backed by an oil roughing pump (Edwards Vacuum) and a small turbo pump (Pfeiffer Vacuum) constantly in operation to keep the pressure at $\sim 10^{-8}$ mbar. A fast-entry door has been installed to enable convenient access for sample transfer to the vacuum system. The mounted sample is usually assisted by a special tool to be secured on the transfer rod. After the load lock is pumped down, the sample can be transferred onto the

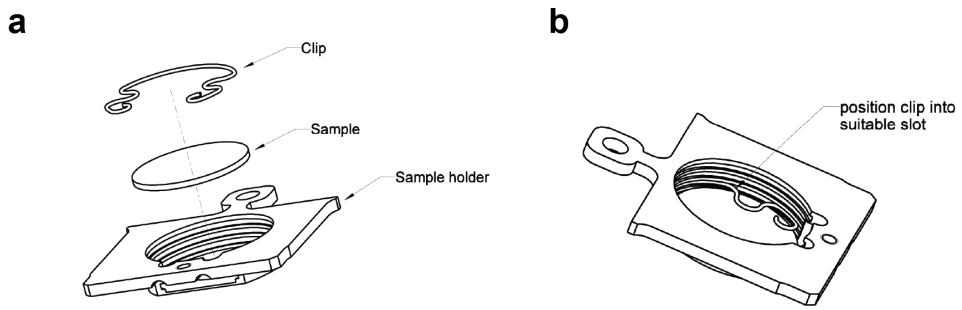

Figure A.3: The schematic of the FOCUS sample holder. (a) The exploded assembly drawing showing the configuration of the mounting. (b) The back view of the completed assembly. Adapted from FOCUS PEEM manual.

manipulator by pushing the magnet on the transfer rod to the preparation chamber, which is kept at a base pressure of 10^{-11} mbar with a scroll pump (Edwards Vacuum) and a turbo pump (Pfeiffer Vacuum), and the pressure is indicated by a double-filament ion gauge.

The samples can be resistively heated via a filament under the sample plate, or directly heated by applying electrical current through the sample surface. Since the built-in thermal couple is connected to the bottom of the manipulator, the temperature reading doesn't necessarily reflect the real temperature on the surface. Careful temperature calibrations vs. the applied heating current need to be performed using pyrometers. The manipulator has x, y, z, and rotation degrees of freedom to accommodate different locations and orientations required for the sample preparation apparatus installed in the preparation chamber.

The chamber is equipped with a residual gas analyzer (RGA 100, Stanford Research System) and it's connected with a z-linear shift. RGA works as a mass spectrometer and can monitor the partial pressures of trace residual gases in the UHV environment up to 60 atomic mass unit (amu) with <1 amu resolution. Such high sensitivity is beneficial for leak checking of the high vacuum system: Helium (He) gas can be purged around suspicious flanges or connections. The partial pressure of He (amu $= 4$) would spike if a leak indeed existed. The RGA is switchable between the preparation chamber and analysis chamber depending on the needs. Experimentally, the RGA is required for applications such as temperature-controlled desorption (TCP) and thermal desorption spectroscopy (TDS), which are in development for future projects.

A thermal evaporator (MBE Komponenten) for organic materials is mounted from the side of the preparation chamber. The evaporator can operate at 50-700 °C to deposit organic thin films on a substrate programmably. A quartz micro-balance (QMC, INFICON) is installed on the symmetric side of the chamber to monitor the accumulated film thickness. The two instruments usually operate in a pair to achieve precise control of the deposited film, and this combination is currently still open for future potential applications.

A sputter gun (Princeton Instrument[double check]) is built from a bottom flange on the chamber. Sputtering is a process where the material surface is bombarded by an accelerated particle beam (e.g. Ar^+) to eject surface contaminates. A leak valve with a separate gas manifold is attached to the sputter gun to enable precision control of Argon (Ar) gas flowing into the preparation chamber. Ar^+ ions are produced by impact with electrons that are thermoemitted from the filament of an electron gun. Combining the sample heating capability on the manipulator, sample surfaces such as single crystalline metals can be rigorously cleaned through cycles of annealing and sputtering.

A low-energy electron diffraction (LEED) unit (Scienta Omicron Inc.) is available in the preparation chamber. LEED is one of the most powerful techniques to characterize surface structures of single crystalline materials. As the name implies, LEED detects the diffraction with a low-energy electron beam bombarding the surface and the pattern and intensity shown on a fluorescent screen contain information on crystal unit cells and the degree of order. To date, only cleaned Cu (111) has been used for testing purposes with this LEED. The diffraction pattern was successfully obtained yet no further analysis has proceeded.

The analysis chamber also has an oil pump (Edwards Vacuum) for the roughing line and a turbo pump (Pfeiffer Vacuum). Normally, the gate valve connecting the pumps to the vacuum chamber is closed and both pumps are switched off for imaging stability. An ion getter pump (IGP) is routinely running to maintain the base pressure at 10^{-11} mbar, indicated by an ion gauge. A titanium sublimation pump (TSP) with three active filaments is also installed in the analysis chamber and it's regularly fired manually to remove residual gases in the chamber to maintain the vacuum. A six-slot sample carousel is available in the analysis chamber for sample storage.

A cryostat is available to cool the sample down to liquid nitrogen (LN2) temperature (77 K) and will be modified to adapt to liquid helium cooling (4 K) in the future. The LN2 cooling is realized by constantly pumping liquid nitrogen fluid from a dewar at a controlled flow rate with the adjusting valve in a closed-loop vacuum system. Heating tapes are usually necessary to wrap the vacuum bellows to avoid frosting. Thermal couples attaching to the cryostat as well as the back of the sample plate allow for temperature reading. The PID controller (Lake Shore Cryotronics) regulates and maintains the sample at the set temperature.

A.2.2 ELMITEC system

The Elmitec PEEM has a more compact vacuum system, consisting of a load lock, a small preparation chamber, the main chamber, and the optics chamber, and the layout is shown in the photo (Figure A.4). The load lock is normally backed by an oil roughing pump (Edwards Vacuum), and the pressure is monitored by a cold cathode pressure gauge (Kurt Lesker). Typically, the sample is transferred onto an "elevator" in the load lock, and then a turbo pump (Pfeiffer Vacuum) is turned on till the pressure reaches the low 10^{-6} mbar regime. The elevator acts as a gate valve. When it is pulled entirely out, a flange installed on the side of the elevator seals the connection between the load lock and the preparation chamber so that the pressures can be separately controlled. The elevator can be pushed into the preparation chamber to exchange the sample on the transfer rod. The pressure preparation chamber is indicated by an Agilent ion gauge. This ion gauge isn't sensitive to pressures lower than 10^{-8} mbar, rather a non-physical reading of 10^{-13} mbar is given, which regardless, is still an indication of a good vacuum. A sputter gun was attached to the preparation chamber when the Elmitec system was received, however, it has not been functioning due to a broken filament connection.

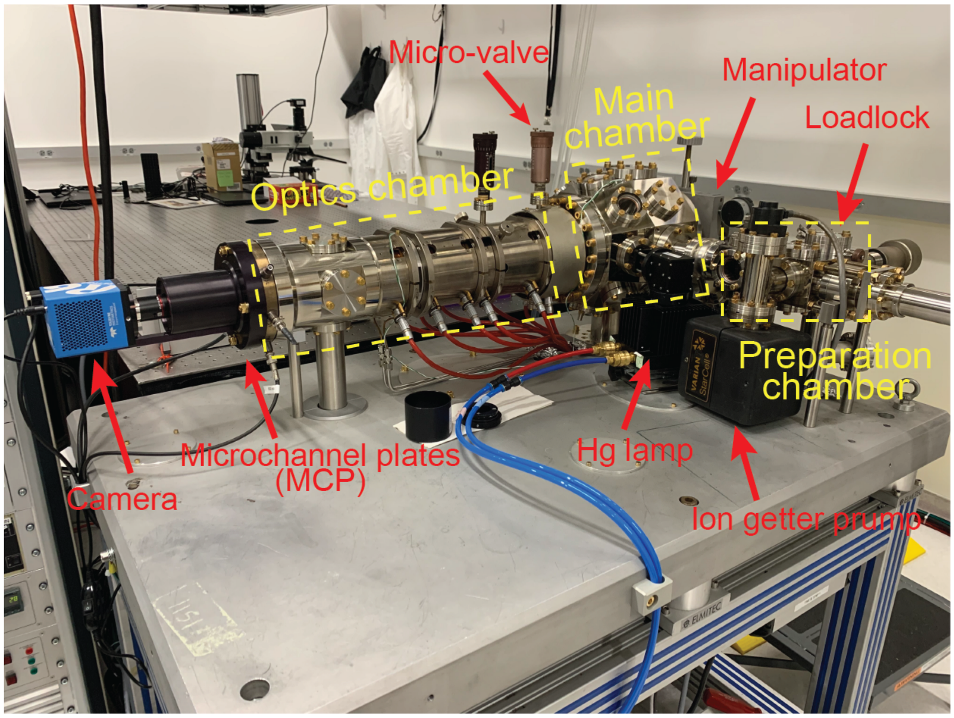

Figure A.4: A photo of the Elmitec PEEM system with main components annotated.

The main chamber is isolated from the preparation chamber by a gate valve, and a micro-valve is installed between the main chamber and the optics chamber. The micro-valve also acts as an aperture in the optics system and therefore is frequently open unless the main chamber needs to be independently vented. Both the pressures in the optics chamber and the main chamber are measured by ion gauges (Varian) and they share the same controller with two separate channels. The chambers are routinely kept at 10^{-11} mbar with ion getter pumps (Varian StarCell). There are also two bakeable metal valves connecting the main chamber and/or the optics chamber to the turbo which are normally closed during operation. The turbo pump is switched off during image acquisition to avoid vibrations from the cooling fan. A lead (Pb) evaporator is installed at the bottom flange of the main chamber. The evaporator allows *in situ* deposition that is commonly used to lower sample work function.

The sample cartridge for the ELMITEC system allows mounting of a single chip with a dimension of no larger than 1×1 cm^2. The circular opening of the sample holder is variable (5 mm, 7mm, or 10 mm in diameter), allowing more flexibility in sample size as well as compatibility with the FOCUS PEEM sample holder. Figure A.5 shows a photograph of the sample cartridge designed for the ELMITEC PEEM system. In particular, this sample holder has a built-in thermo-element and filament for irradiative and e-bombardment heating, allowing in-situ heating without interrupting the imaging session. The sample can reach temperatures up to 2000 K for short flashes and can be cooled down to 100 K with liquid nitrogen. The heating ability facilitates an annealing procedure to remove surface contaminants which usually results in improved image quality. In addition, precise temperature control opens opportunities for the observations of thermal-dependent surface modifications in a live mode.

Figure A.5: Sample cartridge for the ELMITEC PEEM system. The sample is mounted by screwing a cap with a circle opening from the top. A thermocouple wire is in physical contact with the back of the sample, allowing accurate temperature reading.

A.3 Determination of absolute work function

In order to measure the absolute values of the work function, a careful calibration of the PE spectra with respect to the kinetic energy detector (normally referred to as an analyzer) needs to be performed. This is because the sample and the analyzer are electrically connected during photoemission measurements. Therefore, their Fermi levels are in equilibrium, or in other words, aligned at the same energy level. Since the analyzer has a work function Φ_{ana}, there exists a contact potential between the sample and the analyzer $\Phi_{\text{sample}} - \Phi_{\text{ana}}$. In most cases, the sample has a larger work function than the analyzer, resulting in an acceleration of the photoelectrons through the analyzer. As a consequence, the raw spectrum collected from the photoemission process is shifted by $\Phi_{\text{sample}} - \Phi_{\text{ana}}$ to a higher energy level (assuming $\Phi_{\text{sample}} > \Phi_{\text{ana}}$).

The difficulty naturally becomes how to determine the work function of the analyzer, which is unknown. The trick is to use the Fermi edge of a metal surface, to calibrate for an internal energy scale relative to the analyzer. If the kinetic energy of the fastest electrons at the Fermi edge is defined as $\mathrm{E_{kin}} = \mathrm{h}\nu$, where $\mathrm{h}\nu$ is the total photon energy, one or multiple, that enables the photoemission process, an offset between the measured position of Fermi edge and the photon energy can be calculated. The PE spectrum can then be shifted accordingly to show the kinetic energies of the respective electrons as they leave the sample surface. The other convenience of this energy offset is that the work function can now be directly read from the secondary edge cutoff, as it represents the electrons that were in electronic states just above the vacuum level.

In principle, the Fermi edge calibration is required each time for a new sample, as there are slight variations in the analyzer for each measurement. However, this is simply impossible if the work function of a semiconductor is to be determined, as a semiconductor doesn't have enough states around the Fermi level and thus no Fermi edge is observed in the PE spectra. In this case, a metal is still used to provide an energy reference to the analyzer, providing the change in analyzer work function is insignificant. Once the semiconductor is mounted on the sample plate, its Fermi level is immediately equilibrated with that of the analyzer, and the work function of the semiconductor can be extracted similarly by applying the previously measured energy offset. A good reference for this section can be found at the tutorial documents provided Dr. Rudy Schlaf.[310]

A.4 Supplementary information for Chapter 4

A.4.1 Methods

Sample Preparation and Characterization

Few-layer black phosphorus (BP) is mechanically exfoliated from bulk crystals (Smart Elements) using a polydimethylsiloxane (PDMS) stamping method.[83] In brief, 2D BP is freshly cleaved from a bulk crystal with scotch tape, folded and peeled 3-4 times before it is transferred onto a piece of homemade PDMS stamp. The as-obtained PDMS is pressed onto a 380 μm-thick pre-cleaned Si chip with native oxide and gently peeled off from the surface, leaving thin BP flakes on the substrate. The flakes are first inspected using an optical microscope (Amscope, ME580TA-PZ-2L-18M3) with a 50x objective to estimate the thickness and morphology. After satisfying flakes are optically identified, the sample is mounted onto a PEEM sample plate with an optically accessible inner diameter of 5 mm. The aforementioned preparation is conducted in N_2 atmosphere with O_2<1 ppm. After sample mounting the sample is removed from N_2 atmosphere, immediately transferred into the vacuum-chamber loadlock equipped with a fast-entry door, and pumped down to ultrahigh vacuum (UHV) conditions. The air exposure time during the whole transfer process is well controlled to under 20 seconds. After PEEM experiments are finished in UHV, the sample is removed from the vacuum and stored in N_2 atmosphere again to prevent sample degradation before further characterization.

When removed from N_2 atmosphere for further characterization, an air-tight sample holder is used for transport to maintain inert atmosphere conditions. Raman microscopy is performed using a confocal optical microscope (Horiba LabRAM HR Evolution). BP is excited by a 532 nm laser and the scattered signal is collected using a 100x objective lens. Measurements take up to 20 minutes, during which the sample is exposed to ambient conditions. Tapping mode AFM (Bruker MultiMode 8) of the same flake is performed immediately after the Raman measurements.

Polarization-Dependent Photoemission Electron Microscopy

Polarization-dependent photoemission electron microscopy (PEEM) measurements use laser illumination from an optical parametric chirped pulse amplifier (OPCPA) (Class 5 Photonics, 1 MHz) with central wavelengths of 800 nm (1.55 eV, FWHM 44 nm) and 515 nm (2.4 eV, FWHM 12 nm), and pulse durations <40 fs. The linearly polarized laser illumination is directed onto the BP sample in the PEEM chamber via a near-normal incidence

Rh mirror, with an angle of incidence of 4°. Before entering the UHV chamber the laser light is transmitted through a thin-film polarizing beamsplitter (Eksma) and rotated with an appropriate zero-order $\lambda/2$ waveplate (Thorlabs). We estimate fluences from the beam profile on the bare Si/native oxide substrate using the reported work function of n-doped Si, <4.6 eV[311], meaning two-photon photoemission with 2.4 eV illumination and three-photon photoemission with 1.55 eV illumination. The fluence on the sample is $\sim 100\mu\text{J/cm}^2$ for 2.4 eV illumination and $\sim 700\mu\text{J/cm}^2$ for 1.55 eV illumination and is adjusted to limit space charging from the BP flake.

Annealing

Black phosphorus flakes are annealed at 300°C and 350°C for 1 hour at each temperature and allowed to cool for ~30 minutes before transferring to the PEEM. 350°C is the upper limit of the temperature range required to remove oxides and prepare a pristine black phosphorus surface while also avoiding degradation of black phosphorus.[147,148]

A.4.2 Rh Reflectivity Correction

The PEEM sample is illuminated via pulsed laser that is reflected from a near-normal incidence (NNI) rhodium mirror inside the PEEM UHV chamber. The angle of incidence is 4° from normal, which means the electric field is effectively parallel to the sample plane. Therefore, polarization rotation of the laser illumination results in the rotation of the electric field in the sample plane. The reflectivity correction used here is adapted from Neff et al.[137] The effective intensity on the sample is dependent on the polarization-dependent reflectivity of the rhodium mirror, which can be described as the following:

$$I_{refl} = I_o[R_S \cos^2(\theta_{Rh}) + R_P \sin^2(\theta_{Rh})] \tag{A.1}$$

where I_o is the intensity of the illumination before the mirror (measured outside the chamber), R_S is the reflectivity of rhodium for s-polarized light, R_P is the reflectivity of rhodium for p-polarized light, and θ is the angle of polarization such that $\theta_{Rh} = 0°$ refers to s-polarization and $\theta_{\mathrm{Rh}} = 90°$ refers to p-polarization with respect to the plane of incidence of the rhodium mirror.

For pump photon energy of 2.4 eV, we use a monolayer graphene/300 nm $\mathrm{SiO_2}$/Si substrate to calibrate the reflectivity of the rhodium mirror. A representative image of the PEEM illumination on graphene/$\mathrm{SiO_2}$/Si is shown in A.9(a). We empirically determine the relative values of $\mathrm{R_S}$ and $\mathrm{R_P}$ and the angle $\theta_{\mathrm{Rh}} = 0°$ by a power series (A.9(b)) and a polarization dependent measurement (A.9(c)) of a graphene/$\mathrm{SiO_2}$/Si substrate. The work function of graphene is reported to be 4.6 eV.[312] We empirically determine the n-photon process of 2.4 eV with a power series. For a fixed polarization, $\theta_{\mathrm{Rh}} = 0°$, we integrate the signal across the field of view for each power step and then fit the resulting data with a fitting model $\mathrm{I_{PE,graphene} = Ax^b}$ where x is the incident laser power, A is a coefficient, and b corresponds to the number of photons required for photoemission from graphene/$\mathrm{SiO_2}$/Si (A.9(b)). We extract a value of 3.57 for b. For a given polarization, the intensity of the illumination reflected by the rhodium mirror, I_{refl}, is related to the photoemission intensity from graphene as $\mathrm{I_{refl}} = \sqrt[m]{I_{PE,graphene}}$ such that m = b. In A.9(c), we integrate across the entire field of view (FOV) and report the photoemission intensity as a function of polarization angle, θ. We fit the photoemission response with the fit $\mathrm{I_{PE}} = \mathrm{A}\cos^2(\theta - \beta) + \mathrm{C}$. where A is the amplitude, β is the phaseshift, and C is the offset. For 515 nm, $\beta = 11.2°$. We take $\theta = \beta$, where the photoemission intensity is maximized, to be the angle at which the incident laser light is s-polarized with respect to the rhodium mirror, and the angle of minimum photoemission intensity $\beta + 90°$ to be the angle at which it is p-polarized.

To confirm the accuracy of our calibration, we extract a ratio of $\frac{R_S}{R_P}$ from our fit such that $\frac{R_S}{R_P} = \sqrt[m]{\frac{I_{PEfit,max}}{I_{PEfit,min}}}$. For m=b=3.57, $\frac{R_S}{R_P} = 1.20$. The reported polarization-dependent reflectivity of rhodium is $R_{S,lit}$=0.82 and $\mathrm{R_{P,lit}}$=0.68.[313] $\frac{\mathrm{R_{S,lit}}}{\mathrm{R_{P,lit}}}$=1.21, which means that our experimental calibration is in good agreement with known experimental values. The final polarization dependent photoemission signal from black phosphorus, $I_{PE,BP}(\theta)$, is from the photoemission signal, $\mathrm{I_{meas}}(\theta)$, and the fit to the reflectivity of graphene: $I_{PE,BP}(\theta) = \frac{I_{meas}(\theta)}{[\sqrt[m]{I_{PE,graphene}(\theta)}]^n}$ where n is the number of photons required for photoemission from the black phosphorus sample and $\mathrm{I_{PE,graphene}}(\theta)$ is normalized to 1. For an excitation photon energy of 2.4 eV, n = 2 (A.10(b)).

For excitation energy 1.55 eV, we generate a polarization-dependent calibration by using the literature values for the reflectivity of rhodium $\mathrm{R_{S,lit}}$=0.81 and $\mathrm{R_{P,lit}}$=0.76.[313] We perform a polarization-dependence on graphene/$\mathrm{SiO_2}$/Si and extract $\beta = 11.8°$, which is consistent with the β extracted from 2.4 eV polarization dependence. The consistency of the phase shift is to be expected, because that should be dependent on the orientation of the rhodium mirror inside the UHV chamber. Owing to a possible resonance state in graphene 3 eV below the Fermi level, we use the extracted β and previously reported R_S and R_P and model the reflectance of the rhodium mirror as:

$$I_{refl,1.55eV} = I_{refl} = I_o[R_S \cos^2(\theta_{Rh}) + R_P \sin^2(\theta_{Rh})] \tag{A.2}$$

where $\theta_{\mathrm{Rh}} = \theta - \beta$. We normalize $I_{refl,1.55eV}$ to 1 and for each data set, we have $I_{PE,BP}(\theta) = \frac{I_{meas}(\theta)}{I^n_{refl,1.55eV}}$, where n = 3, as empirically determined by a power series on the black phosphorus flakes (A.10(e)).

A.4.3 Across-Bandgap Polarization Dependence

In order to confirm that the polarization dependence is from the across-bandgap absorption and not the final state photoionization process, we perform a polarization dependence measurement with a 1.55 eV pump and a 3.1 eV probe such that the polarization of the pump is rotated from $\theta = 0°$ to 400° in increments of 10°. With respect to time-zero, where the pump and probe pulses are temporally overlapped, negative time delays are where the 3.1 eV probe pulse arrives before the 1.55 eV pump pulse, and positive time delays are where the pump arrives before the probe. Because the work function of few-layer BP is >4 eV,[140] the dominant photoemission process at negative time delays should be from the absorption of two 3.1 eV photons from the valence band or the absorption of one 3.1 eV photon and photoionization by a 1.55 eV photon. In contrast, the dominant photoemission process at positive time delays should be from the across-bandgap absorption of a 1.55 eV photon and the subsequent photoionization of the intermediate state by a 3.1 eV photon. Another process, namely the absorption of two 1.55 eV photons and photoionization by a 3.1 eV photon is also possible, but less likely because it requires three photons instead of two. The power of the 3.1 eV illumination is 1.34 mW (333 kHz), and the 1.55 eV illumination is attenuated to 16.6 mW (333 kHz) such that there is no photoemission (3PPE) process from only 1.55 eV illumination. In this scheme, if the across-bandgap absorption is indeed responsible for the observed polarization dependence, then the rotation of the polarization of the 1.55 eV pump should modulate the photoemission intensity only at positive time delays and not negative time delays, despite maintaining the same fluence of the pump and probe. In Figure A.18(a) and (b), we show the PEEM images at time delays of +0.475 ps and -0.475 ps, respectively, and in Figure A.18(c), we plot the integrated photoemission intensity from the body of the flake, which is marked in red in Figure A.18(a) and blue in (b). These time delays are chosen to avoid the cross-correlation of the pump and probe. We clearly observe a polarization modulation at +0.475 ps, but not at -0.475 ps, which confirms that the observed polarization modulation is not a polarization modulation of the final absorption. Because the β maps for 1.55 eV, a 3PPE process, and 2.4 eV, a 2PPE process, are extremely similar (Figure 4.2 and Figure A.12), we can conclude that the polarization modulation is due to the across-bandgap absorption.

A.4.4 Sublimation Experiments

To probe the possibility of specific edge reconstructions contributing to the edge-dependent optical anisotropy, we heat a BP flake in UHV to the point of sublimation (>400°C) to create eye-shaped holes with well-defined edges in the [100] (AC) direction.[146,147] A.19(a) and (b) show PEEM images taken with broadband Hg-lamp (5.1 eV) illumination before and after sublimation. In addition to some sublimation at the edges of the flakes, we see obvious eye-shaped holes in the interior of the flakes with a depth of 1-3 nm, as confirmed by AFM in A.19(c). Power series with $h\nu = 2.4$ eV before and after sublimation confirm a 2-photon photoemission process, as shown in figures A.20 and A.21. The polarization-dependence at hν= 2.4 eV shown for the unannealed and sublimated flake in figures A.22 and A.23, respectively. A comparison between the direction of the holes in Figure A.19(b) and Figure A.23(a) and the β values in Figure A.22(c) and Figure A.23(c) shows that the elongated holes are roughly aligned along $\theta = 110°$, providing secondary affirmation of our assignment to β as the AC direction. Close inspection of Figure A.22 and Figure A.23 show the appearance of holes in the ρ map of A.23(d), but we do not observe any strong phaseshift around the hole edges in A.23(c). Because the edges of the holes have a maximum depth of ~3 nm on top of ~100 nm (A.19(c) and (d)), we surmise that the absence of an apparent phaseshift is because of the small contribution of the edge signal compared to interior signal within the signal to noise ratio of our experiments. This observation is consistent with our DFT results discussed below and in the main text where the transitions from the interior are more intense than transitions at the edges, making it challenging to observe edge transitions with thin BP flakes.

A.4.5 Angle-dependent electronic dipole transitions

For an optical transition from an electronic state i to another state f, the electronic transition dipole moment is given by $\mathbf{D} = f\nabla i$, where the electronic wavefunctions i and f can be obtained by first-principles DFT calculations through the VASP package.[139] Then the transition dipole moment $\mathbf{D}$ is computed using the VASPKIT code.[143] It is typically a complex vector and can be defined as $\boldsymbol{D} = \begin{pmatrix} D_x \\ D_y \\ D_z \end{pmatrix} = \begin{pmatrix} |D_x|e^{i\phi_x} \\ |D_y|e^{i\phi_y} \\ |D_z|e^{i\phi_z} \end{pmatrix}$. When the electron-photon interaction is treated within the dipole approximation, the optical transition matrix element is proportional to $\boldsymbol{P} \cdot \boldsymbol{D}$, where $\boldsymbol{P}$ is the electric polarization vector of the light and defined as $\boldsymbol{P} = (\cos\theta, \sin\theta,\ 0)$. The optical absorption intensity is then given by $I \propto |\boldsymbol{P} \cdot \boldsymbol{D}|^2$. To obtain a nonzero intensity, $\boldsymbol{D}$ should have a component parallel to the light polarization vector $\boldsymbol{P}$, which is an important selection rule for the optical transition.[139]

The relation between the intensity and light polarization angle can be shown as

$$
\begin{aligned}
I &\propto \left| (\cos\theta, \sin\theta,\ 0) \begin{pmatrix} |D_x| e^{i\phi_x} \\ |D_y| e^{i\phi_y} \\ |D_z| e^{i\phi_z} \end{pmatrix} \right|^2 \\
&\propto \left| (|D_x| \cos\theta e^{i\phi_x} + |D_y| \sin\theta e^{i\phi_y}) \right|^2 \\
&\propto (|D_x| \cos\theta e^{i\phi_x} + |D_y| \sin\theta e^{i\phi_y})\ (|D_x| \cos\theta e^{-i\phi_x} + |D_y| \sin\theta e^{-i\phi_y}) \\
&\propto |D_x|^2 \cos^2\theta + |D_y|^2 \sin^2\theta + |D_x||D_y| \cos\theta \sin\theta (e^{i(\phi_x - \phi_y)} + e^{-i(\phi_x - \phi_y)}) \\
&\propto |D_x|^2 \cos^2\theta + |D_y|^2 \sin^2\theta + 2|D_x||D_y| \cos\theta \sin\theta \cos(\phi_x - \phi_y) \\
&\propto |D_x|^2 \left[\cos^2\theta + \frac{|D_y|^2}{|D_x|^2} \sin^2\theta + 2\frac{|D_y|}{|D_x|} \cos\theta \sin\theta \cos(\phi_x - \phi_y) \right] \\
&\propto |D_x|^2 \left[\cos^2\theta + r^2 \sin^2\theta + 2r \cos\theta \sin\theta \cos\phi_{xy} \right] \qquad \text{(A.3)}
\end{aligned}
$$

The formula suggests that the maximum intensity direction depends on the ratio $r = \frac{|D_y|}{|D_x|}$ and the phase angle difference $\phi_{xy} = \phi_x - \phi_y$. To determine the angle corresponding to the maximum intensity, we need to do $\frac{\partial I}{\partial \theta} = 0$, which gives

$$
\tan 2\theta_{\text{max}} = -\frac{2r \cos\phi_{xy}}{r^2 - 1}
$$

To understand the experimentally observed phase-shifted behavior at the edges of BP flakes, we carried out first-principles DFT calculations on a (1,3) reconstructed edge of monolayer BP that has been studied previously.[120] The armchair (AC) direction is defined as (1,0) while the zigzag (ZZ) direction corresponds to (0,1). Figure A.24(a) shows the calculated electronic band structure of the BP nanoribbon with the (1,3) edge, where the valence band maximum and conduction band minimum are denoted as VBM and CBM, respectively. By computing the contribution of the edge atoms to each band state (see the red circles), we can determine the two bands below the Fermi level (VBM and VBM-1) as edge bands. To determine whether different electronic transitions respond differently to the linear polarization of the excitation photons, we selected two representative transitions around 0.95 eV involving different valence and conduction states, as indicated by the arrows in Figure A.24(a). Note that the indices of transitions (#2 and #11) indicate the ordering of these transitions among all possible transitions of 0.95 eV, as will be discussed in Table A.2 below. For transition #2 in Figure A.24(b), the spatial distributions of charge densities of its initial valence state and final conduction state are plotted. The initial state is from an edge band (VBM-1) that has charge densities localized around the edges of the nanoribbon, while the final state has charge densities that are mostly localized around the edges with a certain degree of extension towards the interior. Similar charge density distributions are found for the initial and final states in transition #11 in Figure A.24(c), where the initial state is from another edge band (VBM). For both transitions, because the electronic wavefunctions and charge densities are confined at the rough edges of BP that have significant symmetry reduction compared to the interior atomic structure, their spatial distributions and symmetries are considerably modified compared to those in the interior of BP. Consequently, the transition dipole moments of both transitions are notably rotated away from the AC direction, i.e., the horizontal direction or 0.0° in Figure A.24. Such phase shifts are evident in the polarization-angle-dependent optical absorption profiles shown in Figure A.24(b-c), where the angle of maximum absorption is 47° and 69°, respectively. These results are in stark contrast to typical optical transitions that occur in the interior of BP. Taking the transition from VBM-2 to CBM at k-point #2 as an example (Figure A.25(b)), both initial and final states correspond to typical ones from the interior of the nanoribbon (i.e., the bulk part), and thus the transition dipole moment and the maximum absorption are along the AC direction, an expected result for 2D BP systems, where the absorption coefficient for an electric field polarized along the armchair direction of the lattice significantly exceeds that of the zigzag direction when the excitation energy is below 3 eV.[12,139] In short, our calculations demonstrate that the optical selection rule is clearly changed at the edges due to the 1D confinement and symmetry reduction in comparison with the 2D BP, leading to orientation changes of the transition dipole moments at the edges and subsequently experimentally observed phase variations in the maximum absorption direction between the edges and interior. Similar modifications of optical selection rules due to edges have been observed in BP by Raman spectroscopy with the appearance of edge-dependent Raman modes.[101]

In addition to studying a few representative optical transitions in the (1,3)-edge nanoribbon, as described above (also in the main text), we considered all possible transitions between the valence bands and conduction bands in the Brillouin zone (BZ) that satisfy the energy conservation relation: $|\epsilon_{c\mathbf{k}} - \epsilon_{v\mathbf{k}} - \omega| \leq 0.03$ eV, where $\epsilon_{c\mathbf{k}}$ ($\epsilon_{v\mathbf{k}}$) indicates the energy of an conduction (valence) band state at the k-point $\mathbf{k}$, ω corresponds to the incoming photon energy, and 0.03 eV represents the δ function. Please note that because of the limitations of energy accuracy with DFT, this discussion is for qualitative rather than for quantitative comparison with photon energies discussed in the main text of the paper. For an optical transition of 0.95 eV, there are 13 eligible transitions in total, as shown in Table A.2. For each transition, we calculated the transition dipole moment and the polarization-angle-dependent optical absorption. The maximum intensity and the maximum absorption direction are shown in Table A.2, where different transitions clearly show different intensities and maximum absorption directions. Since all 13 transitions are related to edge states, their maximum absorption directions are all shifted away from the armchair direction. Finally, we computed the averaged angle-dependent intensity by considering contributions from all the transitions, following the formula

$$\overline{I}(\theta) = \frac{\sum_{i=1}^{N} I_i(\theta) W_i}{\sum_{i=1}^{N} W_i}, \tag{A.4}$$

where N is the total number of transitions (13 in this case), $I_i(\theta)$ is the intensity of transition i at the polarization angle of θ, and $\mathrm{W_i}$ represents the weight of transition i (set as 1 for equal contribution). As shown in Table A.2, the maximum absorption direction for the optical transition of 0.95 eV is at 22.0° after averaging (in other words, 22.0° phase shift away from the armchair direction). For an optical transition of 1.00 eV, the situation becomes more complicated, since it involves 24 eligible transitions between the valence and conduction bands at different k-points, as shown in Figure A.25 and Table A.3. More importantly, there are 4 transitions from VBM-2 to CBM (transition #1-#4) where both initial and final states correspond to the interior (or bulk) states (see Figure A.25(b) as an example), and therefore the optical selection rule is unaffected and the maximum absorption direction is along the AC direction (i.e., 0.0°) for these 4 transitions. For the other 20 transitions shown in Table A.3, their initial and/or final states are localized at the edges (Figure A.25(c-d)), and thus their maximum absorption directions are shifted away from the AC direction. We note that transitions #1-#4 originating from the interior show significantly stronger intensities than other transitions related to the edges, and hence they make dominant contributions to the averaged intensity shown in Equation A.4. Eventually, the averaged angle of maximum intensity is at 2.0° for the optical transition of 1.00 eV, as shown in Table A.3.

Finally, for the monolayer BP nanoribbon with the (1,3) edge, we calculated the averaged angle of maximum intensity as a function of the excitation photon energy in the range of 0.75-1.40 eV (Figure A.26). The averaged phase shift is mostly within ±10°. For excitation energies that do not involve transitions between the interior states (e.g., around 0.95 eV and around 1.20 eV), the phase shift is notably larger and can be more than 20°. Note that DFT calculations tend to underestimate the electronic band gap of BP systems, and the calculated band gap of monolayer BP is less than 50% of the experimental optical gap.[12,120]

Therefore, the excitation energies discussed in our calculations cannot be directly compared to the experimental values such as 1.55 and 2.40 eV. Nevertheless, the DFT results discussed above provide insightful information regarding optical transition processes and reveal the underlying microscopic picture of how the edges of BP modify the electronic wavefunctions and the optical selection rules, giving rise to edge-specific absorption profiles that are different from the absorption behaviors observed in 2D (or interior) BP flakes. Numerically, our calculations corroborated the experimental findings that the phase shifts with respect to the AC direction can be significant at the edges.

A.4.6 Supplementary figures and tables

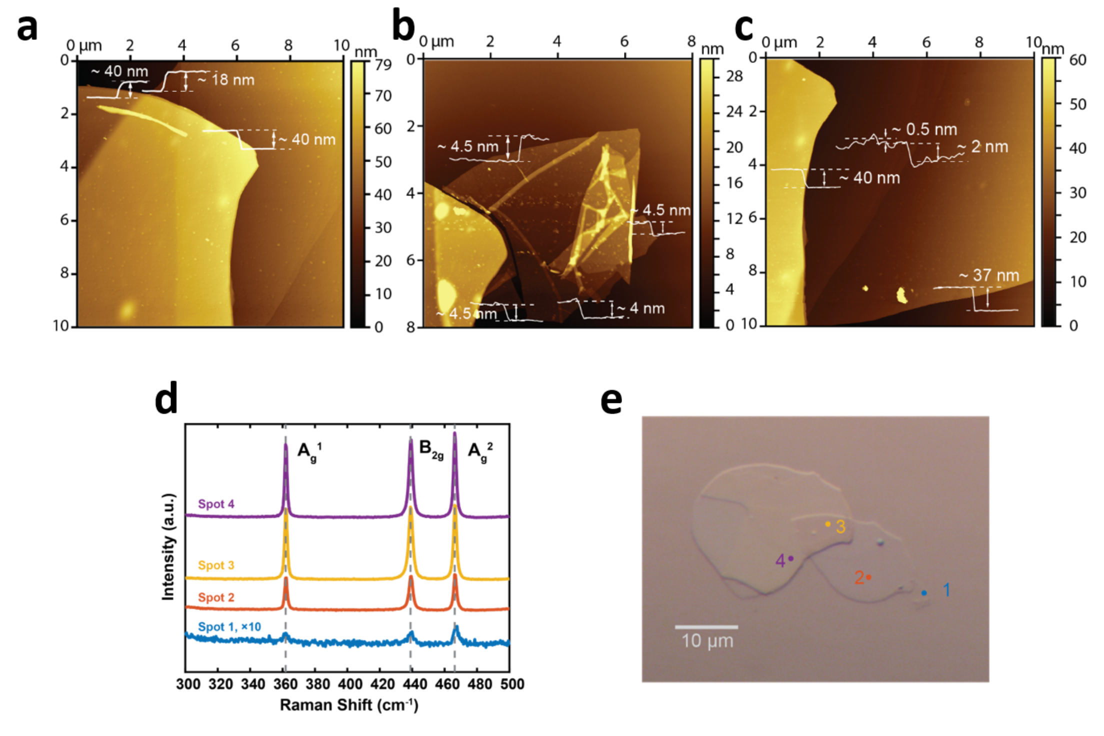

Figure A.6: Characterization of few-layer BP flake 1. (a)-(c) AFM images of different portions of few-layer black phosphorus sample on Si with 2 nm native oxide layer. Thicknesses range from 4 nm (8 layers) to 58 nm (116 layers). (d) Raman spectroscopy of black phosphorus, with characteristic A_g^1, B_{2g}, and A_g^2 peaks at 362, 439, and 466 cm^{-1}, respectively. Raman spectra were taken from the marked spots on the optical image. (e) Optical image of BP flake on Si substrate with native oxide.

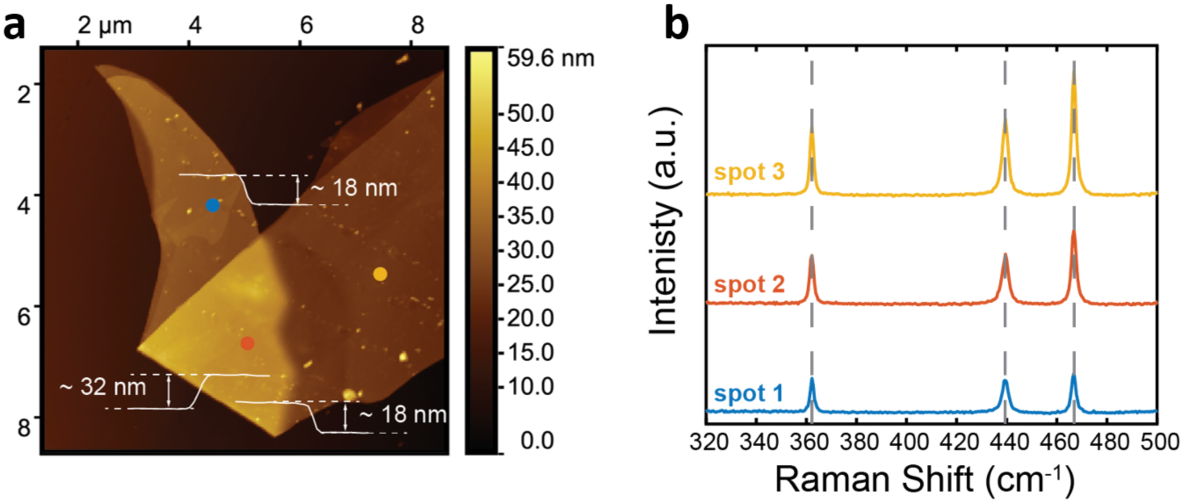

Figure A.7: Characterization of few-layer BP flake 2. (a) AFM image of few-layer BP sample on Si with 2 nm native oxide layer. The upper left piece of the flake is folded under the main body of the flake. The non-overlapped regions of the flake are each ∼18 nm (36 layers) thick, and the region of overlap is measured to be 32 nm thick. The blue, red, and yellow points denote where Raman spectra were taken. (b) Raman spectroscopy of black phosphorus, with characteristic A_g^1, B_{2g}, and A_g^2 peaks at 362, 439, and 466 cm^{-1}, respectively.

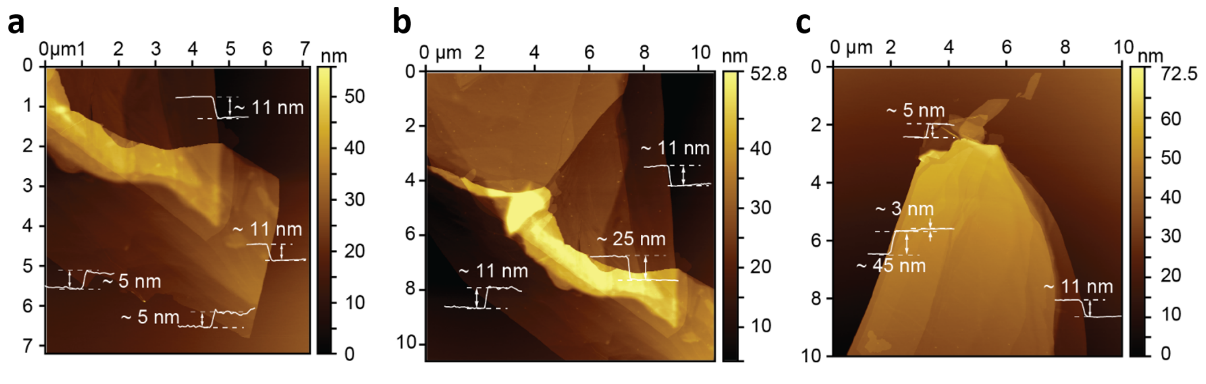

Figure A.8: Characterization of few-layer BP flake 3. (a)-(c) AFM images of few-layer BP sample on Si with 2 nm native oxide layer. The measured thicknesses range from 5 nm (10 layers) to 45 nm (90 layers). In (a) and (b), a portion of the flake (11 nm thick) appears to have broken during mechanical exfoliation. A thicker portion (25 nm thick) appears to be the region in which these two broken pieces overlap. AFM images were taken post-annealing at 350°C.

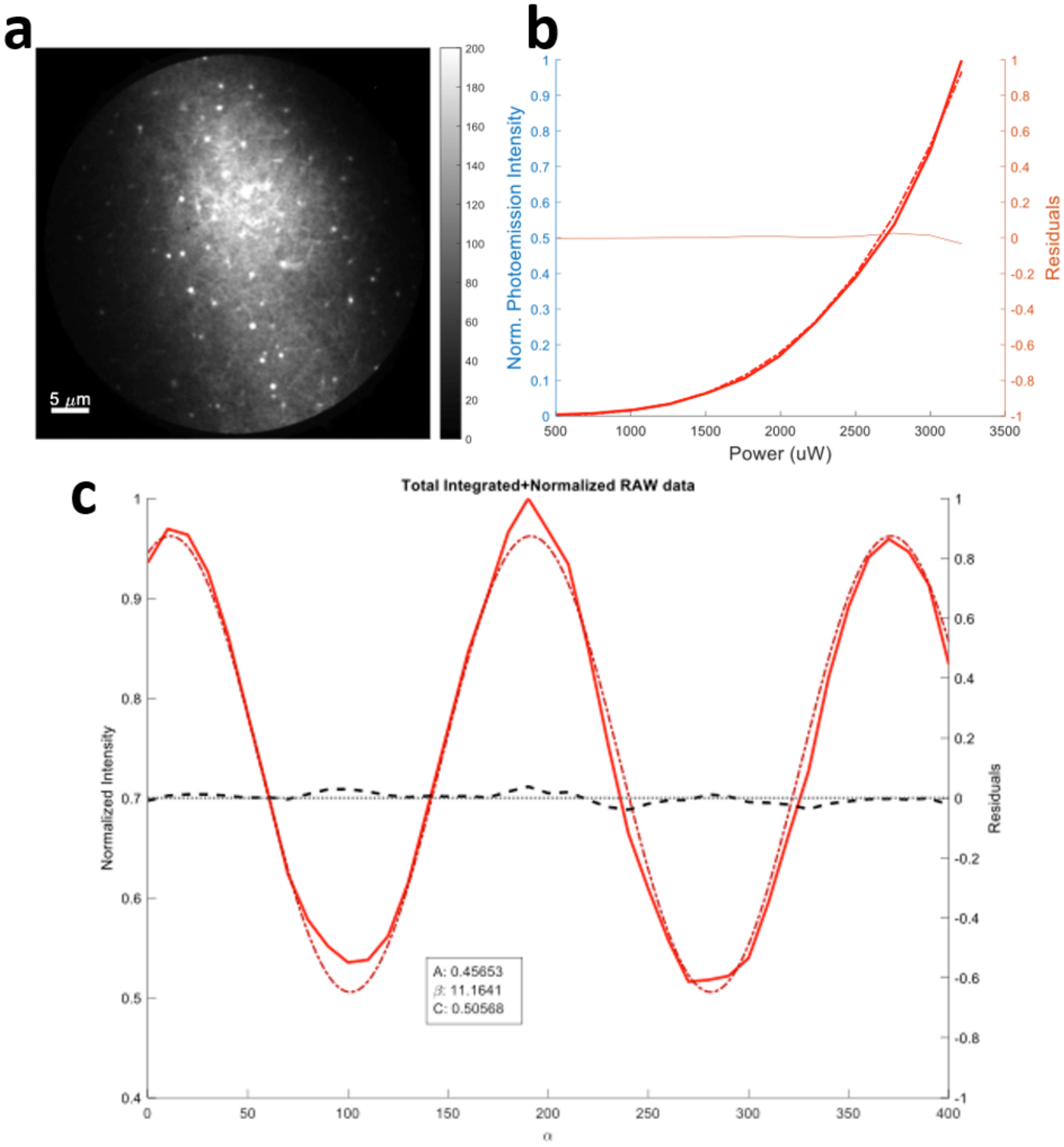

Figure A.9: Rh mirror calibration for 2.4 eV with graphene/SiO_2/Si substrate. (a) PEEM image with 2.4 eV illumination. The scale bar is 5 μm. (b) Power dependence of the integrated field of view (FOV) shown in (a). Power series is fit with the equation $I_{PE} = Ax^b$ where x is the incident laser power, A is a fitting coefficient, and b is the number of photons required for the photoemission process. The residuals of the fit are plotted against the right-hand y-axis. (c) Polarization dependence with an incident power of 3.21 mW (solid line) and fit with Equation 4.1 (dashed line).

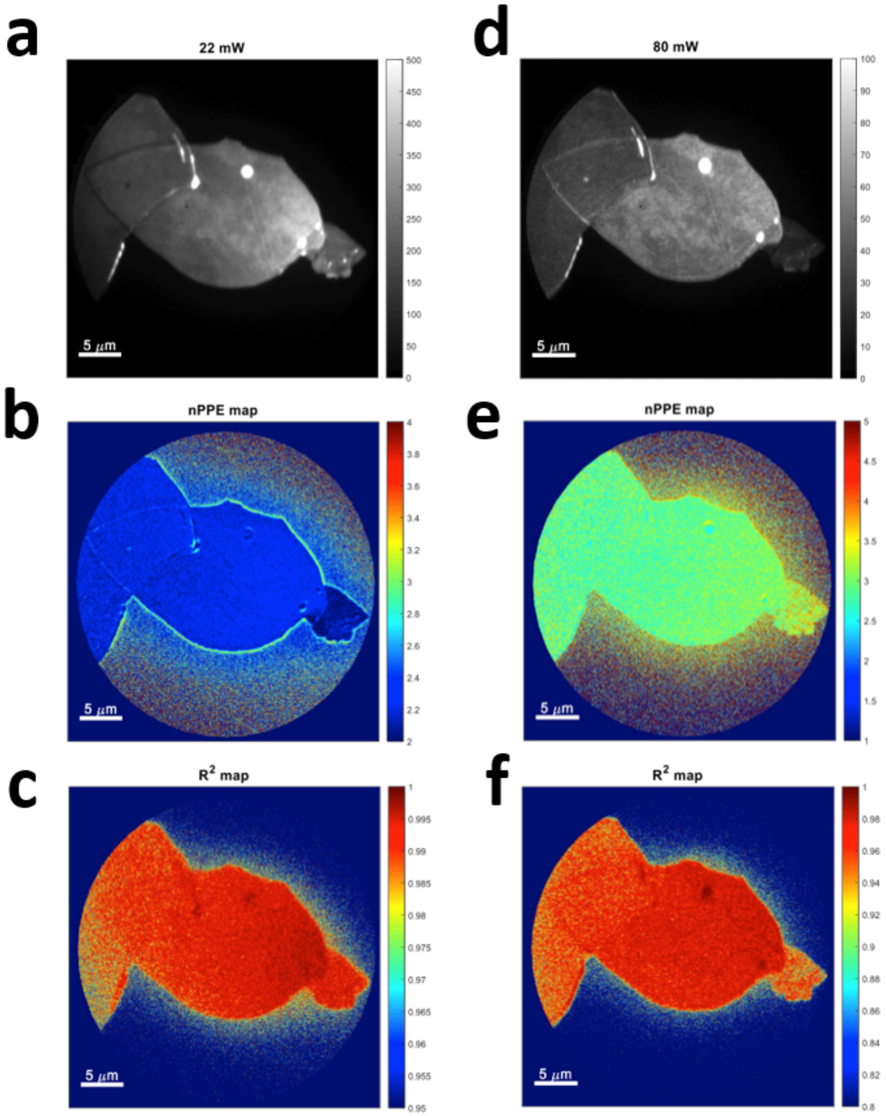

Figure A.10: Representative power series for 2.4 eV and 1.55 eV illumination. (a)-(c) Power series data for BP flake 1 with 2.4 eV. Data was taken with laser powers from 8 mW to 22 mW in 2 mW increments, staying under the space charging limit. (a) PEEM image taken with 22 mW. (b) Pixel-by-pixel map fit with equation $I_{PE,graphene} = Ax^b$ where x is the incident laser power, A is a fitting coefficient, and b is the number of photons required for the photoemission process. The value of b is shown for each pixel. For hν=2.4 eV, the photoemission is clearly a 2-photon process, as expected for few-layer BP. (c) The pixel-by-pixel map of the goodness-of-fit parameter, R^2, as extracted from the fit described in (b). (d)-(f) Power series data with 1.55 eV. Data was taken with laser powers from 30 to 80 mW in 5 mW increments. (d) PEEM image taken with 80 mW. (e) Pixel-by-pixel map as described in (b). For hν=1.55 eV, the photoemission is clearly a 3-photon process, as expected for few-layer BP. (f) Pixel-by-pixel map of R^2 from fit in (e).

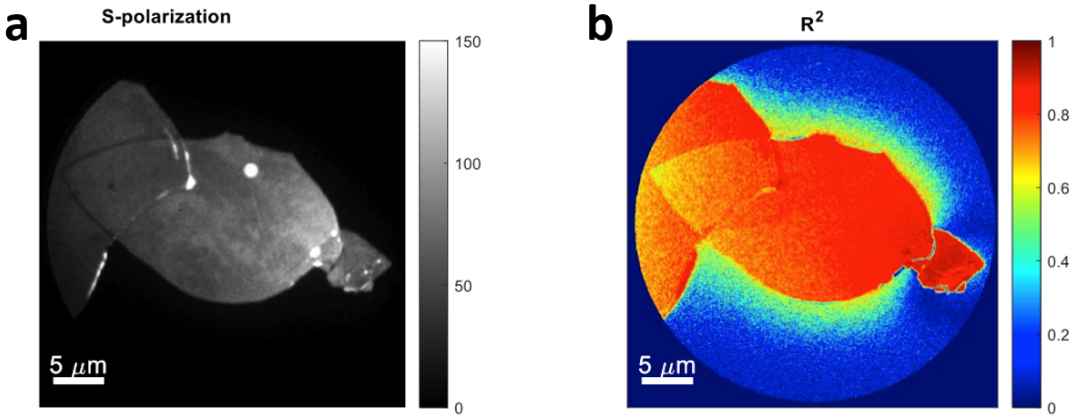

Figure A.11: PEEM images of flake 1 with 2.4 eV illumination. (a) S-polarized ($\theta = 0°$) PEEM image with correction for rhodium mirror reflectivity. (b) R^2 pixel-by-pixel map corresponding to β and ρ mapping shown in Figure 4.2(a) and (b).

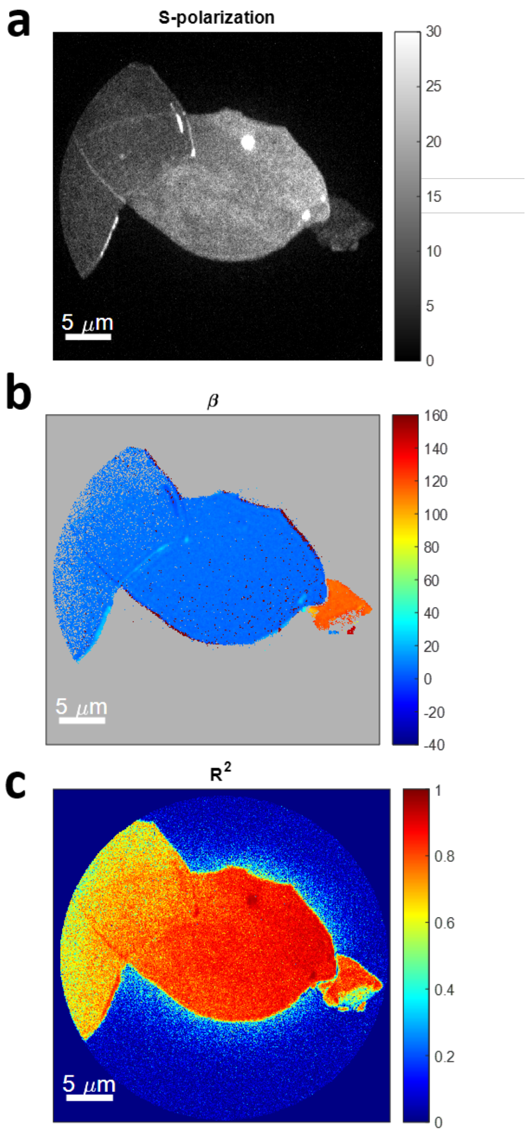

Figure A.12: PEEM images of flake 1 with 1.55 eV illumination. (a) S-polarized ($\theta = 0°$) PEEM image with correction for rhodium mirror reflectivity. (b) β map with goodness-of-fit thresholding for R^2>0.6. The behavior is qualitatively similar to that observed in Figure 4.2(a). (c) R^2 pixel-by-pixel map corresponding to β and ρ mapping shown in (b) and Figure 4.2(c).

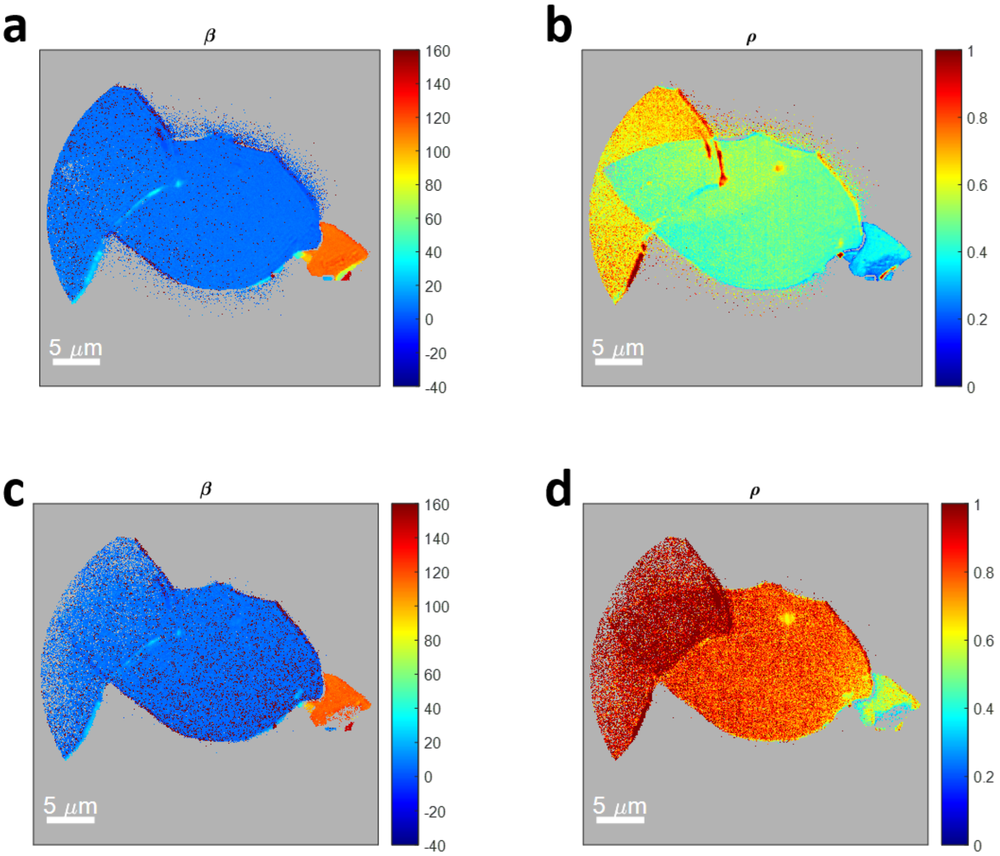

Figure A.13: Unfiltered β and rho maps for 2.4 eV and 1.55 eV illumination. (a), (b) Unfiltered maps for hν=2.4 eV. (c), (d) Unfiltered maps for hν = 1.55 eV. All maps are shown with R^2>0.6 as shown in Figure 4.2, Figure A.11, and Figure A.12.

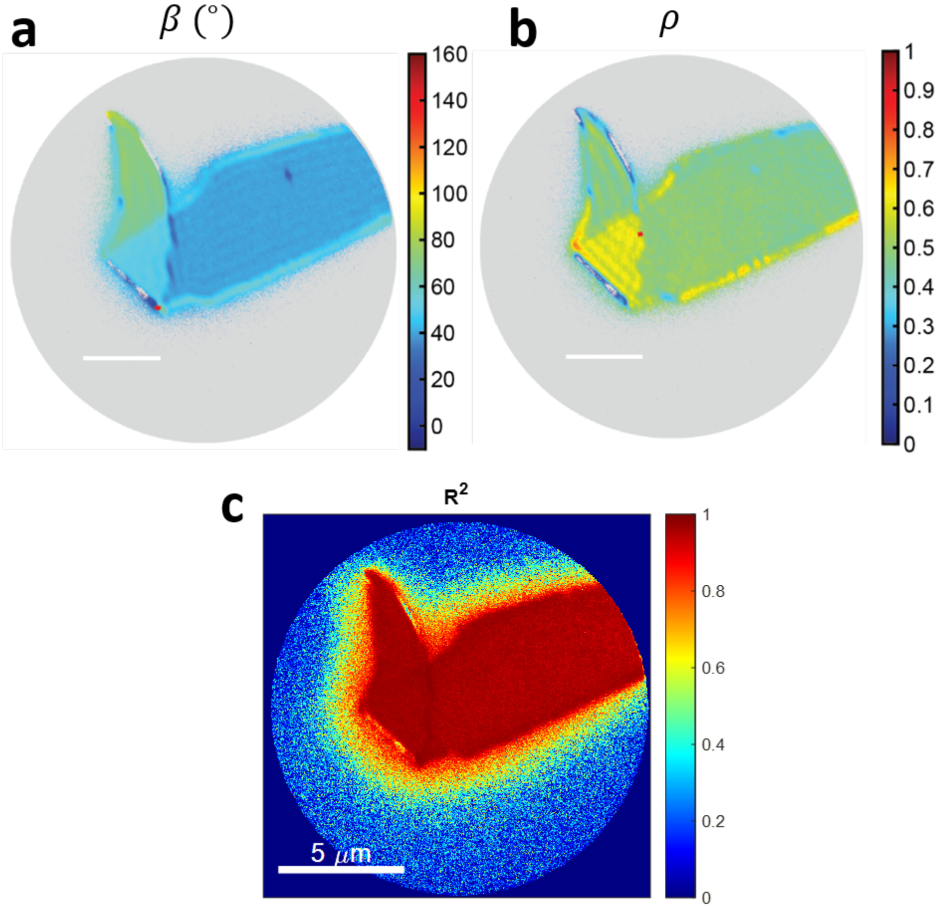

Figure A.14: Pixel-by-pixel mapping for flake 2 with 2.4 eV illumination. (a) β map, (b) ρ map. Both maps are shown with $R^2 > 0.8$. The locations of the β and ρ line cuts in Figure 4.3 of the main paper are shown with small red lines. (c) R^2 goodness of fit map for Figure 4.3 and (b).

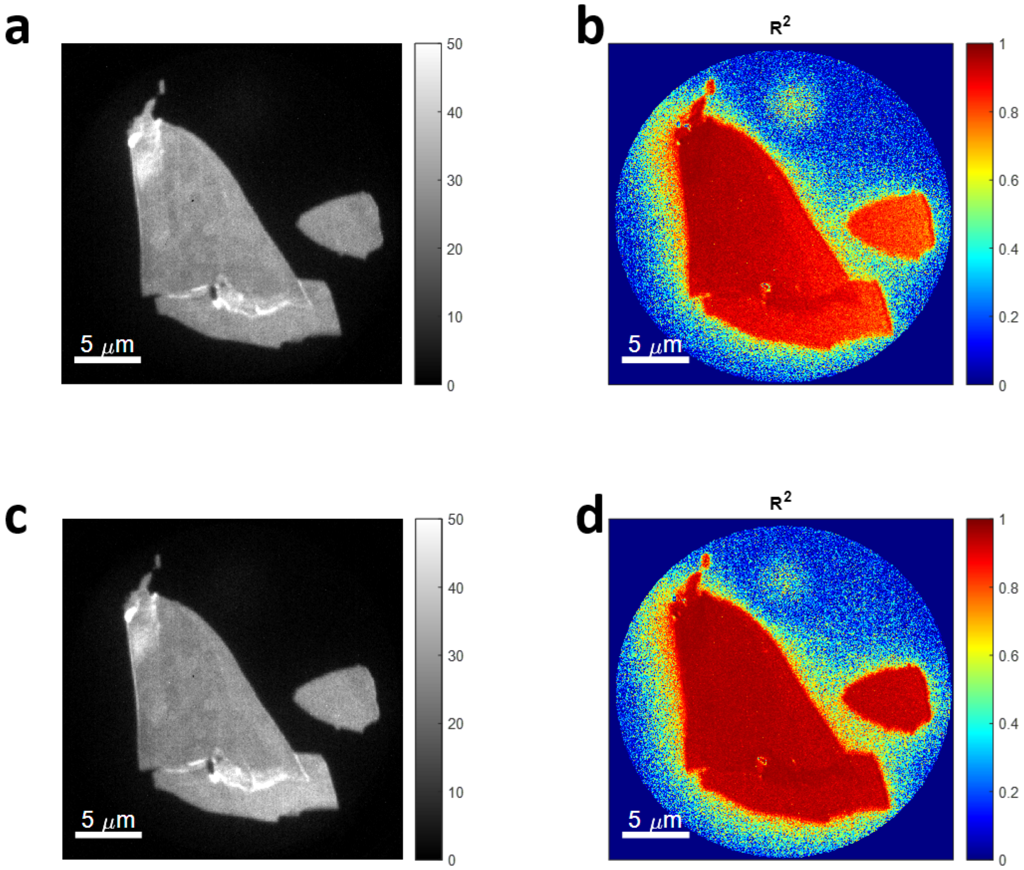

Figure A.15: PEEM images and R^2 maps for unannealed and annealed flake of Flake 3 with 2.4 eV illumination. (a) and (c) are the PEEM images taken at $\theta = 0°$ for the unannealed and 350°C annealed flake, respectively. (b) and (d) are the R^2 maps for the unannealed and 350°C annealed flake, respectively. Annealing marginally improves the photoemission signal and pixel-by-pixel fitting quality.

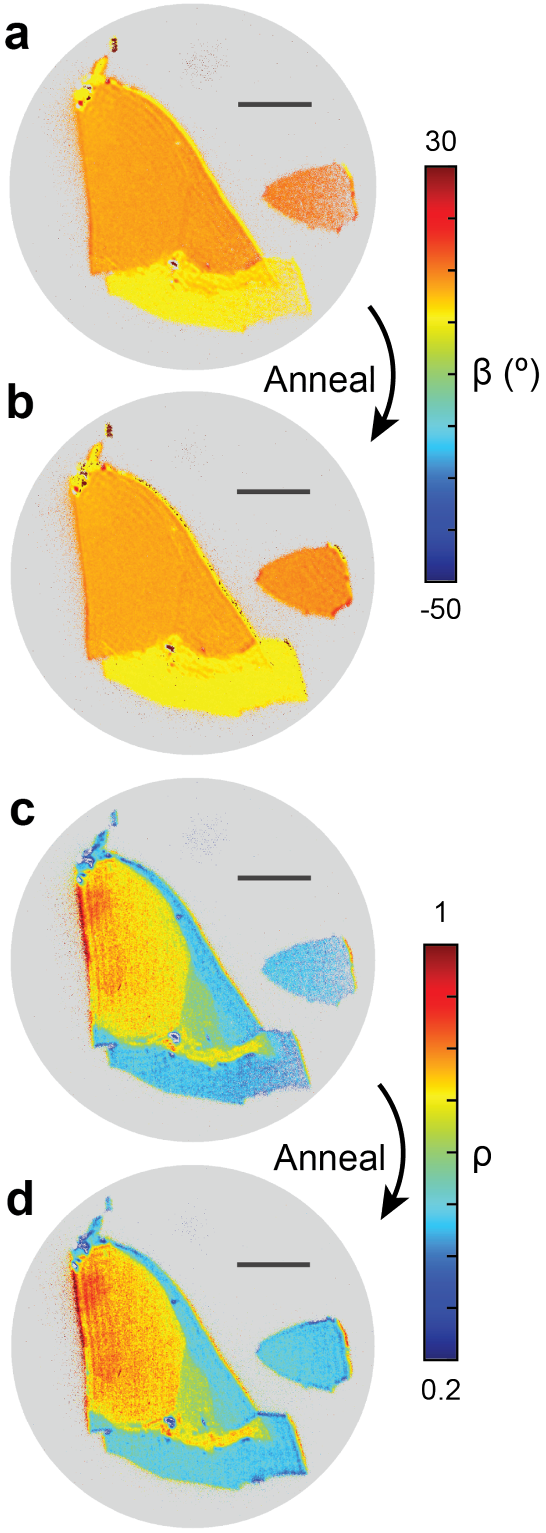

Figure A.16: (a) 2.4 eV β mapping of Flake 3 before and (b) after annealing at 350°C. (c) 2.4 eV ρ mapping before and (d) after annealing at 350°C. Scale bar: 5 μm. All maps are median-filtered and only pixels with an $\mathrm{R}^2$0.8 are shown.

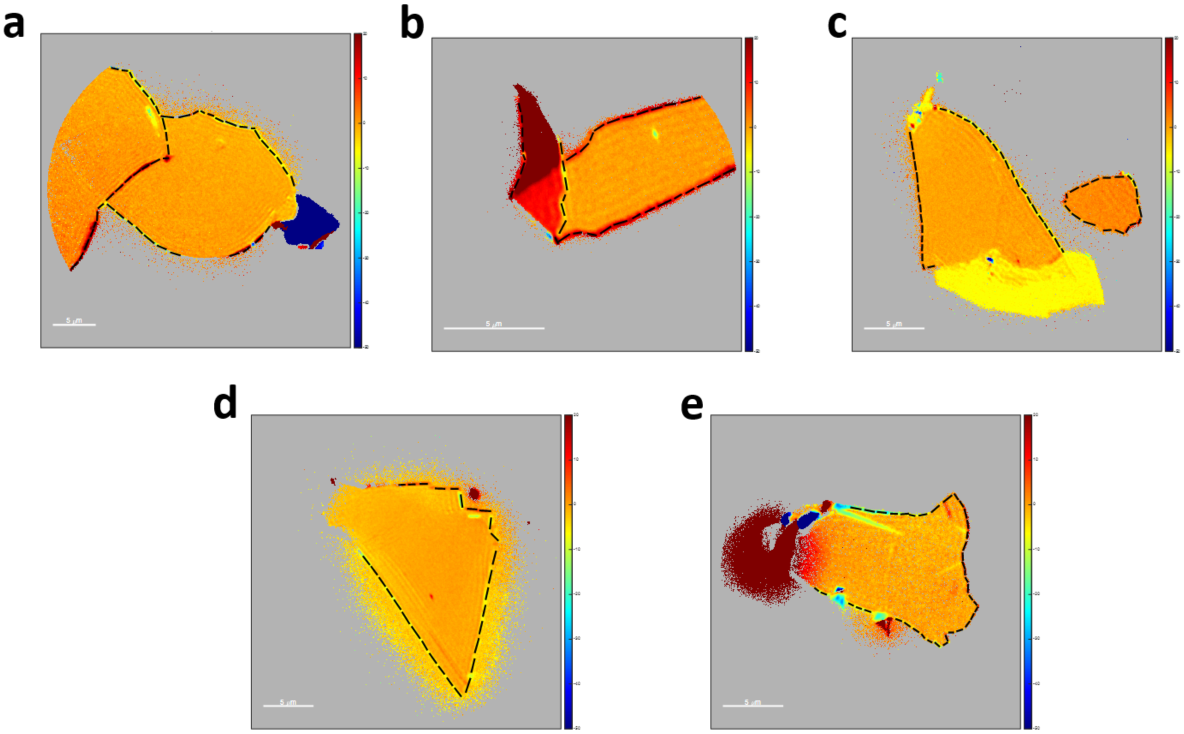

Figure A.17: $\delta\beta$ map linecuts of flake edges in Figure 4.4. (a) Flake 1 (b) Flake 2 (c) Flake 3 (d) Flake 4 (e) Flake 5. R^2thresholds for (a) and (e) are 0.6, (b), (c), and (d) are 0.8. The β values for the flake interiors represent the rotation of the lattice armchair axis with respect to the lab frame in Figure 4.1.They are as follows for these flakes: (a) Flake 1: 7°, (b) Flake 2: 40°, (c) Flake 3: 7°, (d) Flake 4: 38°, (e) Flake 5: 156°.

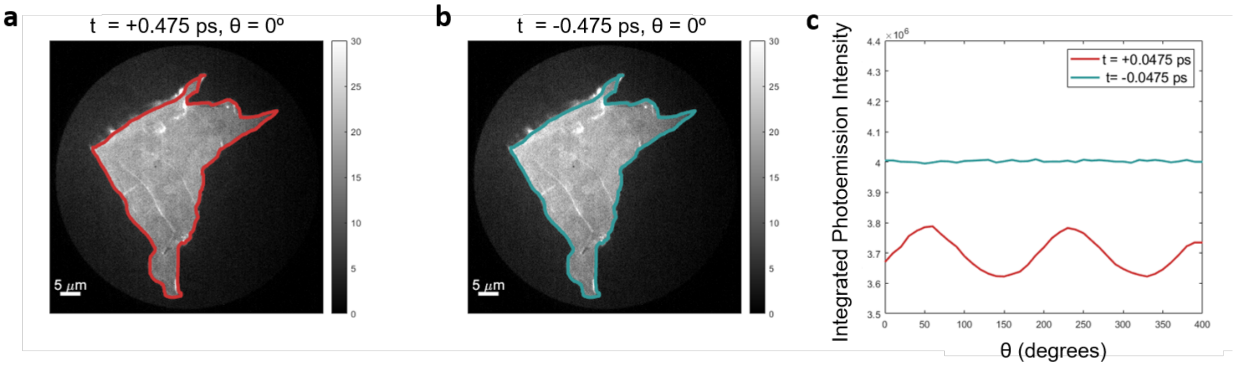

Figure A.18: Polarization dependence of hν=1.55 with 1.55 eV pump and 3.1 eV probe of flake 6. (a) Photoemission with $\theta = 0^\circ$ where 1.55 eV pump arrives 0.475 ps before probe (+0.475 ps) (b) Photoemission with $\theta = 0^\circ$ where 1.55 eV pump arrives 0.475 ps after probe (-0.475 ps) (c) Polarization dependence at +0.475 and -0.475 ps of the integrated areas shown in (a) and (b). The polarization response is clearly not due to the final state and is dependent on the absorption of the first photon.

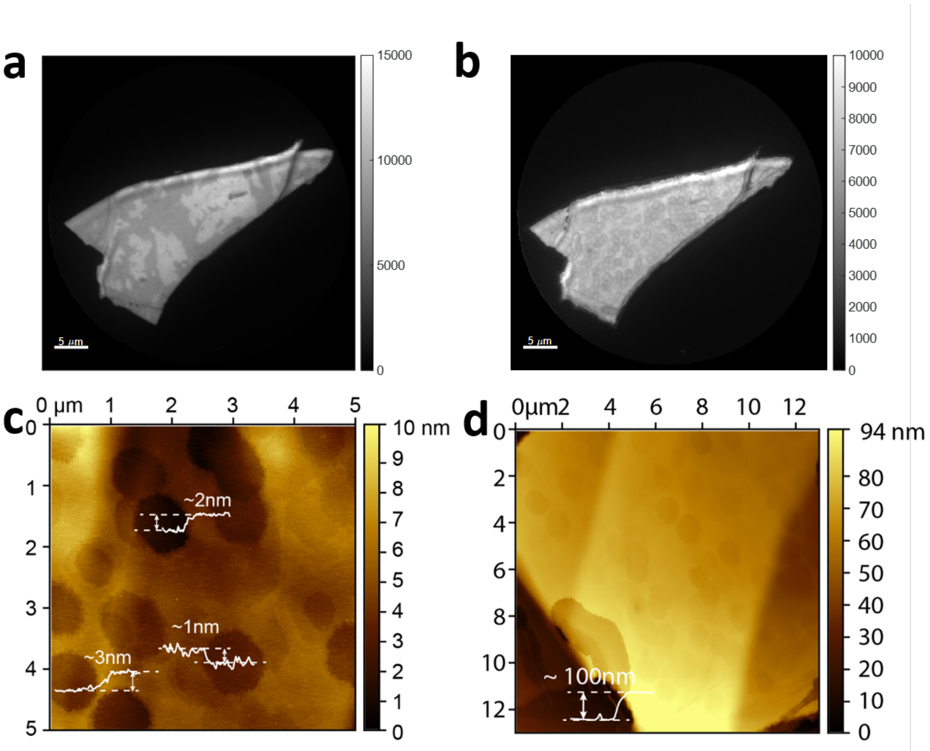

Figure A.19: Sublimation of BP flake 7. (a) PEEM image of BP flake taken with continuous-wave broadband Hg illumination before heating (b) PEEM image of BP flake with Hg illumination after heating to >400°C (c) AFM of holes with depth profiles of 1-3 nm (d) AFM of flake edge showing a thickness of ~100 nm.

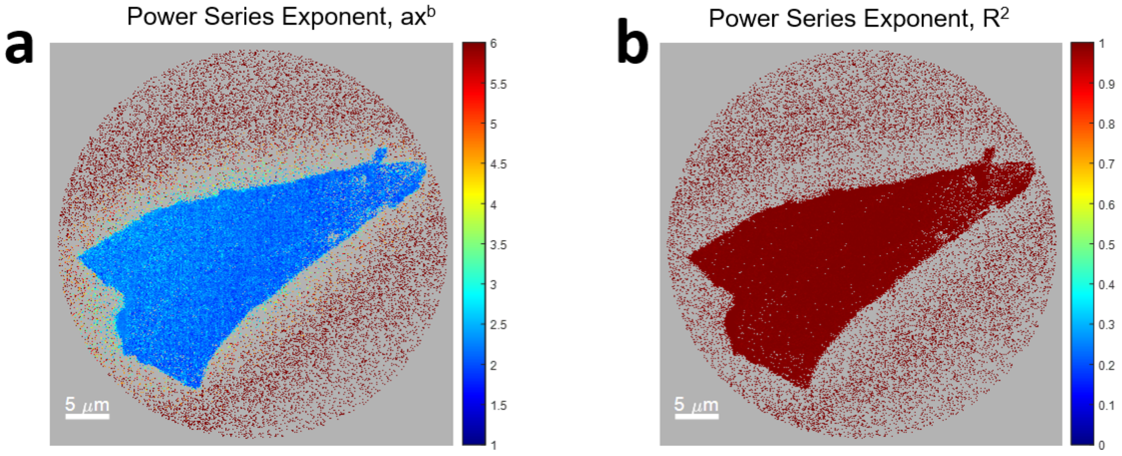

Figure A.20: Pixel-by-pixel power series map of unannealed BP flake 7 with $h\nu$=2.4 eV excitation. Intensities are fit to Ax^b, where b indicates the number of photons required for photoemission. (a) Map of b for each pixel and (b) goodness of fit R^2. Maps are pixels that exceed the threshold R^2=0.98.

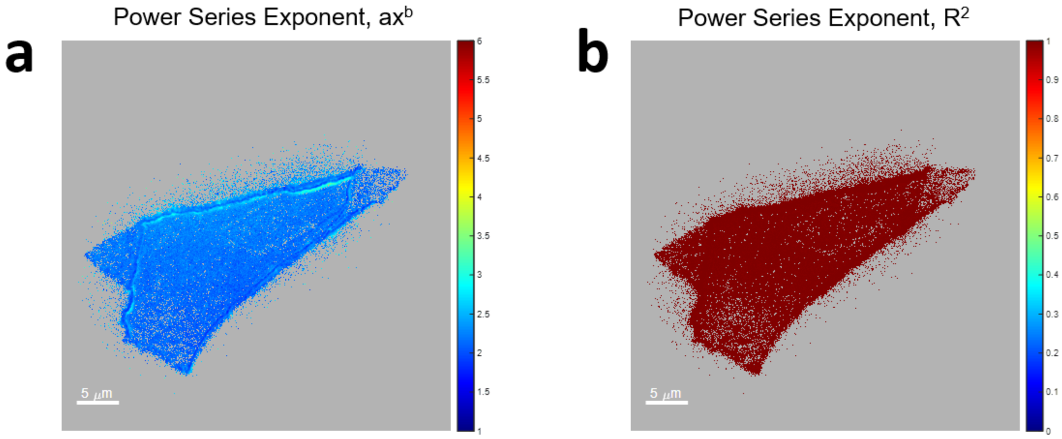

Figure A.21: Pixel-by-pixel power series map of sublimated BP flake 7 with $h\nu$=2.4 eV excitation. Intensities are fit to Ax^b, where b indicates the number of photons required for photoemission. (a) map of b for each pixel and (b) goodness of fit R^2. Maps are pixels that exceed the threshold R^2=0.99.

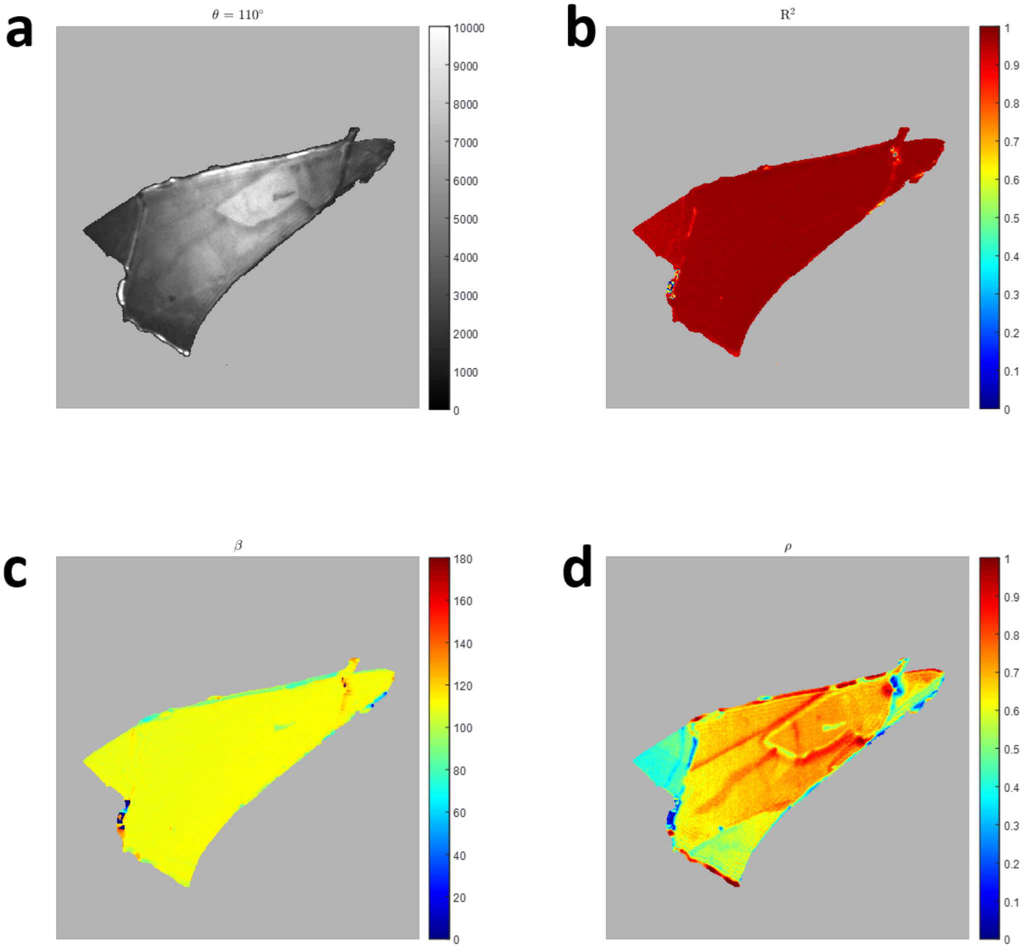

Figure A.22: Pixel-by-pixel polarization dependence map of unannealed BP flake with $h\nu$=2.4 eV excitation. (a) PEEM image where $\theta = 110°$ and (b) goodness of fit R^2 map (c) β map, which shows that the AC direction is aligned approximately along $\theta = 110°$ (d) ρ map. All maps show pixels that correspond to those that exceed a photoemission intensity of 1200 counts.

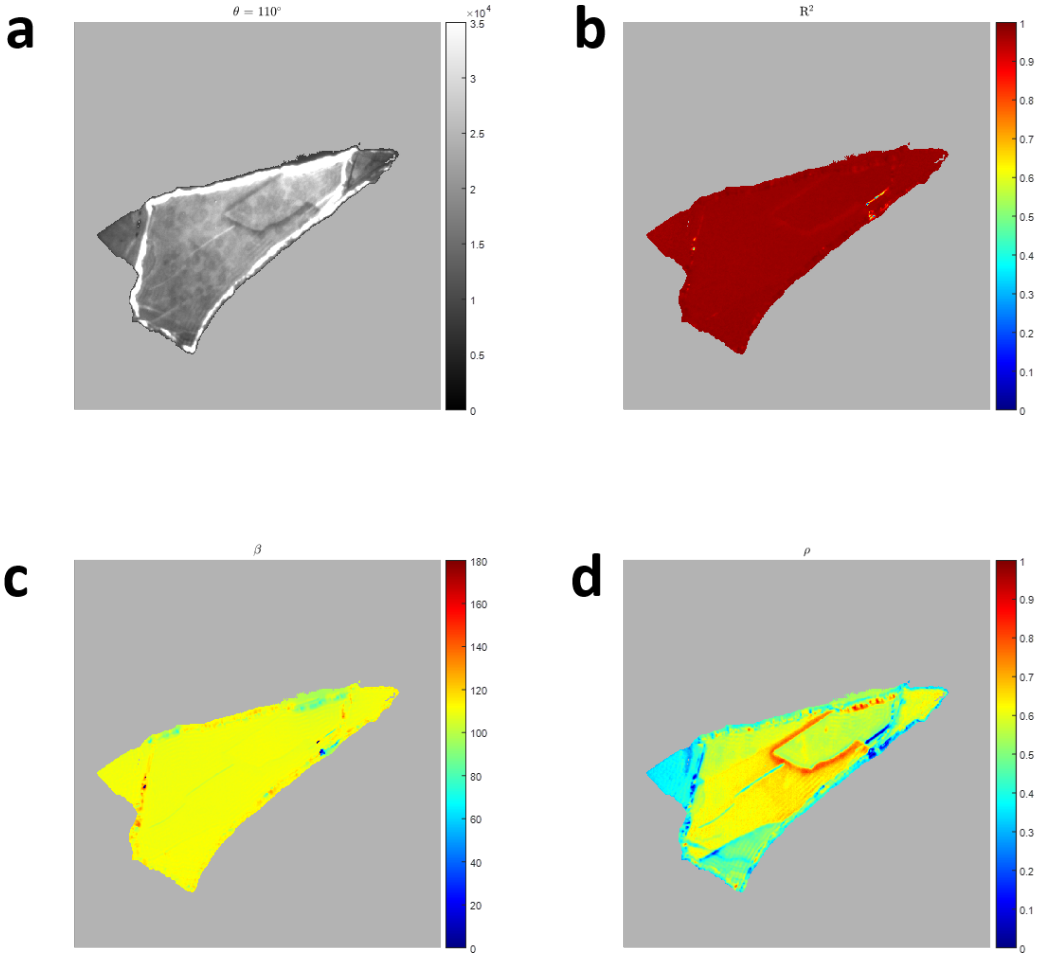

Figure A.23: Pixel-by-pixel polarization dependence map of sublimated BP flake with $h\nu$=2.4 eV excitation. (a) PEEM image where $\theta = 110^\circ$ (b) Goodness of fit R^2 map (c) β map, which shows that the AC direction is aligned approximately along $\theta = \mathbf{110}^\circ$ (d) ρ map. All maps show pixels that correspond to those that exceed a photoemission intensity of 8000 counts.

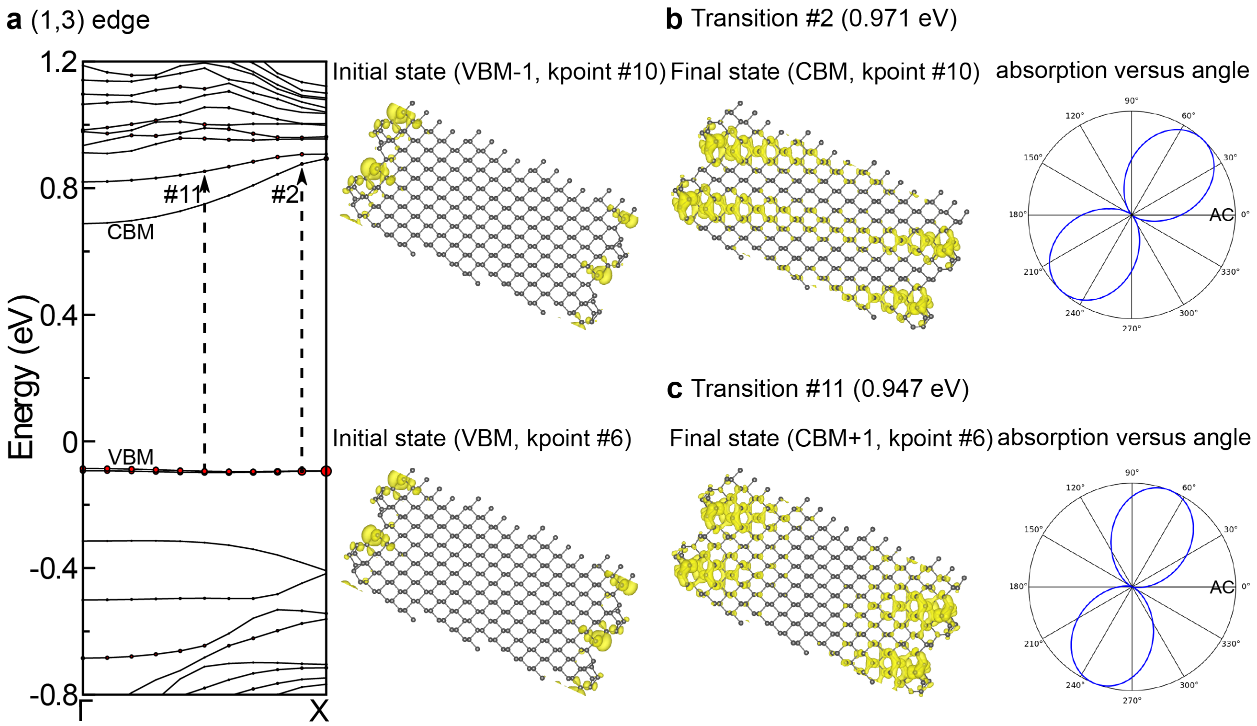

Figure A.24: (a) DFT calculated electronic band structure of the monolayer BP nanoribbon with a (1,3) reconstructed edge. The Fermi level is set at 0 eV. The valence band maximum and conduction band minimum are denoted as VBM and CBM, respectively. Red circles superimposed on the bands correspond to projected bands from the edge atoms. The size of a circle is proportional to the amplitude of the contribution of the edge atoms to a band state. The VBM and VBM-1 which are very close in energy are the only bands that have dominant contributions from the edge (i.e., edge bands). Two optical transitions around 0.95 eV are indicated by the arrows, and their charge density distributions of initial and final band states are shown in (b-c). For each transition, the polar profile of the absorption intensity versus the polarization angle is also presented. The armchair (AC) direction of BP is along the horizontal direction (i.e., 0.0°).

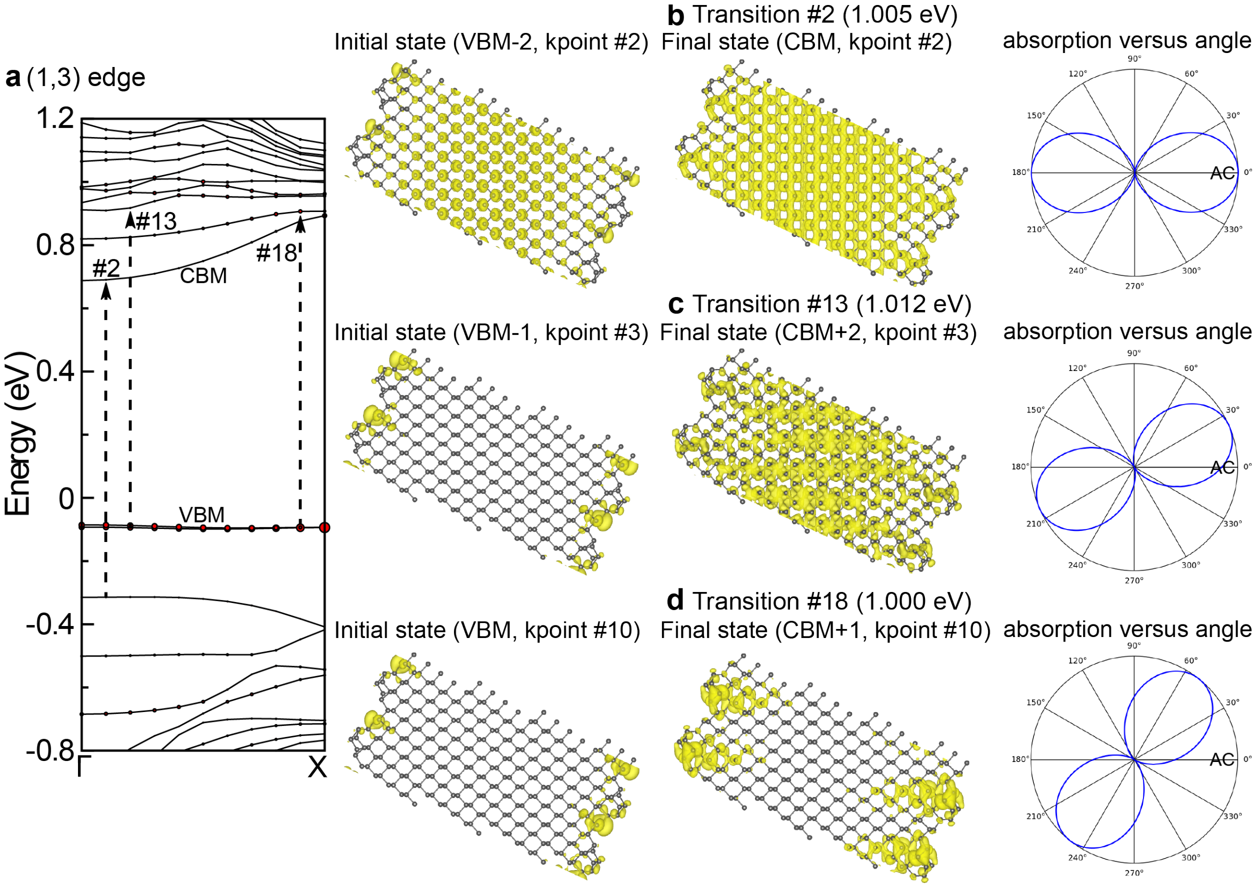

Figure A.25: (a) DFT calculated electronic band structure of the BP nanoribbon with the (1,3) edge. Red circles superimposed on the bands correspond to projected bands from the edge atoms. Three optical transitions at or near 1.0 eV are indicated by the arrows, and their charge density distributions of initial and final states are shown in (b-d). For each transition, the polar profile of the absorption intensity versus the polarization angle is also presented. The armchair (AC) direction of BP is along the horizontal direction (i.e., 0.0°).

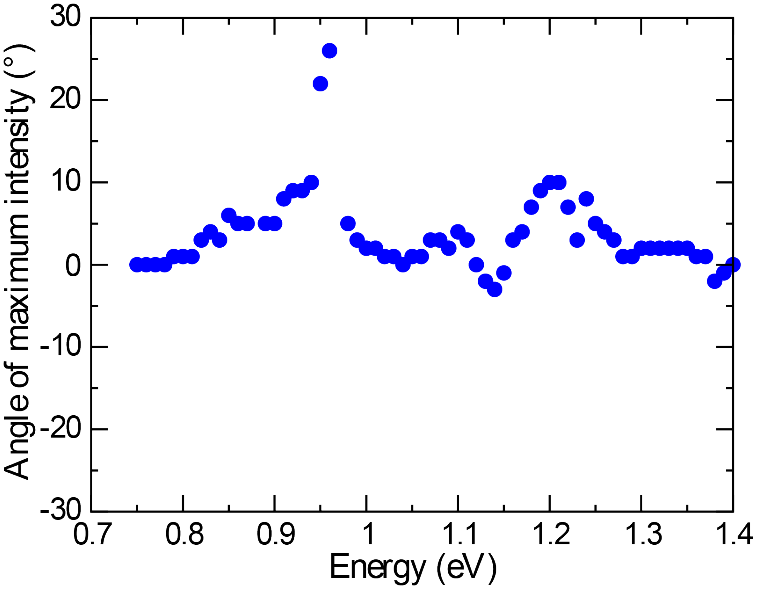

Figure A.26: DFT calculated averaged angle of maximum intensity as a function of the excitation energy for the BP nanoribbon with the (1,3) edge. The AC direction of BP is defined at 0°, so the angle of maximum intensity for the (1,3) edge is equivalent to the phase shift with respect to the AC direction. In the studied energy range, the averaged phase shift is mostly within ±10°.

Transition #	Energy (eV)	Band indices of initial and final states	kpoint #	Maximum intensity	Angle of maximum intensity (°)
1	0.939	349 → 351	9	8.69	57.0
2	0.971	349 → 351	10	13.40	47.0
3	0.927	349 → 352	4	27.37	5.0
4	0.938	349 → 352	5	24.55	8.0
5	0.951	349 → 352	6	21.22	12.0
6	0.966	349 → 352	7	17.52	15.0
7	0.938	350 → 351	9	22.97	8.0
8	0.970	350 → 351	10	10.96	13.0
9	0.921	350 → 352	4	4.91	73.0
10	0.933	350 → 352	5	6.29	72.0
11	0.947	350 → 352	6	6.97	69.0
12	0.963	350 → 352	7	7.48	65.0
13	0.979	350 → 352	8	8.58	60.0
average				11.73	22.0

Table A.2: For an optical transition of 0.95 eV in the monolayer BP nanoribbon with the (1,3) reconstructed edge, we considered all possible transitions between the valence and conduction bands (13 in total). For each transition, its energy, band indices of the valence and conduction states, and the kpoint index are shown. The indices of the valence band maximum (VBM) and conduction band minimum (CBM) are 350 and 351, respectively. For each transition, the transition dipole moment is calculated, which subsequently yields the polarization-angle-dependent optical absorption according to Equation A.3. The maximum intensity and the polarization angle corresponding to the maximum are shown in the table. The armchair (AC) direction of BP is at 0.0°. The averaged angle-dependent intensity is obtained by considering equal contributions from all the transitions, and its maximum value and the corresponding angle are listed at the bottom of the table. Two representative transitions (#2 and #11) as highlighted in light pink color are illustrated in Figure A.24.

Transition #	Energy (eV)	Band indices of i and f states	kpoint #	Maximum int.	Angle of maximum int. (°)
1	1.002	348 → 351	1	386.26	0.0
2	1.005	348 → 351	2	384.81	0.0
3	1.011	348 → 351	3	380.35	0.0
4	1.023	348 → 351	4	372.56	0.0
5	0.971	349 → 351	10	13.40	47.0
6	0.987	349 → 351	11	19.12	39.0
7	0.981	349 → 352	8	13.22	19.0
8	0.994	349 → 352	9	8.02	24.0
9	1.001	349 → 352	10	2.83	37.0
10	1.001	349 → 352	11	1.67	68.0
11	1.004	349 → 353	1	0.004	53.0
12	1.003	349 → 353	2	1.08	27.0
13	1.012	349 → 353	3	1.29	23.0
14	1.027	349 → 354	1	5.45	29.0
15	0.987	350 → 351	11	4.22	33.0
16	0.979	350 → 352	8	8.58	60.0
17	0.993	350 → 352	9	10.61	55.0
18	1.000	350 → 352	10	12.93	51.0
19	1.001	350 → 352	11	11.99	54.0
20	0.997	350 → 353	1	1.64	20.0
21	0.995	350 → 353	2	0.81	10.0
22	1.005	350 → 353	3	0.28	167.0
23	1.029	350 → 353	4	0.09	118.0
24	1.020	350 → 354	1	0.01	30.0
average				66.29	2.0

Table A.3: Possible optical transitions with 1.0 eV in the BP nanoribbon with the (1,3) edge. For each transition, its energy, band indices of the valence and conduction states, the k-point index, the maximum intensity, and the polarization angle corresponding to the maximum are shown were 0.0° is the AC direction. The averaged angle-dependent intensity is considered equal contributions from all the transitions, and the corresponding intensity and corresponding angle are listed at the bottom. Highlighted transitions are shown in Figure A.25.

A.5 Supplementary information for Chapter 5

A.5.1 Optical selection rule of PDI

Linearly polarized light that oscillates an electromagnetic field in one direction can induce anisotropic optical responses. PDI is a conjugated molecule and has a stronger absorption coefficient along the backbone (major axis, $k_{||}$) than in the orthogonal direction ($k_{\perp}$). This corresponding optical anisotropy is called linear dichroism (LD). STM studies show that PDI molecules exhibit an ordered brick-wall structure when they crystallize as an in-plane monolayer film, where the molecules are all aligned in the same direction, resulting in one molecule per unit cell. Consequently, the transition dipole moment of a single-crystalline molecular film is parallel with the major axis of the constituent molecules. Based on the optical selection rule, when light is linearly polarized along the transition dipole of the molecular crystal, a strong absorption should occur, whereas if the light polarization is aligned perpendicular to the major axis, the absorption process is inefficient. If we define the electric polarization vector of the light $\mathbf{P}$ as

$$\mathbf{P} = (cos\theta, sin\theta, 0) \tag{A.5}$$

where θ is the polarization angle of the light. Here we define s-polarization (orthogonal to tabletop) as $\theta = 0°$.

Thus the optical absorption intensity is given by

$$I \propto |\mathbf{P} \cdot \mathbf{D}| \tag{A.6}$$

where $\mathbf{D}$ is the electronic transition dipole moment of the molecule, which can be written as

$$\mathbf{D} =< \Phi_i|\nabla|\Phi_f > \tag{A.7}$$

where $< \Phi_\mathrm{i}|$ and $< \Phi_\mathrm{f}|$ are the wavefunctions of the initial and final states, and ∇ is the three-dimensional vector differential operator. Because of the two-fold rotational symmetry of the molecular structure (C_2), two degenerate optical responses are expected within a full 180° rotation of the polarization angle.

A.5.2 Power series of pump and probe excitation

We use single-beam excitation to measure a series of PEEM images of the same sample location as a function of laser power, shown in Figure A.27 We fit the photoemission intensity with a function:

$$I_{PE} = a\,x^b \tag{A.8}$$

The power dependence indicates the number of photons required to photoemit electrons from the sample surface. The fitting result from the 575 nm beam suggests a three-photon photoemission (3PPE) process (b = 2.9), whereas the 300 nm needs at least two photons (2PPE) to eject an electron (b=2.0). We additionally measured the power dependence of a 515 nm beam and the fit shows a predominantly 2PPE process (b=2.9). The photon-dependent power series additionally suggests that the work function of the bilayer is approximately in the range of 4.32 eV to 4.82 eV.

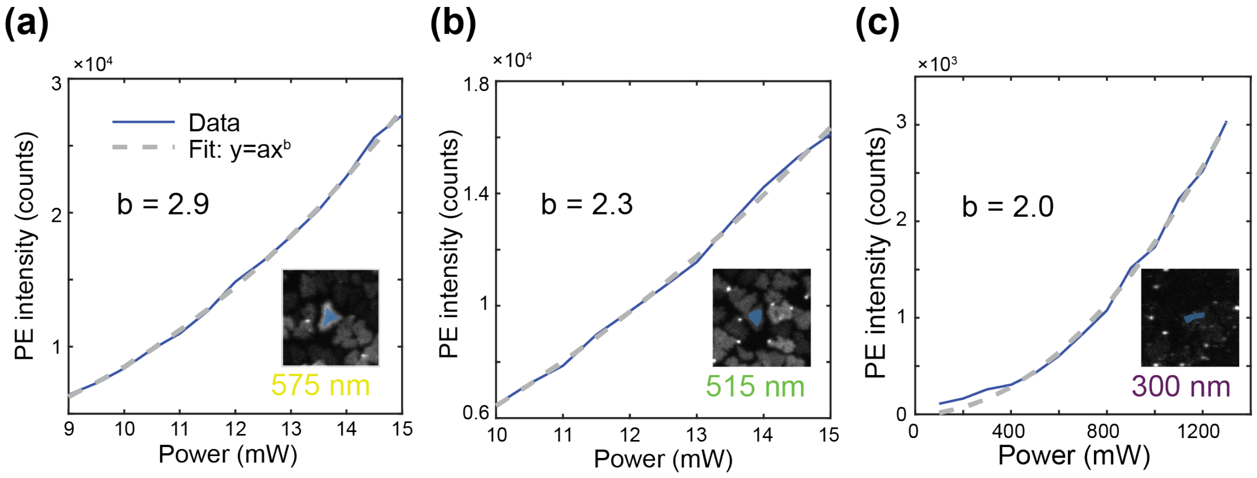

Figure A.27: Power series and fitting for (a) 575 nm (2.16 eV), (b) 515 nm (2.41 eV), and (c) 300 nm (4.13 eV).

A.5.3 Pulse duration characterization

The pulse duration of the 575 nm pump and 300 nm probe are measured by the cross-correlation with a pulse of a known temporal profile. The cross-correlation is obtained by collecting time-dependent PEEM images of a polycrystalline graphene sample, as graphene is metallic and the hot electrons have extremely fast dynamics of ∼30 fs[314,315]. An energy filter is set to detect the hottest accessible photoelectrons during the time-resolved experiments. The separation distances as well as the insertion lengths of the visible or UV prism compressor pair are adjusted after each temporal profile measurement until the optimal compression is achieved.

We define the pulse duration of a Gaussian pulse as the full width at half maximum (FWHM) of its temporal profile. The pulse duration of the 300 nm THG pulse is measured from the cross-correlation with an 816 nm pulse generated from the laser fundamental output. We determine the pulse duration of the 816 nm pulse by a frequency-resolved optical gating (FROG) setup as 35±1 fs. Figure A.28(a) shows the FROG trace as well as the Gaussian profile extracted from the integrated intensity of a certain spectral width (indicated by the white dashed lines). The cross-correlation of the 300 nm-800 nm is measured with an energy filter at 6.2 eV, and the FWHM from Gaussian fitting is 104±3 fs (Figure A.28(b)). Based on the relation:

$$\mathrm{FWHM}_{\mathrm{Xcorr}}^2 = \mathrm{FWHM}_1^2 + \mathrm{FWHM}_1^2 \tag{A.9}$$

The pulse duration of the 300 nm pulse is calculated as 27±1 fs.

We then perform a similar cross-correlation measurement with the 300 nm UV pulse and the 575 nm SHG pulse with an energy filter at 6 eV. The FWHM of the cross-correlation 99±2 fs (Figure A.28(c)), which determines the temporal resolution of the time-resolved experiments conducted in the main text. The pulse duration of the 575 nm pump pulse can be calculated then as 27±1 fs.

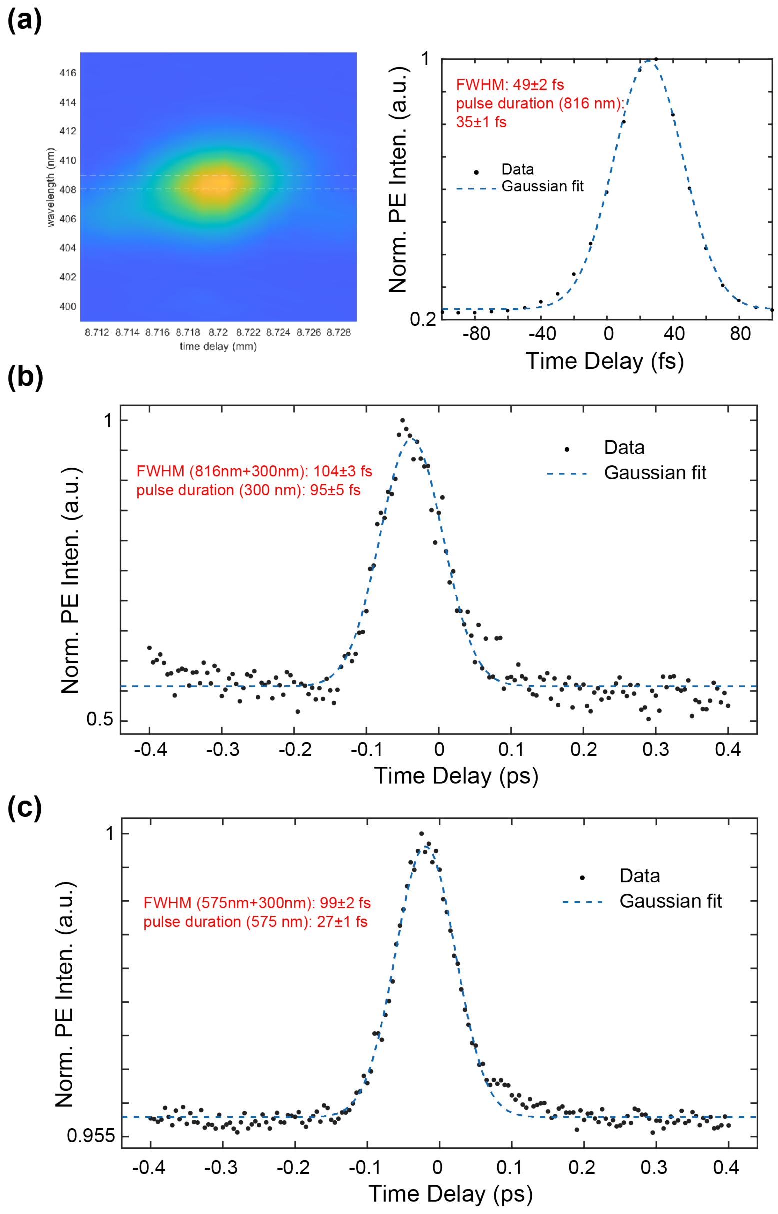

Figure A.28: Pulse duration measurements of 575 nm pump pulse and 300 nm probe pulse. (a) The FROG trace of 816 nm output and the Gaussian fit of the integrated intensity profile. (b) Cross-correlation of 816 nm and 300 nm pulses. (c) Cross-correlation of 575 nm and 300 nm pulses.

A.5.4 Pixel-by-pixel fitting algorithm

To accelerate the pixel-by-pixel fitting process, a few steps are implemented before the full frame analysis.

Polarization-dependent measurements mapping

(1) Background removal: The 1024×1024 pixels frame is cropped to a circular FOV by using a 1000-pixel diameter binary mask to remove the edges of the micro-channel plates (MCP), which is irrelevant to the photoemission signals from the sample.

(2) Linear regression fit: A matrix division method is used to extract the coefficients from the fits directly. The mathematical derivative is explained as follows. The photoemission intensity of the sample can be written as a function of light polarization angle β:

$$I = A\,cos^2(\theta - \beta) + C \tag{A.10}$$

which can be further written as:

$$\begin{aligned} I &= \frac{A}{2}\,(1 + cos(2(\theta - \beta))) + C \\ &= \frac{A}{2}\,(1 + cos2\theta\,cos2\beta + sin2\theta\,sin2\beta) + C \\ &= \frac{A}{2}\,C + \frac{A}{2}\,cos2\beta\,cos2\theta + \frac{A}{2}\,sin2\beta\,sin2\theta \\ &= k_1 + k_2\,cos2\theta + k_3\,sin2\theta \end{aligned} \tag{A.11}$$

where

$$\begin{aligned} k_1 &= \frac{A}{2} + C \\ k_2 &= \frac{A}{2}\,cos\,2\beta \\ k_3 &= \frac{A}{2}\,sin\,2\beta \end{aligned}$$

Equation A.11 can be solved by matrix division in MATLAB to obtain the coefficients k_1,

k_2, and k_3, and thus

$$\beta = \frac{1}{2} arctan(\frac{k_3}{k_2}) \tag{A.12}$$

A and C can then be numerically solved by plugging the obtained parameters:

$$A = \frac{2}{k_2} cos2\beta \tag{A.13}$$

which is also equivalent to

$$A = \frac{2}{k_3} sin2\beta \tag{A.14}$$

and,

$$C = k_1 - \frac{A}{2} \tag{A.15}$$

Thus the values of the linear dichroism can be calculated by

$$\rho = \frac{A}{A + 2C} \tag{A.16}$$

(3) Intensity threshold: As silicon does not have strong intensity modulation with rotating polarization angles, we sum the intensities of PEEM images of a stack of polarization-dependent image series. As shown in Figure A.29)(a), the substrate shows a significantly lower photoemission intensity compared to the bilayer domains and thus can be filtered out by applying an intensity threshold (Figure A.29(b)).

(4) R^2 threshold: The goodness of the fit, in this case, the linear regression relation between the real data and the fitted intensity can be evaluated by the R^2 values. If $\bar{\mathrm{I}}$ is the mean of the measured intensity $\mathrm{I}_{\mathrm{i,raw}}$,

$$\bar{I} = \frac{1}{n} \sum_{i=1}^{n} I_{i,raw} \tag{A.17}$$

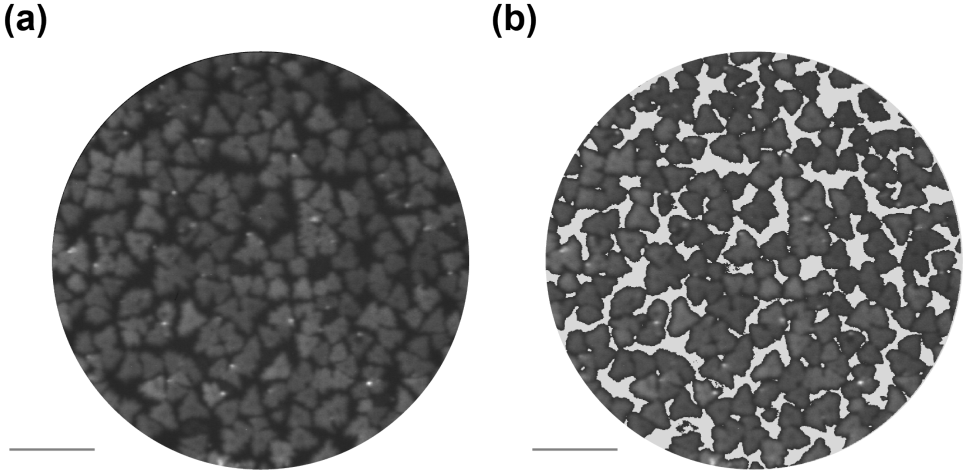

Figure A.29: (a) PEEM image integrated over a full polarization-dependent image series. (b) Intensity-filtered image from (a), where the majority of the Si background is removed. Scale bars are 3 μm.

Then R^2 is calculated based on the definition:

$$R^2 = 1 - \frac{SS_{res}}{SS_{tot}} \tag{A.18}$$

where $\mathrm{SS_{res}}$ is the residual sum squarew given by

$$SS_{res} = \sum_i (I_{i,raw} - I_{i,fit})^2 \tag{A.19}$$

and $\mathrm{SS_{tot}}$ is the total sum squares as

$$SS_{tot} = \sum_i (I_{i,raw} - \bar{I})^2 \tag{A.20}$$

Applying those formulas to each pixel, we extract an R^2 map for the PD meausurements, where the closer R^2 is to 1, the better the linear regression represents the measured intenstiy modulation. We filter the calculated θ_{TDM} map and ρ map by using an R^2 threshold of 0.5 to remove values resulted from poor fits. An R^2 map after filtering for the PD data in the main text is shown in Figure A.33.

(4) Median filter: Finally, a 3-by-3 median filter was applied to smoothen the noise for better visuliazation of the data.

Time-resolved measurements mapping

For the mapping of two time constants, the raw PEEM images are first resized by 2×2 binning, then the biexponential fitting is applied to each pixel using the Research Computing Center (RCC) at the University of Chicago. The final mapping is filtered by a threshold of the goodness of the fits (R^2).

A.5.5 Resolution determination

Figure A.30 shows a line cut from θ_{TMD} map of a more continuous bilayer sample, which has more drastic changes in θ_{TDM} at the grain boundaries. We fit the θ_{TDM} profile with an error function (dashed line), and the spatial resolution of the image (Δx) is determined by the width between 16% and 84% of the maximum. The fit shows $\Delta x = 41 \pm 10$ nm. The steps for calculating the error bar are detailed below in Section **??**.

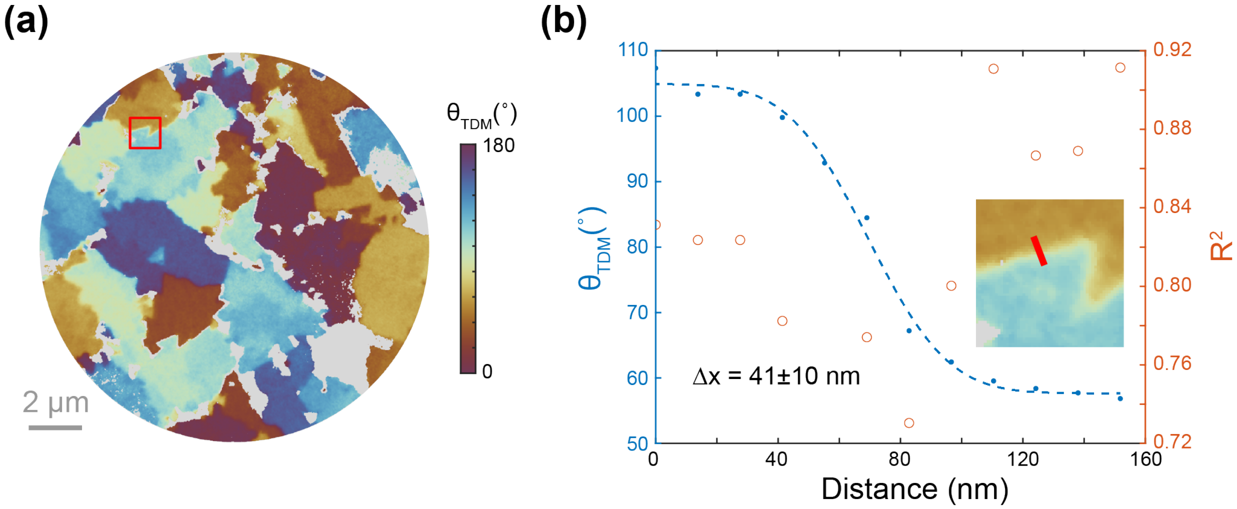

Figure A.30: (a) θ_{TDM} map of a more continuous bilayer sample. An R^2=0.6 threshold has been applied to the map. (b) θ_{TDM} profile and the corresponding R^2 values of a line cut (inset, zoom-in from the boxed region in (a)) along the grain boundary of two single crystalline PDI domains.

A.5.6 Error estimation for resolution fitting

This section explains how to calculate the 84%/16% width of the fitted function for determining resolution, as well as to estimate the fitting errors using error propagation. Suppose the collected data from the line profile is (x_i, y_i). For $y_1 > y_{end}$, the function form for the fitted curve is expressed as:

$$\hat{y}_i = f(x_i) = \frac{1}{2} A\, erfc\,[(x_i - B) \cdot C] + D \tag{A.21}$$

where $erfc(z) = 1 - erf(z)$ is the **complementary error function**. Since $erfc$ has the range (0,2), $\hat{y}_i$ has range

$$(\frac{1}{2} A \cdot 0 + D, \frac{1}{2} A \cdot 2 + D) = (D, A + D) \tag{A.22}$$

We denote the desired parameter $d_{a,b}$ as the 84%/16% width of the fitted function with the criteria:

- let p be a percentile (*i.e.* $p = 0.5$ corresponds to the 50^{th} percentile); denoted by x_p the $x - value$ such that $f(x_p)$ is at the p^{th} percentile in the range (D, A + D), *i.e.*

$$f(x_p) = pA + D \tag{A.23}$$

- **$d_{a,b}$ is defined as the difference between x_a and x_b.**
- the convention is to set $a = 0.16$ and $b = 0.84$, corresponding to the 16^{th} and 84^{th} percentiles, *i.e.* one standard deviation around the center.

To find $d_{a,b}$, we first translate a and b to the range of an erf function, which is (-1, 1):

$$p \in (0, 1) \mapsto \tilde{p} = 2p - 1 \in (-1, 1); \tag{A.24}$$

so $a = 0.16$ and $b = 0.84$ corresponds to $\tilde{a} = -0.68$ and $\tilde{b} = 0.68$, respectively.

Then

$$f(x_p) = pA + D \Leftrightarrow \frac{1}{2}\,erfc\left[(x_p - B) \cdot C\right] = p \tag{A.25}$$

$$\Leftrightarrow 1 - erf\left[(x_p - B) \cdot C\right] = p \tag{A.26}$$

$$\Leftrightarrow erf\left[(x_p - B) \cdot C\right] = 1 - 2p = -\tilde{p}, \tag{A.27}$$

therefore

$$(x_p - B) \cdot C = erf^{-1}(-\tilde{p}) \Leftrightarrow x_p = \frac{erf^{-1}(-\tilde{p})}{C} + B \tag{A.28}$$

finally,

$$\mathbf{d_{a,b}} = |\mathbf{x_a} - \mathbf{x_b}| = \frac{\left|\mathbf{erf^{-1}}(-\tilde{\mathbf{a}}) - \mathbf{erf^{-1}}(-\tilde{\mathbf{b}})\right|}{\mathbf{C}} \tag{A.29}$$

To calculate the error, write

$$d_{a,b} = K_{a,b}/C \tag{A.30}$$

where

$$K_{a,b} = \left|erf^{-1}(-\tilde{a}) - erf^{-1}(-\tilde{b})\right| \tag{A.31}$$

then, according to the general form for error propagation,

$$\frac{\Delta d_{a,b}}{d_{a,b}} = \frac{\Delta C}{C} \Leftrightarrow \mathbf{\Delta d} = \frac{\mathbf{K_{a,b}}}{\mathbf{C^2}} \cdot \mathbf{\Delta C} \tag{A.32}$$

A.5.7 Supplementary Figures

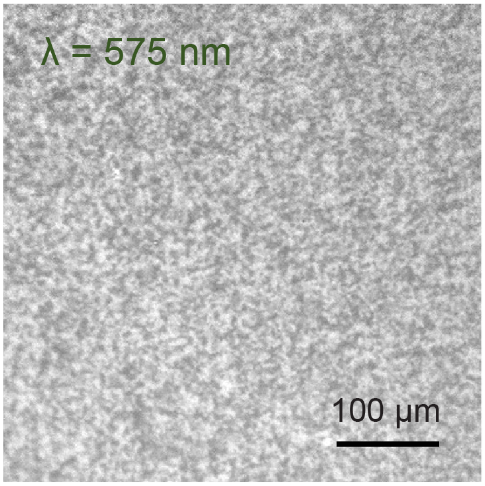

Figure A.31: Photoluminescence image of PDI/MoS_2 bilayer samples. The excitation source is a continuous-wave (CW) linearly polarized laser filtered at 575 nm. The different intensities in grayscale show the polarization-dependent absorption of the molecular domains, but the resolution is much less comparable to PEEM images.

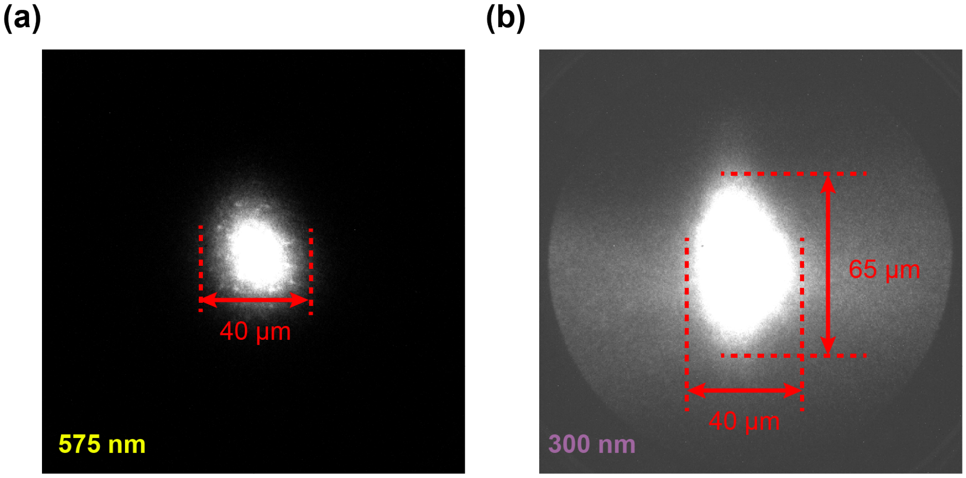

Figure A.32: Measurements of the 575 nm and 300 nm beam sizes, measured on a polycrystalline graphene sample. The contrast of the images is adjusted such that the beam profile is fully exposed.

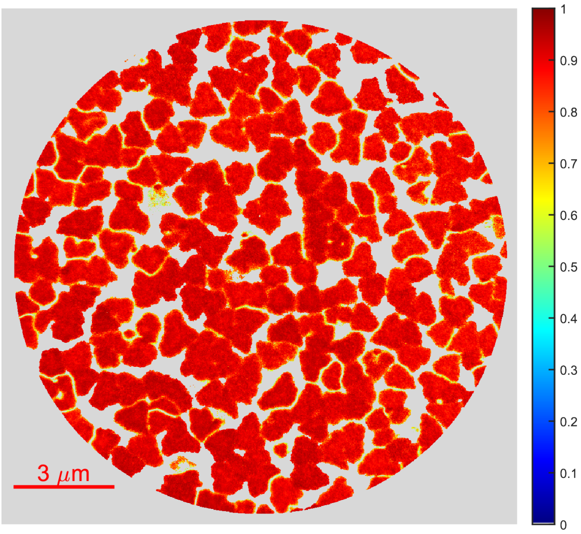

Figure A.33: Goodness of fit (R^2) map of the PD-PEEM measurements.

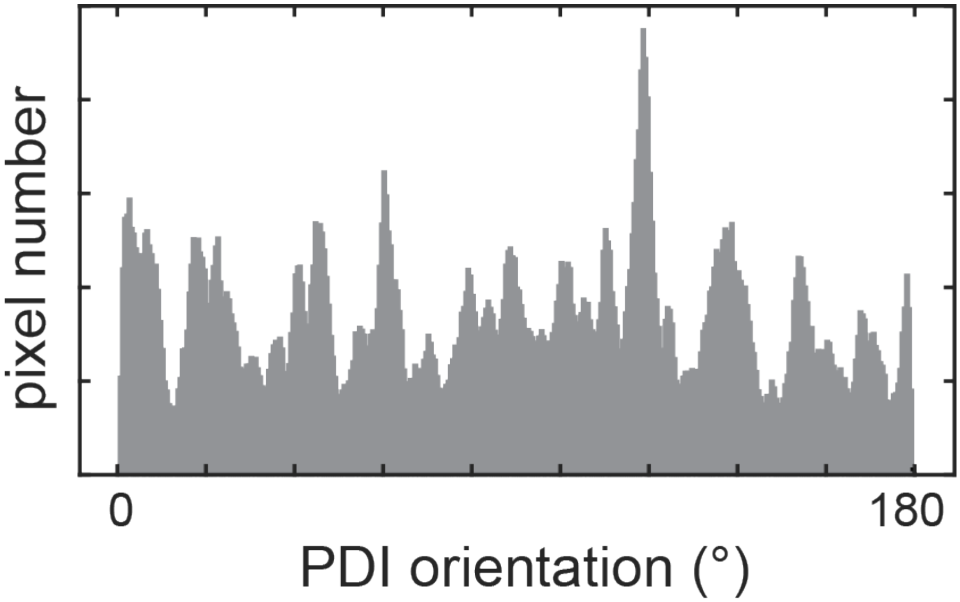

Figure A.34: Histogram of the θ_{TDM} map in the main text, showing a relatively random distribution of molecular orientations.

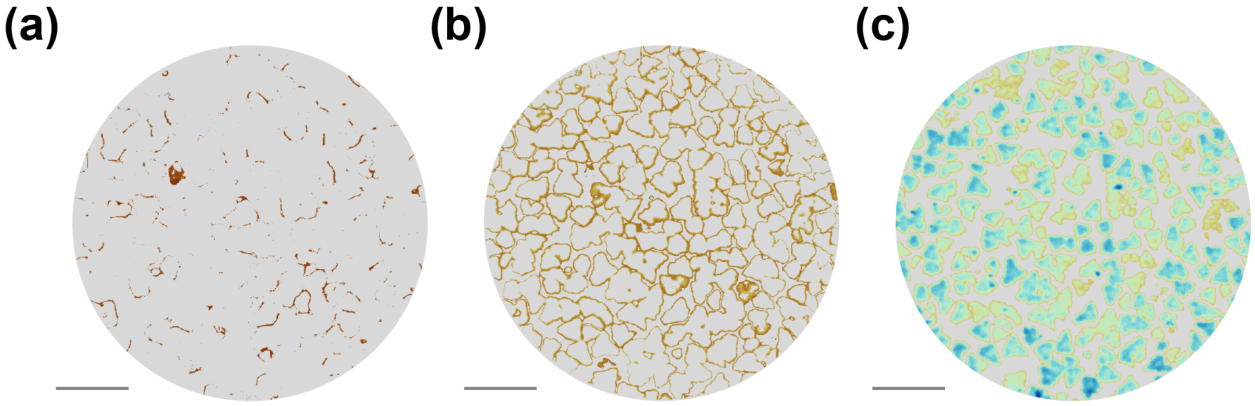

ρ<0.15

0.15<ρ<0.35

ρ>0.35

Figure A.35: ρ maps plotted of different value ranges. (a) $\rho<0.15$, where the pixels could be mostly contributed by the isotropic Si substrate. (b)$0.15<\rho<0.35$, showing primarily the edges of the bilayer flakes. (c)$\rho>0.35$, showing the interiors of the flakes. Scale bars are 3 μm.

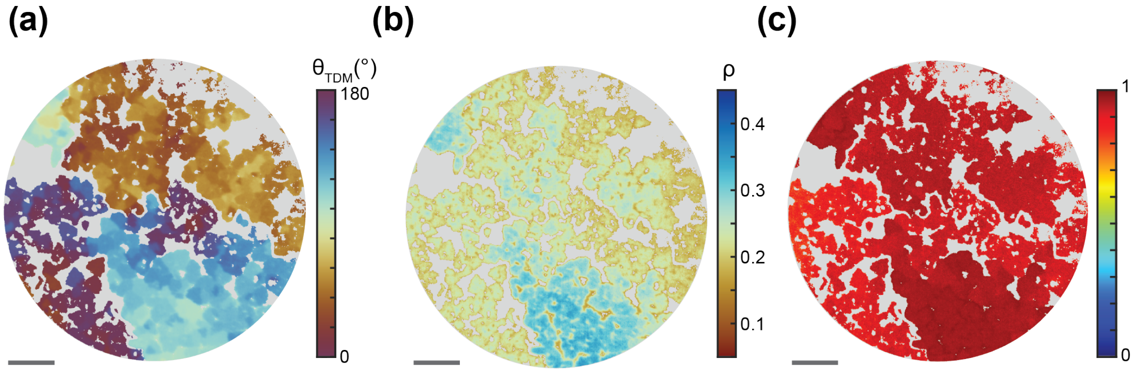

Figure A.36: Polarization-dependent PEEM mapping of the sample used for TR-PEEM measurements. (a) θ_{TDM} map. (b) ρ map. (c) R^2 map. Scale bars are 3 μm.

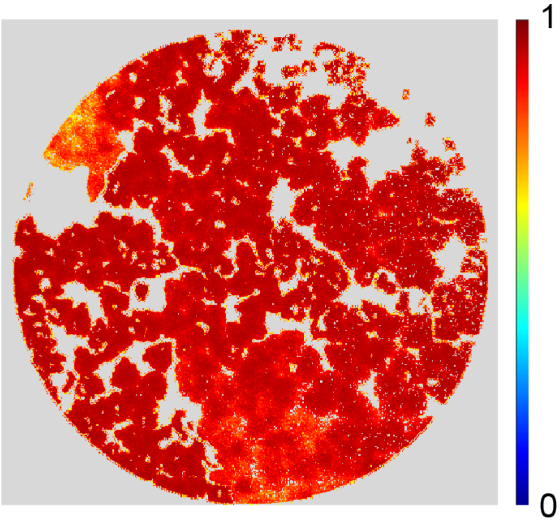

Figure A.37: Goodness of fit (R^2) map for the TR-PEEM measurements.

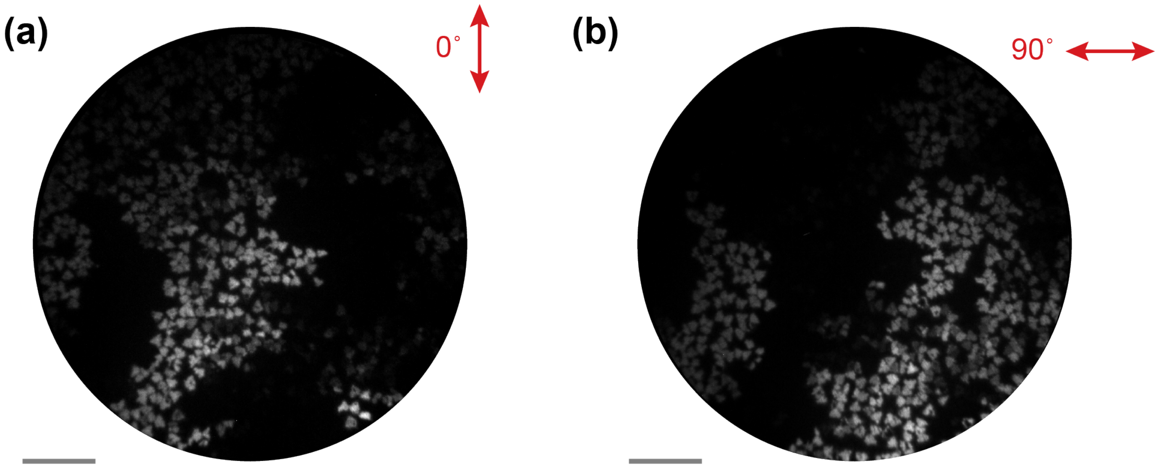

Figure A.38: PDI/MoS_2 bilayers illuminated by 670 nm laser at two vertical polarization angles of the same ROI, showing drastic photoemission intensity difference. The scale bars are both 5 μm.

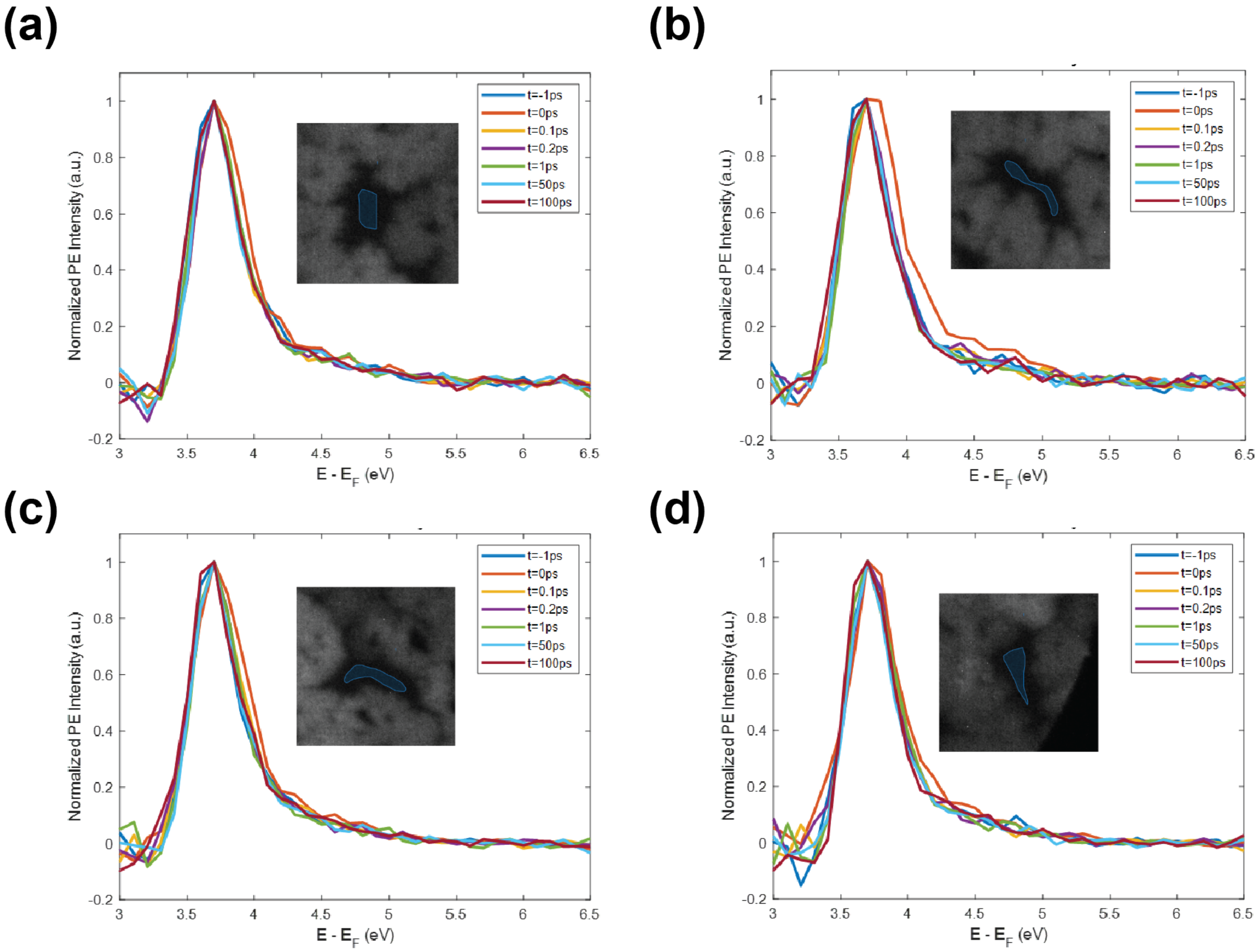

Figure A.39: Time-dependent photoemission spectra integrated from multiple substrate areas, showing that Si has no work function shift upon photoexcitation.

A.6 Supplementary information for Chapter 6

A.6.1 Sample preparation for PEEM imaging

Mouse brain tissue processed in the Kasthuri lab was prepared as previously described[226]. Briefly, mice were deeply anesthetized until unresponsive to pinch in limbs and tail. Mice were then transcardially perfused first with buffer (0.1 M sodium cacodylate, pH 7.4) followed by fixative (0.1 M sodium cacodylate, pH 7.4, 2% paraformaldehyde, and 2.5% glutaraldehyde). The brain was then extracted and incubated for 24 hours in fixative at 4 °C. Brains were vibratome sliced into 300 µm thick coronal sections. Next, a piece of cortical brain tissue ≈ 1 mm^2 was cut out with a scalpel, stained with heavy metals (i.e., osmium tetroxide, uranyl acetate, lead nitrate), dehydrated, and embedded in epoxy plastic. 40 nm ultrathin sections were cut on a Leica UC7 ultramicrotome using a Diatome Ultramaxi diamond knife and manually picked up on a 7 mm-by-7 mm silicon chip (with ≈ 2 nm native oxides) coated with 50 nm polycrystalline gold (AJA E-beam evaporator).

A.6.2 Energy-dependent PEEM imaging

Energy-dependent PEEM images were obtained by applying a high-pass energy filter to allow photoelectrons with kinetic energies higher than the threshold to be collected on the detector. As an example, Figure A.40 is a PEEM image of a 40 μm-thick mouse brain slice at energy filter E-E_F= 2 eV, where E_F is the calibrated Fermi level of the analyzer, and E-E_F is the work function difference between the sample and the ground that defines the absolute energy cut-off. For a selected region of interest (ROI), as in the boxed region in Figure A.40(a), intensity integrated over all pixels within the ROI can be plotted as a function of the energy filter as shown in Figure A.40(b).

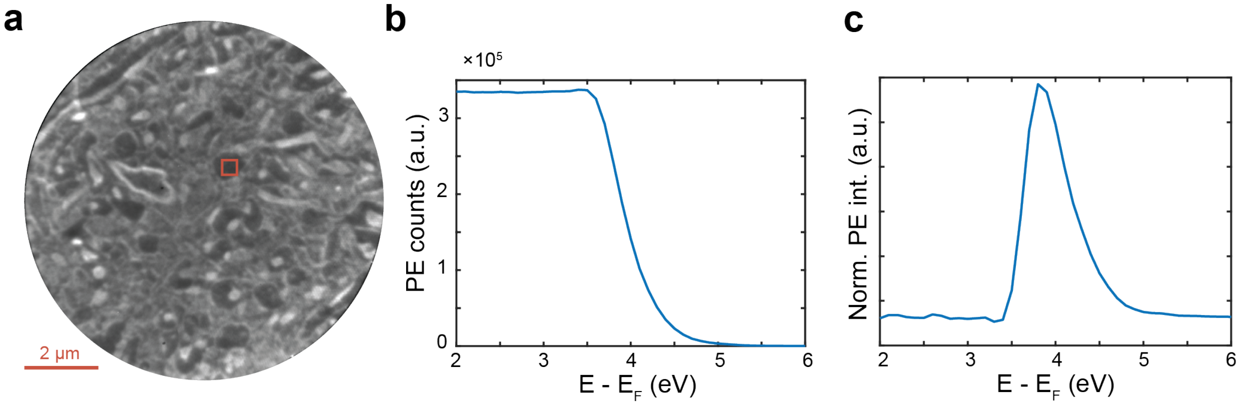

Figure A.40: (a) A representative PEEM image of an ultra-thin brain slice (UTBS) at energy filter E-E_F= 2 eV. The red box indicates the ROI for integrating photoemission intensities. (b) Photoemission counts as a function of the high-pass energy filter. Intensities are integrated from all pixels within the boxed area in (a). (c) Difference spectrum of the sum photoemission counts from (b). The spectrum is normalized to the peak intensity.)

The spectral information is extracted by subtracting subsequent high-pass energy-filtered images of total number N to obtain difference images Image diff(i) following the algorithm:

Image_diff(1)=(Image(1)-Image(2))×2 for i = 1
Image_diff(i)=Image(i-1)-Image(i+1) for i = 2 to N-1
Image_diff(N)=(Image(N-1)-Image(N))×2 for i = N

Figure A.40(c) shows the photoemission spectrum of the ROI in Figure A.40(a) after applying numerical differentiation, as the ones presented in the main text. This can then be utilized for comparing the work function difference from various regions of the specimen.

A.6.3 Fitting of photoemission spectra

The photoemission lineshape of secondary electrons can be reasonably described by an exponentially modified Gaussian function. The Gaussian distribution is written as:

$$G(x) = a_1 \frac{1}{\sqrt{2\pi}} e^{-\frac{(x-\mu)^2}{2\sigma^2}} \tag{A.33}$$

where a_1 is the amplitude, μ is the lateral offset, and σ is the standard deviation. The exponential decay is:

$$E(x) = a_2\, e^{-\lambda(x-\mu)} \tag{A.34}$$

where a_2 is the amplitude and λ is the rate of the decay. The functional form used to fit the photoemission spectrum is the convolution of the two functions, which takes of form of:

$$\begin{align} f(x) &= G(x) * E(x) \tag{A.35} \\ &= a\, e^{\frac{\lambda^2\sigma^2}{2} - \lambda(x-\mu)}\, erfc\left[\frac{1}{\sqrt{2}}\left(\lambda\sigma - \frac{x-\lambda}{\sigma}\right)\right] + I_0 \tag{A.36} \end{align}$$

where erfc is the complementary error function that is given by:

$$erfc(x) = 1 - erf(x) = \frac{2}{\sqrt{\pi}} \int_x^\infty e^{-t^2}\, dt \tag{A.37}$$

Here, a is the amplitude of the photoemission intensity, and I_0 is the intensity offset. μ represents the energy of the peak position.

As shown below in Figure A.41, the difference spectrum obtained above, namely the photoemission spectrum, is fitted with Equation A.35, where the secondary electron cutoff is calculated from the energy position that corresponds to half of the peak intensity. Here, the cutoff is found to be 3.63 eV, and the goodness of the fit is evaluated by the R^2, which is 0.997.

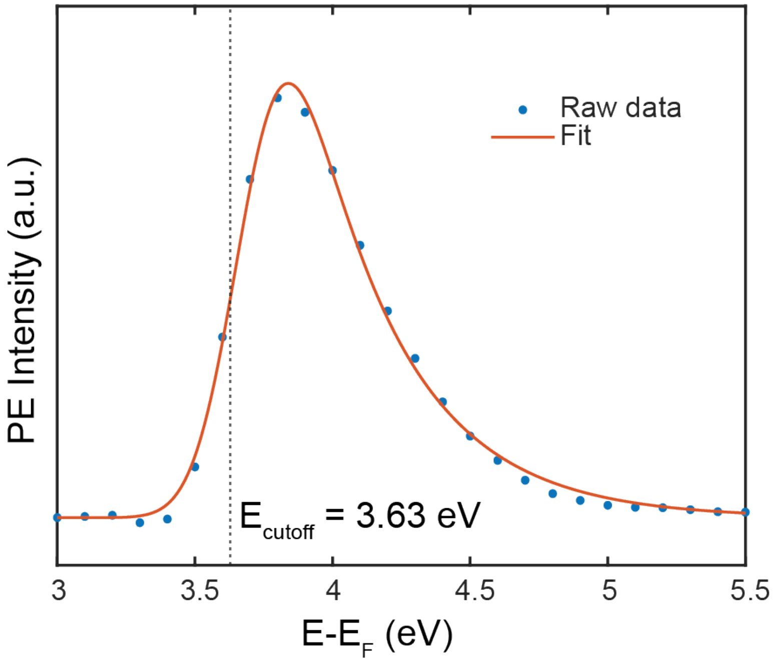

Figure A.41: Photoemission spectrum fitted with exponentially-modified Gaussian function, showing the secondary electron cutoff at 3.63 eV.

A.6.4 STEM and EDS measurements

The UTBS were deposited on lacey carbon grids to improve electron conductivity, then imaged with a JEOL ARM200-CF equipped with a cold field-emission electron source, operated at 200 kV. Imaging and spectroscopic measurements were conducted with the emission current at 15 μA, an electron probe semi-convergence angle of 24 mrad, as well as inner and outer detector angles of 68 mrad and 280 mrad for high-angle annular dark-field (HAADF) imaging. To conduct nanoscale elemental identification and quantification, the JEOL ARM200CF is equipped with an Oxford XMAX100TLE X-ray windowless silicon drift detector (SDD) with a 100 mm^2 detector area. A full spectrum of the EDS measurements shown in Figure 3(c) in the main text is provided below (Figure A.42).

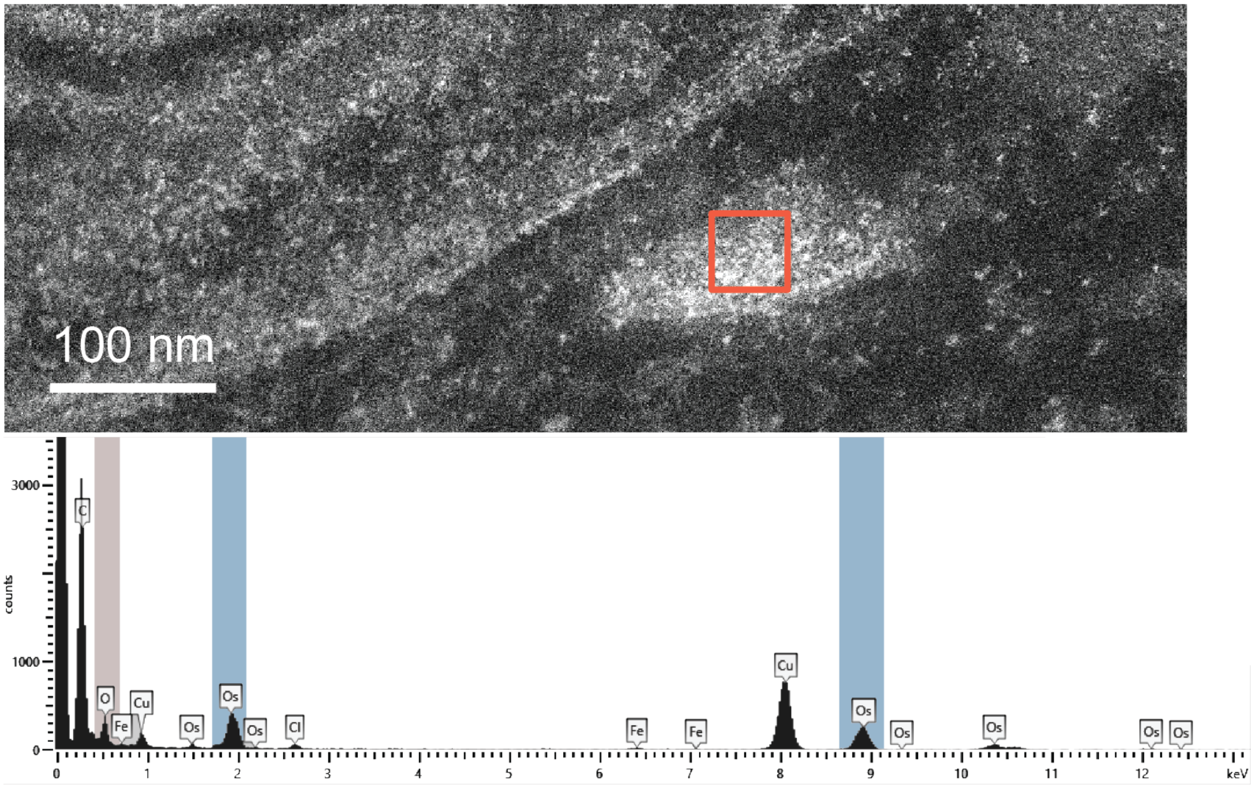

Figure A.42: The full spectrum of the EDS measurements and the corresponding ROI.

A.6.5 EELS measurements

Electron energy-loss spectroscopy (EELS) measurements were conducted on Os-rich regions as well, using a post-columns Gatan Continuum GIF ER spectrometer, with an electron probe semi-convergence angle of 17.8 mrad and a collection angle of 53.4 mrad, as seen in Figure A.43. A clear O edge and Os edge can be observed in the spectra. This corroborates the EDS results that Os is likely in an oxide form that also binds with the ligands around it, ruling out the possibility that Os exists as a majority of elemental Os. The low O concentrations detected by EDS rule out OsO_4 as the main chemical species. However, this does not rule out its existence entirely and there can still be a small amount of Os(VIII) in the sample. The combination of the EDS and EELS results indicates that Os most likely takes the valence state of IV, with some mixture of higher and lower states.

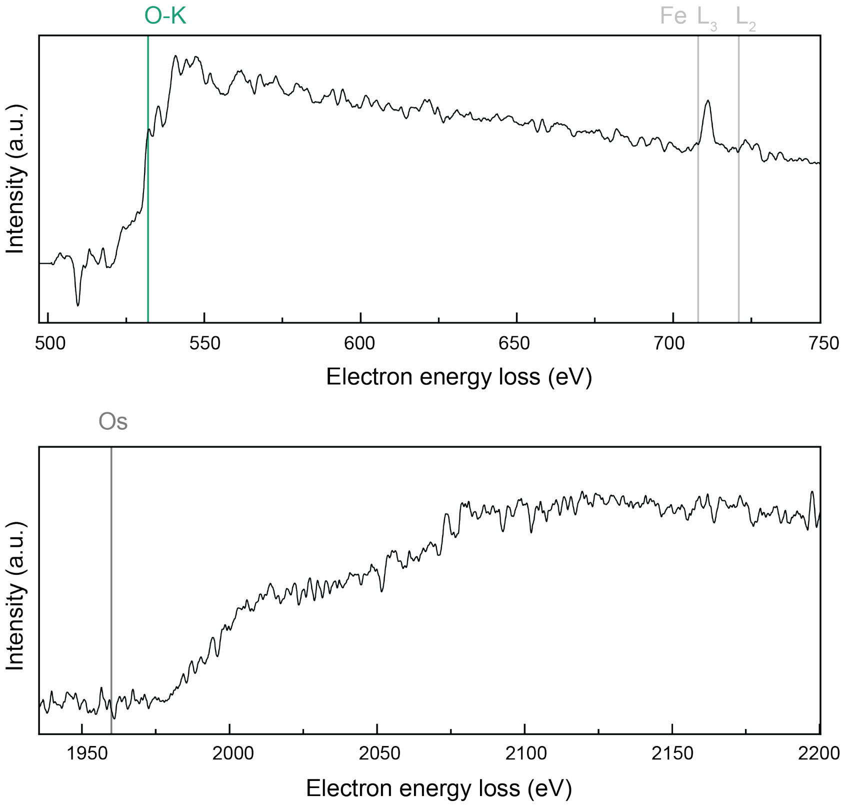

Figure A.43: EELS spectra of two energy ranges, showing characteristic edges of oxygen (top spectrum) and osmium (bottom spectrum), respectively.

A.6.6 Additional PEEM images of mouse brain tissues

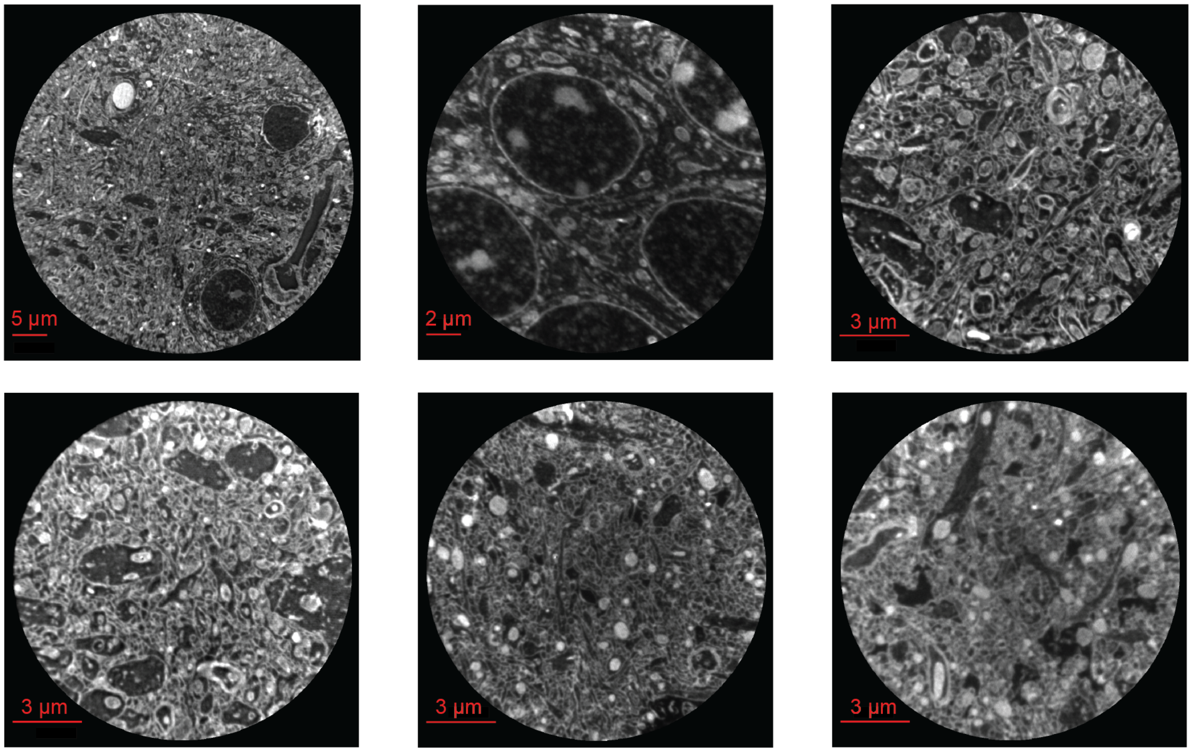

Figure A.44: Additional PEEM images collected from different sets of mouse brain samples and at different dates, and with varying FoVs. These images demonstrate the reproducibility of PEEM imaging method on Os-stained samples.

A.7 Publication list from graduate work

1. **R. Li**, T. Chowdhury, C. Liang, C. L. Keenan, J. Park, S. B. King, "Mapping excited state dynamics of molecular film/MoS_2 bilayers using ultrafast photoemission electron microscopy." *Manuscript in preparation.*

2. **R. Li**, G. Wildenberg, K. Boergens, J. Rieger, Y. Yang, R. Klie, N. Kasthuri, S. B. King, "Contrast mechanism of osmium staining in electron microscopy of biological tissue." *ChemRxiv* (2023).

3. K. M. Boergens*, G. Wildenberg,* **R. Li**, L. Lambert, A. Moradi, G. Stam, R. Tromp, S. J. van der Molen, S. B. King, N. Kasthuri, "Photoemission electron microscopy for connectomics." *bioRxiv* (2023). (* indicates equal contribution)

4. P. P. Joshi, D. Unruh, T. E. Gage, **R. Li**, H. Liu, L. Liang, I. Arslan, M. K. Y. Chan, S. B. King, "Anomalous reduction in black phosphorus phonon velocities driven by lattice anisotropy." *ChemRxiv.* (2023).

5. B. Guzelturk, V. Kamysbayev, D. Wang, H. Hu, **R. Li**, S. B. King, A. H. Reid, M.-F. Lin, X. Wang, D. A. Walko, X. Zhang, A. Lindenberg, D. V. Talapin, "Understanding and controlling photothermal responses in MXenes." *Nano. Lett.* **23**, 7, 2677–2686 (2023).

6. P. P. Joshi*, **R. Li***, J. L. Spellberg, L. Liang, S. B. King, "Nanoimaging of the edge-dependent optical polarization anisotropy of black phosphorus." *Nano. Lett.* *22*, 8 (2022). (* indicates equal contribution)